

AD-A113 621

TRANSPORTATION SYSTEMS CENTER CAMBRIDGE MA

F/G 20/4

8-747 VORTEX ALLEVIATION FLIGHT TESTS: GROUND-BASED SENSOR MEAS--ETC(U)

JAN 82 D C BURNHAM

DOT-TSC-FAA-81-19

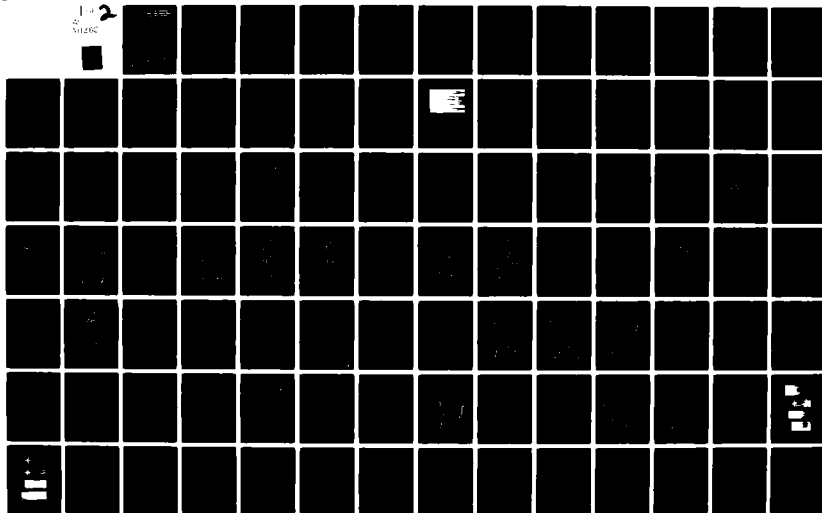
DOT/FAA/RD-81-99

NL

UNCLASSIFIED

1-4  
VOL 200

2



DOT-FAA-RD-81-99  
DOT-TSC-FAA-81-19

# B-747 Vortex Alleviation Flight Tests: Ground-Based Sensor Measurements

13

AD A113621

D.C. Burnham

Transportation Systems Center  
Cambridge MA 02142

February 1982  
Final Report

This document is available to the public  
through the National Technical Information  
Service, Springfield, Virginia 22161.

DTIC FILE COPY



U.S. Department of Transportation  
Federal Aviation Administration

DTIC  
ELECT  
APR 19 1982  
E

Systems Research and Development Service  
Washington DC 20591

82 04 19 005

**NOTICE**

This document is disseminated under the sponsorship of the Department of Transportation in the interest of information exchange. The United States Government assumes no liability for its contents or use thereof.

**NOTICE**

The United States Government does not endorse products or manufacturers. Trade or manufacturers' names appear herein solely because they are considered essential to the object of this report.

Technical Report Documentation Page

1. Report No. DOT-FAA-RD-81-99	2. Government Accession No. AD-A113 621	3. Recipient's Catalog No. -	
4. Title and Subtitle B-747 VORTEX ALLEVIATION FLIGHT TESTS: GROUND-BASED SENSOR MEASUREMENTS		5. Report Date January 1982	
		6. Performing Organization Code	
		8. Performing Organization Report No. DOT-TSC-FAA-81-19	
7. Author(s) D.C. Burnham		10. Work Unit No. (TRAIS) FA186/R1116	
9. Performing Organization Name and Address U.S. Department of Transportation Research and Special Programs Administration Transportation Systems Center Cambridge MA 02142		11. Contract or Grant No.	
12. Sponsoring Agency Name and Address U.S. Department of Transportation Federal Aviation Administration Systems Research and Development Service Washington DC 20591		13. Type of Report and Period Covered Final Report Jan. 1979 - Sept. 1980	
14. Sponsoring Agency Code			
15. Supplementary Notes			
16. Abstract <p>In 1979, a series of B-747 flight tests were carried out to study the wake-vortex alleviation produced by deploying spoilers in the landing configuration. The alleviation achieved was examined by encounters of probe aircraft and by velocity profile measurements made by a ground-based Laser Doppler Velocimeter. For the first time these two types of measurements were analyzed in a way which allowed direct comparison; they showed reasonable agreement. The velocimeter measurements can be used to evaluate the vortex-induced rolling moment on any following aircraft at any separation. The spoiler alleviation was found to be insufficient to assure safe landings of small aircraft at reduced separation behind the B-747. The persistence of the alleviated vortices appears to be due to the wing-tip vortices which dominate the roll-up of the spoiler-alleviated wake. The addition of rapid roll inputs to the spoiler deployment produced much more effective alleviation, but at the expense of an unacceptable ride quality in the generating aircraft.</p>			
17. Key Words Aircraft Wake Vortices Vortices Vortex Alleviation Laser Doppler Velocimeter Vortex Decay		18. Distribution Statement  DOCUMENT IS AVAILABLE TO THE PUBLIC THROUGH THE NATIONAL TECHNICAL INFORMATION SERVICE, SPRINGFIELD, VIRGINIA 22161	
19. Security Classif. (of this report) Unclassified	20. Security Classif. (of this page) Unclassified	21. No. of Pages 164	22. Price

# METRIC CONVERSION FACTORS

Approximate Conversions to Metric Measures				Approximate Conversions from Metric Measures			
Symbol	When You Know	Multiply by	To Find	Symbol	When You Know	Multiply by	To Find
<b>LENGTH</b>							
m	meters	1.0	meters	m	meters	1.0	meters
cm	centimeters	0.01	centimeters	cm	centimeters	0.01	centimeters
mm	millimeters	0.001	millimeters	mm	millimeters	0.001	millimeters
km	kilometers	1,000	kilometers	km	kilometers	1,000	kilometers
<b>AREA</b>							
m <sup>2</sup>	square meters	1.0	square meters	m <sup>2</sup>	square meters	1.0	square meters
cm <sup>2</sup>	square centimeters	0.0001	square centimeters	cm <sup>2</sup>	square centimeters	0.0001	square centimeters
mm <sup>2</sup>	square millimeters	0.000001	square millimeters	mm <sup>2</sup>	square millimeters	0.000001	square millimeters
ha	hectares	10,000	hectares	ha	hectares	10,000	hectares
<b>MASS (weight)</b>							
g	grams	1.0	grams	g	grams	1.0	grams
kg	kilograms	1,000	kilograms	kg	kilograms	1,000	kilograms
lb	pounds	0.45	pounds	lb	pounds	0.45	pounds
oz	ounces	0.07	ounces	oz	ounces	0.07	ounces
<b>VOLUME</b>							
m <sup>3</sup>	cubic meters	1.0	cubic meters	m <sup>3</sup>	cubic meters	1.0	cubic meters
cm <sup>3</sup>	cubic centimeters	0.001	cubic centimeters	cm <sup>3</sup>	cubic centimeters	0.001	cubic centimeters
mm <sup>3</sup>	cubic millimeters	0.000001	cubic millimeters	mm <sup>3</sup>	cubic millimeters	0.000001	cubic millimeters
l	liters	1.0	liters	l	liters	1.0	liters
gal	gallons	0.26	gallons	gal	gallons	0.26	gallons
qt	quarts	0.09	quarts	qt	quarts	0.09	quarts
p	pints	0.05	pints	p	pints	0.05	pints
c	cups	0.24	cups	c	cups	0.24	cups
f	fluid ounces	0.03	fluid ounces	f	fluid ounces	0.03	fluid ounces
<b>TEMPERATURE (Celsius)</b>							
°C	Celsius temperature	1.8	Fahrenheit temperature	°C	Celsius temperature	1.8	Fahrenheit temperature
°F	Fahrenheit temperature	0.56	Celsius temperature	°F	Fahrenheit temperature	0.56	Celsius temperature

\* 1 in = 2.54 in exactly. For other exact conversions and more detailed tables, see NIST Spec. Publ. 280, (Units of Length and Mass), Price \$2.25, 30 Casing No. C13.10-280.

## PREFACE

The Federal Aviation Administration (FAA) wake-vortex program has designated vortex avoidance considerations to the Department of Transportation's (DOT) Transportation Systems Center (TSC) and possible vortex alleviation via aircraft modifications to the National Aeronautics and Space Administration (NASA). Until 1975 these two efforts were conducted essentially independently. TSC collected data on wake-vortex behavior using a variety of sensors, and NASA studied vortex alleviation techniques by means of wind tunnels and flight tests measuring the effects of vortex penetration by following aircraft. In December 1975 at Rosamond Dry Lake in California the ground-based sensors used by TSC at airports to measure vortex behavior were used to measure the alleviation produced by the NASA-developed techniques on the wake vortices from a B-747 aircraft. The work reported here is the next series of such vortex alleviation flight tests. A smaller number of ground-based sensors were used to study some new vortex alleviation schemes both in and out of ground effect.

I would like to thank Russ Barber of the NASA Dryden Flight Research Center (DFRC) for his role in planning and directing the flight tests. Ivar Tombach and John Blair from AeroVironment (under contract to TSC) were responsible for the photographic tracking of vortices and for the recording of meteorological data. The TSC/FAA Laser Doppler Velocimeter (LDV) van was operated (under contract to TSC) by the Lockheed Missiles and Space Corp. personnel, Charles Craven, Oliver Brandt, and Bert Demon. The latter also took the excellent vortex smoke pictures which appear in this report. I would like to thank the Marchand Construction Company of Moses Lake, Washington, for furnishing a test site and electric power for the high-altitude tests at Moses Lake. The Port of Moses Lake Authority supplied a site and power for the ground effect tests at Moses Lake. The tests at the China Lake Naval Weapons Center in California were coordinated by Dick Truax of that center. Ian McWilliams of TSC participated extensively in collecting the

ground-based sensor data and in the early data processing. Sandy Grace and Andrea Talamas of Systems Development Corporation (SDC) assisted in the final data processing. Alex Sims of the NASA DFRC and Joe Lanza of SDC helped in the vortex-lattice rolling moment calculations. Finally, I would like to acknowledge the helpful discussions with Jim Hallock of TSC, Del Croom of the NASA Langley Research Center, and Joe Tymczyszyn of the FAA Western Region.

Accession For	
NTIS GRA&I	<input checked="" type="checkbox"/>
DTIC TAB	<input type="checkbox"/>
Unannounced	<input type="checkbox"/>
Justification	
By	
Distribution/	
Availability Codes	
Dist	Avail and/or Special
A	



## TABLE OF CONTENTS

<u>Section</u>	<u>Page</u>
1. SUMMARY.....	1
2. INTRODUCTION.....	2
2.1 Vortex Alleviation.....	2
2.2 History of Joint National Aeronautics and Space Administration/Department of Transpor- tation (NASA/DOT) Effort.....	3
2.3 1979 B-747 Flight Tests.....	5
2.4 1980 L-1011 Flight Tests.....	8
3. TEST DESCRIPTION.....	9
3.1 Aircraft Configuration.....	9
3.2 Sensor Capabilities.....	11
3.2.1 Laser Doppler Velocimeter.....	11
3.2.1.1 Principles of Operation.....	11
3.2.1.2 Scan Mode.....	13
3.2.2 Ground Wind Vortex Sensing System.....	15
3.2.3 Photography.....	17
3.3 Sensor Utilization.....	17
3.4 Test Flights.....	18
3.4.1 Series 1: Moses Lake.....	18
3.4.2 Series 2: Southern California.....	22
3.4.2.1 China Lake Naval Weapons Center.....	22
3.4.2.2 Edwards Air Force Base (AFB)..	24
4. DATA ANALYSIS.....	27
4.1 Laser Doppler Velocimeter.....	27
4.1.1 Vortex Identification.....	27
4.1.2 Range Determination.....	30
4.1.3 Strength Determination.....	33
4.1.4 Rolling Moment Determination.....	41
4.1.5 Crosswind Corrections.....	44
4.1.6 Limitations of LDV Measurements.....	44
4.2 Ground Wind Vortex Sensing System.....	49
4.3 Photography.....	52
5. RESULTS.....	54
5.1 Vortex Strength.....	54
5.2 Comparisons With Other Measurements.....	66



## TABLE OF CONTENTS (CONTINUED)

<u>Section</u>	<u>Page</u>
5.2.1 Probe Aircraft.....	66
5.2.2 Wind Tunnel Measurements.....	70
5.3 Effect of Spoilers on Vortex Roll-Up.....	73
5.4 Periodic Rolling Configuration.....	76
6. RECOMMENDATIONS.....	79
6.1 Future Alleviation Studies.....	79
6.2 Role of Ground-Based Sensors in Alleviation Tests.....	79
6.3 Optimum Use of Ground-Based Sensors in Future Tests.....	80
6.4 Sensor Training.....	81
6.5 Comparison of Alleviation Tests With Operational Tests.....	81
6.6 Implications for Scale-Model Testing.....	81
REFERENCES.....	83
APPENDIX A: LASER DOPPLER VELOCIMETER (LDV) SOFTWARE DEVELOPMENT.....	A-1
A.1 History.....	A-1
A.2 Data Collection.....	A-1
A.3 Data Processing.....	A-2
A.3.1 Vortex Tracking.....	A-2
A.3.2 Range Algorithm.....	A-5
APPENDIX B: ROLLING MOMENT CALCULATIONS.....	B-1
APPENDIX C: EVALUATION OF GROUND-BASED SENSOR MEASUREMENTS OF VORTEX-VELOCITY PROFILES.....	C-1
C.1 1975 B-747 Velocity Profiles.....	C-1
C.2 Laser Doppler Velocimeter.....	C-5
C.2.1 LDV Simulation.....	C-5
C.2.2 LDV Data.....	C-7
C.3 The MAVSS.....	C-7
C.3.1 MAVSS Simulation.....	C-7
C.3.2 MAVSS Data.....	C-15
C.4 Comparisons With Instrumented Tower Data.....	C-16
C.5 Sensor Conclusions.....	C-18

## TABLE OF CONTENTS (CONTINUED)

<u>Section</u>	<u>Page</u>
APPENDIX D: ROSAMOND LAKE MONOSTATIC ACOUSTIC VORTEX SENSING SYSTEM (MAVSS) DATA.....	D-1
APPENDIX E: LASER DOPPLER VELOCIMETER (LDV) DATA.....	E-1
APPENDIX F: LATERAL POSITION PLOTS.....	F-1
APPENDIX G: METEOROLOGICAL DATA.....	G-1

## LIST OF ABBREVIATIONS

AFB	Air Force Base
AGL	Above ground level
CW	Continuous wave
DFRC	Dryden Flight Research Center
DOT	Department of Transportation
FAA	Federal Aviation Administration
GWVSS	Ground Wind Vortex Sensing System
LDV	Laser Doppler Velocimeter
LOS	Line-of-sight
MAVSS	Monostatic Acoustic Vortex Sensing System
NASA	National Aeronautics and Space Administration
SAW	Surface Acoustic Wave
SDC	Systems Development Corporation
TSC	Transportation Systems Center
B-707	Boeing Model 707
B-747	Boeing Model 747
DC-8	McDonnell-Douglas Model 8
DC-9	McDonnell-Douglas Model 9

## 1. SUMMARY

In 1979, a series of B-747 flight tests were carried out to examine the vortex alleviation produced by deploying spoilers during landing. The alleviation achieved was measured by two methods: 1) penetrating the vortex with a small probe aircraft and 2) measuring the vortex velocity profile with a ground-based sensor. The original goal of the tests was to achieve a manned landing of a small aircraft at reduced separation (less than 6 nautical miles) behind the B-747; the alleviation produced by the spoilers was judged to be insufficient to assure safety in such an operation.

Although the original goal of the tests was not achieved, significant discoveries were made which would serve to guide the vortex alleviation program in the future. First, two promising new concepts for alleviation were identified: 1) Rolling the aircraft with spoilers deployed was found to enhance the alleviation by a factor of two. 2) The persistence of the spoiler-alleviated vortices was traced to the wing-tip vortex which forms the core of such vortices; destroying the wing-tip vortex should lead to much improved alleviation. Second, for the first time the ground-based-sensor velocity measurements of wake vortices were converted to a form where they could be directly related to probe aircraft measurements. The sensor and probe results were in reasonable agreement. This agreement indicated that special care is needed when relying on wind-tunnel measurements to predict alleviation behavior; the wind-tunnel results show both qualitative and quantitative disagreements with flight-test results. Third, the errors associated with the ground-based sensors used to measure vortex strength were examined in detail so that the limitations of the measurements are now well documented (Appendix C). Fourth, the best way of using ground-based sensors in vortex alleviation work was determined. Such sensors would play an important role in future alleviation testing because they give information that would be either more costly or impossible (because of safety considerations) to obtain from aircraft probe measurements.

## 2. INTRODUCTION

The wake-vortex hazard is a primary factor in setting the minimum safe separation of aircraft in the airport environment. At the busiest airports these wake-vortex mandated separations contribute to the large delay costs incurred by the airlines. Since airport expansion is not a practical option in the current environment, these delay costs can be reduced only by increasing the capacity of presently existing runways. Any plan to increase capacity by closer aircraft spacing must therefore deal with the wake-vortex problem.

During the past decade, the Federal Government has expended substantial resources in seeking a solution to the wake-vortex problem. Two fundamentally different approaches have been studied: vortex alleviation and vortex avoidance. Vortex alleviation reduces the vortex strength at its source, the generating aircraft. Vortex avoidance makes use of the very conservative nature of the current wake-vortex separations which must provide safe spacing under all meteorological conditions; in fact, reduced spacings would be safe most of the time. The variable spacings mandated by a vortex avoidance system are not easily accommodated by the present air traffic control system. Difficulties in implementing a simple avoidance system, the Vortex Advisory System, led to a renewed interest in vortex alleviation.

The introduction of this report will examine the current concepts and requirements of vortex alleviation in considerable detail since they have not been reported elsewhere. The main body of the report will concentrate on the ground-based sensor measurements for which the Transportation Systems Center (TSC) was responsible.

### 2.1 VORTEX ALLEVIATION

The operational goal of the vortex alleviation program is to modify the configuration of the generating aircraft in such a way that its wake-vortex hazard will no longer impose safety limits on

the separations of following aircraft. Such a resolution of the wake-vortex problem is philosophically appealing since the producer of the hazard takes the responsibility for alleviating it and, moreover, the system would be available at any airport. A fundamental question which must be faced by the alleviation program is the definition of how much alleviation is enough. Wrestling with this question has been a persistent part of the work reported here.

The wake-vortex alleviation program (Ref. 1), implemented at several NASA centers, has made an extensive investigation of aircraft modifications which might be expected to reduce wake-vortex strength and/or accelerate wake-vortex decay. In addition to effectively alleviating the wake vortices, a successful alleviation technique must be economical to install and not produce excessive aircraft operational penalties. The vortex alleviation technique examined in recent flight tests makes use of spoiler deployment during flight. Spoiler techniques are appealing since spoilers are present on all jet transport aircraft and can be tested (and retrofitted) without adding any aerodynamic components. Some modification of the spoiler control system may be required, however, to establish the desired alleviating configuration.

## 2.2 HISTORY OF JOINT NATIONAL AERONAUTICS AND SPACE ADMINISTRATION/ DEPARTMENT OF TRANSPORTATION (NASA/DOT) EFFORT

Until 1975, the NASA vortex alleviation work and the DOT vortex avoidance work were carried out essentially independently. The two groups used different measurement techniques for flight tests and, as one might expect, the results were incompatible.

The NASA work relied primarily on high-altitude wake penetrations by a probe aircraft, usually the NASA T-37. The vortex-induced response of the probe aircraft is used to determine the strength of the wake as a function of aircraft separation. The wake is marked with smoke so that the pilot of the probe aircraft can locate and maneuver into the vortex center. This experimental technique has the virtue of giving a direct indication of the vortex hazard to the specific probe aircraft; however, it does not

give a good indication of the hazard to a different-sized aircraft. It is also difficult to prove that the vortex has actually decayed by means of probe aircraft penetrations, since a vortex which has lost its smoke marking (but not necessarily its hazard) is hard to locate and probe. Because of the safety requirements for recovery from a vortex encounter, vortex probing must be carried out at high altitudes, where the vortex decay characteristics may be quite different from those near the ground where the operational hazard exists.

The DOT studies have used ground-based sensors which have limited range. At first, instrumented towers were used to measure the velocity profiles of aircraft in dedicated flybys. Later, remote sensing systems were developed which allowed data collection during normal airport operations. Since no aircraft costs are then incurred, large statistical data bases on vortex behavior near the ground could be collected at reasonable cost.

The results of the NASA and DOT tests diverge on some significant points. For example, the NASA tests indicate that a small aircraft (like the T-37) should remain more than 19 km (10 nautical miles) behind a B-747 in landing configuration. On the contrary, DOT results indicate that 11 km (6 nautical miles) is a safe separation. Some of this difference may be due to differences in the criterion for safety, but most of it is probably due to the differences in the test altitude and the test meteorological conditions.

In 1975, the DOT and NASA measurement techniques were combined in a joint project to study various configurations of the Boeing 747 (Ref. 2). The ground-based sensor measurements were made on Rosamond Dry Lake which is part of Edwards Air Force Base, the home of the NASA Dryden Flight Research Center (DFRC). The Rosamond Lake tests showed that it is difficult to correlate data between the various ground-based sensors because of differences in coverage. It is even more difficult to correlate low-altitude (<250 meters) sensor data with high-altitude vortex encounter data.

A fundamental problem in comparing sensor data to encounter data is that different quantities are being measured. A model for how a vortex affects a probe aircraft is required to convert vortex-velocity profiles into induced moments on the wing of an aircraft. One of the goals set for this report was to make this transformation in order to plot sensor and encounter data on graphs with identical coordinates.

### 2.3 1979 B-747 FLIGHT TESTS

The initial impetus for the 1979 flight tests came from wind-tunnel measurements (Ref. 3) identifying two B-747 spoiler configurations which were superior to the spoiler configurations flight-tested in 1975. The wind-tunnel data indicated that more alleviation could be achieved with a smaller drag penalty.

The 1979 test design was influenced by major improvements which had been made in the ground-based Laser Doppler Velocimeter (LDV) since the 1975 tests. A new mode of operation was developed which allows simultaneous tracking and measurement of wake vortices. In addition, the data can be partially analyzed on site as soon as a test sequence has been completed.

The 1979, flight test program was organized by NASA DFRC and supported by DOT/TSC. Meteorological forecasting and measurements were supplied by AeroVironment, Inc. The generating aircraft was leased from the Boeing Company.

The first series of tests were carried out in February at the Grant County Airport in Moses Lake, Washington. Vortex strength measurements were made with the NASA DFRC T-37 probe aircraft and with the TSC/FAA LDV. The T-37 encounters indicated that the vortex-induced rolling moment with spoiler alleviation was within the control capability of the aircraft. The first examination of the LDV data showed relatively small alleviation. The LDV results were not considered definitive because of a systematic error whose magnitude had not been estimated at that time. Some of the LDV data were also of short duration.



The T-37 probe results at Moses Lake were promising enough that a second series of tests was planned for the fall of 1979 with the goal of landing the T-37 behind an alleviated B-747 at less than the standard separation of 11 km (6 nautical miles). This goal was approached gradually to assure safety at each step of the operation. First, the standard higher altitude T-37 probes were extended down to 200-meter altitude above ground level (AGL) at Edwards Air Force Base (AFB). Second, probes of the B-747 wake down to landing were carried out with an unmanned F-86 drone aircraft at the China Lake Naval Weapons Center, about 80 km north of Edwards AFB. Third, manned T-37 probes down to landing were to take place back at Edwards AFB.

The tests produced a number of surprises which eventually led to significant changes in the test plan. The first surprise was the existence of "hard spots" in the alleviated wake where the induced roll was greater than the roll control of the T-37. The hard spots appeared to be correlated with vortex waviness, which was induced by very light turbulence at the test altitudes. The vortices had remained straight during the Moses Lake tests. These hard spots were viewed as an obstacle to achieving the goal of a manned landing at reduced separation. The F-86 flights were carried out, nevertheless, in the hope that more rapid vortex decay near the ground might still allow safe landings in spite of the hard spots. Unfortunately, the F-86 results did not show the desired effect. The F-86 experienced vortex-induced rolls as large as  $60^{\circ}$  at 30-meter altitude (AGL) and 7 km (4 nautical-mile) spacing. The F-86 subsequently executed 7 landings at 7 km (4 nautical miles) behind the alleviated B-747, but the ground-based sensors indicated that the F-86 was never close to a vortex when the F-86 got near the runway.

An analysis of the F-86 results led to a decision to cancel the planned manned T-37 landings behind the alleviated B-747. Because the F-86 is flown remotely using a television camera mounted in the nose, it undoubtedly suffers from a slower response to a vortex encounter than would a manned T-37. On the other

hand, the F-86 has a 50 percent greater roll control authority than the T-37. Taking these differences into account, those responsible for the safety of the tests concluded that the B-747 alleviation was not adequate to assure safe T-37 landings at reduced separations.

Perhaps the biggest surprise of the tests was discovered inadvertently. Previously tested alleviating configurations showed a loss of alleviation during aircraft maneuvers. During an examination of the effects of maneuvers on spoiler alleviation, the alleviation was found to be dramatically improved when the aircraft was rolled periodically with a 3-second period. Both the spoilers and ailerons are active during this maneuver. The spoilers oscillate above their static deployment angle and also drop to zero angle, thereby eliminating momentarily the alleviation on one wing. The T-37 pilots described the wake from the rolling maneuver as having "no rotary motion." The measured maximum induced rolling moment was about half the T-37 roll control authority. Because of the interest generated by the discovery of this new configuration, a final phase of testing at Edwards AFB was devoted to examining its characteristics. Spoiler deployment was found to be an essential part of the configuration.

The rolling maneuver produces very unpleasant accelerations in the passenger compartment and is therefore totally unacceptable as an operating configuration. However, if the cause of the enhanced alleviation could be understood, the same result might be attainable by means of an acceptable method.

A working hypothesis was developed which explained all the observations on the rolling configuration. The deployment of spoilers on the B-747 was observed to cause a transition in the dominant vortex core around which the wake rolls up. In normal landing configuration, the vortex emanating from the outboard edge of the outboard flap dominates the rollup. When spoilers are deployed, the wing-tip vortex becomes the dominant vortex. Only a small spoiler deployment angle ( $<15^{\circ}$ ) is needed to trigger this transition. The rolling alleviation may be related to

periodic crossings of this transition so that the tip and flap vortices are alternately dominant. Such an alternation may trigger a vortex instability. If this mechanism is responsible for the enhanced vortex alleviation of the rolling configuration, the same result might be achieved by spoiler modulation alone.

The observation that the wing-tip vortex dominates the rollup of spoiler alleviated vortices may explain the incomplete success of spoiler alleviation. The spoilers are too far from the wingtip to disrupt the vortex core originating there. The spoiler-alleviated vortices are observed to have a persistent tight core. If the wing-tip vortex could be disrupted in the same way that the spoilers disrupt the flap vortex, the alleviation might be markedly improved.

#### 2.4 1980 L-1011 FLIGHT TESTS

A series of flight tests were conducted in the summer of 1980 with a Lockheed L-1011 aircraft to evaluate some of the alleviation concepts developed during the 1979 B-747 flight tests. The L-1011 appeared to be an ideal test aircraft because of its flexible computerized control system. However, a number of significant differences from the B-747 made it impossible to duplicate the B-747 results. The first difference is that the spoiler deflection angle required to induce the transition from flap vortex to wing-tip vortex dominance is much larger for the L-1011. The second difference is the way in which the spoiler control system operates. If the spoilers are preset at a specific angle, rolling the aircraft causes the angle to increase, but never to decrease. An attempt was made to weaken the wing-tip vortex by uprigging the outboard ailerons and increasing the airspeed. It was not possible to unload the wingtip enough to significantly reduce the tip vortex strength. Mechanical difficulties on the aircraft produced schedule delays which made it impossible to collect ground-based sensor data on the L-1011.

### 3. TEST DESCRIPTION

The first series of tests, in February 1979, were conducted at Grant County Airport in Moses Lake, Washington, because of its proximity to the Seattle home base of the Boeing 747 aircraft used for the tests. The later tests in October and November 1979 were conducted in southern California because the greater length of the tests justified bringing the generator aircraft to the home bases of the probe aircraft.

#### 3.1 AIRCRAFT CONFIGURATION

The B-747 test aircraft was fitted with 8 Corvus-oil smoke generators located as shown in Figure 1. These smoke generators marked the vortices so that they could be seen. They also allowed some details of the wake roll-up process to be understood.

The vortex alleviation configuration was obtained by deactivating the normal spoiler controls for some of the 12 spoilers on the aircraft (see Figure 1). The remaining spoilers were then deflected by a set amount to produce the desired alleviation. The spoiler configurations which have been flight tested are listed in Table 1. Configurations 2 and 3 were proposed as improvements on configuration 1 on the basis of wind-tunnel measurements (Ref. 3). Both were tested at Moses Lake with various deflection angles. The

TABLE 1. B-747 SPOILER CONFIGURATIONS

Configuration Number	Spoilers Deflected	Flight Tests
1	1,2,11,12	December 1975 (Ref. 2)
2	2,4,9,11	February 1979
3	2,3,4,9,10,11	February 1979 October 1979 November 1979

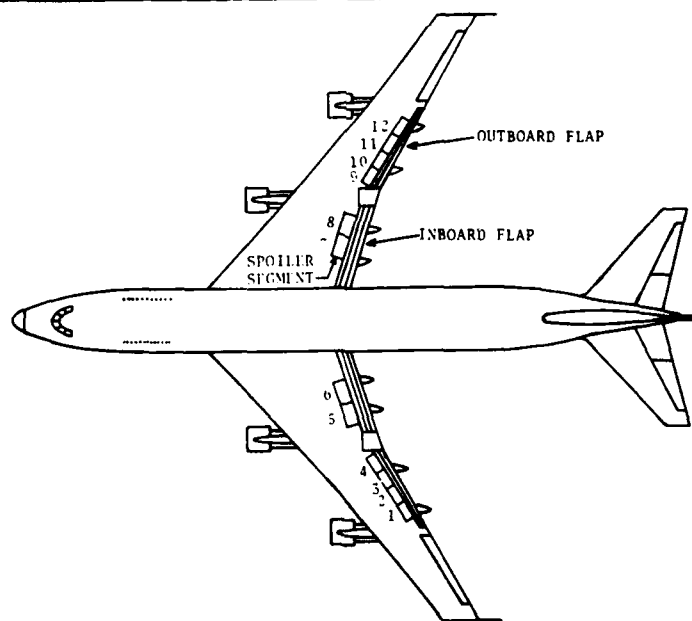
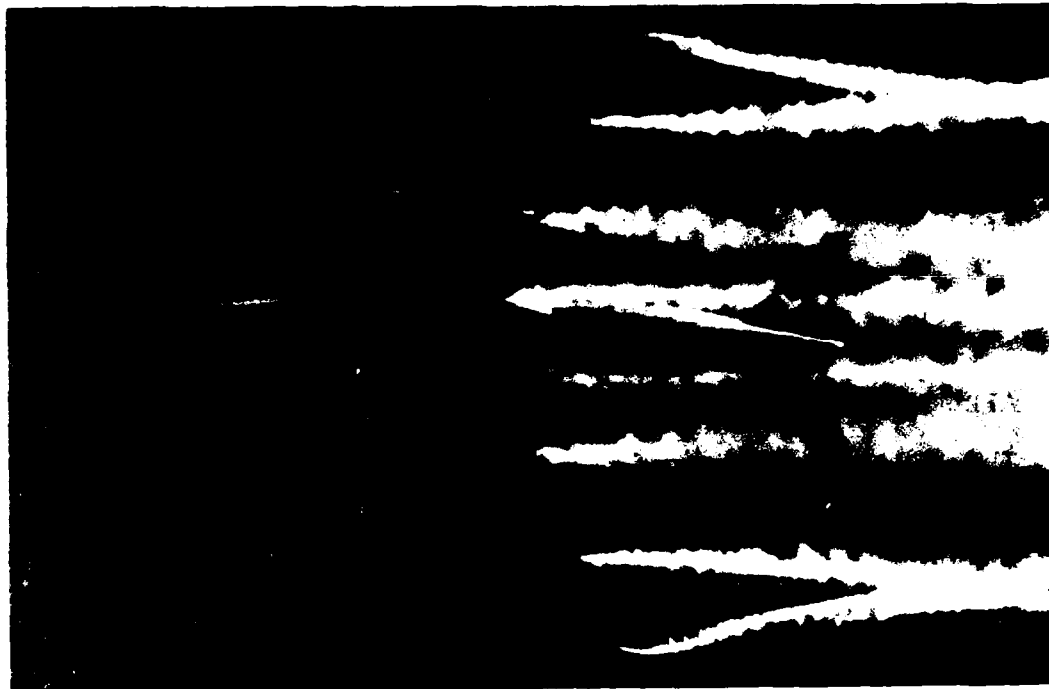


FIGURE 1. B-747 SPOILERS, FLAPS, AND SMOKERS

selection of which spoilers to deploy requires mechanical changes, so that only one configuration could be tried on a particular test day. The Boeing Company prepared a report (Ref. 4) on the operational penalties associated with the spoiler deployment and the actual spoiler angles used in these configurations. Spoiler configuration 3 was judged to be best and was used on all later tests.

### 3.2 SENSOR CAPABILITIES

This section outlines the principles of operation and capabilities of the ground-based wake-vortex sensors used in the tests.

#### 3.2.1 Laser Doppler Velocimeter

3.2.1.1 Principles of Operation - The use of the LDV to measure wake vortices is illustrated in Figure 2. The LDV utilizes a continuous wave (cw) CO<sub>2</sub> laser operating in the far infrared (10.6  $\mu$ m wavelength) on a single frequency. Range resolution is achieved by focusing the beam with a 30 cm diameter telescope at the desired point in space. The focal spot can be scanned in range by changing the focus of the telescope and in angle by means of a scanner using two large motorized mirrors. Because the typical distance to a vortex is 100 m or greater, the LDV beam is relatively narrow and the length of the focal region is relatively long, as shown in Figure 2a. The resulting range resolution is proportional to the square of the range with a full width at half response of  $\Delta f = 10$  m at  $f = 100$  m focal distance. Although the LDV range resolution is poor, the angular resolution is very good because of the narrowness of the focal region.

The way in which the LDV beam probes a vortex is shown in Figure 2b. The beam is so narrow that it can be represented as a line through the vortex. The LDV signal is generated by aerosol particles within the beam scattering radiation back into the transmitting telescope. This scattered radiation has its frequency Doppler shifted by the component of the aerosol velocity along the

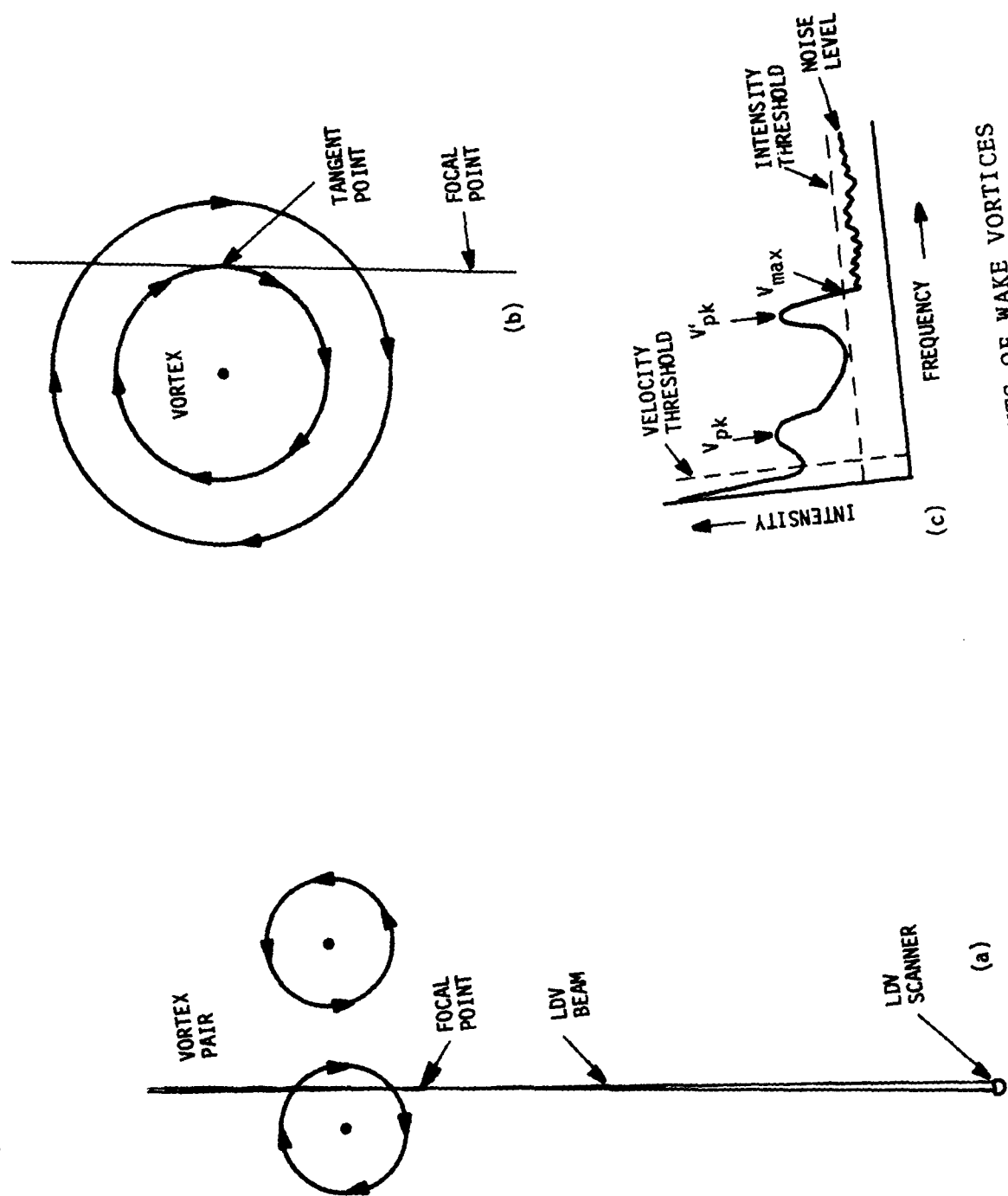


FIGURE 2. LASER DOPPLER VELOCIMETER MEASUREMENTS OF WAKE VORTICES

line-of-sight (LOS) of the beam. The scattered radiation is mixed with the transmitted radiation at the detector to produce a Doppler signal in the frequency range of 0 to 8 MHz. Unfortunately, this procedure eliminates all information about the sign of the Doppler shift. The Doppler signal is processed by a spectrum analyzer which resolves the spectrum into 100 kHz bins ( a velocity resolution of 0.53 m/sec). Figure 2c shows what the spectrum from the vortex in Figure 2b would look like. The low frequency peak ( $V_{pk}$ ) represents the LOS velocity at the focal point of the beam. The high frequency peak ( $V'_{pk}$ ) comes from the region where the LDV beam is tangent to the vortex streamlines. In that region a considerable length of the beam contributes to the spectrum at the same velocity. Because of this tangent effect, it is possible to measure the vortex tangential velocity in spite of the poor range resolution of the LDV. The data processing technique uses  $V_{max}$ , the highest spectral bin above an intensity threshold, to represent the vortex tangential velocity.

3.2.1.2 Scan Mode - The scan mode of the LDV plays a major role in setting the capabilities of the LDV system to measure the properties of wake vortices. The 1975 B-747 tests (Ref. 2) made use of two scan modes (See Figure 3a,b):

1. Finger Scan (range oscillates rapidly, elevation angle oscillates slowly; used to track vortices)
2. Arc Scan (range fixed, angle oscillates; used to measure velocity profiles).

The analysis of the 1975 arc-scan data indicated that a third mode would yield both velocity profiles and vortex location (see Figure 3c).

3. Stepped-Arc Scan (range stepped to a new value at the end of each angle scan).

The stepped-arc scan mode was first used (Ref. 5) with 8 ranges and fixed angle limits. Since each angle scan takes 1 second, this mode gave a vortex measurement approximately every 8 seconds.



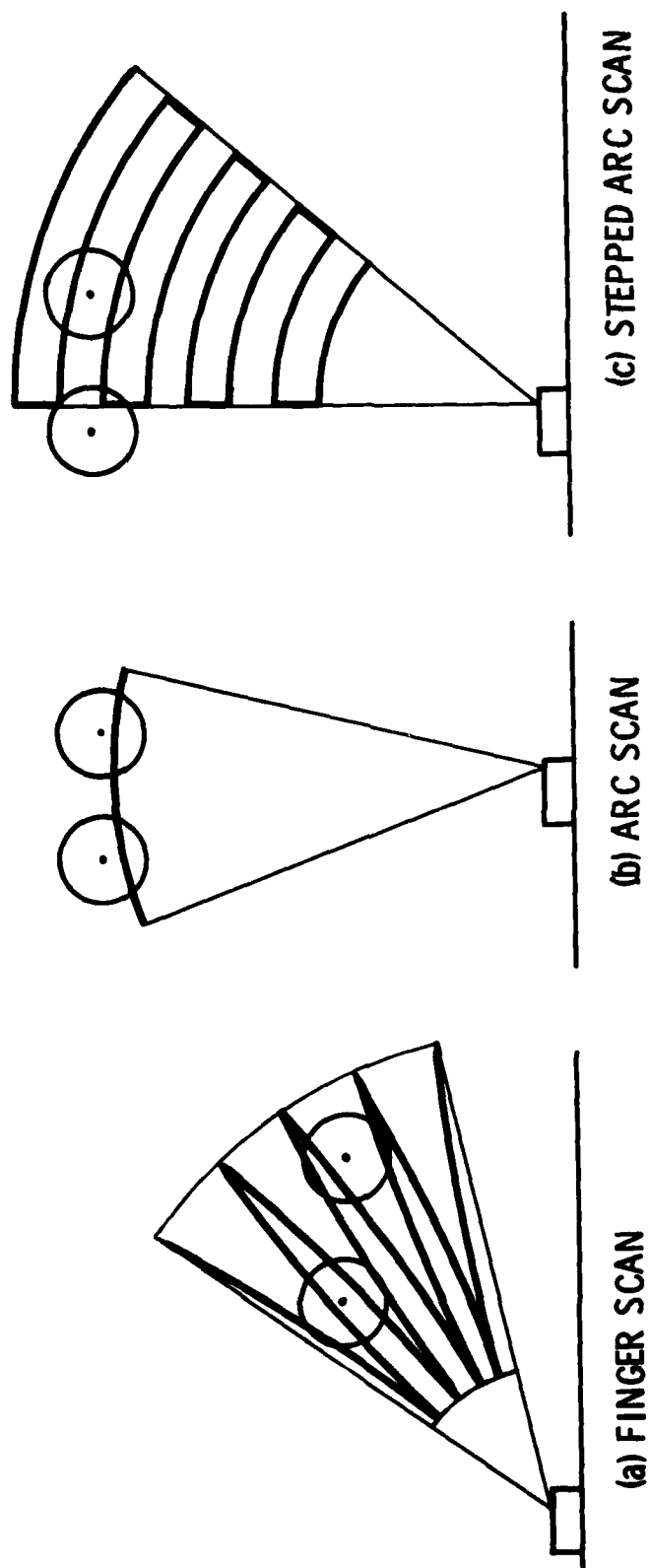


FIGURE 3. LASER DOPPLER VELOCIMETER SCAN MODES

The data in this report were collected in a more flexible stepped-arc scan mode where the number of ranges is selectable and the angle limits are varied to keep the vortices in view. The operator makes use of a real-time display of the vortex velocity profiles to determine when the scan parameters should be changed. Usually three to five ranges are used with an angle scan of  $60^{\circ}$ .

The ranges are kept in sequence from the highest to lowest since the display is keyed to start a new scan picture or "frame" when the range increases. If a vortex drops to the bottom of the display, a new lower range is added and perhaps the highest range is deleted if it shows little vortex signal. The real-time display used for tracking is similar to that shown later in Section 4.1.1 for playback. The problems encountered in the real-time tracking of vortices are similar to those discussed there in connection with data analysis.

### 3.2.2 Ground Wind Vortex Sensing System

Wake vortices below about 60-meter altitude AGL can be detected and tracked by means of their induced winds at ground level. The Ground Wind Vortex Sensing System (GWVSS), illustrated in Figure 4, consists of an array of anemometers laid out perpendicular to the aircraft flight path. The anemometers are single-axis propeller anemometers which respond linearly to the component of the wind perpendicular to the flight path. The two counter-rotating vortices generate deviations from the ambient crosswind of opposite sign. The peak and valley in the ground wind signature give an accurate measurement of the lateral positions of the two vortices (Ref. 6).

The GWVSS used in the alleviation tests was simpler than normally used. Eight anemometers were recorded on an eight-channel strip chart recorder which gave a real-time indication of vortex positions as well as a permanent data record.

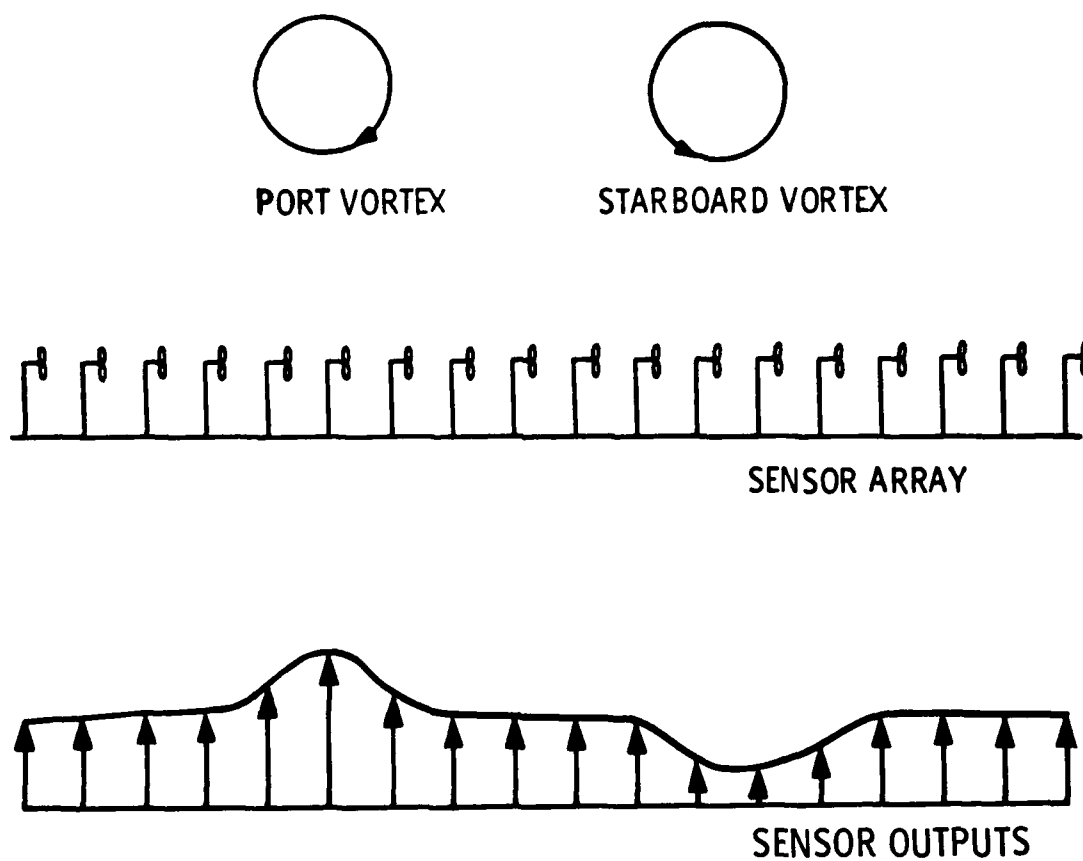


FIGURE 4. SCHEMATIC VIEW OF GWVSS ANEMOMETER ARRAY AND SIGNAL OUTPUTS

### 3.2.3 Photography

Photography of smoke-marked vortices can provide information on vortex position and decay. Vortex tracking is accomplished by taking synchronized photographs (35 mm color slides) every 3 seconds from two separate camera locations, usually one beneath the vortices and one to the side. A calibrated scale located between the camera and the vortices is included in each picture so that the positions of the two vortices can be read off directly without calibrating the picture itself.

### 3.3 SENSOR UTILIZATION

The primary ground-based sensor for vortex measurements was the scanning Laser Doppler Velocimeter (LDV). The 1975 B-747 tests (Ref. 2) showed that the LDV can produce superb vortex tangential velocity profiles. The smoke injected into the vortices is an essential requirement for such measurements since it produces a large scattered signal for the LDV. The velocity profiles at Moses Lake from unsmoked vortices exhibited signal drop-outs at the vortex core because there were not enough scattering aerosols to mark the tangential velocity. The LDV performs more satisfactorily in an urban environment where the aerosol content is high. This problem was accentuated by an unexplained drop in the LDV signal-to-noise ratio for both series of alleviation tests, compared to its normal operation at Chicago's O'Hare Airport.

Although the LDV was known to produce excellent vortex measurements for vortices generated well above the ground, it was not certain how well it would perform for vortices in ground effect where the ambient crosswind can disturb the measurements and the signals from the two vortices can interfere. The measurements at Moses Lake were the first definitive tests of the stepped-arc scan mode for vortices in ground effect.

In addition to LDV measurements, photographic tracking of the vortices was provided for two purposes.

1. An independent absolute measurement of the vortex range is very useful in interpreting the LDV data which have a rather poor range accuracy.

2. It was hoped to observe some vortex core bursts via the smoke pictures and use the corresponding LDV velocity profiles to assess the nature of core bursting in a quantitative fashion. A definitive measurement of how a burst affects the vortex-velocity profile has so far eluded researchers.

Because of range difficulties experienced with the LDV in ground-effect measurements at Moses Lake, later tests included a simple GWVSS consisting of 8 single-axis anemometers spaced along a line under the LDV scan plane. The GWVSS data assisted in the selection of LDV ranges for real-time tracking and also gave additional information for subsequent data processing.

A tethered kitoon (meteorological balloon) was used to obtain profiles of the following meteorological parameters:

1. Temperature
2. Relative Humidity
3. Wind Speed
4. Wind Direction

### 3.4 TEST FLIGHTS

This report addresses only the low-altitude test flights where ground-based sensor data were collected.

#### 3.4.1 Series 1: Moses Lake

The three test flights at Moses Lake are listed in Table 2. The B-747 flew instrument approaches to Runway 32R. The first two flights used the configuration shown in Figure 5 where the sensors were located 4600 m from the runway threshold. For the third flight the sensors were moved to the middle marker location 1050 m from threshold, as shown in Figure 6.

The first flight (2/9/79) used spoiler configuration 3 (Table 1, termed 2,3,4 for simplicity). The weather was partly cloudy with snow cover melting on the ground. The crosswind

TABLE 2. SERIES 1 FLIGHTS

<u>2/9/79</u> <u>Run</u>	<u>Spoilers 2,3,4</u> <u>Time (PST)</u>	<u>4600 m From Threshold</u> <u>Spoiler Angle (deg)</u>	<u>C<sub>L</sub></u>
1	1130	0	1.40 $\pm$ .02
2	1137	15	
3	1145	30	
4	1154	0	
5	1202	7.5	
6	1212	15	
<u>2/10/79</u> <u>Run</u>	<u>Spoilers 2,4</u> <u>Time (PST)</u>	<u>4600 m From Threshold</u> <u>Spoiler Angle (deg)</u>	<u>C<sub>L</sub></u>
1	952	0	1.40 $\pm$ .02
2	1000	30	
3	1006	45	
4	1013	15	
5	1028	0	
<u>2/12/79</u> <u>Run</u>	<u>Spoilers 2,3,4</u> <u>Time (PST)</u>	<u>1050 m From Threshold</u> <u>Spoiler Angle (deg)</u>	<u>C<sub>L</sub></u>
1	1325	0	1.40 $\pm$ .02
2	1344	15	
3	1355	30	
4	1407	0	
5	1430	15	
6	1445	30	
7	1450	0	

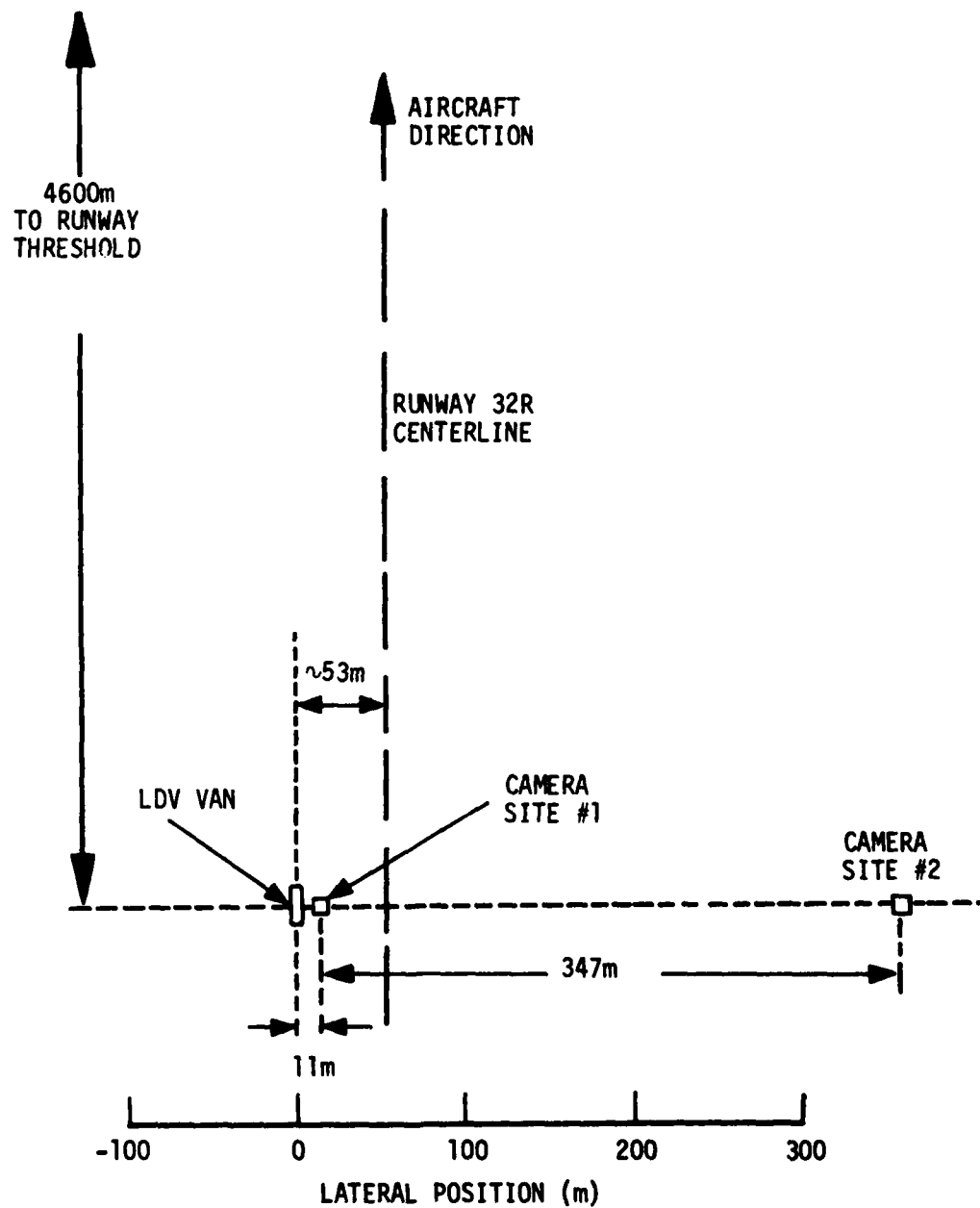


FIGURE 5. MOSES LAKE TEST CONFIGURATION (2/9/79, 2/10/79)

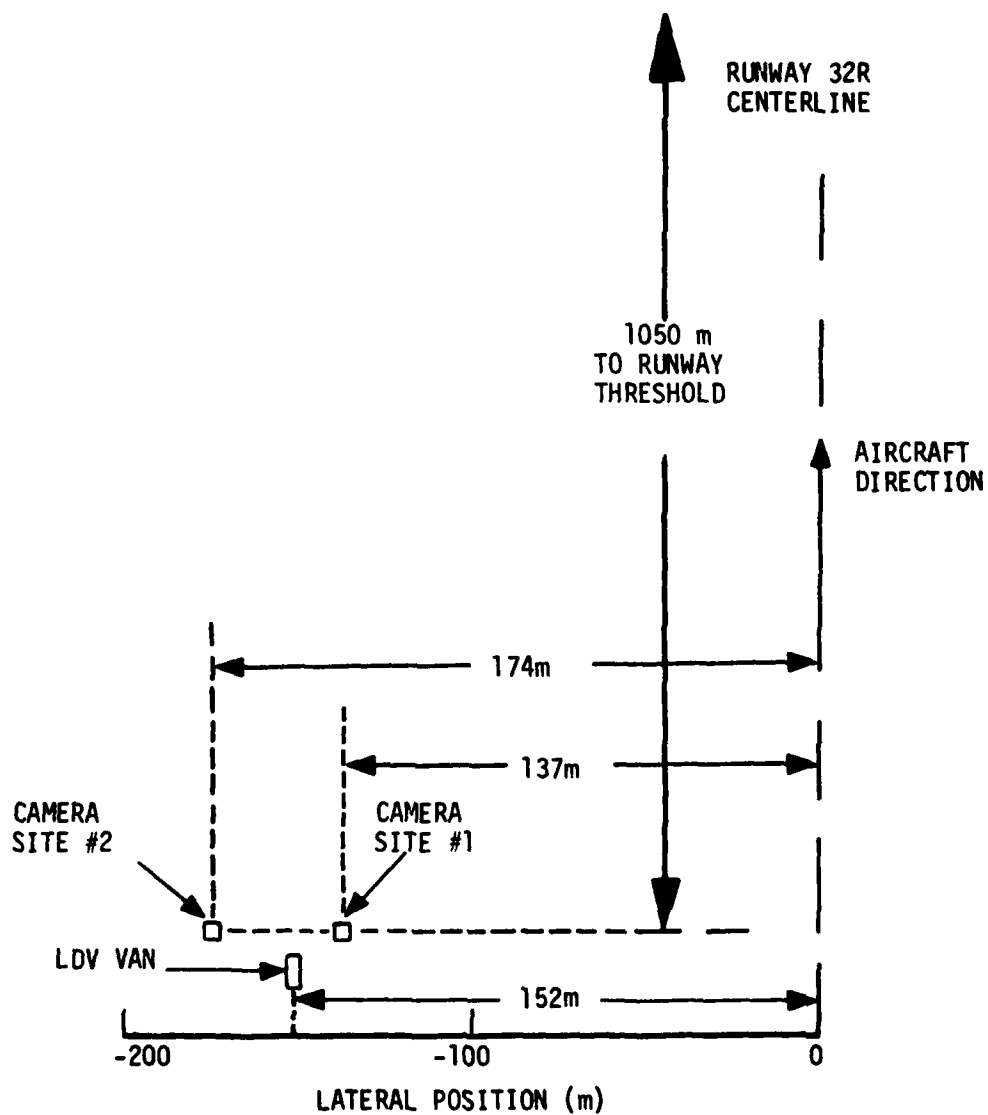


FIGURE 6. MOSES LAKE TEST CONFIGURATION (2/12/79)



tended to blow the vortices away from the LDV location. After several runs, the aircraft was requested to fly somewhat upwind of the runway centerline so that the LDV could track the vortices longer. The test aircraft flew the normal  $2.75^{\circ}$  runway glideslope (nominal altitude of 220 m at the test site).

The second flight (2/10/79) used spoiler configuration 2 (Table 1, termed 2,4). The sky was totally overcast and there was little crosswind. The snow cover had practically disappeared by this time. The test aircraft was requested to fly 100 m above the glideslope so that the vortices could be observed for a longer period of time.

The third flight (2/12/79) used spoilers 2,3, and 4, which appeared to give greater vortex alleviation. The sky was overcast with poor visibility and there was a crosswind tending to blow the vortices toward the LDV van which was located 150 m to one side of the extended runway centerline.

#### 3.4.2 Series 2: Southern California

The series 2 flights are listed in Table 3. Spoiler configuration 3 (Table 1, termed 2,3,4) was used throughout this series.

3.4.2.1 China Lake Naval Weapons Center - The China Lake flights all used spoilers 2,3,4 at  $30^{\circ}$  deflection which was the best alleviating configuration tested at Moses Lake. A remotely piloted F-86 aircraft was used to probe the B-747 wake.

On 11/2/79 the B-747 flew down a  $3^{\circ}$  glideslope to 30 meters AGL and then leveled off for 30 seconds. The F-86 aircraft probed the wake at 7-km separation. In order to limit damage in the case of an uncontrollable encounter, the test site was located remote from the China Lake airfield. The only ground-based sensor used was the meteorological kite which was raised and lowered between each run.

TABLE 3. SERIES 2 FLIGHTS

11/2/79 China Lake Naval Weapons Center

<u>Run</u>	<u>Time (PST)</u>	<u>C<sub>L</sub></u>
Sunrise	613	
1	822	1.41
2	837	1.40
3	851	1.41
4	906	1.40
5	920	1.40

11/3/79 China Lake Naval Weapons Center

<u>Run</u>	<u>Time (PST)</u>	<u>C<sub>L</sub></u>
Sunrise	615	
1	810	1.48
2	821	1.45
3	832	1.41
4	844	1.38
5	854	1.41
6	905	1.35
7	915	1.46
8	925	take off, no smoke

11/8/79 Edwards AFB

<u>Run</u>	<u>Time (PST)</u>	<u>C<sub>L</sub></u>	<u>Spoiler Angle (deg)</u>
Sunrise	619		
1	715	1.42	15
2	725	1.39	22.5
3	737	1.35	30
4	749	1.27	30 (roll)
5	801	1.43	0 (roll)
6	813	1.43	15-30
7	826	1.35	30 (roll)
8	838	1.35	30 (roll)
9	845	1.37	0

On 11/3/79 the F-86 followed the B-747 to touchdown on Runway 21. The LDV and GWVSS sensors were deployed as shown in Figure 7. Because of a misunderstanding, the meteorological kitoon was used only before and after the complete flight sequence on this day. There was no cloud cover and the wind was light on both 11/2 and 11/3, so that the meteoroglogical data on 11/2 are also useful for 11/3.

3.4.2.2 Edwards Air Force Base (AFB) - On 11/8/79 data were collected on a variety of configurations. The B-747 flew approaches to Runway 18 on Rogers Dry Lake at Edwards AFB. The sensor layout is shown in Figure 8. Unfortunately, the wind was much too strong (9.5 m/s at Run 9 )to give good sensor results. The crosswind quickly moved the vortices out of the sensor volume and also made the LDV data hard to interpret. Runs 4 and 7 (Table 3) were made in a configuration which showed significantly improved alleviation compared to the standard spoiler configuration, according to T-37 probes. In addition to deploying the spoilers, strong rapid roll inputs were introduced at a period of 3 seconds per cycle. Both the spoilers and ailerons were active in producing roll. The control inputs were large enough that the spoilers dropped to near zero angle. Run 8 was a variation on this configuration where the period was reduced to 2 seconds per cycle. Two runs were included in an attempt to understand the reasons for the roll-induced alleviation. Run 5 employed only ailerons to produce roll with no spoiler deployment, while Run 6 involved modulating the spoilers between 15° and 30° with no roll inputs. Neither produced the same improved alleviation.

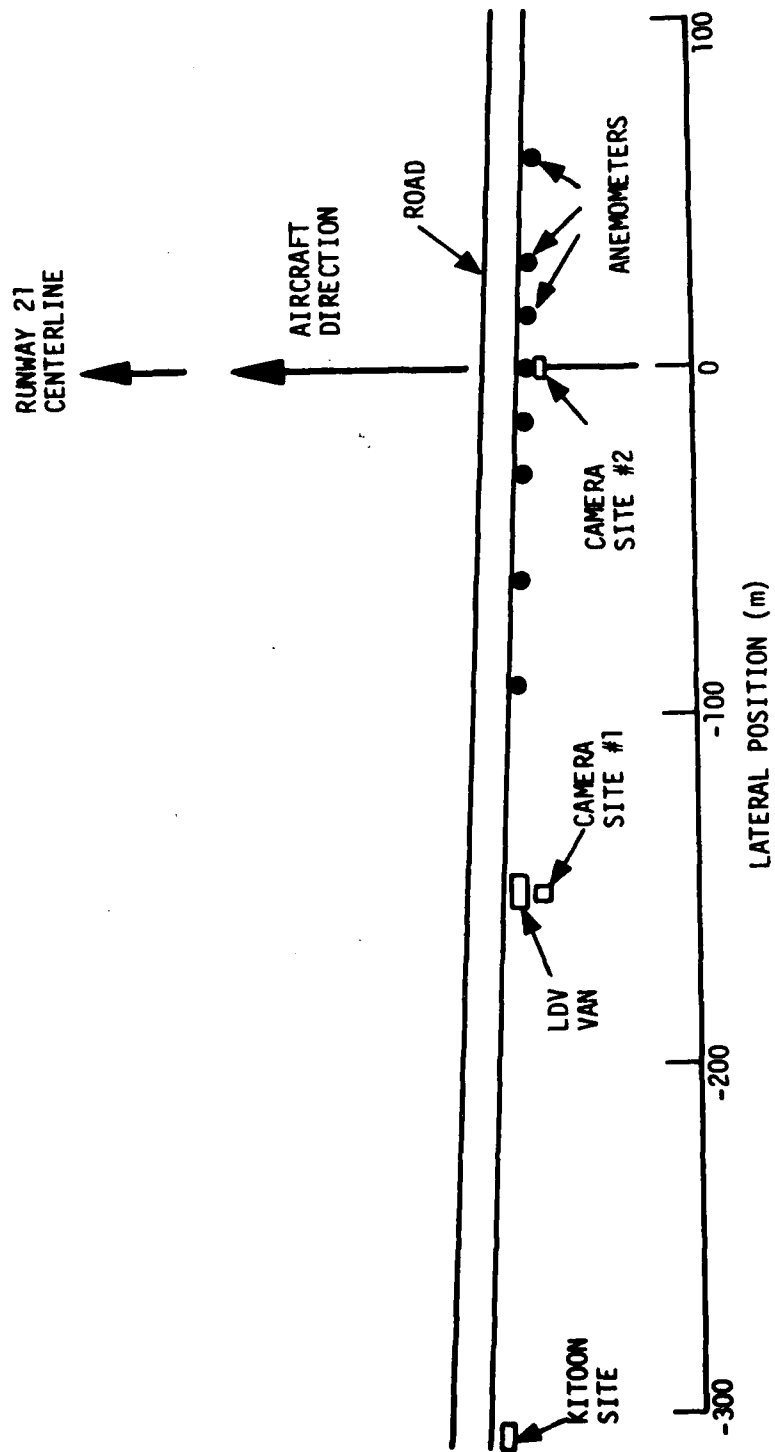


FIGURE 7. CHINA LAKE TEST CONFIGURATION (11/3/79)

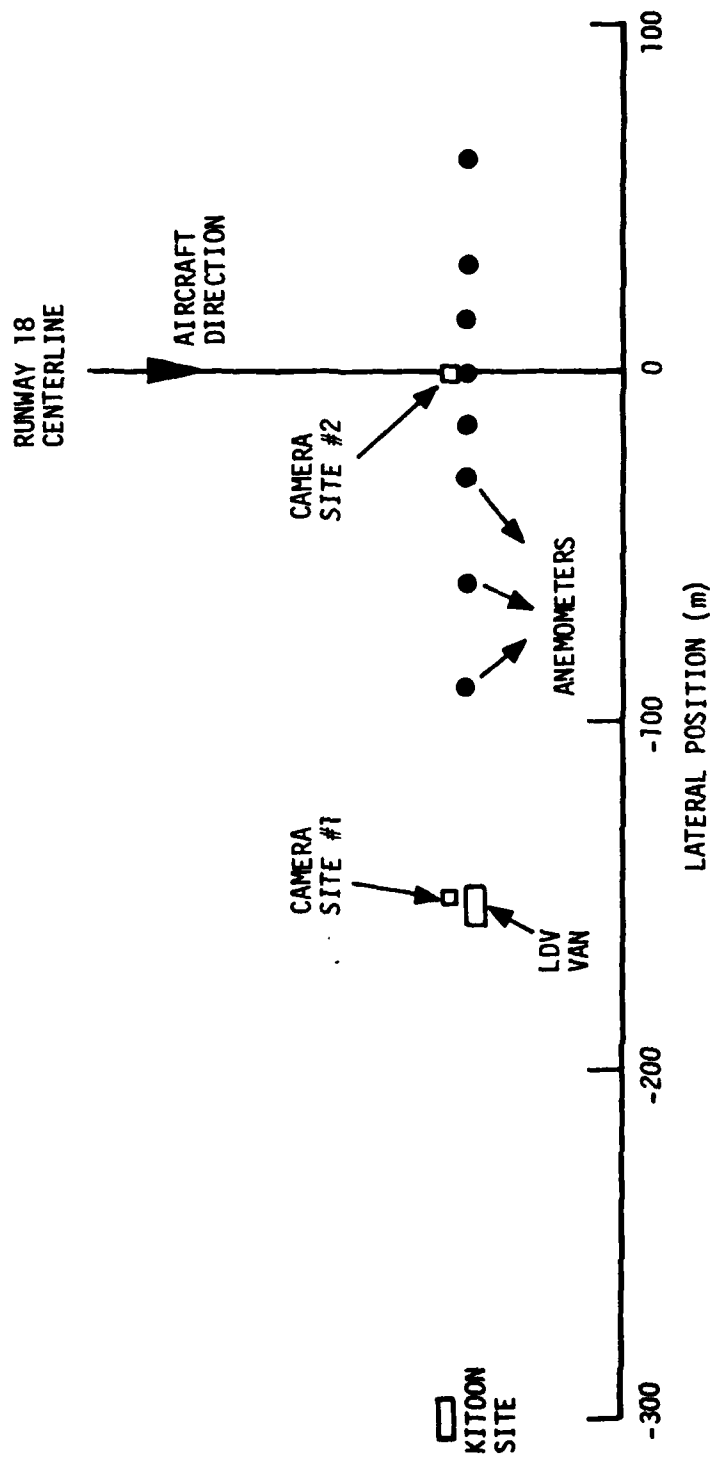


FIGURE 8. EDWARDS TEST CONFIGURATION (11/8/79)

## 4. DATA ANALYSIS

### 4.1 LASER DOPPLER VELOCIMETER

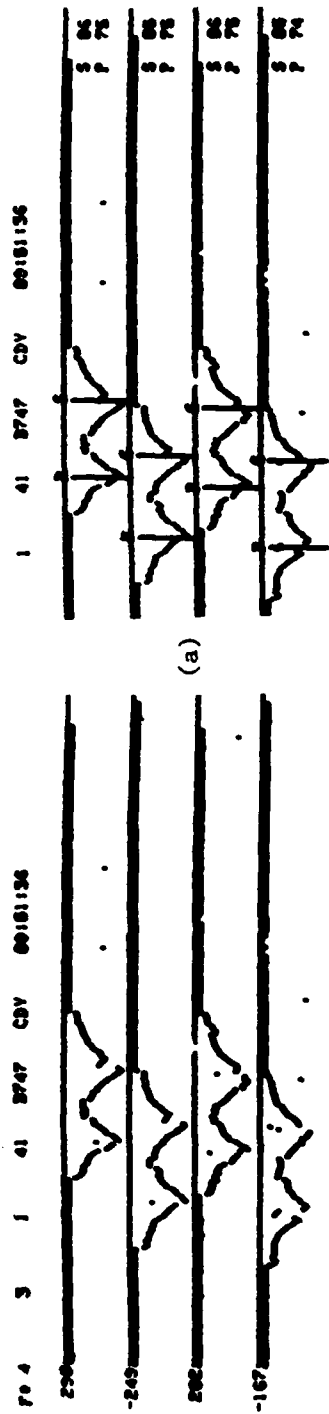
The analysis of the LDV data is complicated; many of the details have been relegated to Appendix A. This section will supply enough information so that the LDV results and their limitations can be understood. Only sample plots are included here; a complete set of plots for all runs is included in Appendix E.

The LDV data are processed in three passes:

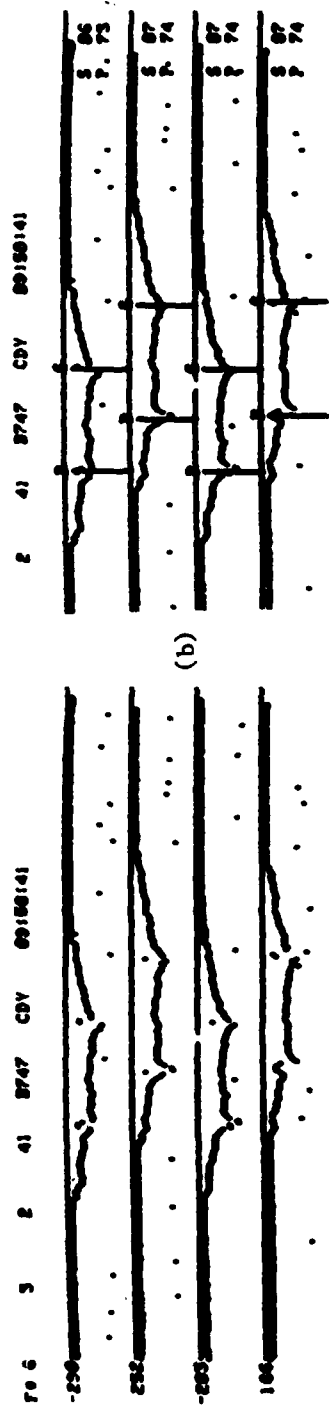
1. The vortex elevation angles are identified visually and the data within 30 m of the vortices are saved.
2. The range to the vortex is determined and a vortex track is fitted to the data.
3. The fitted vortex range is used to calculate vortex strength and to generate plots of vortex velocity and circulation profiles.

#### 4.1.1 Vortex Identification

Figure 9 shows the display used to identify the elevation angle locations of the vortices. One frame (i.e., sequence of range scans) is shown for each of two runs, one alleviated and one non-alleviated. The velocity ( $V_{\max}$ ) profiles versus elevation angle  $\theta$  are plotted on successive horizontal lines for decreasing ranges. Figure 10 shows the spatial geometry of the scan patterns. For historical reasons the velocity is plotted below the lines. The range in meters appears at the left side of each line (a negative sign indicates a reversed angle scan, from right to left). The turn around delay in the angle scanner causes the vortex locations to alternate back and forth from scan to scan. The vortex positions are assigned scan by scan at the dip in the velocity profile. A light pen is used to identify the desired position. The left side of Figure 9 shows the display seen by the operator and the right side shows the display after the operator has identified the vortices. The elevation angle  $\theta$  (degrees) is



RUN 1  
 00181149



RUN 2  
 00180122

FIGURE 9. PLAYBACK CRT DISPLAY: (a) NON-ALLEVIATED (RUN 1, 2/10/79) (b) ALLEVIATED (RUN 2, 2/10/79). THE SELECTED VORTEX CENTERS ARE LISTED ON THE RIGHT.

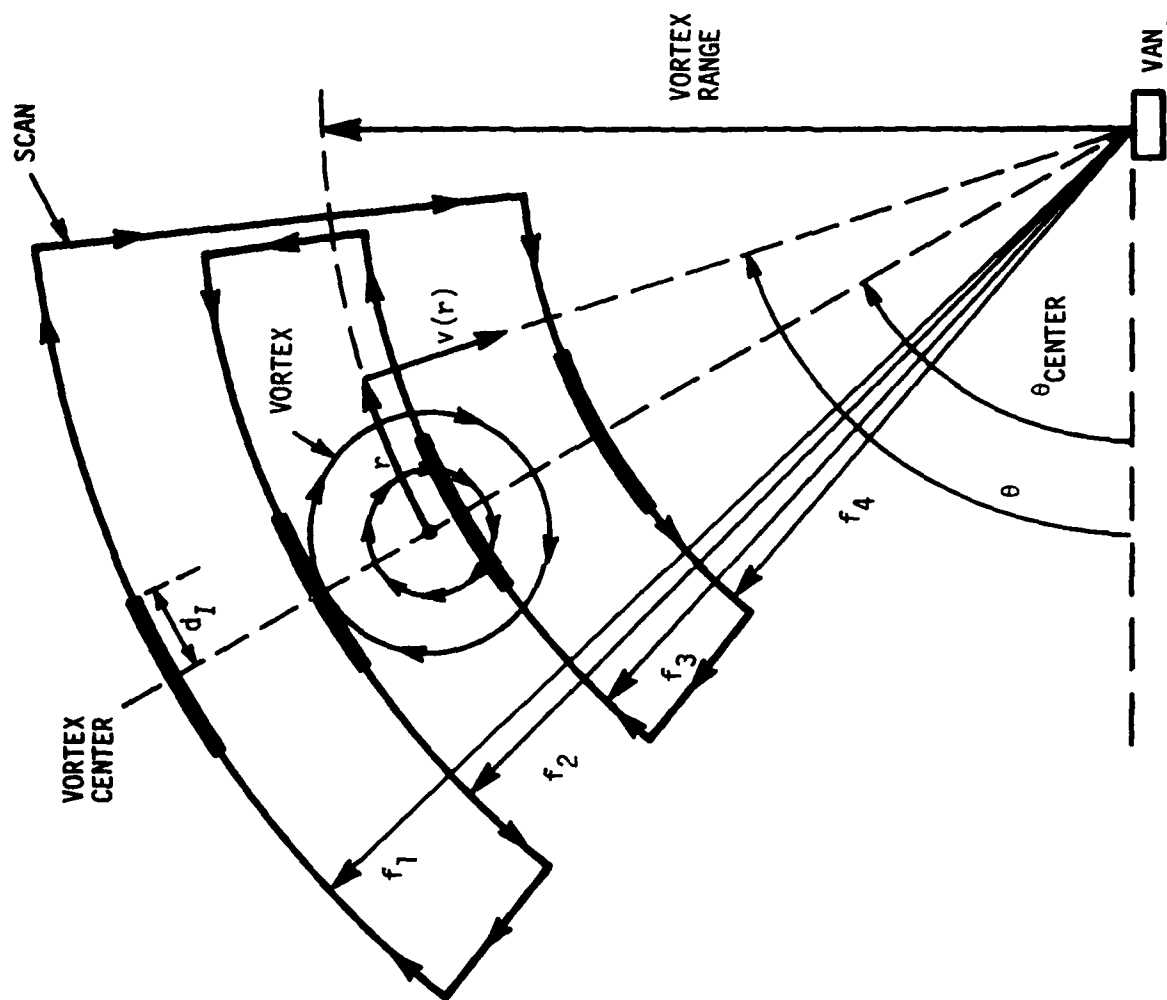


FIGURE 10. GEOMETRY FOR PROCESSING ONE SCAN FRAME OF LDV DATA

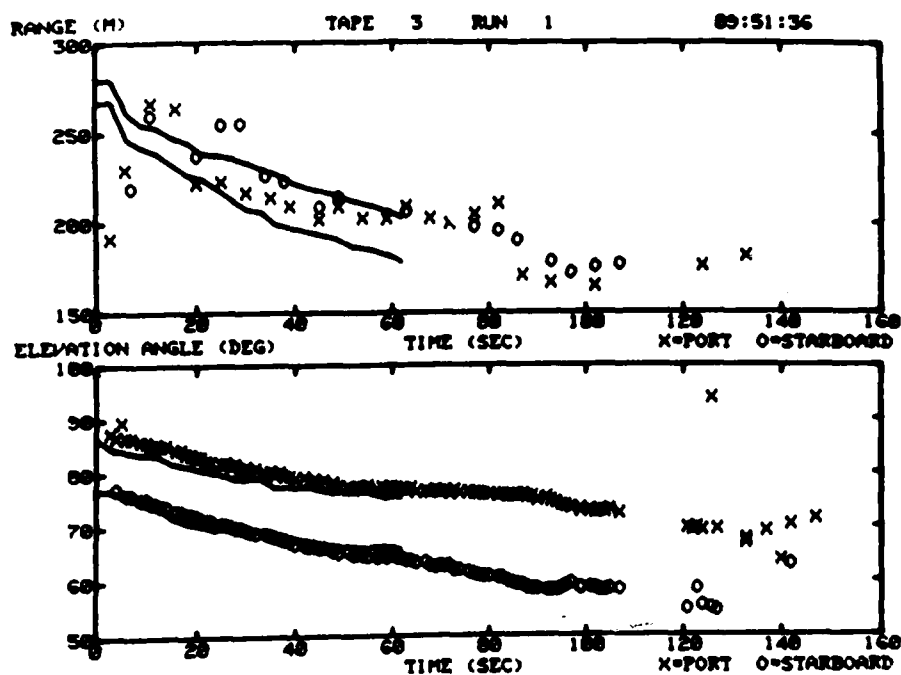


listed at the right edge of the display. Note that the vortex angles are consistent inspite of the jitter in the display. After the two vortex angles are assigned, the data between the vortices and 30 m to either side are stored for further processing.

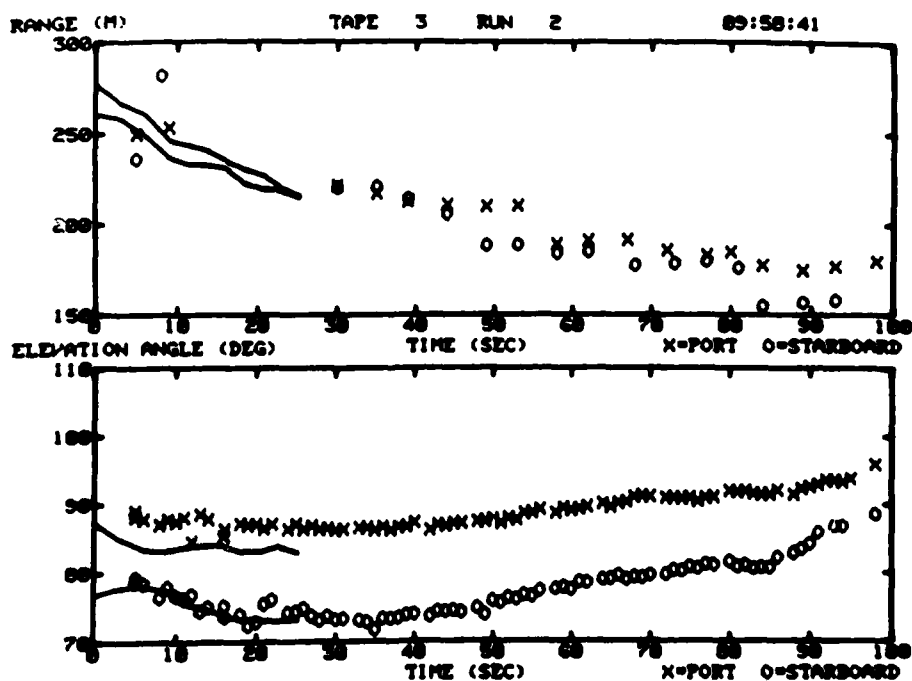
#### 4.1.2 Range Determination

The range determination algorithm is described in Appendix A. It makes use of signal intensity information near the vortex core (the regions marked with thickened arc segments in Figure 10) to interpolate between the LDV scan ranges ( $f_1$  and  $f_2$  in Figure 10). Since the vortex elevation angle has already been determined, a determination of the range completely specifies the vortex location.

The derived vortex locations are plotted in two forms: polar (Figures 11 and 12a) and rectangular (Figure 12b) coordinates. The points (X,0) are the LDV data. When available (Figure 11) the photographic tracking data are plotted as connected line segments. The LDV angle determination is excellent when the vortex cores are well defined. The range determination, however, is poor and exhibits considerable jitter. In order to prevent the range jitter and resulting systematic errors from affecting the circulation measurements, the range data are smoothed by visually matching the vortex trajectories with a sequence of the line segments. Two smoothing methods are used. The simplest is to fit the range directly as in Figure 12c. The solid line is the fitted range. This technique is ideal for high-altitude (200 to 300 m) flybys with little crosswind. However, the range to the two vortices will become different when the elevation angle becomes low. The expected difference does not necessarily show up clearly in the LDV range data but can be roughly accounted for in the fitting process (e.g., the starboard vortex in Figure 12c is assigned a longer range than the port vortex). This problem is eliminated in the second method where the lateral position is fitted directly in Figure 12d. The vortex range and altitude are then calculated from the measured



(a)



(b)

FIGURE 11. POLAR COORDINATE VORTEX TRAJECTORIES: (a) NON-ALLEVIATED (RUN 1, 2/10/79) (b) ALLEVIATED (RUN 2, 2/10/79)

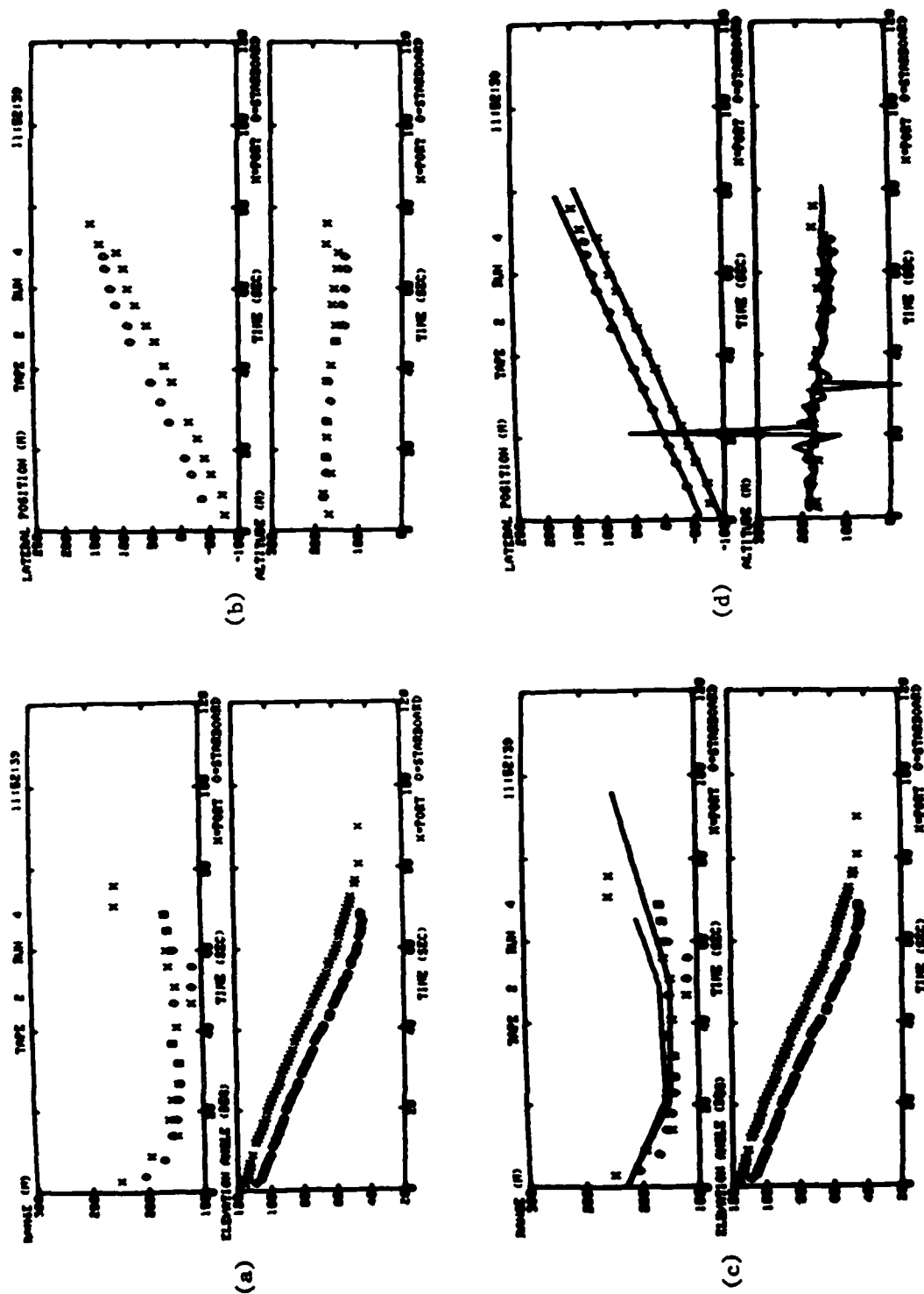


FIGURE 12. VORTEX TRAJECTORIES FOR RUN 4, 2/9/79: (a) POLAR COORDINATES, (b) RECTANGULAR COORDINATES, (c) RANGE FIT, (d) LATERAL POSITION FIT

elevation angles. This method has difficulty with a singularity when the vortex is directly over the LDV (lateral position = 0). The singularity shows up as an anomalous calculated altitude in the solid line altitude plots of Figure 12d. The lateral position fit is particularly useful when the vortices are at low elevation angles and are moving laterally at constant speed. It was developed for the low-altitude runs (see Figure 13) where the initial lateral positions can be accurately assigned. In this case the singularity is never encountered because the vortex is not observed above the van. Figure 13 shows the vortex trajectories for one low-altitude run which is unique in that a vortex was re-acquired after it passed over the van.

#### 4.1.3 Strength Determination

Once the vortex range is defined, the calculation of vortex strength can be carried out with little difficulty. In each frame, the  $V_{\max}$  velocity profile for the arc scan with range closest to the vortex core ( $f_3$  in Figure 10) is used to obtain the tangential velocity profile  $v(r)$  of the vortex. The vortex radius  $r$  is taken as the distance along an arc at the vortex range (see Figure 10). The measured elevation angles  $\theta$  are smoothed by a 5-point running average to eliminate jitter before they are used to calculate the vortex radius. The resulting vortex-velocity profiles are plotted in Figures 14 and 15. The sign of the velocity is reversed at the assigned vortex core location to restore the actual velocity profile. The plots in Figures 14 and 15 are positioned so that the velocity profiles correspond to the actual vertical-velocity profile of the wake, i.e., with the downwash between the vortices. The occasional spikes in the velocity profiles are caused by noise spikes rising above the data acceptable threshold in the  $V_{\max}$  determination (Figure 2c) or by drop outs in the vortex signal.

The vortex circulation is defined by the equation:

$$\Gamma(r) = 2\pi r \ v(r), \quad (1)$$

where  $r$  is the vortex radius and  $v(r)$  is the tangential velocity

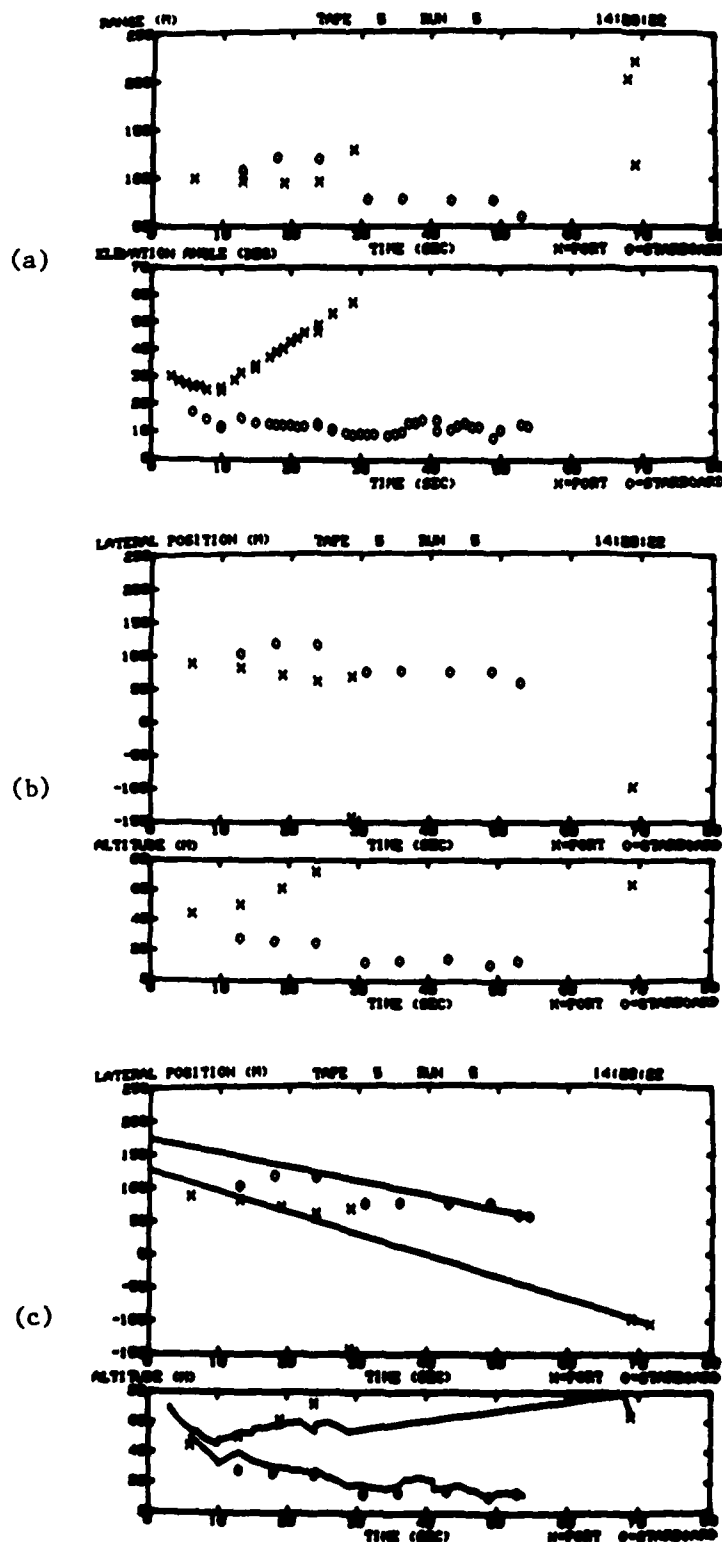


FIGURE 13. VORTEX TRAJECTORIES FOR RUN 5, 2/12/79: (a) POLAR COORDINATES, (b) RECTANGULAR COORDINATES, (c) FITTED TRAJECTORIES. NOTE: THE TWO X'S IN THE UPPER RIGHT CORNER OF THE RANGE PLOT IN (a) ARE ACTUALLY OFF-SCALE ANGLE POINTS.

TAPE 3 RUN 1

00:51:36

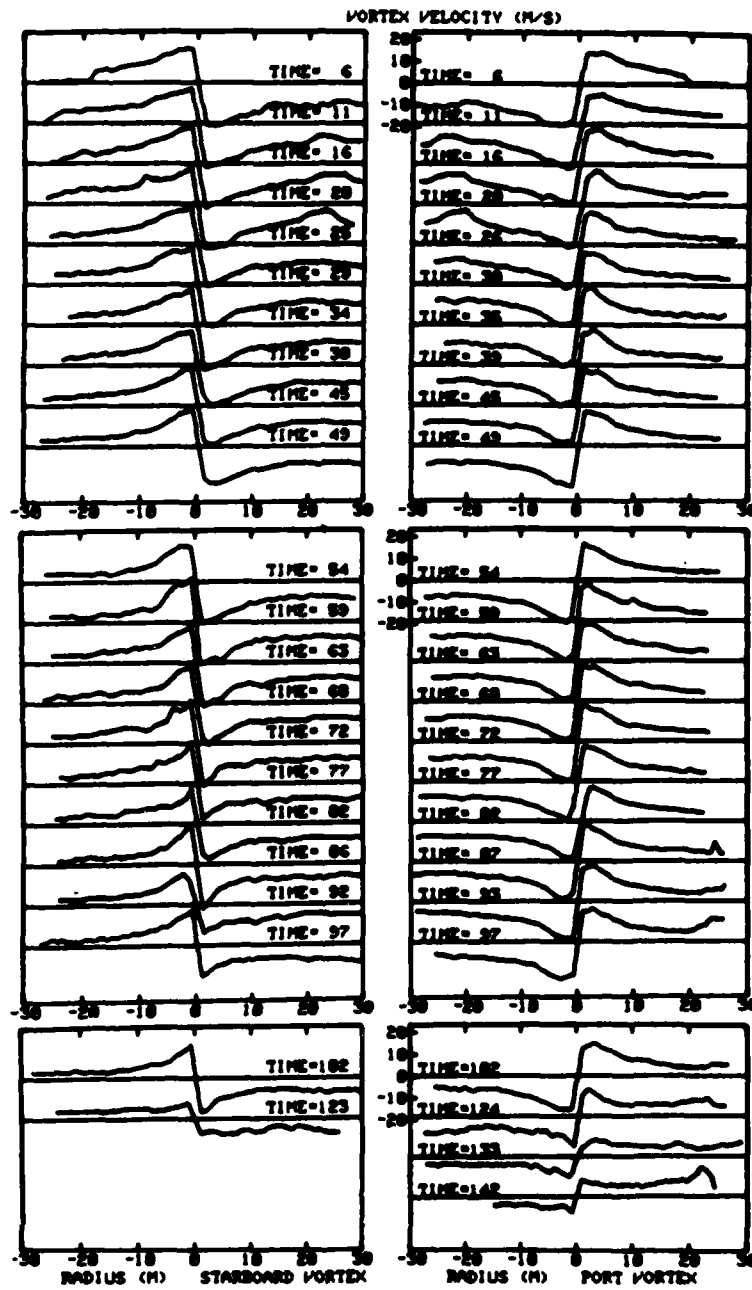


FIGURE 14. VELOCITY PROFILES FOR A NON-ALLEVIATED RUN (RUN 1, 2/10/79)

TAPE 3 RUN 2

09:58:41

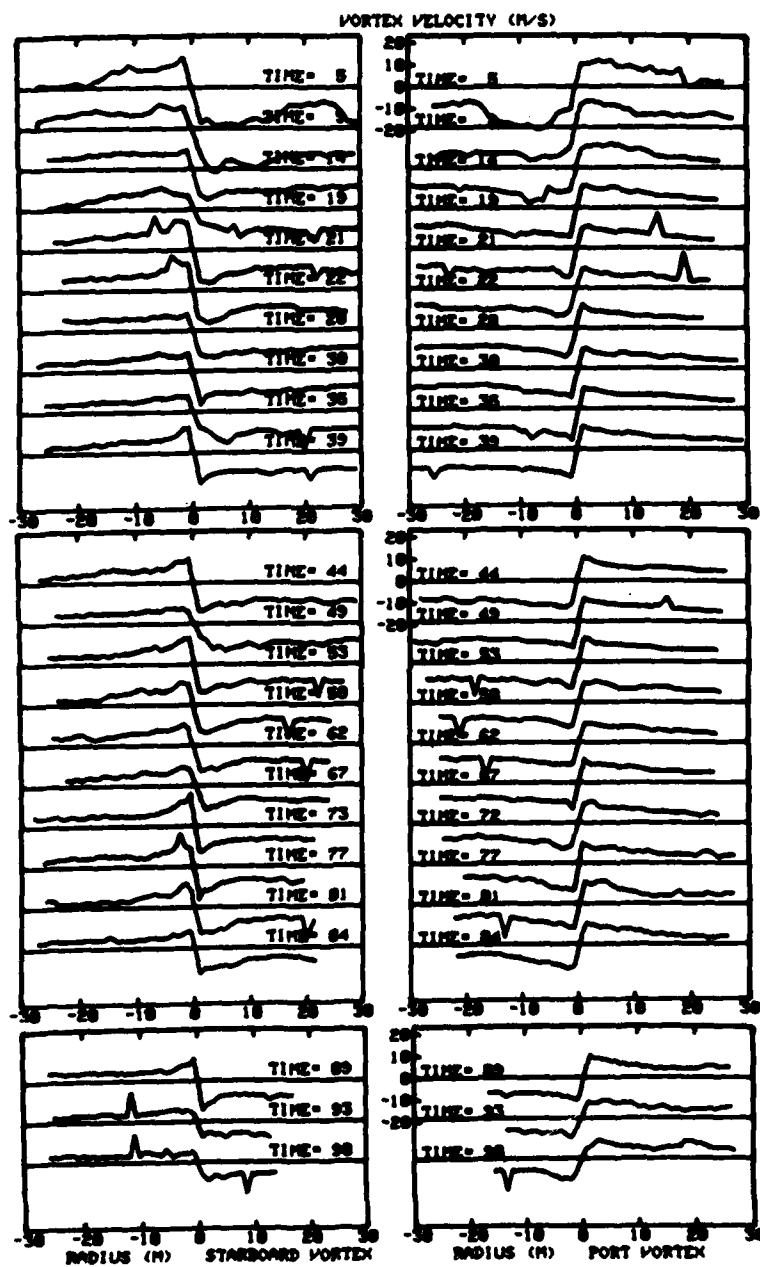


FIGURE 15. VELOCITY PROFILES FOR AN ALLEVIATED RUN (RUN 2, 2/10/79)

profile. It should be noted that, since the circulation is proportional to the radius  $r$ , errors in vortex range produce corresponding errors in circulation. The velocity profiles of Figures 14 and 15 can be converted to the circulation profiles of Figures 16 and 17 by means of this equation. Because each vortex has two sides, there are actually two circulation profiles measured. The side toward the other vortex is marked by an X at the end and the side away from the other vortex is marked by an O. In order to make the two circulation profiles agree for small radii, the velocity offset between the two velocity profiles is averaged up to radius 10 m and used to correct the velocity profiles. This correction corresponds to the vortex transport velocity along the line-of-sight (LOS) to the vortex. The LOS velocity adds to one side of the vortex and subtracts from the other. Figure 18 shows the LOS velocities for the runs in Figures 16 and 17. For comparison, the radial transport velocities of the line-segment fit to the range are also plotted. The LOS velocities appear to be more erratic for these data than for the 1975 data (Ref. 2) and are thus less useful for estimating vortex transport.

Different radial coordinates are used for the circulation profiles in Figures 16 and 17. The 1975 B-747 (Ref. 2) data showed that the non-alleviated circulation profile is proportional to the logarithm of the radius:

$$\Gamma(r) = \Gamma_c(1 + \ln(r/r_c)). \quad (2)$$

The dashed lines in Figure 16 correspond to the 1975 fitted parameters:  $r_c = 2.51$  m and  $\Gamma_c = 253$  m<sup>2</sup>/sec. The results from these tests can thus be readily compared with those in 1975. The alleviated circulation profile was found to be linear in radius in the 1975 tests; the constant of proportionality was  $\Gamma(r)/r = 47$  m/sec. This form corresponds to a constant tangential velocity of 7.5 m/sec. This curve is drawn as a dashed line in Figure 17.



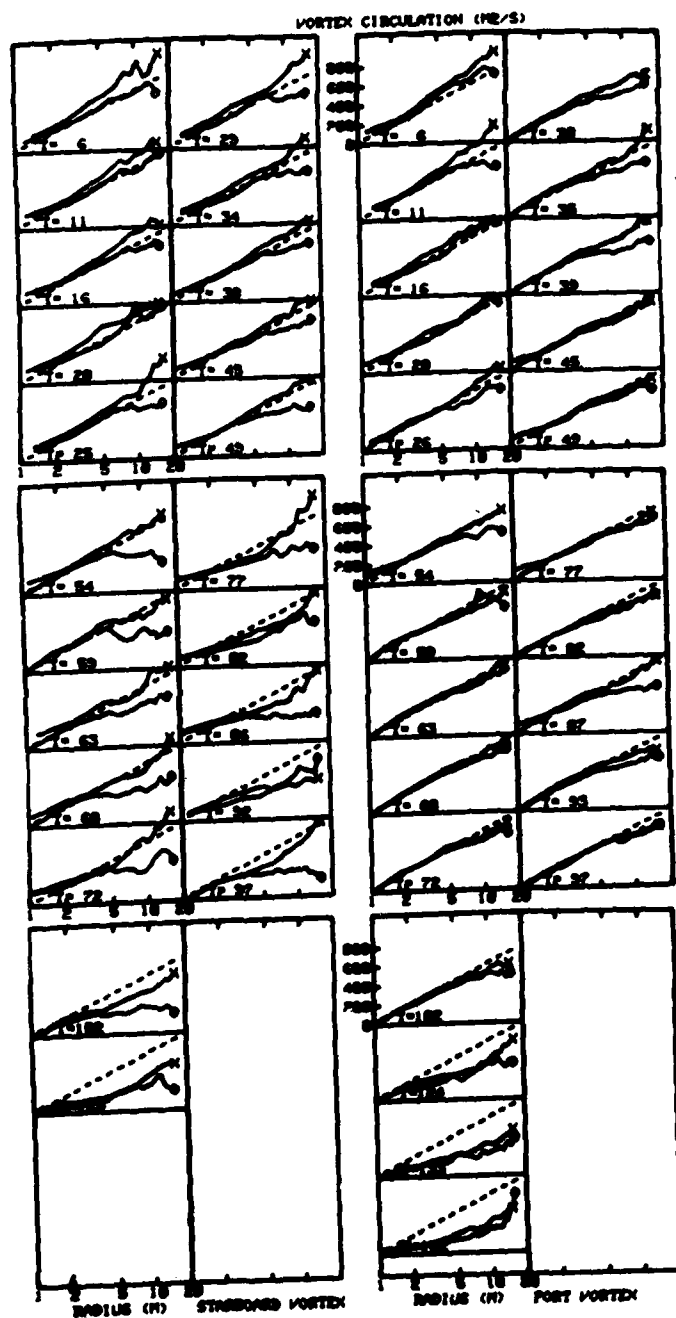


FIGURE 16. CIRCULATION PROFILES FOR A NON-ALLEVIATED RUN (RUN 1, 2/10/79)

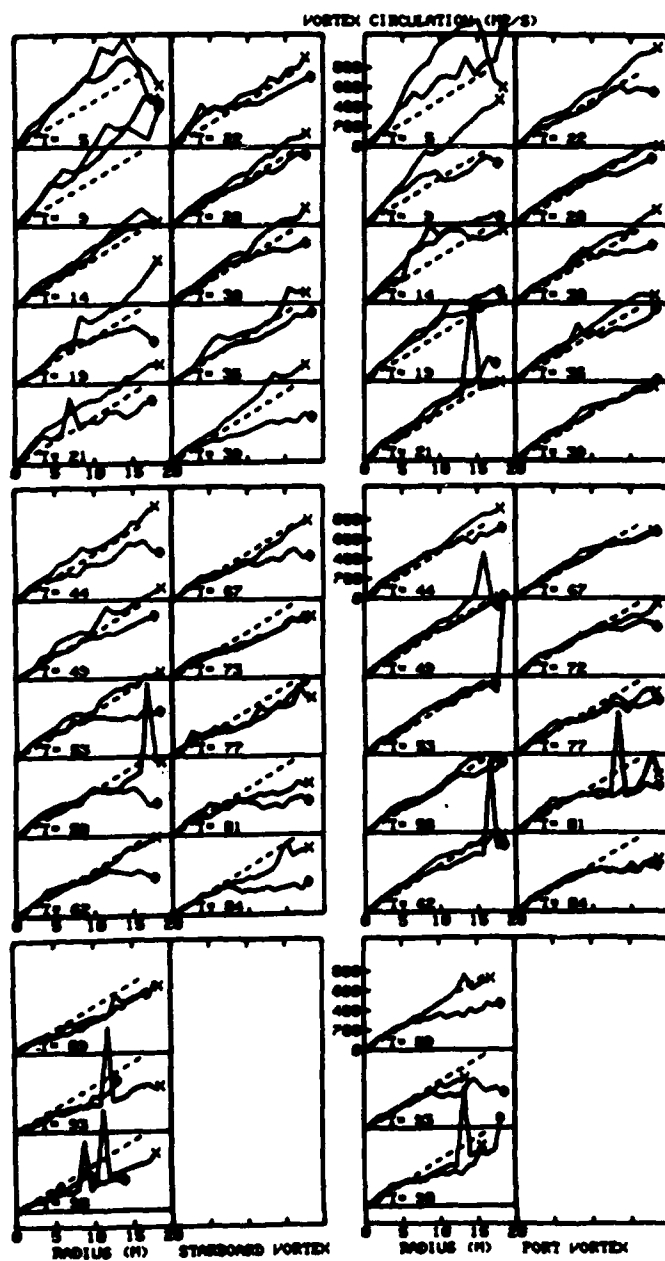


FIGURE 17. CIRCULATION PROFILES FOR AN ALLEVIATED RUN (RUN 2, 2/10/79)

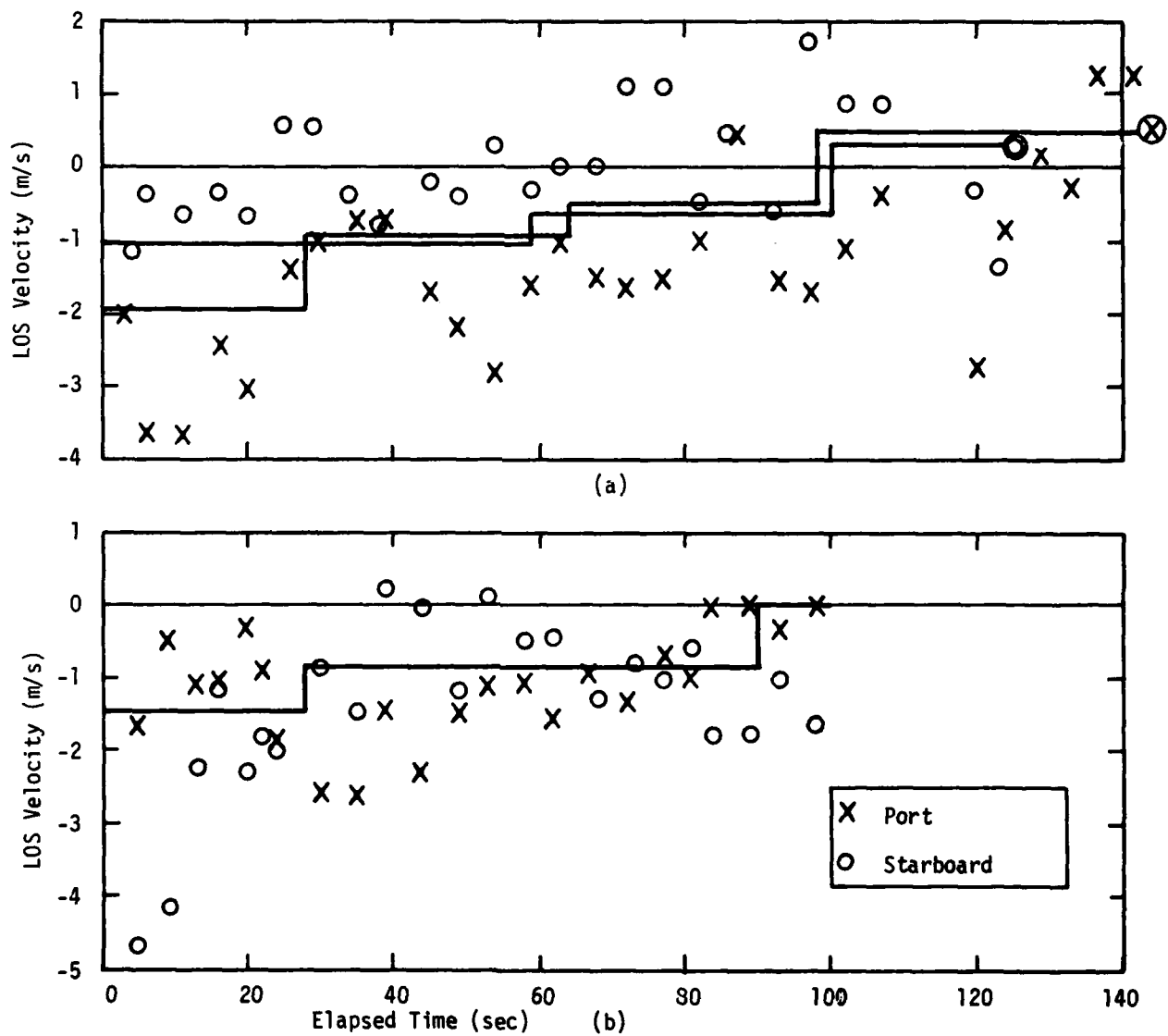


FIGURE 18. LINE-OF-SIGHT VELOCITIES: (a) RUN 1, 2/10/79, (b) RUN 2, 2/10/79

The vortex strength parameter found to be most useful in estimating vortex hazard is the average of the circulation up to a radius  $b/2$ :

$$\Gamma'(b/2) = (2/b) \int_0^{b/2} \Gamma(r) dr. \quad (3)$$

This parameter gives a first approximation to the maximum rolling moment induced on a wing of span  $b$ . The average circulation is evaluated for values of  $b/2 = 5, 10, 15$ , and  $20$  m. A value is not accepted unless data from both sides of the vortex are available. Averaging the two sides together cancels some systematic errors, in particular the effect of the vortex LOS transport velocity. Since the influence of the other vortex is significant at  $20$  m radius (see Figures 14 and 15), this procedure does not strictly measure the effect of a single vortex. However, the analysis is valid, since it properly estimates the effect of the complete wake flow field on an encountering wing. Figure 19 plots the average circulation versus vortex age for one alleviated and one non-alleviated run. Such plots will form the primary means for evaluating the effects of alleviation.

#### 4.1.4 Rolling Moment Determination

Appendix B examines the approximations involved in using average strength to represent maximum induced rolling moment. The conclusion is drawn that the vortex-induced rolling moment coefficient  $C_{\ell V}$  can be related to the average circulation  $\Gamma'$  by a proportionality constant depending upon the wing shape, wing-span, and airspeed. This analysis allows the data of Figure 19 to be replotted in the form of Figure 20. The time axis is changed to aircraft separation by means of the airspeed. Two aircraft types are plotted: the T-37 ( $b/2=5.15$  m), used to probe the wakes and a DC-9 ( $b/2=14.2$  m) which is typical of the small jet transports.

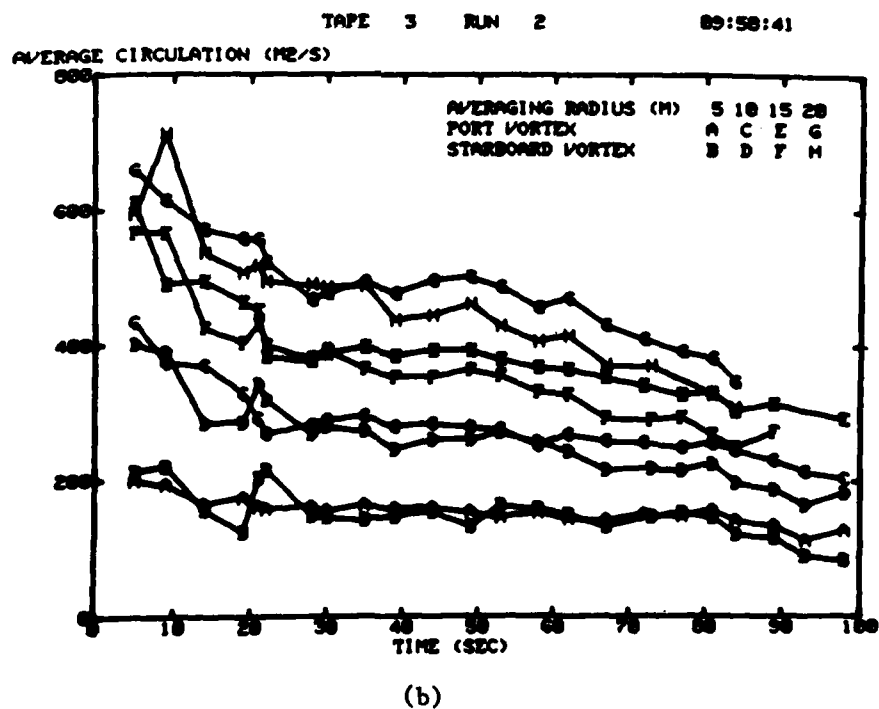
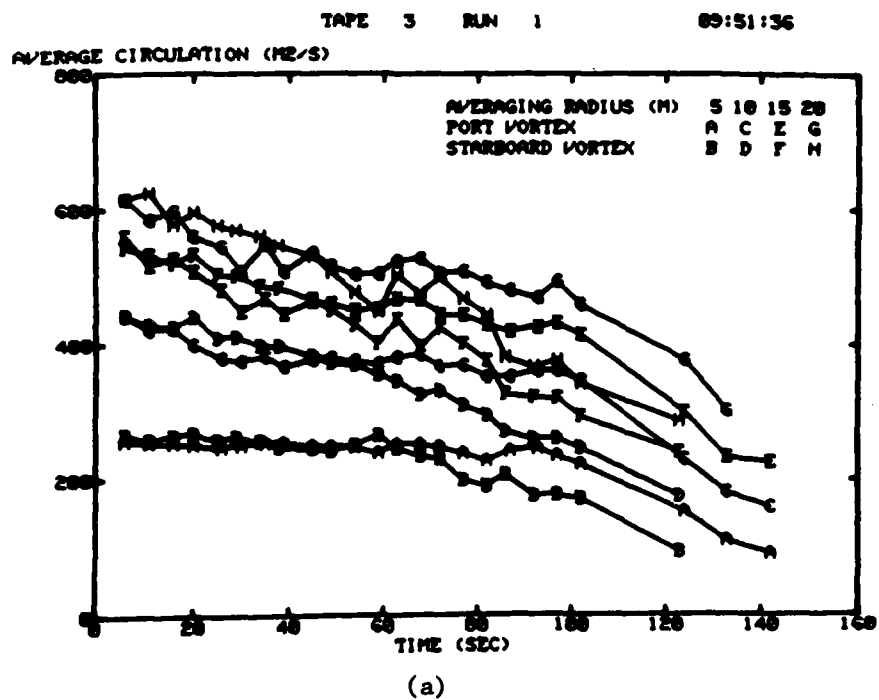


FIGURE 19. AVERAGE CIRCULATION VERSUS AGE: (a) NON-ALLEVIATED RUN (RUN 1, 2/10/79) (b) ALLEVIATED RUN (RUN 2, 2/10/79)

Plots of  $C_{\ell V}$  versus separation in nautical miles allow a direct comparison with the results of aircraft probe measurements. One correction is made in the  $C_{\ell V}$  data which is not included in the average circulation plots. The tangential velocities are decreased by three spectral bins (1.6 m/s) which was found to be the amount that  $V_{\max}$  overestimates the tangential velocity (Appendix C).

#### 4.1.5 Crosswind Corrections

The data analysis to this point makes no correction for the influence of crosswind on the vortex strength. Normally, this influence is cancelled by averaging the two sides of the vortex. This cancellation fails for crosswinds strong enough to drive the vortex velocity below the velocity-detection threshold and also when the other vortex blocks the LDV view of one side of the vortex. In order to deal with strong crosswinds, a procedure was developed to estimate the crosswind for a run and then to correct the velocity profiles by the crosswind component. The crosswind estimate uses the low frequency  $V_{pk}$  peak in the LDV spectrum (see Figure 2c). Only those portions of the scan free of the vortex influence are selected for computing the crosswind. The crosswind data points are averaged for different altitude ranges and the average value corresponding to the vortex height is selected for the analysis. Figure 21 shows the velocity data before and after crosswind correction for the run with the largest crosswind; the corrected values agree with other measurements (Figure 14). When the crosswind is strong, only the side of the vortex to which the crosswind adds is suitable for strength calculations since the other side is lost below the velocity detection threshold.

#### 4.1.6 Limitations of LDV Measurements

The extensive development of the LDV has produced a sensor with remarkable capabilities for tracking and measuring aircraft wake vortices. The sensor does have well defined limitations,

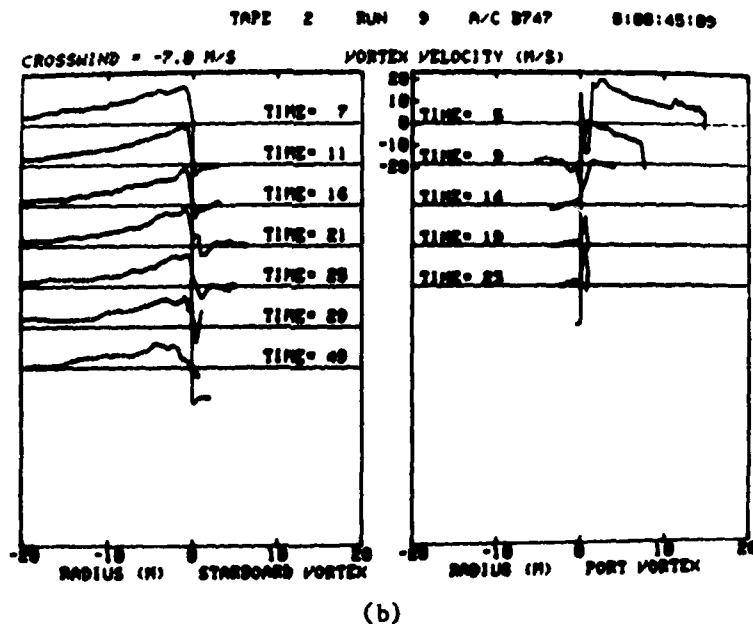
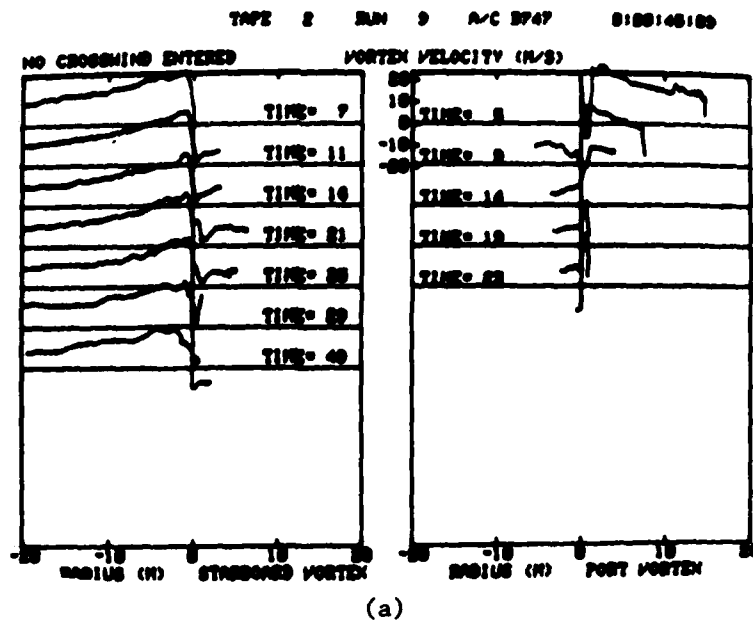


FIGURE 21. VELOCITY PROFILES FOR RUN 9, 11/8/79: (a) NO CROSSWIND, (b) WITH CROSSWIND CORRECTION

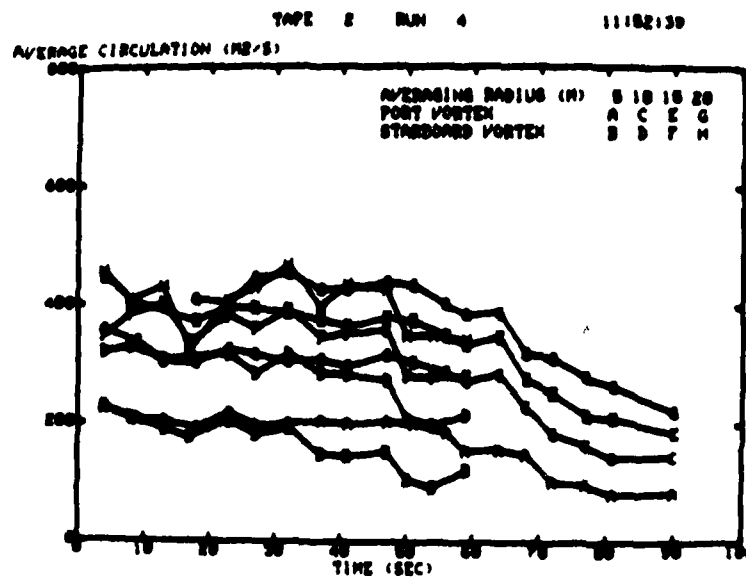
however, which are outlined in this section. These limitations should be kept in mind when the LDV results are being interpreted. The following limitations will be discussed:

- a. Range errors,
- b. Velocity errors,
- c. Residual velocity,
- d. Vortex signature identification,
- e. Crosswind, and
- f. Elevation angle errors.

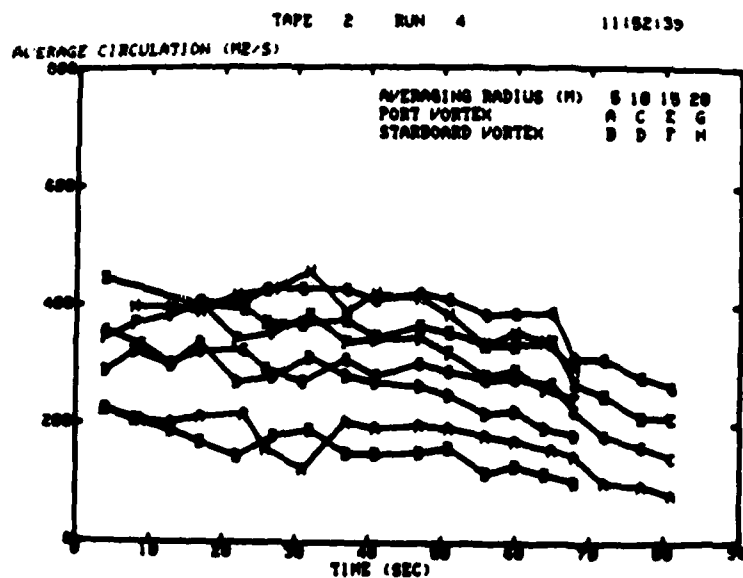
Errors in the estimation of the range to the vortex produce a proportional error in the calculated vortex strength. Errors as large as 20 percent may be introduced by this effect. Figure 22 gives some indication of the sorts of errors which can occur. The average circulation profiles for the same run using the range fit (Figure 12c) and the lateral position fit (Figure 12d) are compared. The results agree generally, but there are differences in detail. The lateral-position-fit data are distorted by range singularities at early times but are more accurate than the range-fit data for later times where the elevation angle becomes small. The difference in the duration of the data for the starboard vortex is a consequence of difference in the duration of the fitted track in Figure 12.

The use of  $V_{\max}$  to represent the vortex tangential velocity leads to an overestimate of vortex strength. The size of this effect is estimated in Appendix C to be three spectral bins (1.6 m/sec.) This error produces an overestimate in average circulation  $\Gamma'$  of 26, 52, 78, and 104  $\text{m}^2/\text{s}$  for averaging radii of 5, 10, 15, and 20 m, respectively. None of the average circulation data in this report include this correction. The induced rolling moment ( $C_{\ell V}$ ) data, however, do include it. The accuracy of this correction under all conditions is likely to be no better than  $\pm$  one spectral bin ( $\pm$  0.55 m/s in velocity).





(a)



(b)

FIGURE 22. AVERAGE CIRCULATION VERSUS AGE FOR RUN 4, 2/9/79:  
 (a) RANGE FIT, (b) LATERAL POSITION FIT

The LDV vortex data show the presence of a large non-zero value of  $V_{\max}$  even when there is no apparent vortex. This effect appears to be caused by the large scattered signals from the smoke which remains even after the vortex has decayed. This residual  $V_{\max}$  appears to have a value of about 3.3 m/sec (see Figures 14 and 15). The effect of this residue is to obscure the vortex when its velocities become low. If the vortex velocity is less than the residual velocity, the resulting value of strength will be an overestimate. This problem will set an absolute lower bound on the average circulation (approximately 50, 100, 150, and 200  $\text{m}^2/\text{sec}$  for averaging radii 5, 10, 15 and 20 m). One must become suspicious of LDV strength measurements near these levels. Unfortunately these lower bounds are exactly the hazard thresholds used for modeling the decay of wake-vortex hazard for different size aircraft (Ref. 7). Thus, we must conclude that the LDV, as presently configured, is not sensitive enough to measure the disappearance of the wake-vortex hazard. It might be possible to use an increased spectral data acceptable threshold (see Figure 2) to reduce the value of the residual  $V_{\max}$ . Preliminary tests of an LDV velocity-translated mode also indicate a reduction in this problem.

The identification of the vortex-velocity signature is affected by the residual  $V_{\max}$ . The computer operator has no problem identifying the center of a strong vortex. However, when it becomes weak, it is difficult to decide whether a particular dip in  $V_{\max}$  is the center of a vortex, or merely a fluctuation. Thus, one must be cautious not only in interpreting the strength of a vortex near the limiting level but also in being sure that the vortex actually exists. The best check on vortex existence is continuity in the vortex position.

The presence of an ambient wind can interfere with the wake-vortex measurements. An overestimate of vortex strength will result if the ambient wind drives one side of the vortex below the residual velocity threshold. In some cases the ambient wind also appears to reduce the residual  $V_{\max}$ , so that the problem is somewhat mitigated. If the crosswind is used to correct  $V_{\max}$ ,

one side of the vortex can be used alone to compute vortex strength; this strength, however, becomes dependent on errors in the cross-wind estimate.

The scanner elevation-angle calibration was in error by as much as  $5^{\circ}$  for some of the tests, particularly those at Moses Lake. These errors have not been corrected in the results. When the vortices are overhead such errors have little consequence, but they can produce significant errors in altitude for vortices at low elevation angle and large range (e.g., in the 2/9/79 data).

#### 4.2 GROUND WIND VORTEX SENSING SYSTEM

The ground wind sensor lines used in the China Lake and Edwards tests were laid out along the same line monitored by the LDV (see Figures 7 and 8). The LDV was located 500 feet (152 m) from the runway centerline and the 8 propeller anemometers were placed at distances of 200, 300, 400, 450, 500, 550, 600, and 700 feet (61, 91, 122, 137, 152, 166, 183, and 213 m) from the LDV. The anemometers were mounted at a height of about 3 feet (0.9 m) on fence posts at China Lake and about 4 feet (1.2 m) on movable stanchions at Edwards AFB.

Figure 23 shows sample GWVSS data from the China Lake tests. The vortices show up as high and low peaks in the crosswind signal. These peaks (marked with arrows) have been shown (Ref. 6) to indicate that the vortex is directly above the particular anemometer. Figure 23 is of particular interest because the vortices from the F-86 probe aircraft are shown in addition to those from the B-747 generator aircraft. The vortex peaks indicated in Figure 23 are used to generate the GWVSS vortex lateral position points plotted in Figure 24. LDV lateral position fits and photographic data are also plotted for comparison. The three measurement techniques give consistent descriptions of the vortex motion, namely that the vortices remain together for about 20 seconds and then spread apart in ground effect, as one would expect in

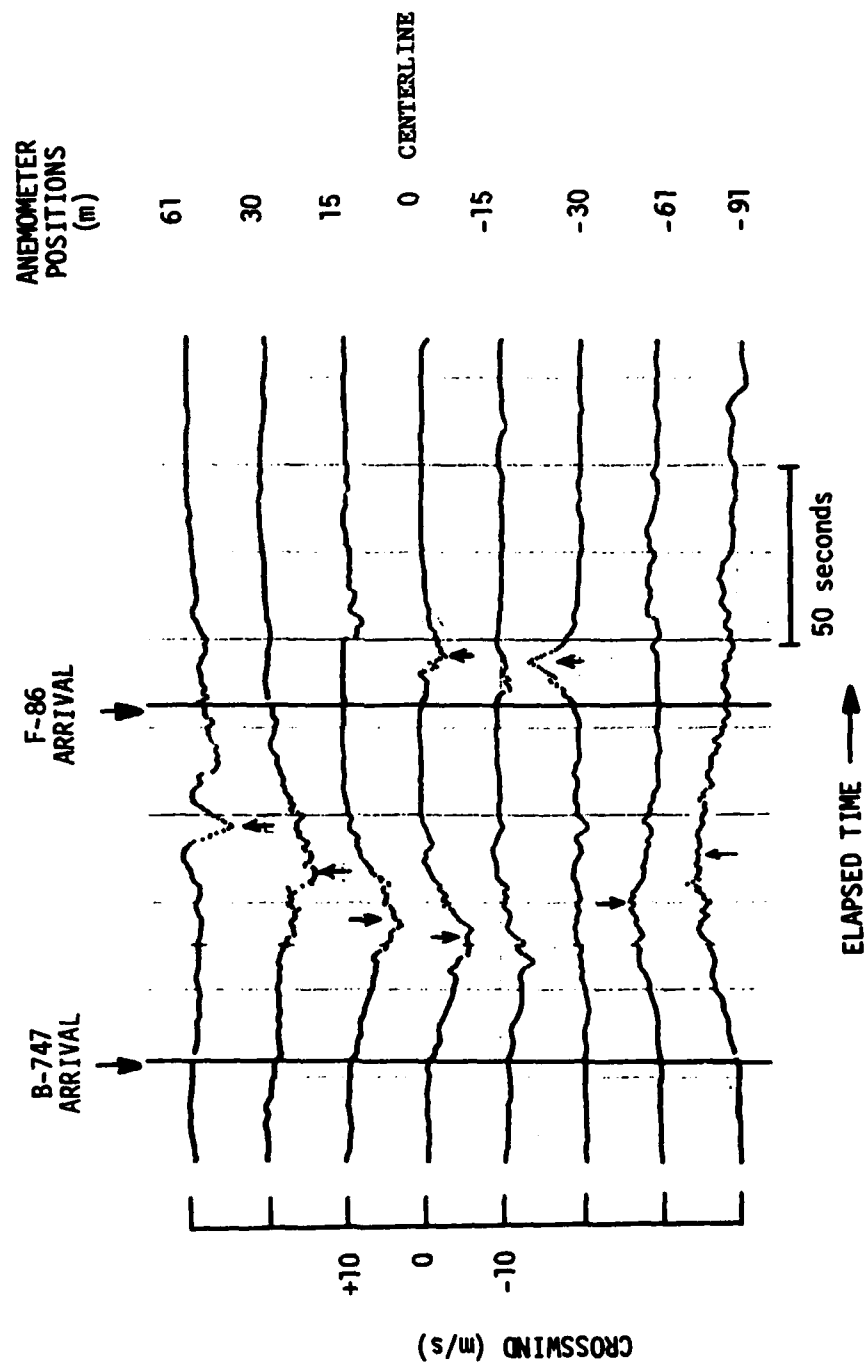


FIGURE 23. GWSS DATA FOR RUN 3, 11/3/79. THE VELOCITY ZERO POINTS FOR EACH ANEMOMETER ARE INDICATED BY THE HASH MARKS AT THE LEFT.

the absence of a crosswind. However, the detailed agreement between sensors is not particularly good. Plots like Figure 24 are shown in Appendix F for all the China Lake and Edwards runs.

The China Lake lateral position plots like Figure 24 are useful for determining the position of the F-86 relative to the B-747 vortices. For example, in Figure 24 the F-86 vortex locations show that the F-86 was very close to the runway centerline and at least 100 m from the B-747 vortices.

#### 4.3 PHOTOGRAPHY

A determination of the vortex location from two simultaneous photographs begins with an identification of which vortex is which on both pictures. Each vortex position is assigned to a point on the scale included in the pictures. A geometrical conversion then yields the vortex spatial location.

The photographic tracking of vortices was much more successful for the high altitude (200 to 300 m AGL) flights than for those at low altitudes where the two vortices may be hard to distinguish and may remain in the field of view for only a short time. The photographic data on 2/9/79 and 11/8/79 were lost because of camera malfunctions. The high altitude data of 2/10/79 gave tracks lasting as long as 1 minute even though the sky was overcast. The photographic tracks are plotted as lines in Figure 11. Unfortunately, no vortex bursts could be distinguished on 2/10/79 because of the overcast. The photographs on 2/12/79 were useless because of the low camera angles (Figure 5) and the low ceiling. The tracks on 11/8/79 are of short duration because the field of view of the vertically pointing centerline camera (24 mm focal length) was small and the vortices moved rapidly. Figure 24 shows the photographic data as solid points. The arrow at time zero marks the centerline of the aircraft. In general, the photographic tracking data are not always consistent with the other sensors (Figure 11b) or with itself. In Figure 24 the aircraft centerline and the vortex centerline appear to be inconsistent.

The results of the photography were disappointing. The combination of inexperienced camera operators, unfavorable geometry (low altitude) for the later flights, and poor backgrounds produced little of value from this potentially valuable technique.

## 5. RESULTS

A number of useful results have come from the ground-based sensor measurements. The LDV data on vortex strength and induced-rolling moment allowed assessing the effectiveness of spoiler alleviation of wake vortices for various types of encountering aircraft. The LDV results agreed well with probe aircraft measurements but poorly with scale-model wind-tunnel measurements. Photographic data elucidated the mechanism of spoiler alleviation. The ground-based sensors gave some information on the promising spoilers-plus-periodic-roll configuration.

The data plots for all the runs are contained in a series of appendixes. Appendix E contains the LDV data. Appendix F contains the lateral position plots, like Figure 24, for the runs in the second series of tests. Appendix G contains all the temperature profile data and some wind data for the second series of tests.

### 5.1 VORTEX STRENGTH

The first series of tests, particularly the high-altitude runs, produced the most useful data on vortex alleviation. The second series concentrated on a single alleviated configuration, spoilers 2, 3, 4 at  $30^{\circ}$ . The last day on the second series of tests, a variety of configurations were studied, but the data were of poor quality because of high winds.

The most convenient form for comparing different runs is the plots of average circulation versus age. Figure 25 shows the high altitude non-alleviated runs. Figures 26 and 27 show the high altitude alleviated runs for 2, 3, 4 and 2, 4 spoilers, respectively. For comparison purposes it is undesirable to use data before 10 seconds for non-alleviated runs, and before 20 seconds for alleviated runs because of the time required for the completion of the vortex roll-up process.

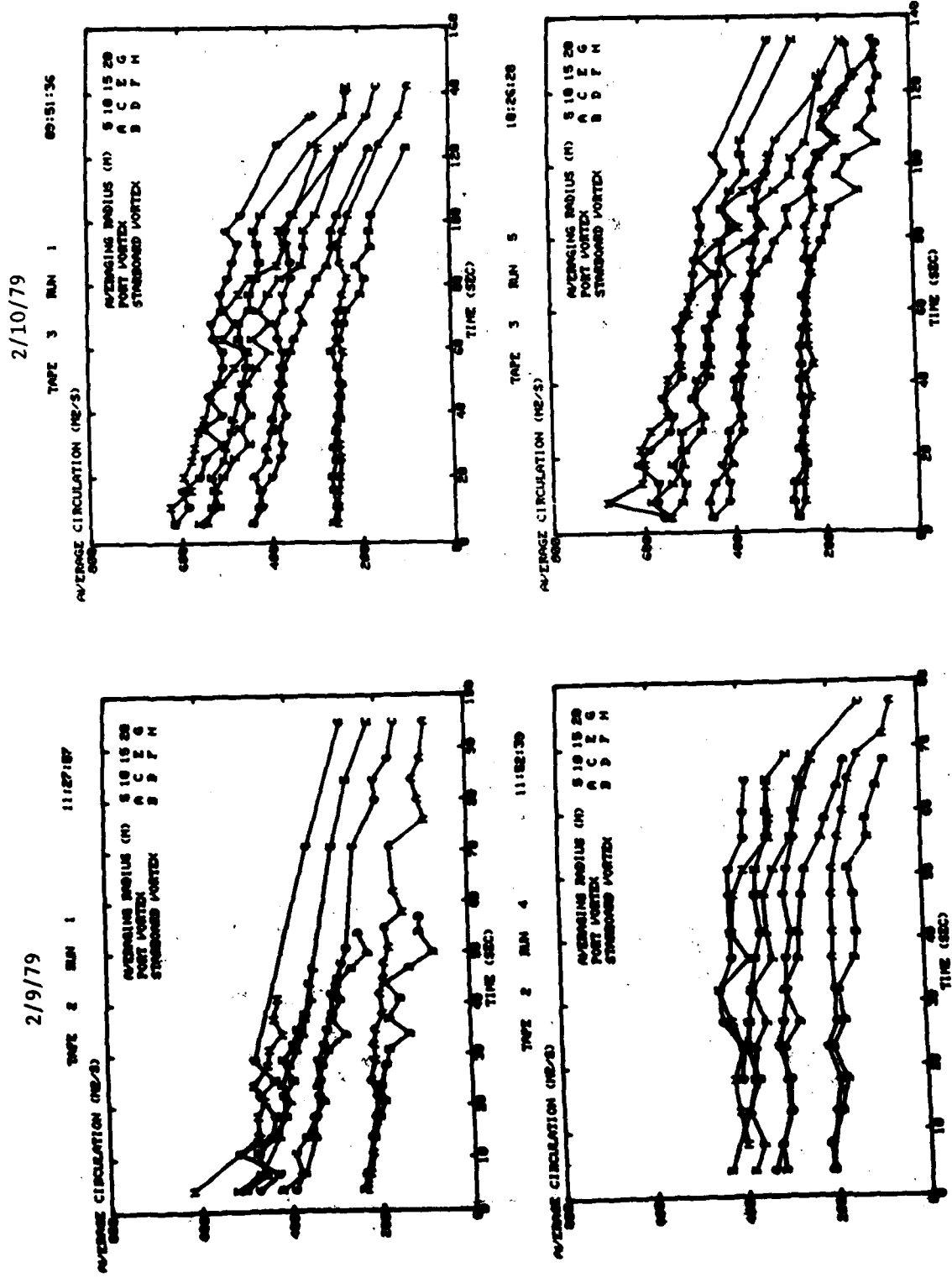


FIGURE 25. AVERAGE CIRCULATION VERSUS AGE FOR RUNS WITH NO SPOILERS



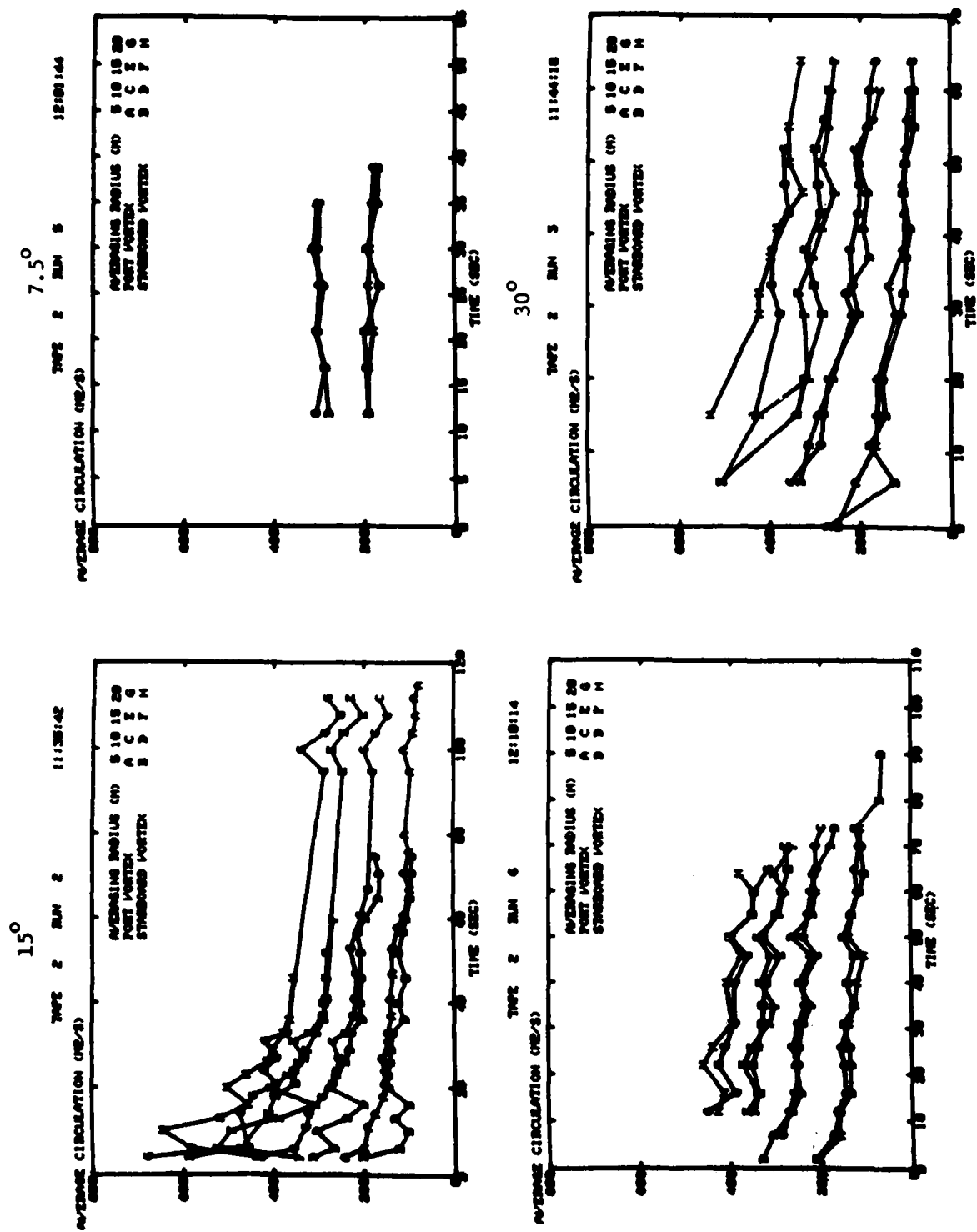
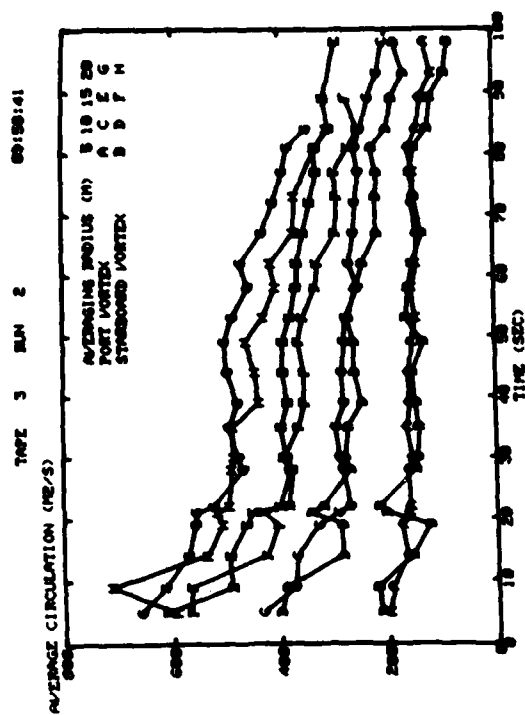
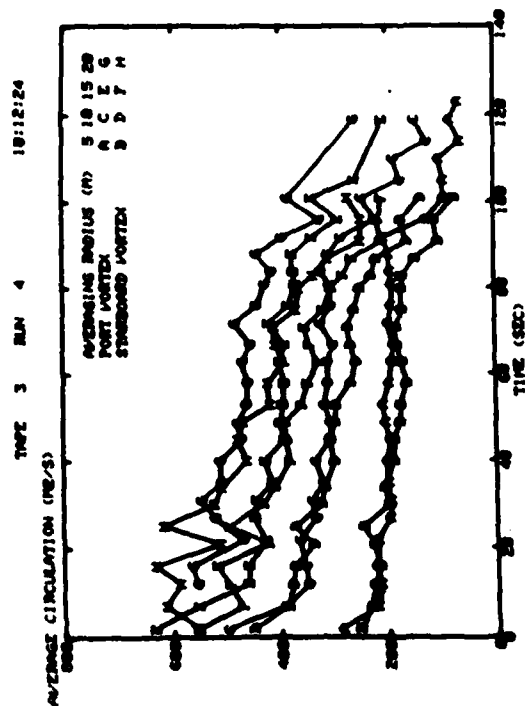


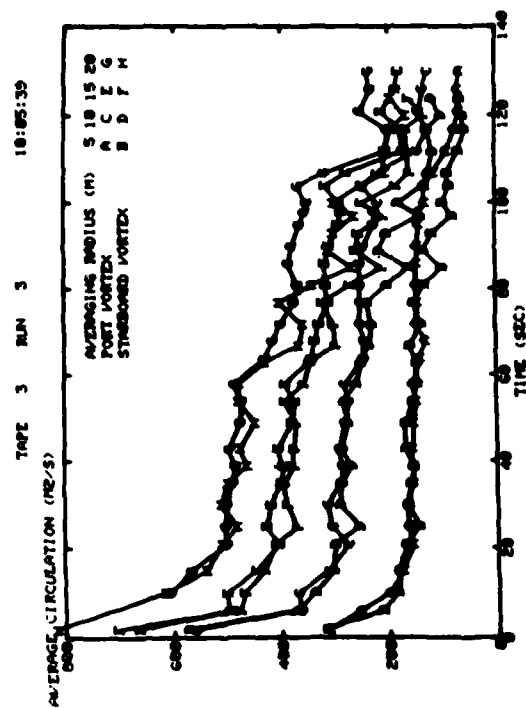
FIGURE 26. AVERAGE CIRCULATION VERSUS AGE FOR SPOILERS 2, 3, 4 ON 2/9/79



30°



15°



45°

FIGURE 27. AVERAGE CIRCULATION VERSUS AGE FOR SPOILERS 2, 4 ON 2/10/79

The non-alleviated runs in Figure 25 show a significant difference for the two days, the initial vortex strengths being 3/4 as strong on 2/9/79 as on 2/10/79. This effect may be partially due to errors in the assigned vortex range, but at least some of the effect is real since the vortex velocities are actually higher on 2/10/79 (see Appendix E). The data from Figures 25 to 27 at 20 and 60 seconds elapsed time are included in Tables 4 and 5; the percent alleviation is calculated by comparing data taken on the same day and at the same elapsed time. Figures 28 and 29 show the non-alleviated and alleviated runs, respectively, for the ground effect runs on 2/12/79. The 20-second alleviation, listed in Table 4, appears to be somewhat greater than that for the high-altitude runs. The non-alleviated strengths are stronger, however, than on 2/9/79, thus leaving some question as to the source of the difference. The reader should note that the percent alleviations in Tables 4 and 5 are reduced if the proper correction for  $V_{\max}$  (Appendix C) is applied; the corrected values are enclosed in parentheses.

The variability of vortex decay is illustrated in Figure 30 which shows all the spoiler runs of 11/3/79 (Spoilers 2, 3, 4 at  $30^\circ$ ). The vortex trajectories are also shown since there appears to be some correlation between vortex strength and height. The variation in vortex trajectories is due to the Crow instability which causes some portions of the vortex to be low (e.g., Runs 1 and 4) and some to be high (e.g., Run 2). The vortex 5-m average strength shows considerable variation also, being high for Runs 2 and 3 and lower for Runs 1 and 4. The decay of the vortex strength tends to affect the outer portion of the vortex more than the core, as noted before (Ref. 2). The most notable feature of the velocity profiles (Figure 31 and Appendix E) is a small persistent vortex core. The vortex duration is generally less for the later runs. The analysis of Appendix G shows that the ground-based inversion broke up at approximately the time of Run 4 or 5.

TABLE 4. ALLEVIATION WITH SPOILERS 2, 3, 4

SPOILER DEFLECTION (Degrees)	$\Gamma'$ (5 m) (m <sup>2</sup> /sec)	Alleviation %	$\Gamma'$ (10 m) (m <sup>2</sup> /sec)	Alleviation %	$\Gamma'$ (15 m) (m <sup>2</sup> /sec)	Alleviation %
Time = 20 seconds (2/9/79)						
0	200	100	320	100	395	100
7.5	190	95(94)	300	94(93)		
15	145	72(68)	275	86(83)	350	89(86)
30	155	77(74)	255	80(76)	310	79(73)
Time = 60 seconds (2/9/79)						
0	165	100	270	100	330	100
15	115	70(64)	205	76(70)	275	83(78)
30	90	55(46)	160	59(50)	260	79(72)
Time = 20 seconds (2/12/79)						
0	225	100	380	100	470	100
15	150	67(62)	265	67(65)	375	80(76)
30	130	58(52)	245	65(59)	360	77(72)

Note: The data are averaged for different runs and vortices.

TABLE 5. ALLEVIATION WITH SPOILERS 2, 4

SPOILER DEFLECTION (Degrees)	$\Gamma'$ (5 m) (m <sup>2</sup> /sec)	Alleviation %	$\Gamma'$ (10 m) (m <sup>2</sup> /sec)	Alleviation %	$\Gamma'_2$ (15 m) (m <sup>2</sup> /sec)	Alleviation %
Time = 20 seconds						
0	225	100	420	100	520	100
15	220	86(63)	355	85(82)	445	86(83)
30	160	63(44)	295	70(66)	410	79(75)
45	160	63(44)	290	69(65)	410	79(75)
Time = 60 seconds						
0	240	100	360	100	435	100
15	180	75(72)	280	78(74)	365	84(80)
30	150	62(58)	255	71(66)	350	81(76)
45	140	58(53)	240	67(61)	340	78(73)

Note: The data are averaged for different runs and vortices.

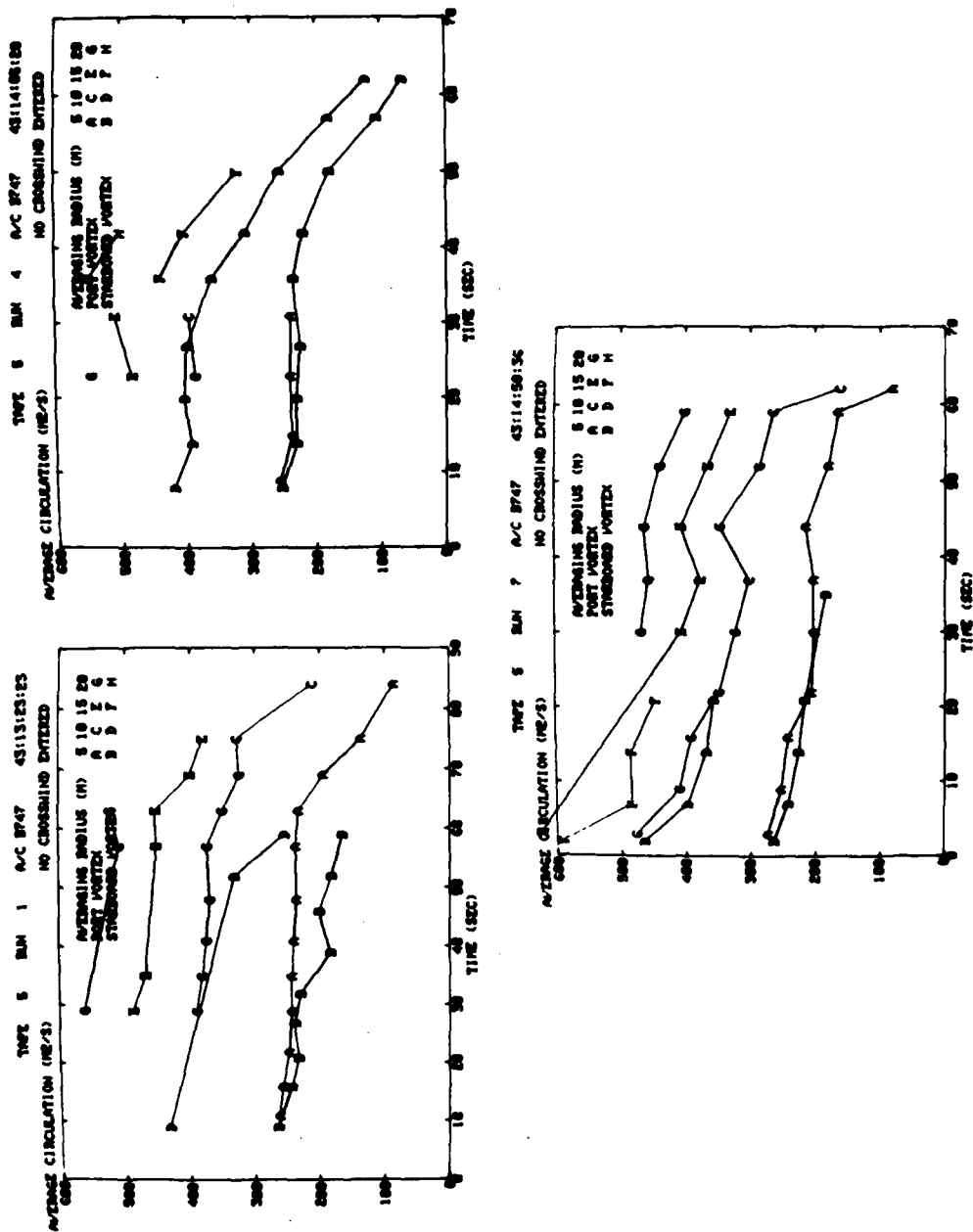


FIGURE 28. AVERAGE CIRCULATION VERSUS AGE FOR NON-ALLEVIATED RUNS ON 2/12/79



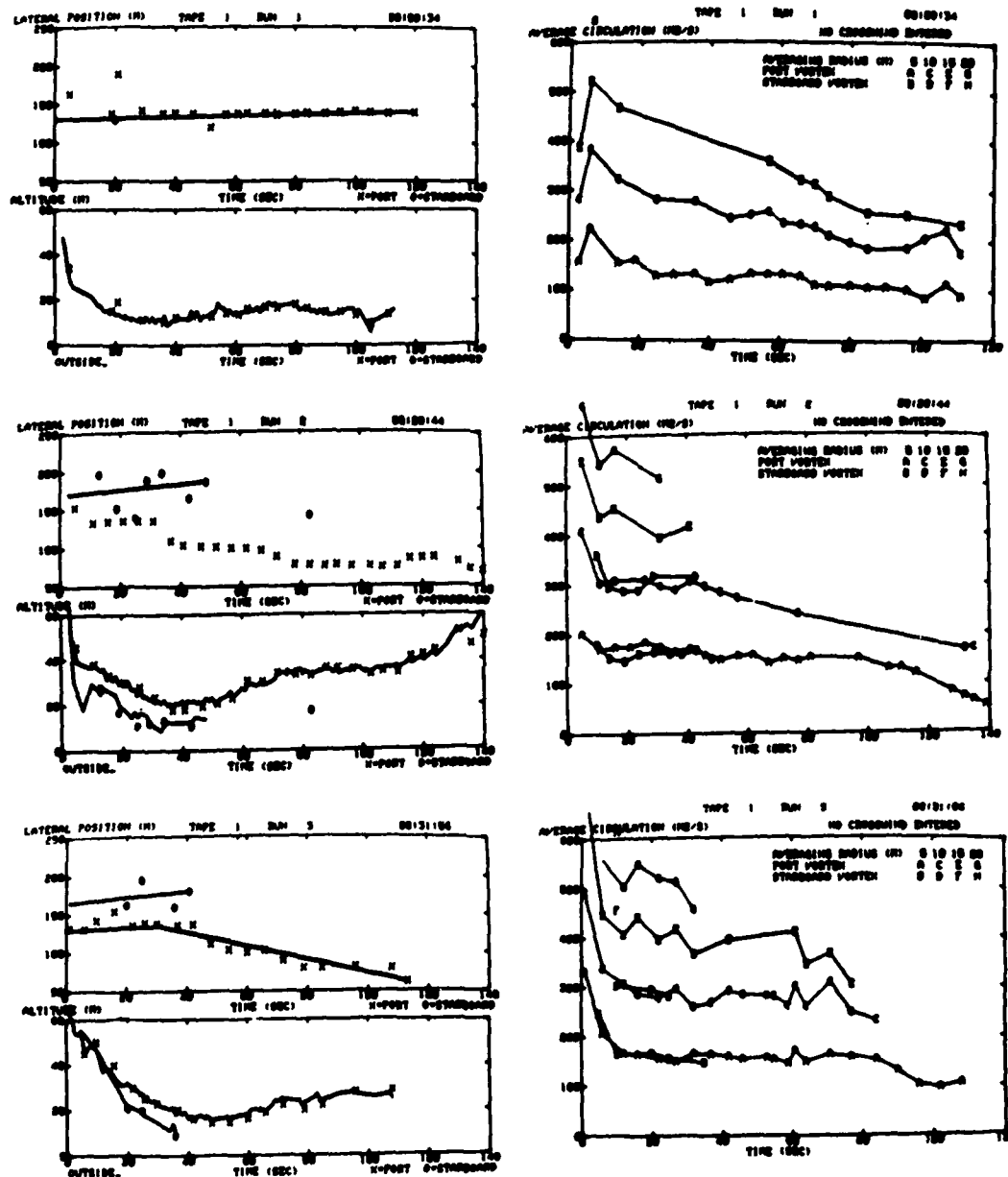


FIGURE 30. LDV TRAJECTORY AND STRENGTH DATA FOR RUNS 1-7 ON 11/3/79



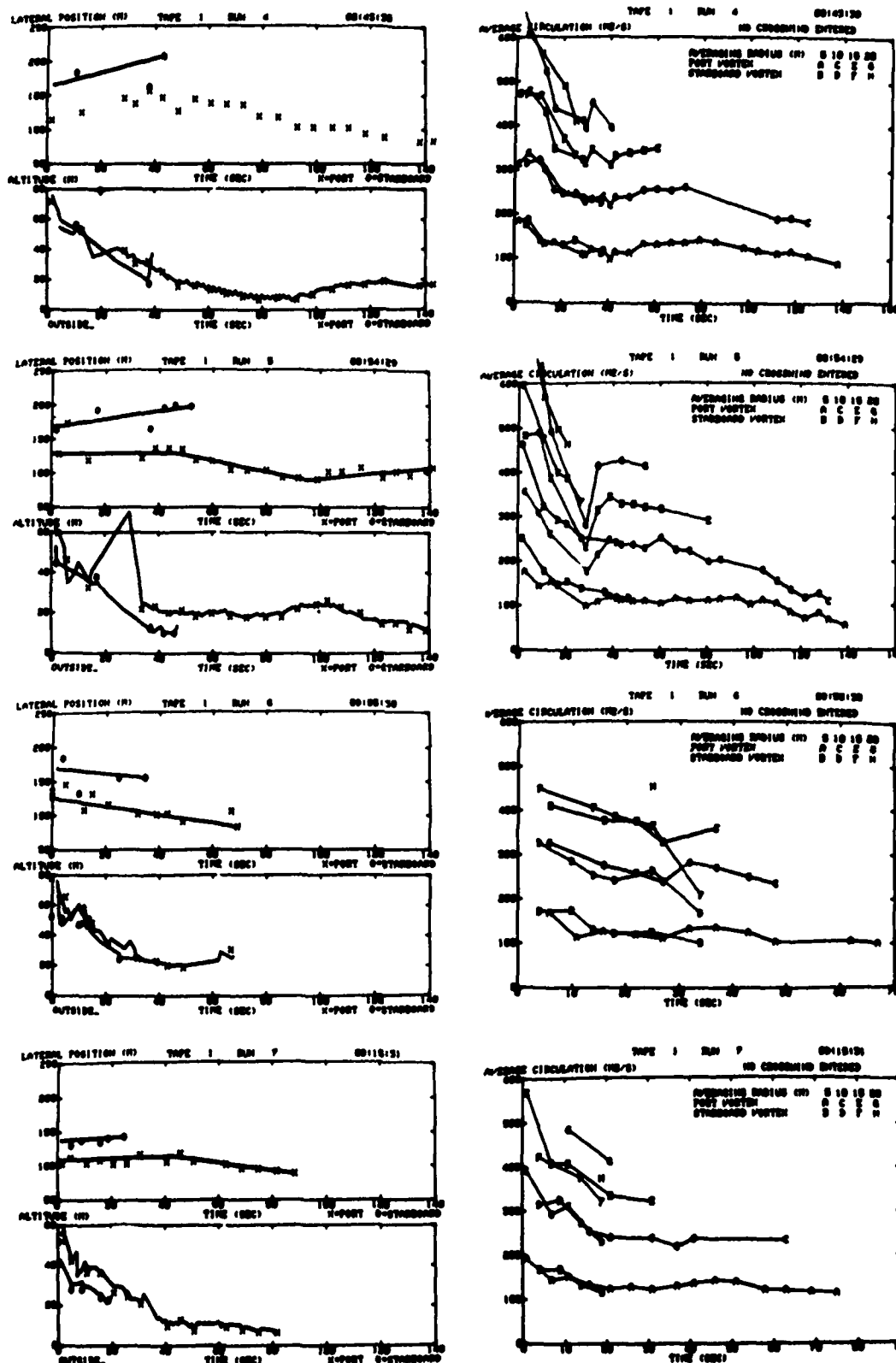


FIGURE 30. LDV TRAJECTORY AND STRENGTH DATA FOR RUNS 1-7 ON 11/3/79 (CONTINUED)



A comparison of the 5-m average circulations of Figure 30 with Figures 26 and 29 shows stronger, more persistent vortices for the same configuration in the second series of tests compared to the first, as was also noted in the T-37 probes.

The last day of testing (11/8/79) was not particularly useful for evaluations of alleviation because of the large ambient winds (see Appendix G). The data are contained in Appendix E.

## 5.2 COMPARISONS WITH OTHER MEASUREMENTS

Data on vortex-induced rolling moments are available from T-37 probes and from wind tunnel measurements (Ref. 3) of torques on a following wing model. The results of the LDV measurements are compared with each technique in the following sections.

### 5.2.1 Probe Aircraft

The analysis of the T-37 aircraft data from these tests has not been completed. Figure 32 shows a preliminary analysis of the 2/9/79 data (supplied by M.R. Barber of the National Aeronautics and Space Administration/Dryden Flight Research Center [NASA/DFRC]). The results are in general agreement with the LDV data on Figure 33c. The LDV data show slightly lower values of  $C_{\ell V}$ . Unfortunately, only a single out-of-ground-effect LDV run was made for this configuration; consequently, the consistency of the LDV measurement cannot be directly verified. Some indication of consistency is available, however, from the ground-effect data for this configuration (Figure 29) which show good agreement (for the limited time covered) with the single high-altitude run (Figure 26).

The source of the small disagreement between the T-37 probe and LDV measurements may lie in the data processing methods for the two types of data. The T-37 probe data are the highest recorded values of induced rolling moment. Any noise in the measurement will cause a high reading. The 1.6-m/s LDV correction (Section 4.1.6) also is about half the final LDV  $C_{\ell V}$  value. If

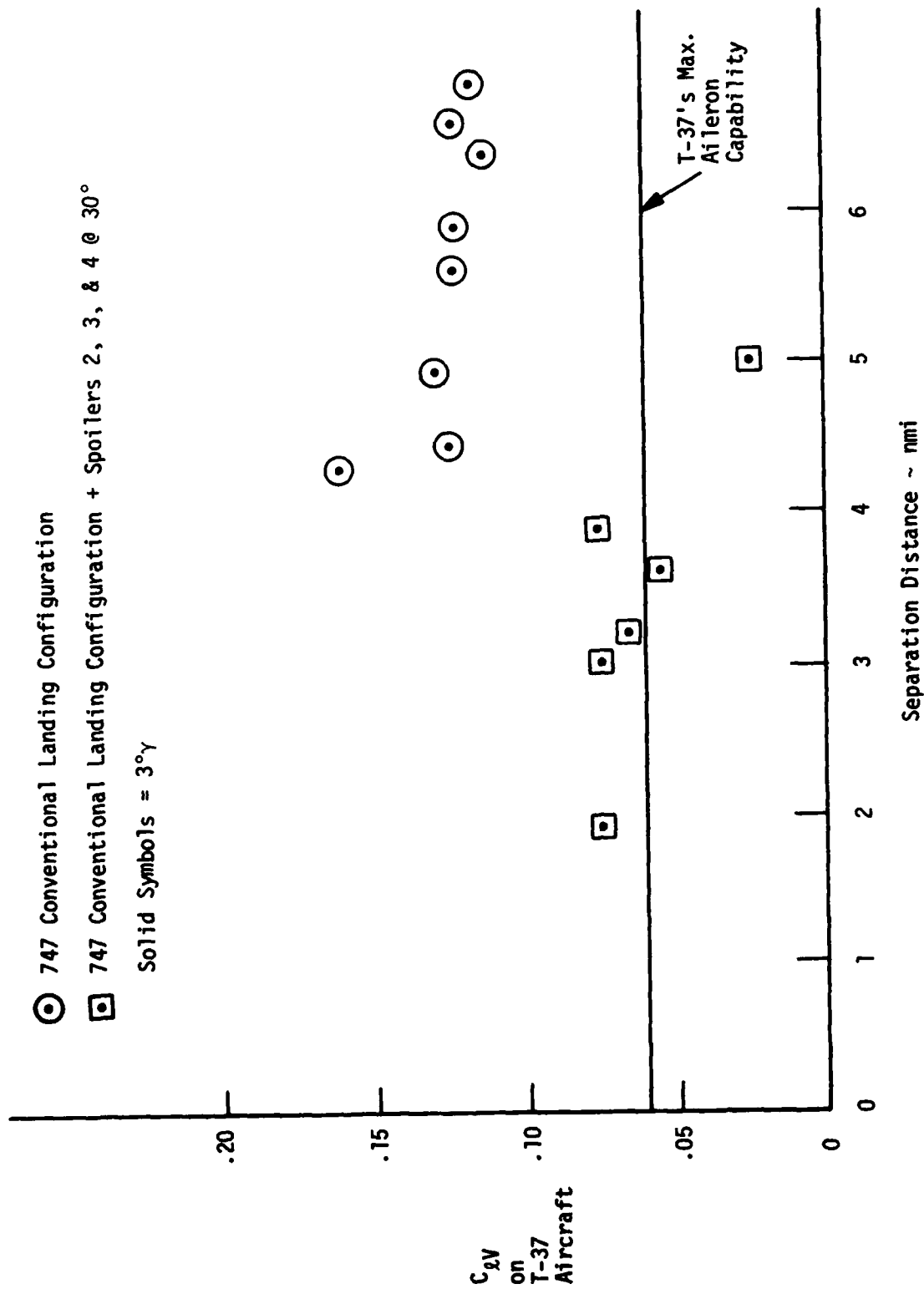


FIGURE 32. T-37 PROBE DATA

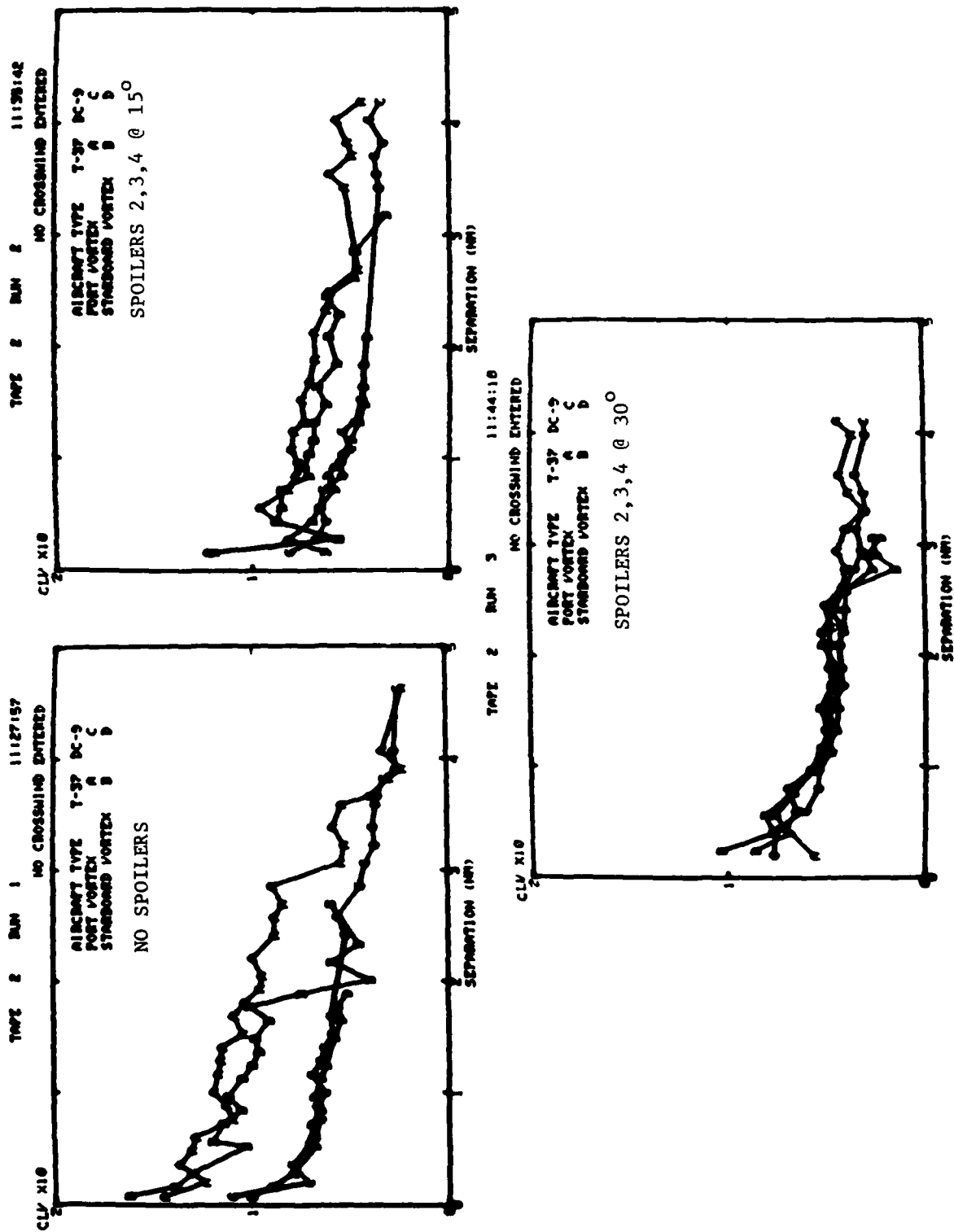


FIGURE 33. CALCULATED VORTEX-INDUCED ROLLING MOMENTS COEFFICIENTS VERSUS SEPARATION (NAUTICAL MILES)

this correction is too large for decayed alleviated vortices, the LDV values could be raised significantly.

The non-alleviated data points in Figure 32 are taken from earlier tests. They show vortices lasting significantly longer than shown by the "high-altitude" LDV measurements. The difference is probably related to decay caused by atmospheric turbulence. The turbulence level at the LDV high altitudes ( $\leq 250$  m AGL) are probably significantly greater than those where the T-37 probes were done ( $> 600$  m AGL). For the non-alleviated vortices, the magnitude of the T-37 induced rolling moment is in reasonable agreement with the LDV data from 2/10/79 (Figure 25), but greater than that from 2/9/79 (Figure 33a).

The LDV measurements exhibit qualitative agreement with the results of the aircraft probe measurements. First of all, the T-37 probes showed that the alleviated vortices (spoilers 2, 3, 4 at  $30^\circ$ ) were stronger in the second test series than in the first. The LDV data show similar results. The LDV data also indicate that spoilers 2, 3, 4 at  $30^\circ$  produce weaker vortices than spoilers 2, 4 at  $45^\circ$ , as was determined from the T-37 probes. The nominal alleviation achieved is about the same, however, if the LDV data are normalized to the strength of the unalleviated vortices on a particular day (see Tables 4 and 5).

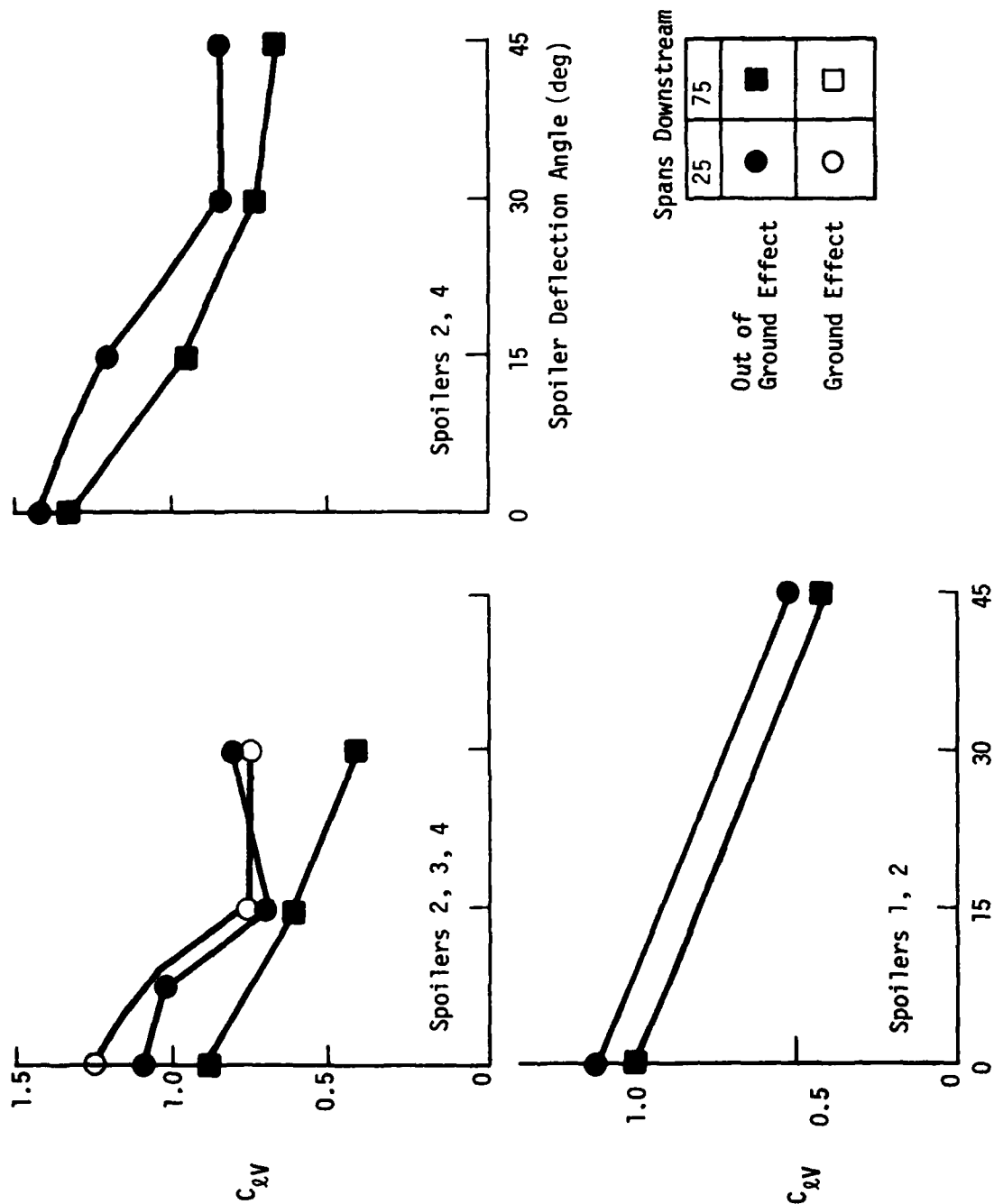
The ground-based sensors also showed qualitative agreement with the F-86 probes. The F-86 probes on 11/2/79 showed a significant decrease in smoke marking and induced roll between Runs 3 and 4. The meteorological data (Appendix G) show that the ground-based inversion had broken up by this time. The LDV data on 11/3/79 show a corresponding reduction in vortex lifetime at Run 4 or 5. The vortex sensors also show (Appendix F) that the F-86 never penetrated a vortex at the sensor line during its actual landings. This result is consistent with the absence of any vortex-induced roll on the final approach to landing.

### 5.2.2 Wind Tunnel Measurements

Wind tunnel measurements commonly refer to vortex age in terms of the number of spans downstream. Figure 34 shows the 5-m LDV data of Tables 4 and 5 converted to  $C_{\delta V}$  (with the 1.6 m/s LDV correction) as a function of spans downstream (airspeed = 75 m/sec). The data for spoilers 1, 2 is taken from Reference 2. Figure 35 compares the 25-span LDV flight data with the corresponding wind tunnel data at 7.8 spans (Ref. 1). The LDV data reproduces the trends in the wind tunnel measurements, even including the rise between  $15^\circ$  and  $30^\circ$  for spoilers 2, 3, 4. This increase between  $15^\circ$  and  $30^\circ$  disappears at 75 spans (Figure 34) where  $30^\circ$  spoilers shows a substantial improvement over  $15^\circ$ .

The LDV data are substantially higher and, in fact, much closer to the T-37 flight data than the wind tunnel results. Some of the difference may be due to the lower  $C_L$  (1.2) for the wind tunnel tests. Three other effects are also likely to be responsible:

1. The wind tunnel measurements are taken as average torques on a small model (0.03 scale). The maximum average torque can be less than the actual maximum torque because of vortex meander.
2. The model rolling moment may also be lower than the flight value because the lower Reynolds number leads to stall at lower angle of attack on the test wing than on the full-scale wing (Ref. 8).
3. The lower wind tunnel  $C_{\delta V}$  could conceivably be caused by incomplete vortex roll-up for the alleviated configurations where the LDV data do not settle down until 25 spans. Increased distance downstream in the wind tunnel, however, generally leads to lower values of  $C_{\delta V}$ , presumably because of meander (Ref. 9).



Spoiler Deflection Angle (deg)

FIGURE 34. EFFECT OF B-747 SPOILER DEFLECTION ANGLE ON MAXIMUM  $C_{dv}$ :  
LDV MEASUREMENTS IN FULL-SCALE FLIGHT TESTS.



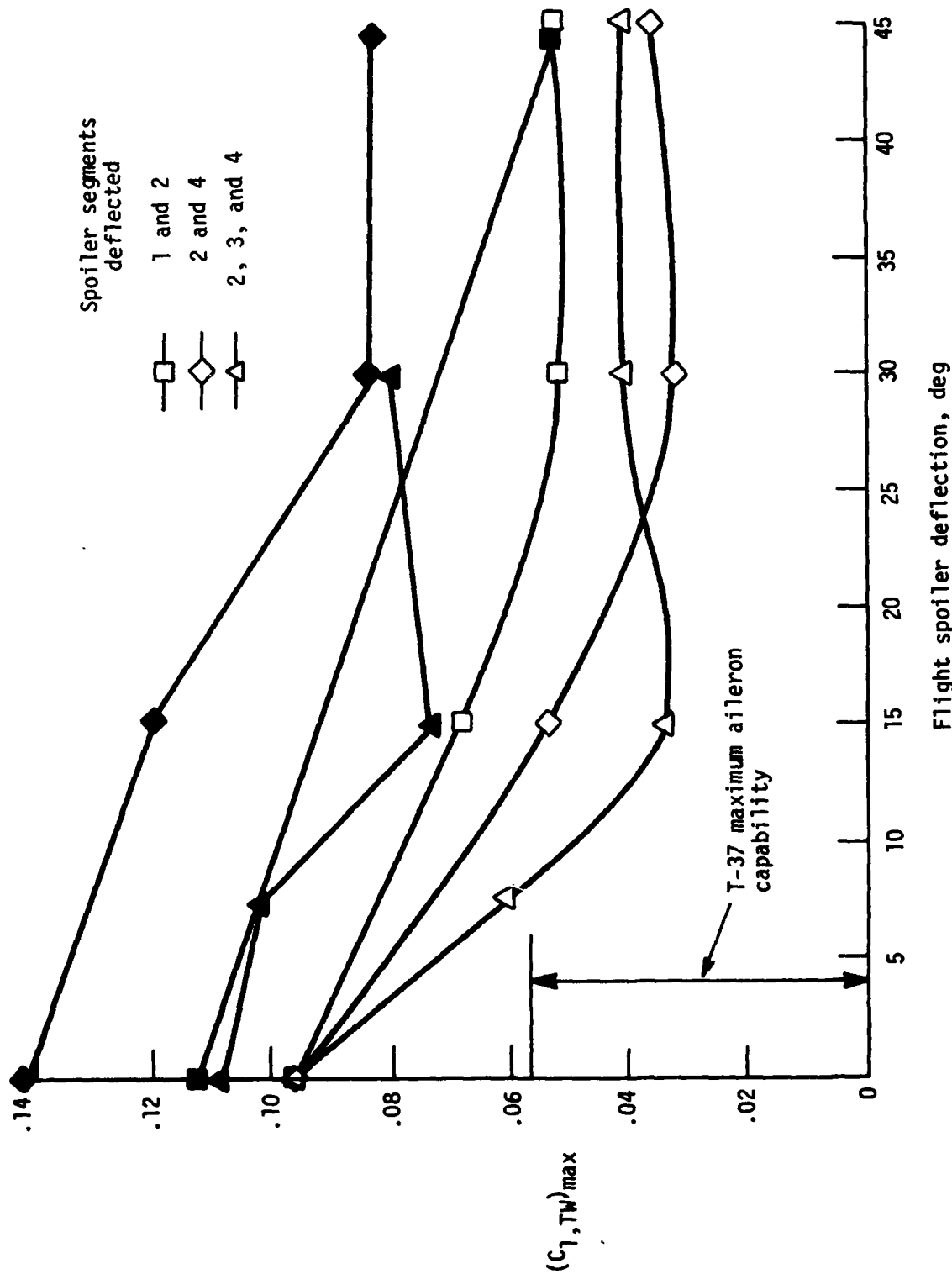


FIGURE 35. COMPARISON OF SPOILER ALLEVIATION ACCORDING TO LDV FLIGHT DATA (SOLID POINTS) (25 SPANS,  $C_L = 1.4$ ) AND WIND TUNNEL DATA (OPEN POINTS) (7.8 SPANS,  $C_L = 1.2$ )

Another discrepancy shows up in a comparison of the  $C_{\ell V}$  values for the DC-9 and the T-37. Contrary to the LDV data in Figure 33, the wind tunnel results (Ref. 9) show higher values of  $C_{\ell V}$  for the DC-9 size following model than for the T-37 size model. Some of this difference may be due to the differing wing shape for the large model (untapered wing) and the DC-9 with flaps. Perhaps the rest may be due to the effects mentioned above which tend to give low readings for the small model wing. The wind tunnel and LDV flight measurements do agree in showing much less alleviation for a large aircraft (DC-9) than for a small one (T-37; see Figure 33).

### 5.3 EFFECT OF SPOILERS ON VORTEX ROLL-UP

The nature of the spoiler-induced alleviation process can be understood by examining the photographs in Figures 36 and 37. As was well established in previous studies of the non-alleviated wake, the vortex emanating from the outer edge of the outer flap ultimately forms the core of the rolled-up vortex ( $0^\circ$  spoilers). For the alleviated wake, however, the effect of the spoilers is to obliterate the flap vortex. The wing-tip vortex is then observed to form the core of the rolled-up vortex ( $15^\circ$  spoilers). This effect explains why the vortex core appears to be well defined and have a small radius for alleviated vortices (Figure 31); the core is the wing-tip vortex. The observed lower maximum velocity for alleviated vortices is consistent with the lower strength of the wing-tip vortex compared to the flap vortex (discussed in Ref. 2). The alleviated vortex core appears to decay surprisingly slowly in view of the large amount of turbulence injected by the spoilers. It appears that the wing-tip vortex remains laminar because the injected turbulence is too far away to disturb it.

The transition from dominant-flap to dominant-tip vortex is a remarkable phenomenon which may have important implications (Section 5.4) for vortex alleviation. The transition occurs between  $7.5^\circ$  and  $15^\circ$  for spoilers 2, 3, 4 (Figure 33) and between  $0^\circ$  and  $15^\circ$  for spoilers 2, 4 (Figure 34).

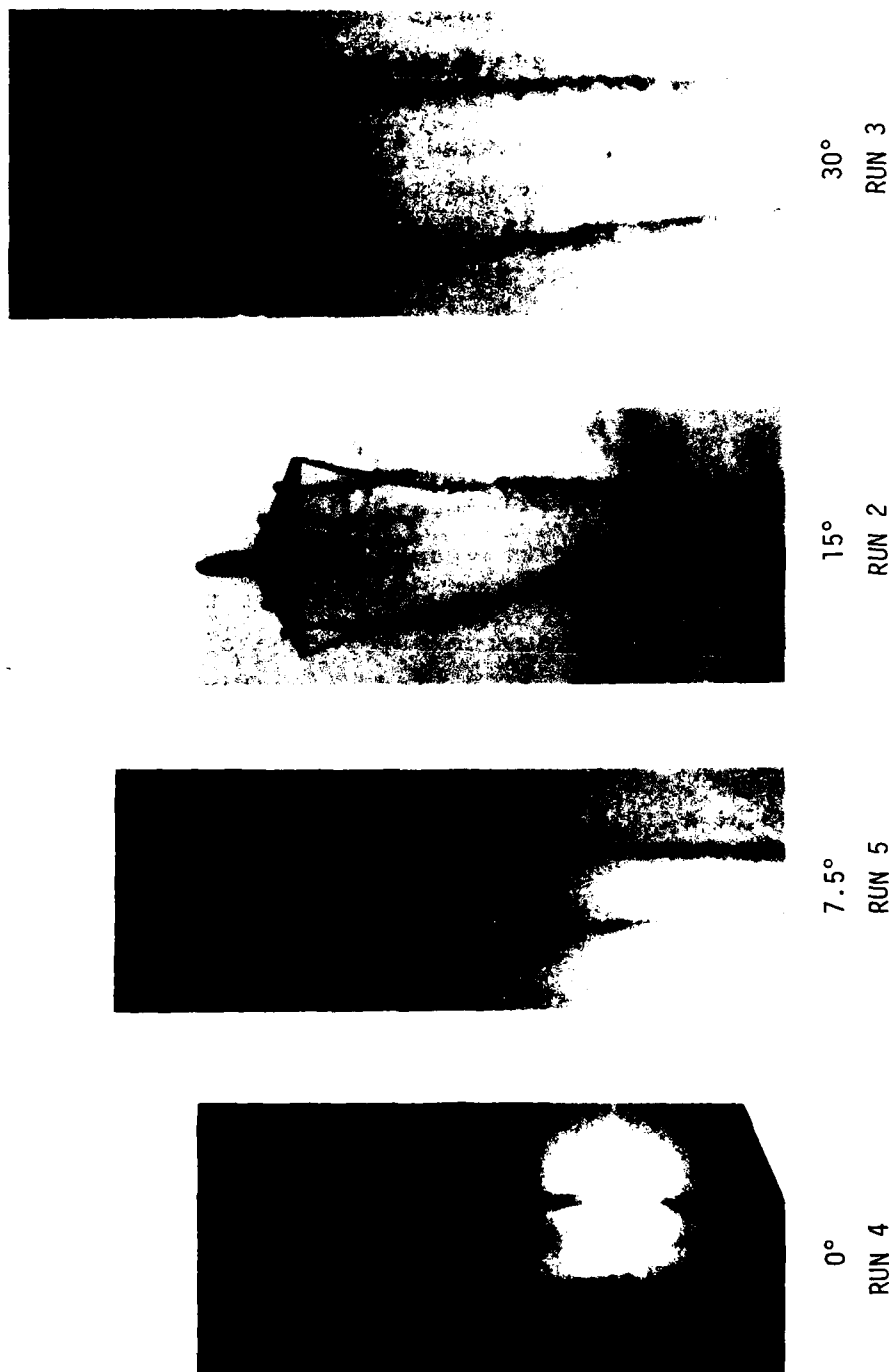


FIGURE 36. EFFECT OF SPOILER ANGLE ON SMOKE MARKING FOR SPOILERS 2,3,4 on 2/9/79



0°

RUN 5



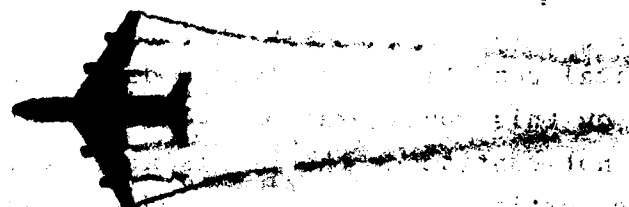
15°

RUN 4



30°

RUN 2



45°

RUN 3

FIGURE 37. EFFECT OF SPOILER ANGLE ON SMOKE MARKING FOR SPOILERS  
2,4 on 2/10/79

#### 5.4 PERIODIC ROLLING CONFIGURATION

Perhaps the most exciting result of the flight tests is the discovery of a way of substantially improving the spoiler alleviation, namely by generating periodic roll inputs. Unfortunately, the meteorological conditions on 11/8/79 did not allow reliable sensor results on this configuration. The LDV data (shown in Appendix E) do not contradict the promising results of the T-37 probes, but the vortices could not be studied long enough to verify rapid decay. The loss of the LDV signals could be due to motion out of the measurement region just as well as due to rapid decay. The GWVSS signals (see Figure 38) from this configuration consistently showed some peculiar pulsations at late times. This effect appears to be related to the strong head wind (Appendix G) which moved different longitudinal portions of the vortex past the sensor line. The motion of the Crow instability loops across the GWVSS baseline was evident visually on later runs, particularly Run 9. The period of the GWVSS pulsations is about 45 seconds and the headwind from Table 7 of Appendix G is about 4 m/s. The resulting spatial period would be 180 m or 3 wingspans. This period is rather short for the Crow instability (6.8 spans is most probable), but agrees well with the expected wavelength (220 m) of the 3-second period roll oscillations. Thus, some residual effect of the roll maneuver apparently lasted for about 100 seconds.

The motion pictures of the periodic roll configuration showed an alternation in the dominant vortex between the tip and flap vortex, as one might expect, since the spoiler angle dropped below the level where this transition takes place (Section 5.3). A tentative explanation for the roll-induced alleviation is that periodically crossing this transition excites an instability which destroys the vortex. If this explanation is correct, the same effect could be produced by spoiler modulation alone. The experimental test of spoilers alone (Run 6;  $15^{\circ}$  to  $30^{\circ}$  spoilers) unfortunately did not cross the transition angle which lies

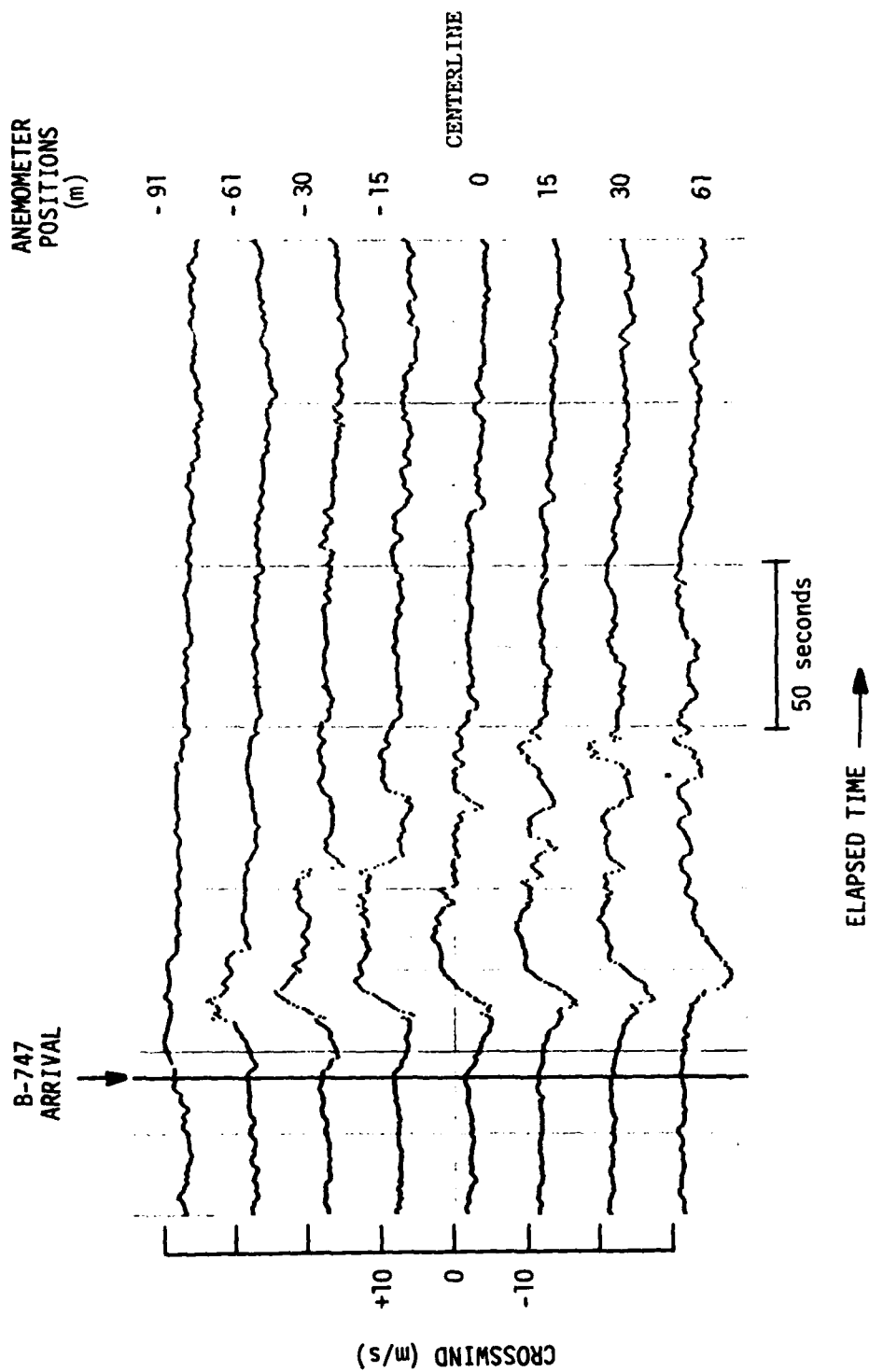


FIGURE 38. GWVSS DATA FOR RUN 4, 11/8/79

between 7.5 and 15°. If modulating the spoilers through a small deflection angle proves to be successful, it offers the promise of an alleviation technique with a small drag penalty and possible application to other aircraft types which have similar flap and spoiler arrangements.

## 6. RECOMMENDATIONS

### 6.1 FUTURE ALLEVIATION STUDIES

The results of these tests have pointed to two promising areas for further alleviation work. The mechanism leading to the success of the spoilers-plus-roll configuration should be determined. One hopes that the same results can be achieved with an operationally acceptable configuration. Modulating the spoilers across the angle where the dominant vortex switches from flap to wingtip may yield the desired results. A second promising approach is based on the observation that the wing-tip vortex dominates the rollup and persistence of spoiler-alleviated vortices. If the wing-tip vortex could be eliminated or disrupted, perhaps the spoilers could then take care of the flap vortex. A wing-tip spoiler is probably the most direct way of testing this approach.

### 6.2 ROLE OF GROUND-BASED SENSORS IN ALLEVIATION TESTS

Ground-based wake-vortex sensors will play an important role in future vortex alleviation flight tests. Sensors have a number of significant advantages over aircraft probes and, in fact, play a necessary role in the low-altitude probe measurements:

- a. Sensors cannot miss a vortex within their scan region. Aircraft penetrations into a diffuse smoke-marked wake are always open to the criticism that the aircraft missed the vortex. This criticism is particularly justified for testing landings behind an alleviated aircraft where the probability of hitting a vortex is small (the F-86 missed in all seven attempts). In this case, sensors are needed to verify that an aircraft indeed passed through the vortex.
- b. Sensors can measure near the ground where a probe aircraft cannot fly until the vortex is proven to be



benign. Thus, ground-based sensors are needed to verify that an alleviation technique works near the ground.

- c. Sensors can estimate the vortex hazard for all aircraft types and all separations from a few runs. Measuring the vortex-velocity profile as a function of vortex age allows the hazard for each run to be calculated for any aircraft at any separation. Multiple runs are needed to verify the consistency of the vortex decay.

### 6.3 OPTIMUM USE OF GROUND-BASED SENSORS IN FUTURE TESTS

These tests have shown that the best LDV data are produced when the aircraft flies overhead at about 250 m AGL. Such measurements are particularly good for documenting the nature of an alleviating configuration with minimal uncertainty. The LDV should be operated in the translated mode in future alleviation tests so that the velocity sign can be unambiguously determined. This change should allow weaker vortices to be detected and may allow completely automatic data processing.

Although the use of the LDV for vortices in ground effect is feasible, the results have enough uncertainties that the LDV should not be used to determine the acceptability of an alleviation technique in ground effect. LDV ground-effect measurements are especially unsuitable for screening new alleviation configurations. Such screening should be done at 250-m altitude over the LDV. The Monostatic Acoustic Vortex Sensing System (MAVSS) (Ref. 2) is much more suited for ground-effect measurements. Although the best MAVSS strength measurements require vortex transport, a close-spaced continuous MAVSS array can verify the demise of a vortex even if it is stalled.

The GWVSS is ideally suited for monitoring the vortex position during low altitude probing. A sequence of arrays can establish the vortex position as well as that of the probe aircraft.

#### 6.4 SENSOR TRAINING

Appendix C contains an evaluation of LDV and MAVSS errors based on a comparison of LDV and MAVSS data for the same B-747 configuration. It would be more desirable to make simultaneous LDV and MAVSS measurements on the same vortex. Such measurements could reduce the uncertainties in the accuracy of these sensors. A more careful examination of LDV errors for weak vortices would also be helpful.

#### 6.5 COMPARISON OF ALLEVIATION TESTS WITH OPERATIONAL TESTS

The vortex alleviation flight tests have been conducted under meteorological conditions much different from those where the large statistical vortex data bases have been collected. The alleviation test conditions were selected for an absolute minimum of turbulence. The statistical data collection at airports has generally involved the normal work day when very low turbulence levels are rare. It is not surprising that the alleviation tests generally show much longer vortex lifetimes. A consistent understanding of the wake-vortex phenomenon should describe both types of conditions. A basic need is to accumulate some vortex statistics under the calm desert conditions used for alleviation tests. One appealing way of collecting such data would be to locate a ground-based sensor facility at the Palmdale, California, airport. The sensors could be used for alleviation tests and also to collect data under both calm and turbulent conditions on the wide-body training aircraft using Palmdale. Some useful information on the differences between alleviation and operational testing could also be obtained from further analysis of LDV and MAVSS data already collected.

#### 6.6 IMPLICATIONS FOR SCALE-MODEL TESTING

The measurements reported here show qualitative agreement with scale-model testing at short distances downstream. However, the short-distance trends do not necessarily persist downstream (Figure 34). The physical phenomena involved at the two

distances can be quite different. The short-distance effects result from rearranging the vorticity in the wake. The long-distance effects can result from turbulent diffusion of vorticity and perhaps also from slowly triggered instabilities. A reliable scale-model evaluation of an alleviation technique should be done at downstream distances corresponding to the desired minimum separation. If such distances are impractical, the scale-model testing should allow at least some time for decay processes to act on the rolled-up vortices.

## REFERENCES

1. "Wake Vortex Minimization," Symposium, February 1976, NASA SP-409, 1977.
2. Burnham, D.C., Hallock, J.N., Tombach, I.H., Brashears, M.R., and Barber, M.R., "Ground-Based Measurements of the Wake Vortex Characteristics of a B-747 Aircraft in Various Configurations," FAA-RD-78-146, December 1978, DOT Transportation Systems Center, Cambridge, MA.
3. Croom, D.R., "Low-Speed Wind-Tunnel Parametric Investigation of Flight Spoilers as Trailing-Vortex-Alleviation Devices on a Transport Aircraft Model," NASA Technical Paper 1419, April 1979.
4. Devore, R.L., "Flight Evaluation of the Impact of Deflected Spoiler Vortex Alleviation Systems on the Operation of the 747 Airplane," Contract No. NAS4-2606, April 1979, Boeing Commercial Airplane Company, Seattle, WA.
5. Burnham, D., Hallock J., McWilliams, I., Fantasia, J., and Winston, B., "Measurement of Aircraft Wakes at 250-Meter Altitude with 10.6 Micron CW Laser Doppler Velocimeter," Proceedings of the Electro-Optics/Laser 78 Conference, Boston, MA, September 19-21, 1978. (Industrial and Scientific Conference Management, Inc., 222 West Adams St., Chicago, IL 60606).
6. Sullivan, T.E. and Burnham, D.C., "Ground Wind Vortex Sensing System Calibration Tests," FAA-RD-80-13, Feb. 1980, DOT Transportation Systems Center, Cambridge, MA.
7. Burnham, D.C. and Hallock, J.N., "Chicago Monostatic Acoustic Vortex Sensing System, Volume II: Decay of B-707 and DC-8 Vortices," FAA-RD-79-103, II, Oct. 1980, DOT Transportation Systems Center, Cambridge, MA. See Section 4.2.1.
8. Claude Patterson (private communication).

## REFERENCES (CONTINUED)

9. Croom, D.R. and Dunham, E.D., Jr., "Low-Speed Wind-Tunnel Investigation of Span Load Alteration, Forward-Located Spoilers, and Splines as Trailing-Vortex-Hazard Alleviation Devices on a Transport Aircraft Model," NASA TN D-8133, Dec. 1975.
10. Margason, R.J. and Lamar, J.E., "Vortex-Lattice FORTRAN Program for Estimating Subsonic Aerodynamic Characteristics of Complex Planforms," NASA TN D-6142, Feb. 1971.
11. Garodz, L.G., Lawrence, D., and Miller, N.J., "The Measurement of the Boeing 747 Trailing Vortex System Using the Tower Fly-By Technique," FAA-RD-73-156, June 1974, FAA National Aviation Facilities Experimental Center, Atlantic City, NJ.
12. Burnham, D.C., Sullivan, T.E., and Wilk, L.S., "Measurement of Wake Vortex Strength by Means of Acoustic Back Scattering," Journal of Aircraft, Vol. 13, No. 11, Nov. 1976, pp. 889-894.

## APPENDIX A

### LASER DOPPLER VELOCIMETER (LDV) SOFTWARE DEVELOPMENT

This appendix describes the LDV software development effort and includes details about the current processing algorithms which were not covered in the main body of the report (Section 4.1).

#### A.1 HISTORY

The LDV used in the 1975 B-747 tests was owned by the Lockheed Missiles and Space Company, who subsequently constructed a similar system for the U.S. Department of Transportation/Transportation Systems Center (DOT/TSC). The TSC system uses a different data acquisition computer (PDP-11/05) so that totally new data collection software was required. The data acquisition system was interfaced to a Surface Acoustic Wave (SAW) spectrum analyzer borrowed from the NASA Marshall Space Flight Center. The original LDV software package was designed for LDV operation at Chicago's O'Hare Airport. The 1979 B-747 alleviation tests provided the incentive for substantial improvements in the data collection and processing software.

#### A.2 DATA COLLECTION

The current LDV data collection technique is based on information learned in prior tests (Refs. 2 and 5). The 1975 B-747 data were sampled at a 500-Hz rate which gave excellent velocity profiles, but with considerable redundancy at lower altitudes. The O'Hare data collection software has a maximum rate of 125 Hz which yielded a rather coarse velocity profile. A number of software changes were made to allow a 250-Hz data rate for the present tests.

Table 6 compares the data stored for the O'Hare software and the present software. The O'Hare software stored complete time, scan position and spectral information for each Doppler spectrum. The present software economizes by reducing the data rate for the

less important parameters. The scan position and the vortex velocity ( $V_{\max}$ ) are generated at the full 250-Hz rate, but the stored spectrum and real-time display are generated at only a 125-Hz rate. The time is recorded only once per 1000-word record. The data are recorded for each run from the time the aircraft passes until the vortices can no longer be seen in the real-time display.

### A.3 DATA PROCESSING

The data processing at TSC is done on a computer system identical to that used in the LDV van for data collection. The software written at TSC for analyzing the Moses Lake data could therefore be used for immediate field processing of the data collected during the second series of tests in California. The computer graphics are generated on a refresh graphics display which has no hard-copy capability. The hard copies in this report are made from instant photographs of the CRT. Routine data recording makes use of a standard instant camera with rectangular format (3-1/4 in. x 4 in). Photographs with higher resolution and less distortion were made for special figures with a long focal length lens on a 4 in. x 5 in. camera.

#### A.3.1 Vortex Tracking

The processing software developed for the O'Hare data collection required that the operator visually assign both the elevation angles of the vortices and the range (to the nearest scan range) in the velocity-profile display (Figure 9). This method was also used at first for data from the alleviation tests, but subsequently was replaced by the present method which gives improved range resolution and frame-to-frame position averaging. The small number of alleviation runs allowed a more comprehensive data analysis than would be appropriate for a large data base.

The visual estimation of the vortex range poses similar problems both in real-time tracking (Section 3.2.1.2) and in the O'Hare type data processing. Both use a similar display (Figure 9). The only difference is that the real-time display shows every other datum point. For the alleviation tests, in particular, it can be difficult to estimate the vortex range from the velocity profiles (see Figure 9) because the large signal produced by scattering from injected smoke tends to give good velocity profiles at many LDV focal ranges. For non-alleviated vortices the width of the velocity dip at the vortex core gives the best clue to range. The dip becomes very narrow and sometimes vanishes when the scan range equals the vortex range. For alleviated vortices, the vortex core is less obvious so that selecting the scan containing the vortex can be more difficult.

The vortex signatures of Figure 9 can be distorted in two ways when the vortices are not directly above the LDV van:

1. The ambient crosswind has a line-of-sight (LOS) component which adds to the vortex velocities. If the LOS velocity is away from the LDV van, as in Figure 39a, the outside edges of the vortex pair are enhanced and the velocity between the vortices is suppressed. Conversely, if the LOS velocity is toward the van, as in Figure 39b, the inside edges of the vortices are enhanced and the outside edges are suppressed.
2. When the vortices are at a low elevation angle, the region between the two vortices contains a mixture of responses from both vortices. The most extreme case of this problem occurs when a strong crosswind is blowing low-altitude vortices away from the van. At long range the signature from both vortices looks like that from a single vortex with a dip in the center and two strong sides (like Figure 39a only with a narrower dip). In this case one side of the apparent single vortex is from one vortex and the other side from the other. The proper



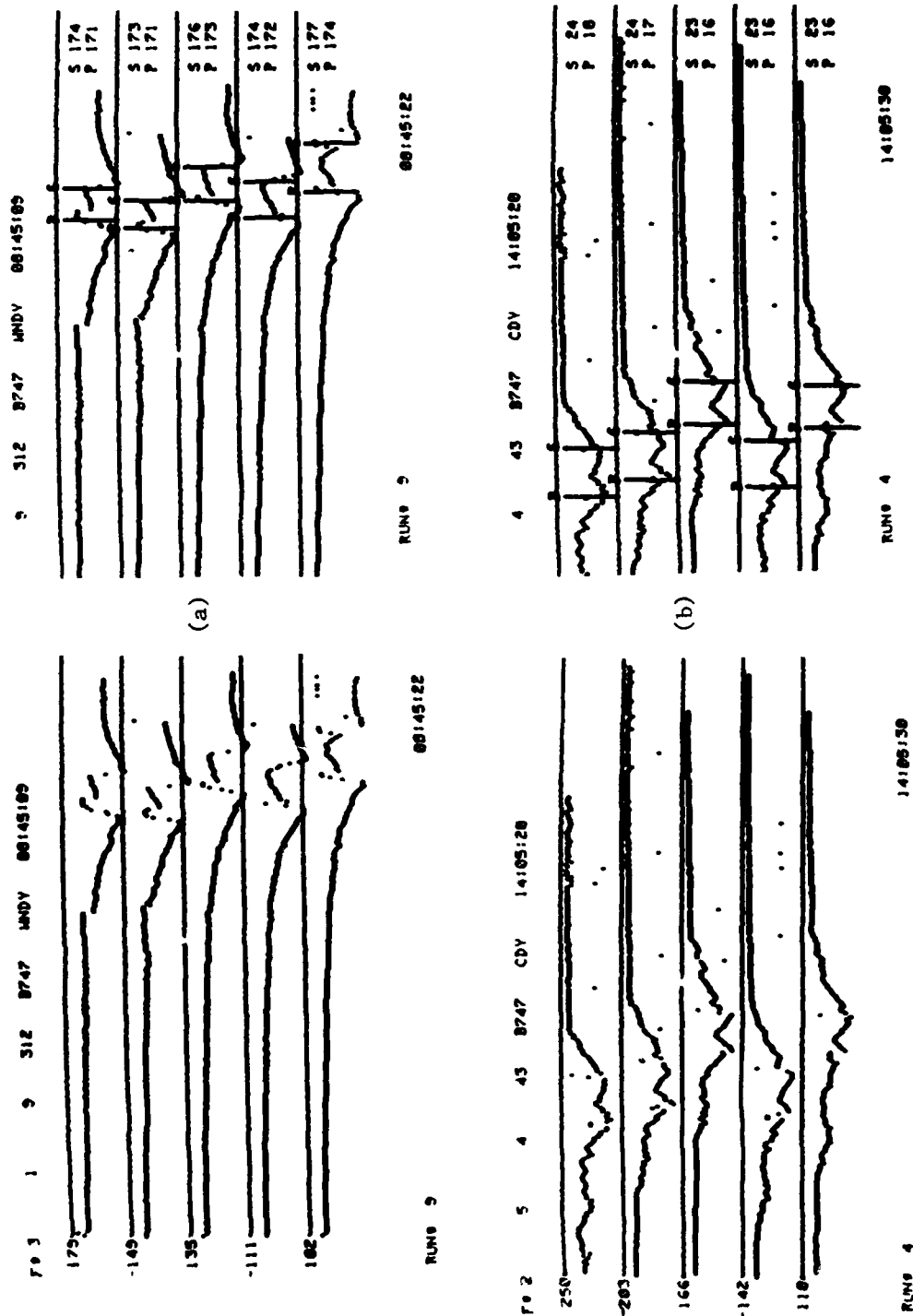


FIGURE 39. VORTEX SIGNATURES: (a) WIND AWAY FROM LDV (RUN 9, 11/8/79), (b) WIND TOWARD LDV (RUN 4, 2/12/79)

AD-A113 621

TRANSPORTATION SYSTEMS CENTER CAMBRIDGE MA  
B-747 VORTEX ALLEVIATION FLIGHT TESTS: GROUND-BASED SENSOR MEAS--ETC(U)  
JAN 82 D C BURNHAM  
DOT-TSC-FAA-81-19

F/6 20/4

UNCLASSIFIED

DOT/FAA/RD-81-99

NL

2  
A  
51,850

END  
DATE  
FILMED  
5 82  
DTIC

identification of vortices at low elevation angles can thus be tricky and requires considerable care and experience.

Since the visual identification of the vortex locations is a very tedious process, considerable effort was expended in trying to detect the vortex centers automatically. The data were correlated with a number of different vortex-shaped functions. No correlator gave satisfactory performance because of the variability of the vortex signatures. The only feasible alternative was to use a human operator to assign the vortex centers. This procedure can become quite arbitrary when the vortices have decayed to a low level. The operator must decide whether a particular dip in the data is a vortex or merely a random variation in  $V_{\max}$ .

The primary reason for the difficulty in automatically locating vortex centers is the loss of sign information in the velocity profiles. The LDV has a mode where the sign is determined (the so-called translated mode) which was not used because it has a substantially degraded signal-to-noise ratio. This mode has been re-examined recently and is now recommended for future alleviation tests where the large scattered signal from the smoke can compensate for any loss in signal-to-noise ratio. A sign determination would allow more reliable detection of weak vortices since the reversal of sign at the vortex core should give an unambiguous indication of a vortex.

#### A.3.2 Range Algorithm

The algorithm used to determine the vortex range was briefly described in Section 4.1.2. A complete explanation is included here. Figure 10 shows the geometry of one scan frame.

The intensity of the signal scattered from the vortex is used to determine the vortex range using algorithms similar to those developed for the 1975 B-747 data (Ref. 2). Three intensity parameters are calculated for each spectrum by summing all spectral intensities above three limiting velocities of 3.2, 4.4, and 6.0 m/sec. The 4.4-m/sec limit works well for non-alleviated vortices,

while 3.2 m/sec is better for alleviated vortices which have lower peak velocities. The intensity parameter is averaged for a certain distance  $d_i$  along the arc on either side of the vortex center (thickened in Figure 10) to give a vortex intensity value  $I_i$  for a particular scan range  $f_i$ .

As discussed in the previous B-747 report (Ref. 2), the theoretical range response of the LDV has the form:

$$I(R,f) = 1/R^2(1+K^2(R^{-1}-f^{-1})^2) \quad (4)$$

where  $R$  is the range to the scatters,  $f$  is the LDV scan range, and  $K$  represents the range resolution of the LDV. If the region near the vortex core produces most of the signal intensity, then  $R$  can be interpreted as the range to the vortex. Set  $Y = 1^{-1}$ ,  $X = f^{-1}$ , and  $Z = R^{-1}$ ; the expression in Equation 4 reduces to

$$Y = Z^{-2}(1 + K^2(Z-X)^2) \quad (5)$$

which is simply a quadratic function of  $X$  (inverse scan range) for a given vortex range ( $Z^{-1}$ ). The minimum in  $Y$ , which occurs when  $Z = X$ , can be found in two ways from the measured intensity  $Y(X)$  for each scan range. If  $K$  is allowed to vary, a fit of this quadratic form to three values of  $Y(X)$  gives both the vortex range  $R$  and the LDV resolution ( $K$ ). One can also assume a nominal value for the LDV resolution parameter  $K$  and fit the quadratic to two points. Some consistency checks are placed on the fits such as a positive minimum value for  $Y$  and a value of  $X$  for minimum  $Y$  not too far away from the points being fitted.

The three-point fits for data on non-alleviated vortices gave rough agreement with the nominal value of  $K=2000$  m. The range resolution was generally poorer (lower values of  $K$ ) for alleviated vortices, presumably because the lower velocity threshold on the intensity parameter gives signal contributions from a larger volume of space. In any case, one would expect the range resolution to be poorer than the theoretical value when

the vortex is larger than the resolution distance (e.g., at close ranges). The requirement of a consistent three-point range fit can significantly reduce the number of range data points under some conditions. Consequently, a two-point fit with  $K = 2000$  m was used to process most of the data.

The distance  $d_I$  over which the intensity is averaged is 10 m for the range-versus-age fit program. Such a fixed number can cause problems, however, for the lateral-position-versus-age fit. The angular difference between the two vortices can become so small at low elevation angles that the intensity average will include both vortices. The lateral-position fit program therefore uses  $d_I$  as the smaller of 7 m and 40% of the arc distance between the vortices.

The use of intensity data between the two vortices often gives poor separation between the vortices at low elevation angles (e.g., see Figure 13b). The data between the two vortices comes from both vortices and tends to produce a range midway between the two vortices. Under such conditions a more reasonable vortex spacing is often produced if only the intensity data from the outside edges are used (see Figure 40). Plots using only outside edge data are labeled "outside."

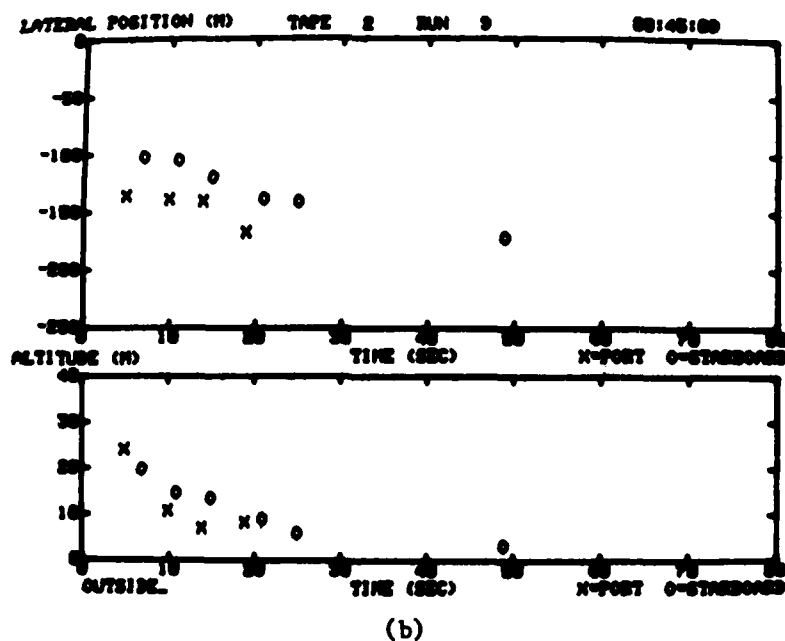
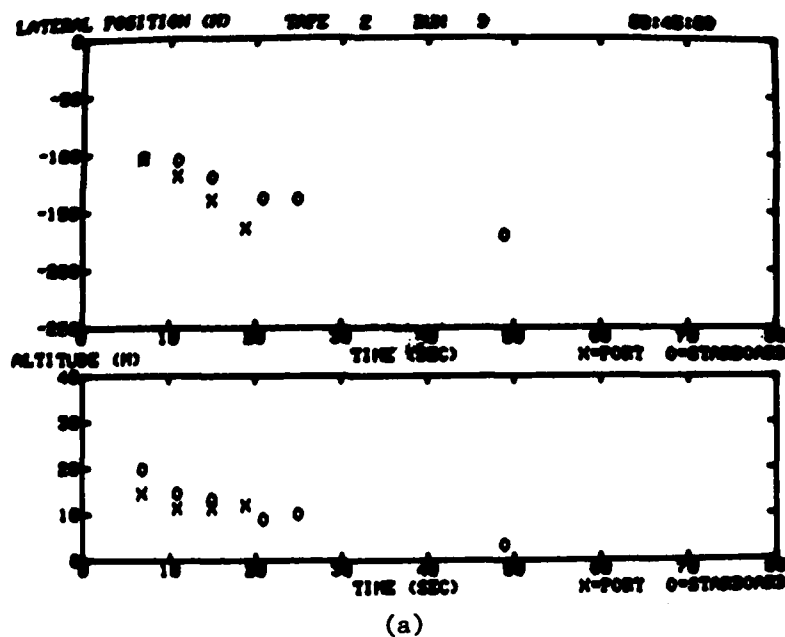


FIGURE 40. VORTEX TRAJECTORIES FOR RUN 9 ON 11/8/79:  
(a) SUM BOTH SIDES, (b) SUM OUTSIDES.

## APPENDIX B

### ROLLING MOMENT CALCULATIONS

This appendix describes the use of vortex lattice theory (Ref. 10) to calculate the vortex-induced rolling moments on an aircraft wing. The theory assumes no flow separation; consequently the rolling moment depends only upon the wing planform. The calculations divided each wing into four chordwise panels and eight spanwise panels. Increasing the number of spanwise panels to sixteen produced only a small change in the results (a decrease of 2 to 4 percent in rolling moment). The vortex velocities are entered into the calculations as a variable angle of attack  $\alpha$  along the wing:

$$\alpha = v(r)/V \quad (6)$$

where  $V$  is the airspeed. The vortex is centered on the aircraft axis to yield the maximum induced rolling moment.

The goal of the calculations described below was to assess the validity of using the average circulation  $\Gamma'$  (equation 3) to estimate the maximum rolling moment induced on a wing. The first calculations thus used the most extreme variations in velocity with the same value of  $\Gamma'(b/2)$ . The velocity profiles shown in Figure 41b were used: 1) inverse radius velocity (ideal line vortex), 2) constant velocity (alleviated vortex), and 3) linear velocity (large core vortex). The results of these calculations are shown in Table 7 which contains the vortex-induced rolling moment  $C_{\ell V}$  for two aircraft types: T-37 and DC-9 at an airspeed of 70 m/s (136 knots). Figure 41a,b shows the T-37 planform and the vortex velocity profiles for  $\Gamma'(b/2) = 100 \text{ m}^2/\text{s}$ . Figure 41c shows the ratio of force to velocity which is taken as a constant in the simple derivation of  $\Gamma'$  as an estimate of rolling moment (Ref. 7). The DC-9 was evaluated with and without flaps extended. The flaps reduced  $C_{\ell V}$  by 12 percent. Figure 42 shows the vortex-induced rolling moment coefficients for the more realistic model vortex-velocity profile of Equation 13. The values for constant and

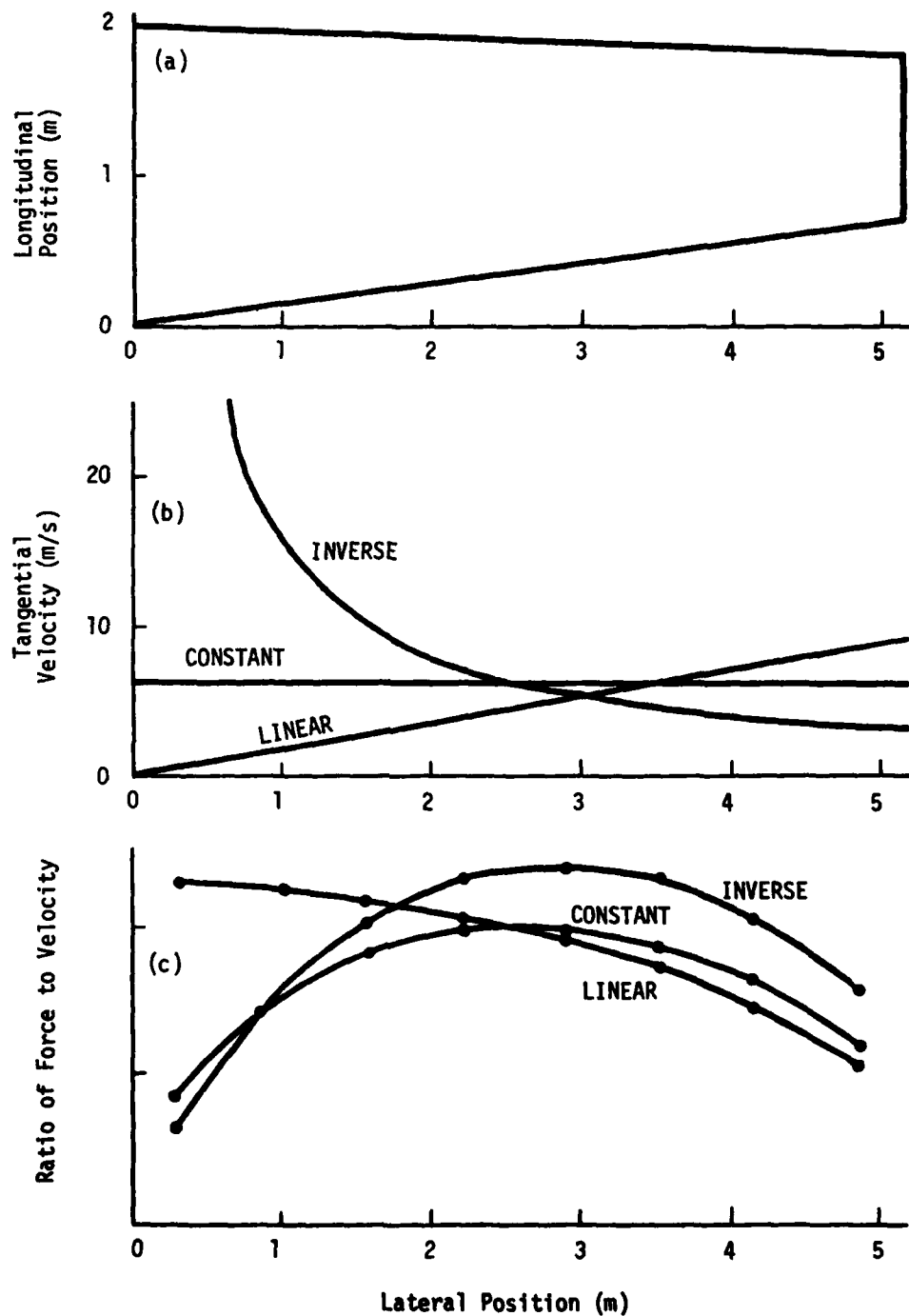


FIGURE 41. T-37 ROLLING MOMENT CALCULATION: (a) WING PLAN FORM (b) VORTEX TANGENTIAL VELOCITY, (c) RATIO OF FORCE TO VELOCITY. THE CURVE LABELS INDICATE THE RADIAL DEPENDENCE OF THE VORTEX TANGENTIAL VELOCITY.



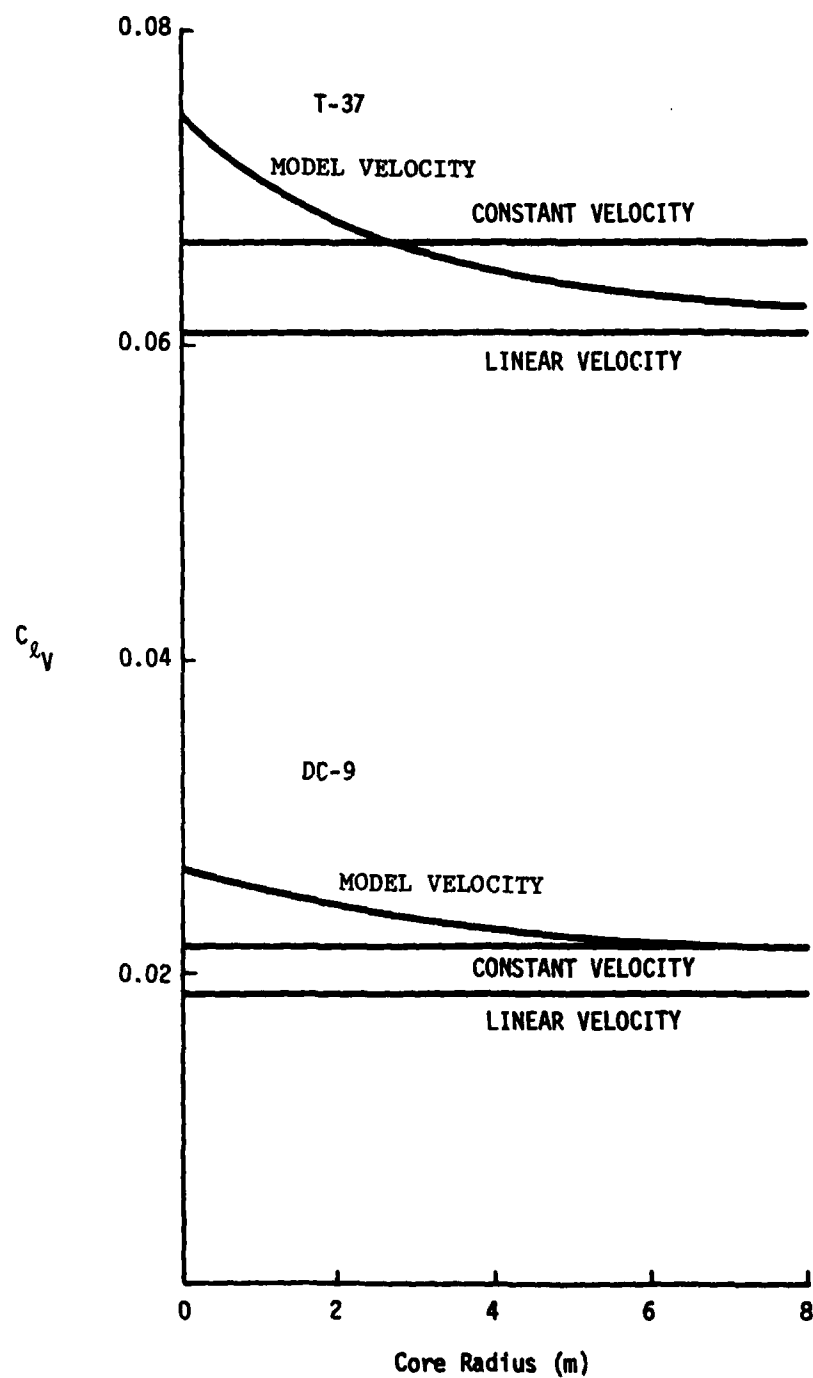


FIGURE 42. VORTEX-INDUCED ROLLING MOMENT COEFFICIENT VERSUS VORTEX CORE RADIUS FOR AVERAGE CIRCULATION =  $100 \text{ m}^2/\text{s}$

TABLE 7. ROLLING MOMENT COEFFICIENTS FOR VORTICES WITH  
AVERAGE STRENGTH OF  $100 \text{ m}^2/\text{s}$

	<u>Wingspan</u>	<u>Velocity Profile</u>		
		$r^{-1}$	constant	$r$
T-37	10.3	.0746	.0663	.0609
DC-9 (no flaps)	28.4	.0297	.0245	.0114
DC-9 (flaps)	28.4	.0264	.0216	.0187

linear velocities are also shown for comparison. The model value for  $r_c = 0$  corresponds to an inverse-radius velocity profile. The DC-9 values are with flaps extended.

The results of the  $C_{\ell V}$  calculations show that  $\Gamma'$  can be used to give a reliable estimate of  $C_{\ell V}$  according to the expression

$$C_{\ell V} = Q(\Gamma'/\Gamma'_{\text{ref}})(V_{\text{ref}}/V) \quad (7)$$

where  $Q$  is a constant depending upon the aircraft planform and wingspan and  $\Gamma'_{\text{ref}}$  and  $V_{\text{ref}}$  are the reference average circulation ( $100 \text{ m}^2/\text{s}$ ) and referenced airspeed ( $70 \text{ m/s}$ ) of the calculation, respectively. The value of  $Q$  is particularly easy to select for the T-37 ( $Q = 0.066$ ) since in Figure 42 the same value of  $C_{\ell V}$  occurs for constant velocity (alleviated vortex) and  $r_c = 2.5 \text{ m}$  (non-alleviated vortex). The value for the DC-9 was taken as  $Q = 0.022$ , the value for  $r_c = 4 \text{ m}$ , which is a compromise between alleviated and non-alleviated vortices. In either case the errors in selecting  $Q$  are less than the experimental errors in measuring the average circulation  $\Gamma'$ .

The results of these  $C_{\ell V}$  calculations can also be used to evaluate the accuracy of the method used to relate average circulation to vortex hazard (Ref. 7). The reference velocity profile in that method is linear in radius, which is simply related to a constant roll rate for the aircraft. The calculations here show that the best estimate of induced rolling moment for realistic vortices is somewhat larger than that given by a linear velocity profile (+8 percent for the T-37, +18 percent for the DC-9 with flaps).

## APPENDIX C

### EVALUATION OF GROUND-BASED SENSOR MEASUREMENTS OF VORTEX-VELOCITY PROFILES

The two wake-vortex sensors capable of making strength measurements have never been calibrated against each other or against a standard. The instrumented tower measurements of wake-vortex velocity profiles (Ref. 11), which might have served as a standard, were terminated before the Laser Doppler Velocimeter (LDV) and the Monostatic Acoustic Vortex Sensing System (MAVSS) were completely developed. This Appendix will assess the errors associated with these sensors by comparing data from the two sensors for similar vortices, by studying simulated data, and by investigating the internal consistency of the data.

#### C.1 1975 B-747 VELOCITY PROFILES

Figure 43 compares the 1975 LDV velocity profiles for B-747 landing configuration vortices with and without spoiler alleviation at age 25 seconds (Ref. 2). These profiles were fitted to the following circulation profiles:

$$\text{Unalleviated: } \Gamma(r) = \Gamma_c(1 + \ln(r/r_c)) \quad (8)$$

$$\text{Alleviated: } \Gamma(r) = \Gamma_c r/r_c \quad (9)$$

where  $r_c$  is the core radius and  $\Gamma_c$  is the strength at the core radius. Both of these forms can be fitted with a solid rotation core to give a realistic linear dependence of velocity upon radius  $r$  for small values of  $r$ . The velocity profiles are related to circulation profiles by  $v(r) = \Gamma(r)/2\pi r$  (Eq. 1):

$$\text{Unalleviated: } v(r) = v_c(1 + \ln(r/r_c)) r_c/r \quad (10)$$

$$\text{Alleviated: } v(r) = v_c \quad (11)$$

where we have defined  $v_c = \Gamma_c/2\pi r_c$ , which is the maximum velocity occurring at the core radius  $r_c$ .

The parameters of the fit to the data in Figure 43 are:

Non-alleviated:  $\Gamma_c = 253 \text{ m}^2/\text{s}$ ,  $r_c = 2.51 \text{ m}$ ,  $v_c = 16.0 \text{ m/s}$

Alleviated:  $\Gamma_c = 45 \text{ m}^2/\text{s}$ ,  $r_c = 1.0 \text{ m}$ ,  $v_c = 7.2 \text{ m/s}$ .

The 1975 B-747 MAVSS data (Ref. 2) were fitted to the forms:

$$\Gamma(r) = 2 \Gamma_c / (1 + (r/r_c)^2) \quad (12)$$

$$v(r) = 2 v_c / r (1 + (r/r_c)^2) \quad (13)$$

Suitable values of the parameters for non-decayed, non-alleviated B-747 landing vortices are  $\Gamma_c = 20 \text{ m}^2/\text{s}$ ,  $r_c = 2.5 \text{ m}$  and  $v_c = 12.7 \text{ m/s}$ . In this model for the vortex velocity profile, the total circulation  $\Gamma_\infty$  is simply  $2\Gamma_c$ . The actual fitted values of  $r_c$  for the MAVSS data (see Section C.3.2) are larger than 2.5 m because of the limited spatial resolution of the MAVSS. The value 2.5 m is selected to agree with the LDV measurements which have very high resolution in vortex radius.

The fitted velocity profiles for the LDV and MAVSS data are shown in Figure 44 for young non-alleviated B-747 landing vortices. The differences for radii beyond 2 m represent a constant velocity offset of 3.5 m/s. The method of processing the LDV data takes the highest spectral point above threshold as the vortex velocity; thus, one would expect the LDV to read high because of turbulence and spectral broadening. On the other hand, the MAVSS tends to read low velocities near the vortex core because of spatial averaging, and low velocities everywhere in the presence of noise or spurious signals. The goal of the rest of this section is to discover how much of the observed 3.5 m/s difference should be ascribed to the LDV, how much to the MAVSS, and how much to the differences in vortex altitude for the two sensors (200 m and 30 m, respectively). The dashed curve in Figure 44 shows the results of a uniform reduction in LDV velocity by 20 percent, which is an alternative method of bringing the LDV and MAVSS data into closer agreement.

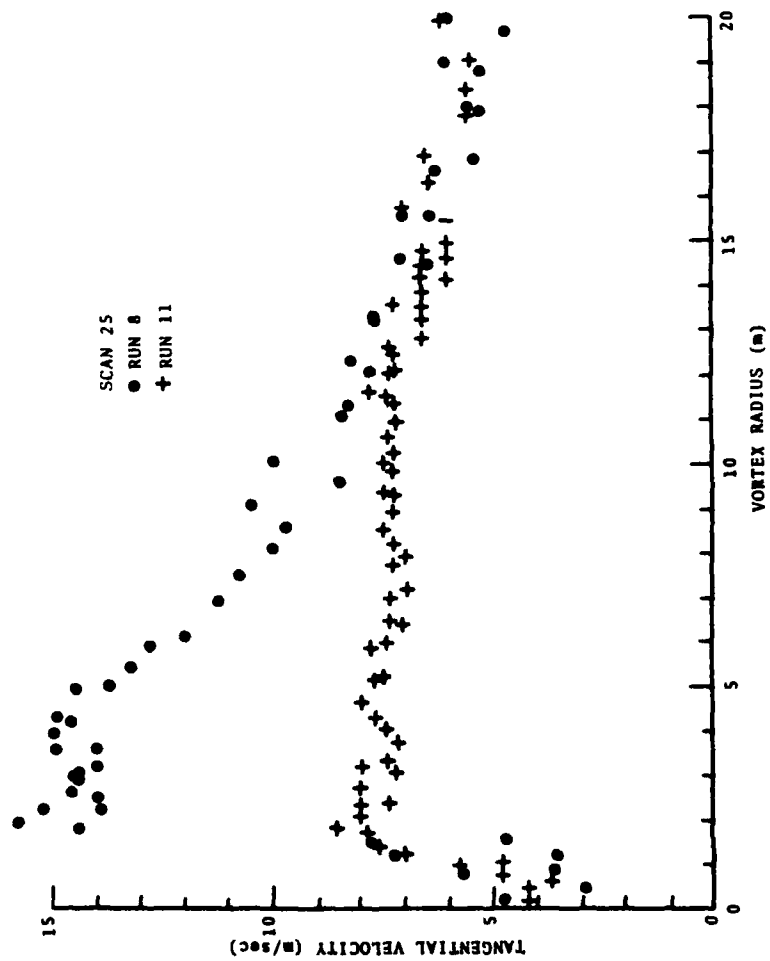


FIGURE 43. EFFECT OF SPOILER DEPLOYMENT ON THE WAKE VORTEX-VELOCITY PROFILE (RUN 8 WITHOUT SPOILERS, RUN 11 WITH SPOILERS 1, 2 AT 45°)

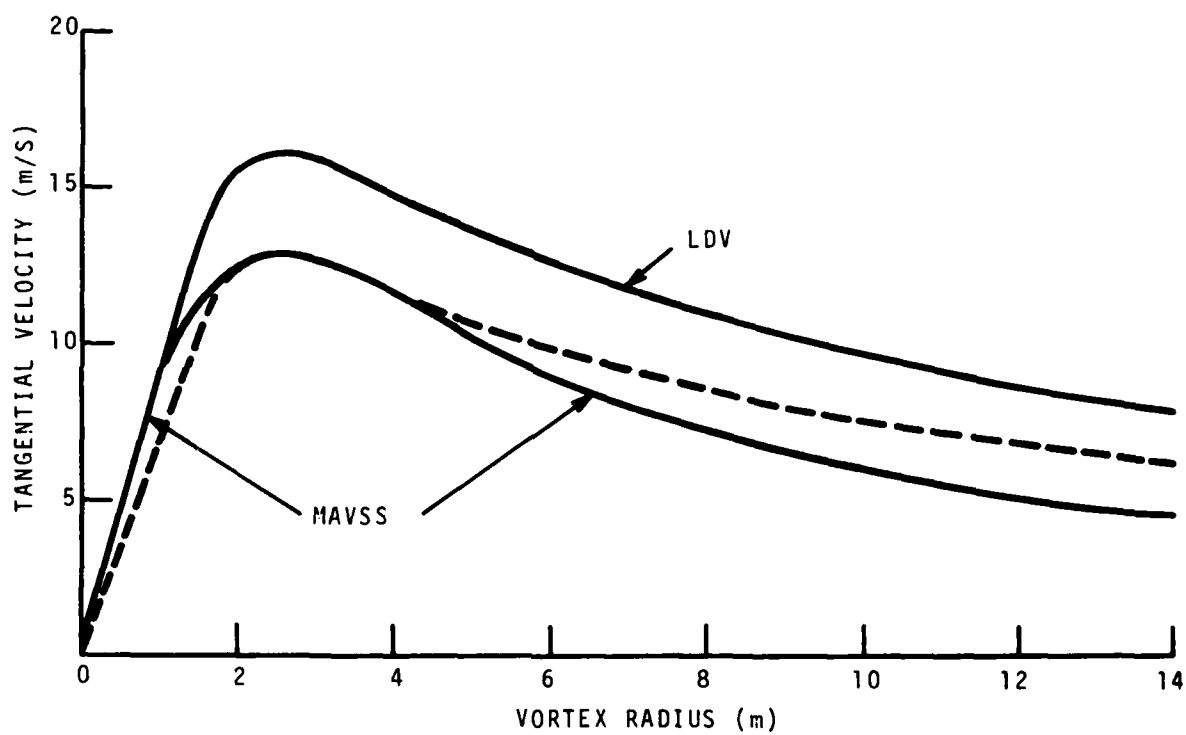


FIGURE 44. COMPARISON OF 1975 B-747 VELOCITY PROFILES

## C.2 LASER DOPPLER VELOCIMETER

### C.2.1 LDV Simulation

The LDV simulation presented here makes the following assumptions:

1. The aerosol scattering cross section is uniform throughout the vortex.
2. The range response of the LDV is given by Equation 4 with  $K=2000$  m.
3. The vortex velocity profile is given by Equation 13 with  $\Gamma_c = 250 \text{ m}^2/\text{s}$  and  $r_c = 2.5$ , which gives reasonable agreement with the LDV curve of Figure 44.
4. The vortex pair is created directly above the LDV at a range of 250 m.
5. The vortex separation is 49 m.
6. The vortex pair descends at its naturally induced descent rate and translates laterally with the ambient crosswind.
7. A minimum spectral detection threshold and a minimum velocity threshold are assigned.

The simulation scans through the stepped-arc-scan patterns for the LDV focus and the spectrum is calculated for each point by summing the intensities from points along the beam into the appropriate velocity bins.

Originally the simulation was used to study ways of determining the vortex range. In the present case the purpose of the simulation is to examine how well  $V_{\max}$ , the last point in the spectrum, agrees with  $V_{pk}$ , the highest intensity point in the spectrum (see Figure 2c). In order to eliminate the large intensity peaks which can occur at low velocities levels, a relatively high value of velocity threshold (5 m/s) was used. The results are shown in Figure 45. Three arc scans are shown: one passing through the vortex core and the other two 50 m above and below the core. The left plots show both  $V_{\max}$  and  $V_{pk}$ . Of course,



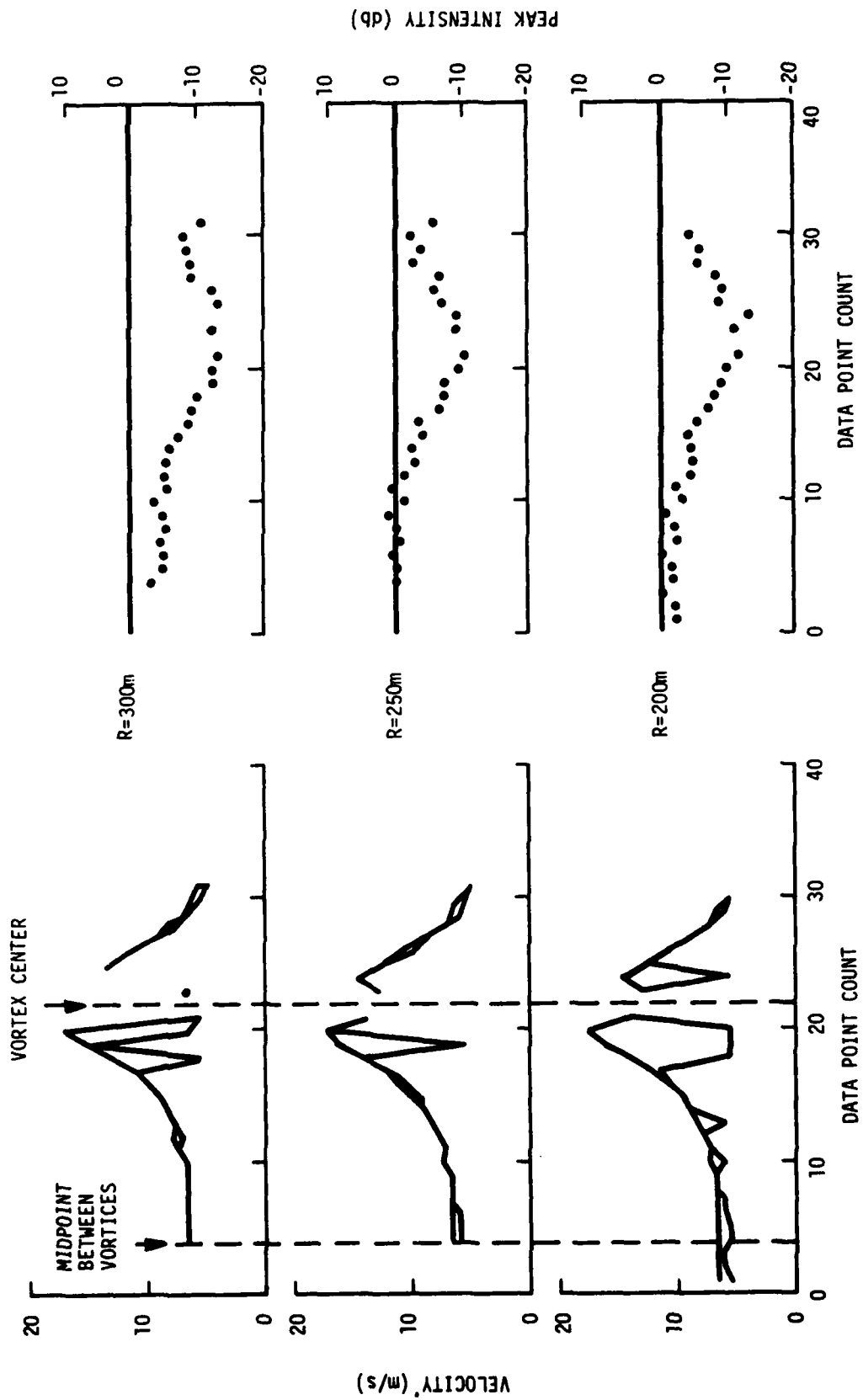


FIGURE 45. RESULTS OF THE LDV SIMULATION. THE DATA ARE PLOTTED SEQUENTIALLY FOR EACH SPECTRUM WITH THE VORTEX CENTERS LINED UP FOR EACH ARC SCAN.

by definition,  $V_{\max}$  is always greater than or equal to  $V_{pk}$ . The simulation shows that  $V_{\max}$  and  $V_{pk}$  agree to within one velocity bin (0.55 m/s) unless  $V_{pk}$  is dominated by the intensity at the velocity threshold of 5 m/s. The right plots show the peak intensity. On this scale +10 db corresponds to the total intensity of the scattered radiation and -13 db corresponds to the detection threshold used. The peak intensities are seen to decrease gradually toward the center of the vortex as the scattered intensity is spread into more velocity bins. The effect of defocusing the LDV beam from the vortex range is shown in the top and bottom plots. The peak intensity is reduced and there are more signal drop-outs near the center of the vortex. The important result of this simulation is that  $V_{pk}$  and  $V_{\max}$  give similar estimates of vortex tangential velocity.

#### C.2.2 LDV Data

Figure 46 shows the same information as Figure 45 for an actual run. The most notable difference from the simulated data is that  $V_{pk}$  is consistently lower than  $V_{\max}$  by about 3 velocity bins (1.6 m/s). Since the simulation showed no consistent offset, this difference must represent the intrinsic width of the velocity peak due to turbulence, filter bandwidth, and other effects. Similar deviations were found for alleviated vortices and aged vortices. Thus, the overestimation of vortex tangential velocities by  $V_{\max}$  can be assigned the value 1.6 m/s.

### C.3 THE MONOSTATIC ACOUSTIC VORTEX SENSING SYSTEM

#### C.3.1 MAVSS Simulation

The simulation model used for the MAVSS makes use of the following assumptions.

1. The acoustic scattering cross section is uniform throughout the vortex.

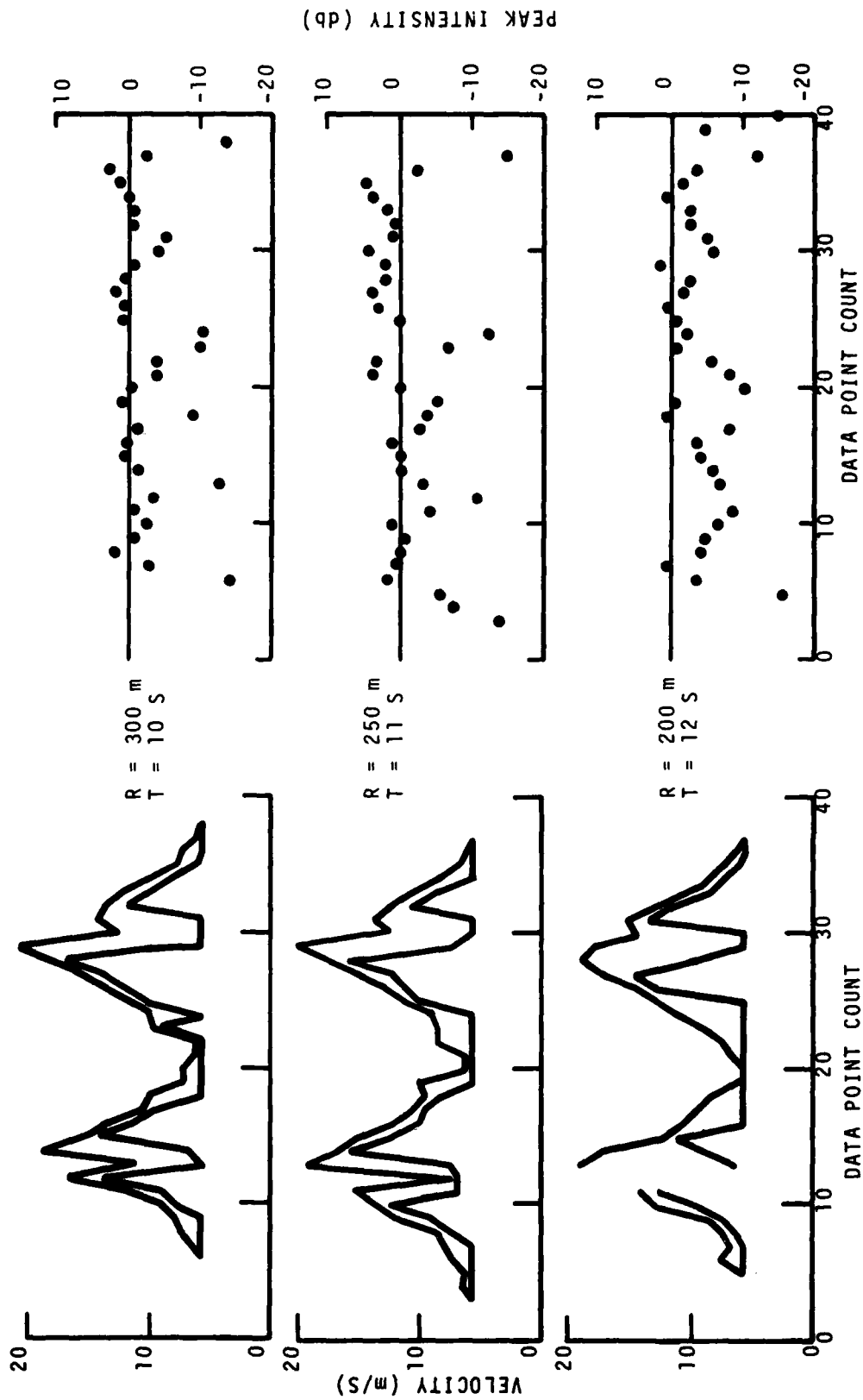


FIGURE 46. LDV DATA FROM RUN 1 ON 2/10/79. VORTEX RANGES ARE ABOUT 250 M.

2. The response of the MAVSS is uniform within a region  $\Delta X$  in width,  $\Delta Y$  in height, and is zero outside this region.
3. The response of the MAVSS is uniform for vertical velocity components between  $-w_m$  and  $w_m$  and is zero outside this range.

The geometry of the model is shown in Figure 47. The vertical component  $w$  of the vortex velocity  $v(r)$  is evaluated at a grid of points within the region  $\Delta X \Delta Y$ . The size of the grid is selected according to the vortex core radius,  $\Delta X$ , and  $\Delta Y$  to give a good representation of the variations in velocity. Two characteristics of the MAVSS spectrum of  $w$  are calculated:

1) the mean vertical velocity  $w$  and 2) the rms deviation about the mean,  $w_{rms}$ . In addition to the effects of velocity variations, the MAVSS measurements of the rms velocity deviation also have a contribution from the intrinsic MAVSS resolution of about 1.3 m/s. This effect is included by summing the squares of the two contributions and then taking the square root.

The MAVSS model was run for a variety of velocity profiles for  $\Delta Y = 3.5$  m and  $\Delta X = 2, 3, 4, 5$ , and 7 m. The vertical resolution  $\Delta Y$  is set by the transmitted pulse width which is normally 20 msec. The horizontal resolution  $\Delta X$  is set by the beam width and overlap which are somewhat uncertain. Two vertical positions  $Y$  were used: 1) vortex centered in the response region and 2) vortex centered on the edge of the response region (i.e., between range gates). The lateral position  $X$  was varied to simulate the observed velocity profiles.

Figure 48 shows some results of running the simulation on the MAVSS velocity profile of Figure 44 ( $r_c = 2.5$  m and  $v_c = 12.7$  m/s in Equation 13). The top plot shows how the vortex velocity profile  $v(r)$  is spread out by the MAVSS spatial resolution to yield  $w(x)$ . The second plot shows how  $w_{rms}$  varies across the vortex. The third plot shows how the vortex circulation profile  $\Gamma(r)$  is changed by the MAVSS spatial resolution. From

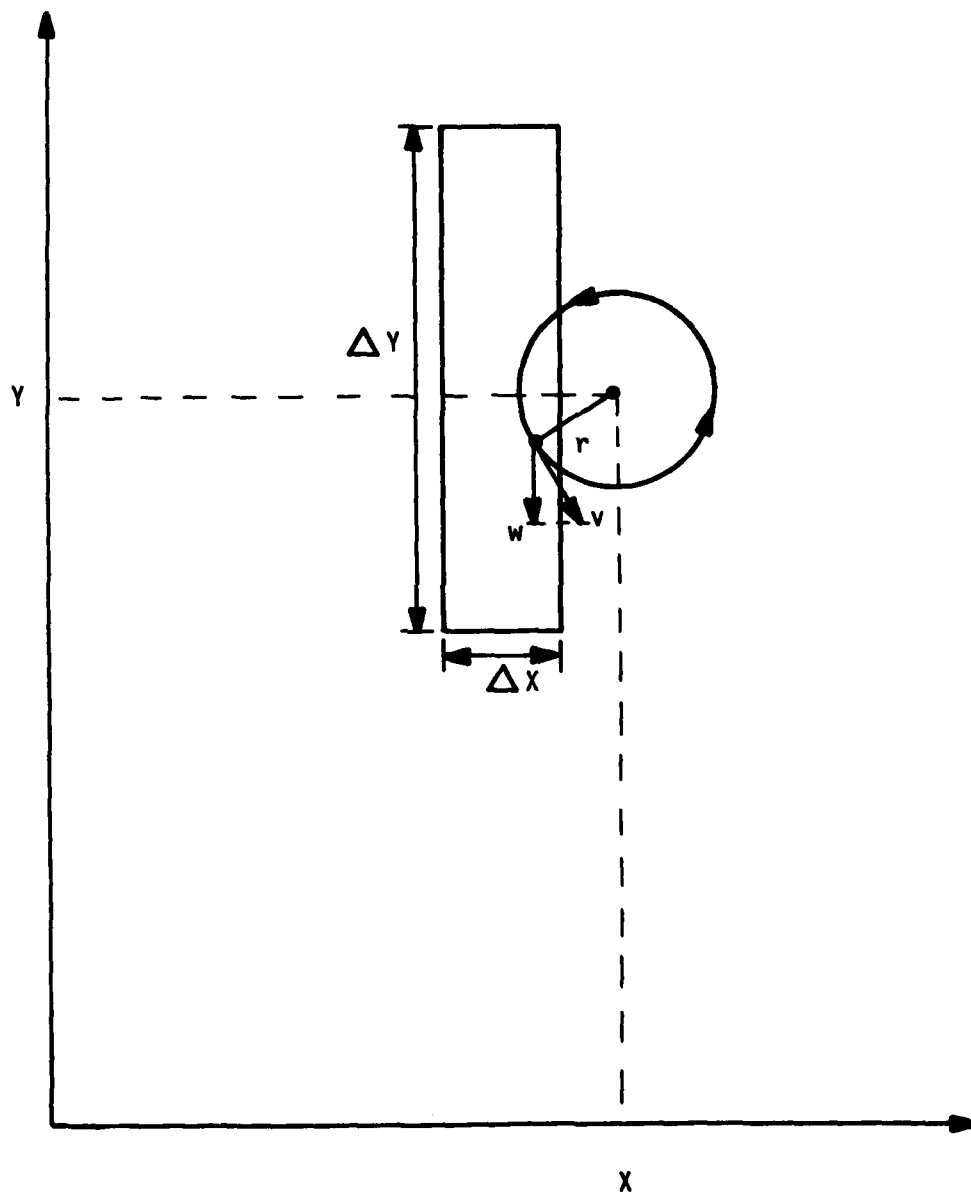


FIGURE 47. GEOMETRY OF THE MAVSS SIMULATION

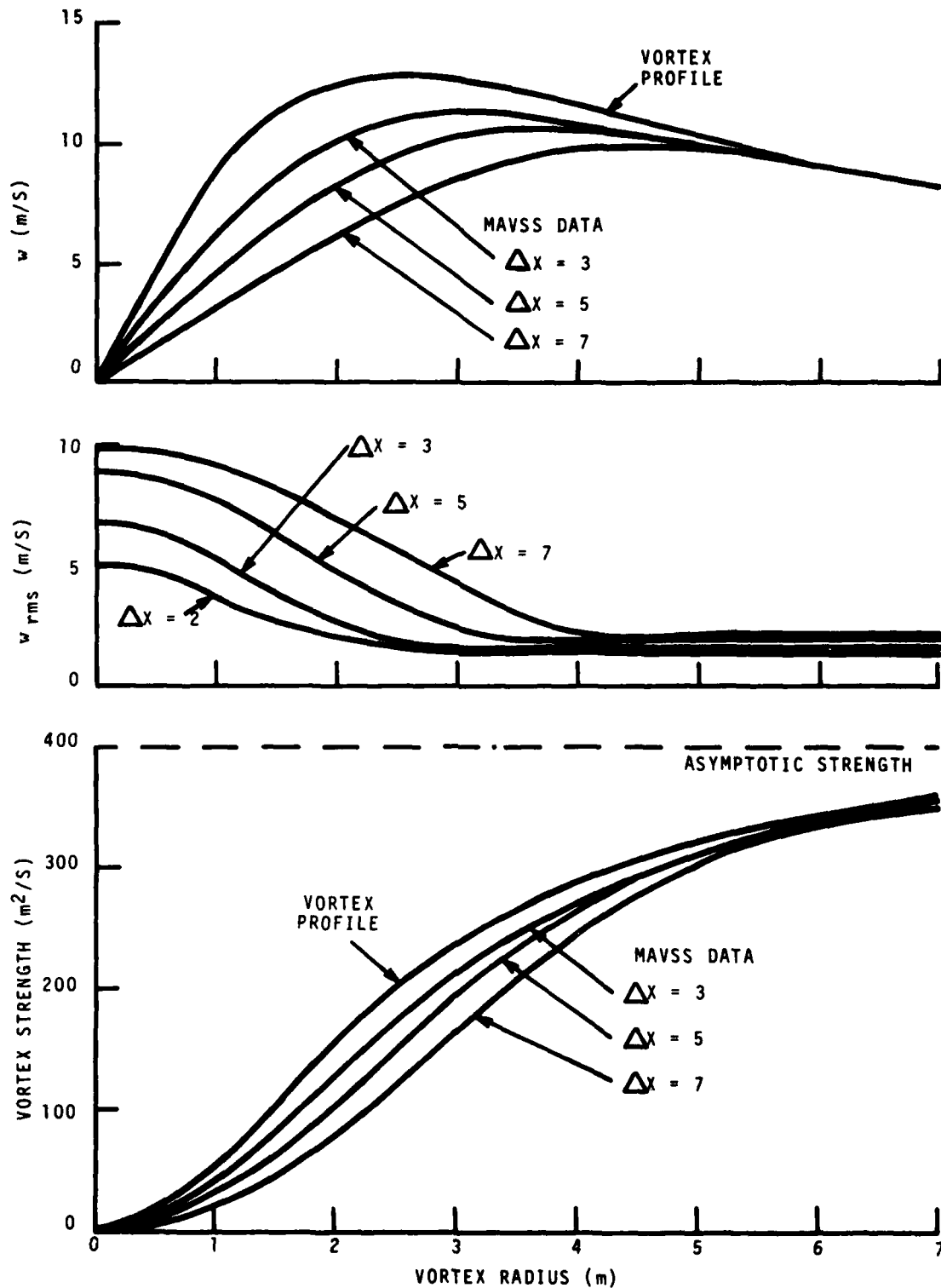


FIGURE 48. RESULTS OF THE MAVSS SIMULATION:  $Y_c = 2.5M = 2.5v_c$ , 12.7 M/SEC, AND  $\Delta Y = 3.5M$

these plots one can see that increasing the lateral averaging distance  $\Delta X$  reduces the peak velocity, increases and broadens the velocity spread ( $w_{rms}$ ), and displaces the circulation profiles. The plots of Figure 48 are evaluated for the vortex centered vertically in the averaging region. Displacing the vortex to the edge of the region results in reduced average and rms velocities, both by about 1.3 m/s in the peak values. The results in Figure 48 are for a velocity limit  $w_m$  greater than the maximum vortex velocity and therefore exhibit no velocity truncation effects.

Figure 49 shows the results of varying the vortex core radius in the model. The maximum value of  $w_{rms}$  is seen to be a sensitive function of both core radius and lateral resolution  $\Delta X$ . The lower graph in Figure 49 shows how the measured value of core radius depends upon the actual core radius. The measured value of core radius is not based on a least-square fit as is used for the actual data. Instead, the core radius is defined as the radius where the vortex strength is half the asymptotic value (see the lower plot in Figure 49). The errors in core radius are remarkably small except at very small radii where the measured core radius reaches an asymptotic value dependent upon the system parameters  $\Delta X$  and  $\Delta Y$ . Such an effect was observed in experimental data (Ref. 12) where the limiting core radius was about 0.08 times the vortex range. The data in Figure 48 also include no velocity truncation effects.

The MAVSS data can be corrupted by two types of spurious signals, both of which tend to reduce the measured average velocities and increase the rms velocity deviation. The first is random noise which can be modeled as a uniform power spectrum between velocities  $-w_m$  and  $+w_m$ . This same model describes a zero offset in the measurement of power spectral density. If the ratio of the total signal power to total noise power is  $R$ , then the resulting values of  $w$  and  $w_{rms}$  can be calculated to be (subscript  $n$  indicating noise effect):

$$w_n = w / (1 + 1/R) \quad (14)$$

$$(R+1)w_{rms,n}^2 = w_m^2 / 3(R+1) + (w^2 + R w_{rms}^2) R / (R+1)^2 \quad (15)$$

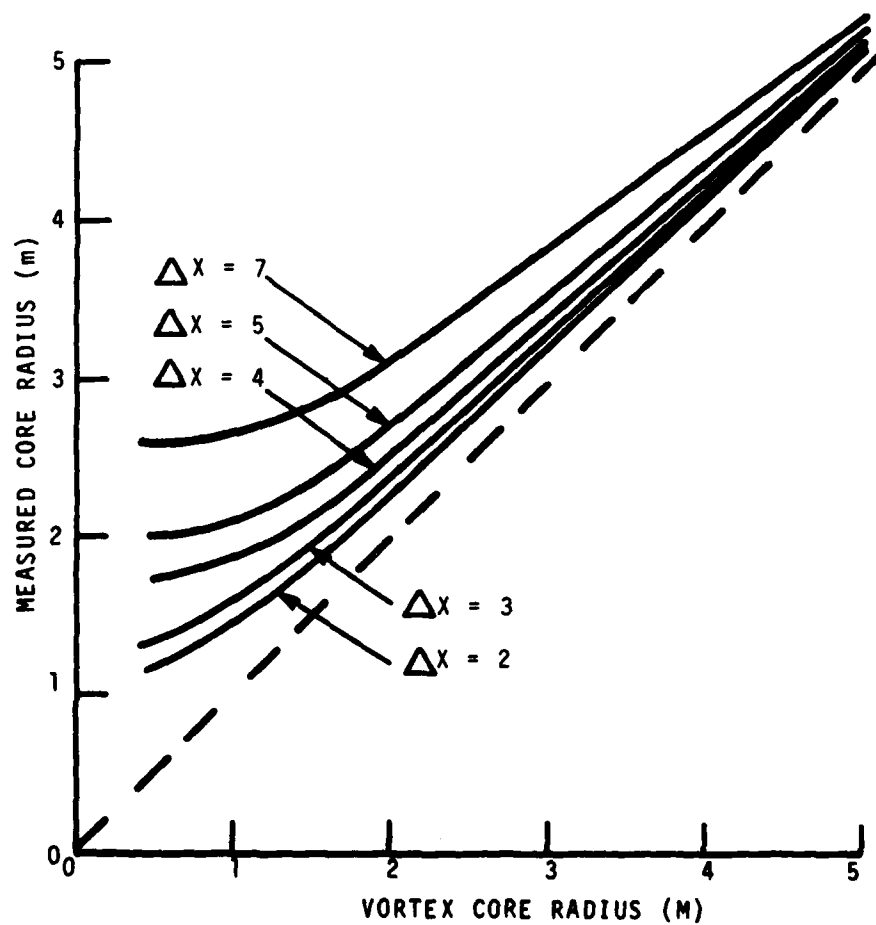
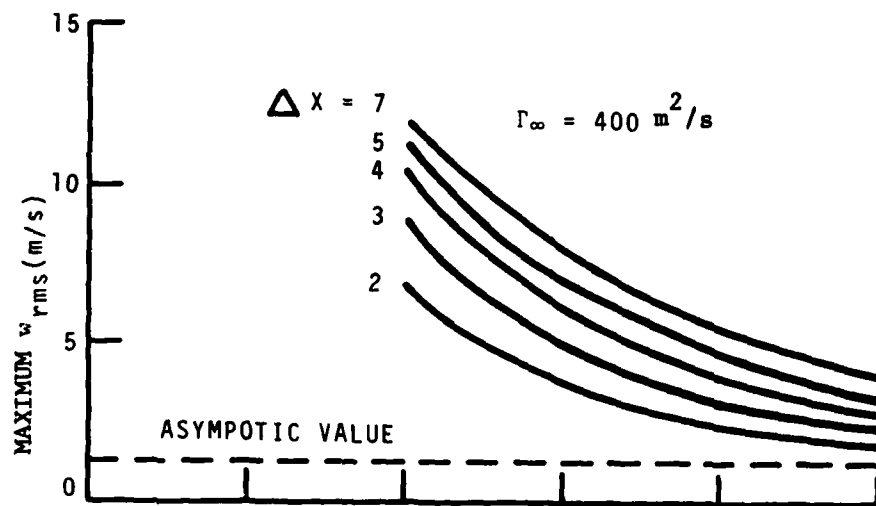


FIGURE 49. DEPENDANCE OF MAVSS MEASURED PARAMETERS ON ACTUAL CORE RADIUS



The usefulness of these equations is that a small measured value of  $w_{rms} \ll w_n$  implies that  $R$  must be greater than  $(w_m/w_{rmsn})^{2/3} - 1$  according to Equation 14.

The second type of spurious signal occurs at the transmitted frequency, which corresponds to zero velocity. Such signals occur at a particular range gate where the direct signal from another antenna is received. For a ratio of scattered signal power to spurious signal power of  $R$ , the values of  $w$  and  $w_{rms}$  become (subscript  $s$  indicating scattered signal effect):

$$w_s = w/(1 + 1/R) \quad (16)$$

$$w_{rms_s}^2 = (w^2 + R w_{rms}^2) R/(R+1)^2 \quad (17)$$

In this case the spurious signal does not show up as an abnormal broadening of the spectrum. Fortunately, this type of error appears only at a particular range gate (equal to the spacing between antennas for uniform spacing).

The MAVSS beam width  $\Delta X$  is a fundamental parameter of the simulation which has received little attention in the past. The angular beam width of  $7^\circ$  previously quoted (Ref. 12) was based on the width between the nulls of the beam pattern which overestimates the effective beam width. In fact, the data shown in the next section are not consistent with such a broad beam. Consequently, a more detailed analysis of the angular beam width was carried out. The far field intensity of the beam from a uniformly illuminated slit is given by

$$I \approx \sin^2 B/B^2 \quad (18)$$

with  $B = (\pi d/\lambda) \sin \theta$  where  $d$  is the width of the slit,  $\lambda$  is the wavelength and  $\theta$  is the angle of measurement. The half response width of the MAVSS occurs when each beam has been reduced by  $1/\sqrt{2}$  or  $B = 1.00$ . The full angular width at half response becomes

$$\Delta\theta = 2.00 \lambda/\pi d \quad (19)$$

for small angles where  $\sin \theta \approx \theta$ . For the MAVSS antennas  $d = 1.14$  m. The acoustic wavelength for nominal values of frequency

(3300 Hz) and sound speed (330 m/s) is 0.10 m. The resulting value of  $\Delta\theta$  is 0.056 rad ( $3.0^\circ$ ). This angle translates to  $X = 1.7$  m at 30-m range, the typical range for data in the next section. The transmitter and receiver beams overlap perfectly only at their point of intersection at about 25 m. At other ranges the beam centers separate by 0.06 m per meter of range. Considering the beam divergence,  $\Delta X = 2$  m is a reasonable estimate.

### C.3.2 MAVSS Data

This section examines the 1975 B-747 (Ref. 2) MAVSS data in the light of the simulation of the previous section.

One example of data for landing configuration is shown in Figure 50. The other vortex arrivals with good quality data (i.e., with few noise bursts) are included in Appendix D. Figure 50 is a condensation of the previous plots (Ref. 2) with five range gates to show just the two range gates closest to the vortex height. In addition, the figure shows the  $w$  and  $w_{rms}$  profiles from the MAVSS simulation for  $\Delta X = 2$  m,  $r_c = 2.5$  m, and  $\Gamma_\infty = 400 \text{ m}^2/\text{s}$ . Many of the measured values of  $r_c$  lie between 2.6 and 3.0 m as one would expect for a core radius of 2.5 according to Figure 49. The circulation  $\Gamma_\infty = 400 \text{ m}^2/\text{s}$  was selected to be typical of the fitted values. The observed peak values of  $w_{rms}$  at the vortex center (note: 100 Hz corresponds to 5 m/s) are too small for values of  $\Delta X$  much larger than 2 m. Thus, the MAVSS simulation with these parameters gives a reasonable description of the observations for fresh vortices with one exception: The observed width of the  $w_{rms}$  peak is consistently wider than the simulation. The most reasonable explanation for this width is the presence of turbulence in the vortex. Thus, the  $w_{rms}$  profiles away from the vortex center may be a measurement of the actual turbulence profile in the vortex. Another potential explanation for the broad  $w_{rms}$  profile is vortex-induced noise, either at the vortex core or by the vortex wind at the antenna. This source of spectral broadening may account for some anomalies in the data but it cannot account for the observed broad  $w_{rms}$  profile since noise

would produce even higher values of  $w_{rms}$  at higher range gates because of the reduction of signal power as inverse range squared. In fact, the consistent broadening is observed only at ranges near the vortex height (see Appendix D).

Figure 51 shows MAVSS data for landing configuration with spoilers deployed. Other examples are in Appendix D. The MAVSS simulated data ( $\Delta X = 2$  m) are plotted for a vortex model corresponding to Figure 43. The velocity increases linearly to 6.0 m/s at a core radius of 1 m, is constant until 10-m radius where it begins to decay as inverse radius ( $\Gamma_{\infty} = 380 \text{ m}^2/\text{s}$ ). This model gives reasonable agreement with the measurements.

#### C.4 COMPARISONS WITH INSTRUMENTED TOWER DATA

In 1972, B-747 wake vortices were probed with tower-mounted hot-wire anemometers at 30-cm spacing (Ref. 11). Unfortunately, a number of problems prevent these measurements from providing standard landing-vortex velocity profiles for comparison with remote sensor data. In the first place, the data show wide variations, even at vortex ages less than 15 seconds. In the second place, the data are biased by the ambient wind; the effects of the ambient wind cannot be cancelled by comparing the two sides of a vortex because of tower shadowing effects. In the third place, the landing configuration used  $25^\circ$  flaps instead of the  $30^\circ$  flaps used in the alleviation work. The upper LDV curve in Figure 44 is a plausible representation for the majority of the tower velocity profiles with suitable adjustments for ambient wind and tower shadowing. A number of runs, however, show a much tighter vortex core. The upper LDV curve in Figure 44 is most suited for comparison with tower data since the processing method for the tower data also picks out the highest velocity component at a particular vortex radius.

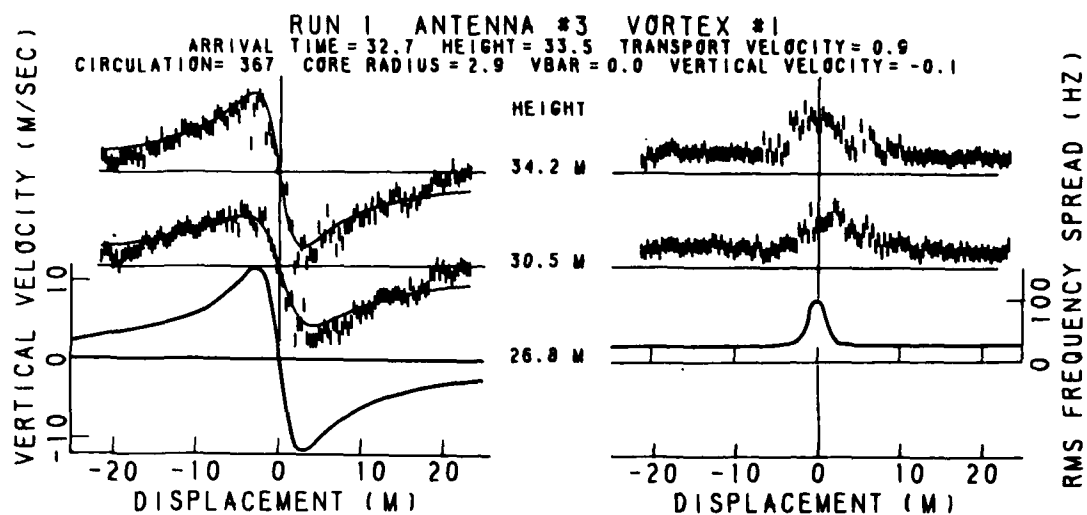


FIGURE 50. NON-ALLEVIATED LANDING CONFIGURATION MAVSS DATA

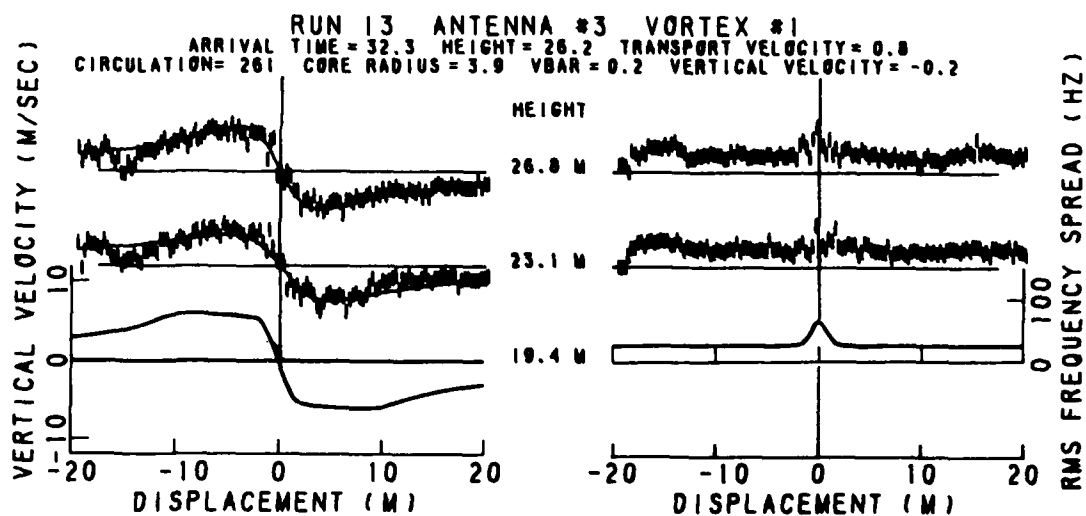


FIGURE 51. SPOILER-ALLEVIATED LANDING CONFIGURATION MAVSS DATA

### C.5 SENSOR CONCLUSIONS

The 3.5-m/s discrepancy (Figure 44) between LDV and MAVSS measurements of similar vortices can be attributed to four possible sources of error:

1. LDV reading high,
2. MAVSS reading low,
3. Altitude dependence of decay,
4. Different vortex ages.

The first source can be assigned the value 1.6 m/s according to Section C.2.2. The second will be estimated using the analysis of Section C.3.1. The 1975 B-747 MAVSS data were processed with  $w_m = 13$  and 16 m/s for the high and low frequencies, respectively (14 m/s will be used for subsequent calculations). The data (Appendix D) are not consistent with a noise or offset generated value of  $w_{rms}$  greater than 1.3 m/s. Equation 15 yields a signal-to-noise ratio of  $R = 5$ . This signal-to-noise ratio would cause the velocity to read 20 percent low according to Equation 14. This error would be 2.4 m/s at 12 m/s and 1.0 m/s at 5 m/s. One must remember that this MAVSS error is an upper limit; the actual error is probably much smaller. This MAVSS error is more than is needed to resolve the LDV/MAVSS discrepancy at the velocity peak of Figure 44 and is almost enough to resolve it at 14-m radius. Any residual discrepancy can be reasonably attributed to altitude effects on vortex decay. The LDV data taken well above the ground show very little vortex decay in the 25-50 second age period. The MAVSS data taken near the ground, however, indicate considerable decay in this age period. The MAVSS measurements in Appendix D are all older than 25 seconds where the LDV velocity profile was evaluated. Thus, it is reasonable to expect vortex decay to contribute to the LDV/MAVSS discrepancy.

APPENDIX D  
ROSAMOND LAKE MONOSTATIC ACOUSTIC VORTEX SENSING SYSTEM (MAVSS)  
DATA

This appendix includes additional examples of MAVSS data for unalleviated (Figure 52) and alleviated (Figure 53) vortices in the same format as Figures 50 and 51, respectively.

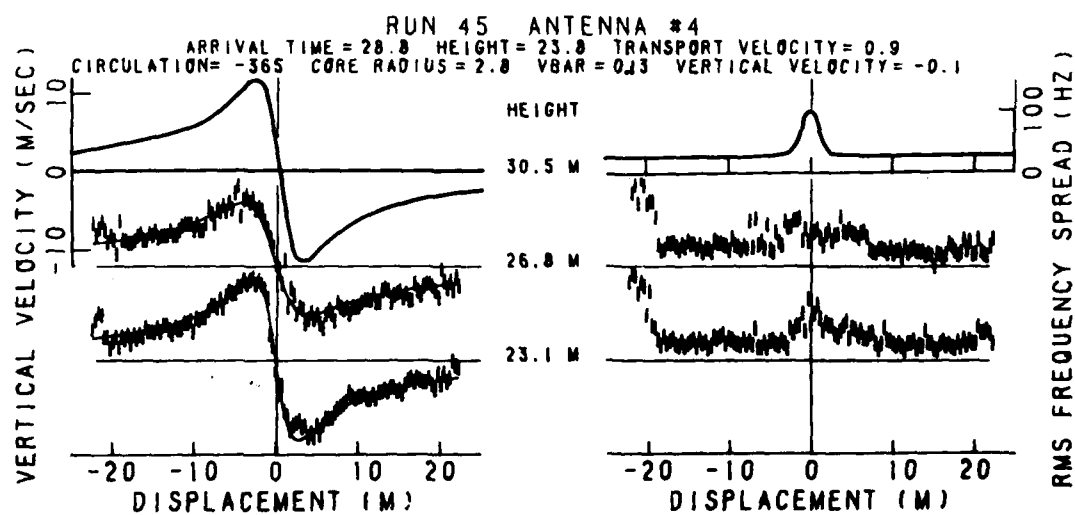
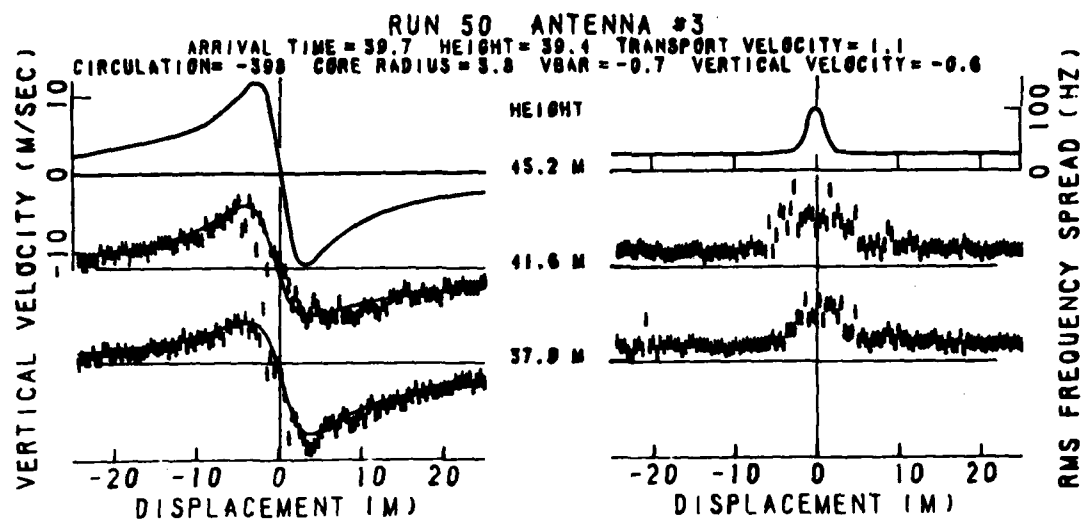


FIGURE 52. ROSAMOND LAKE NON-ALLEVIATED MAVSS DATA

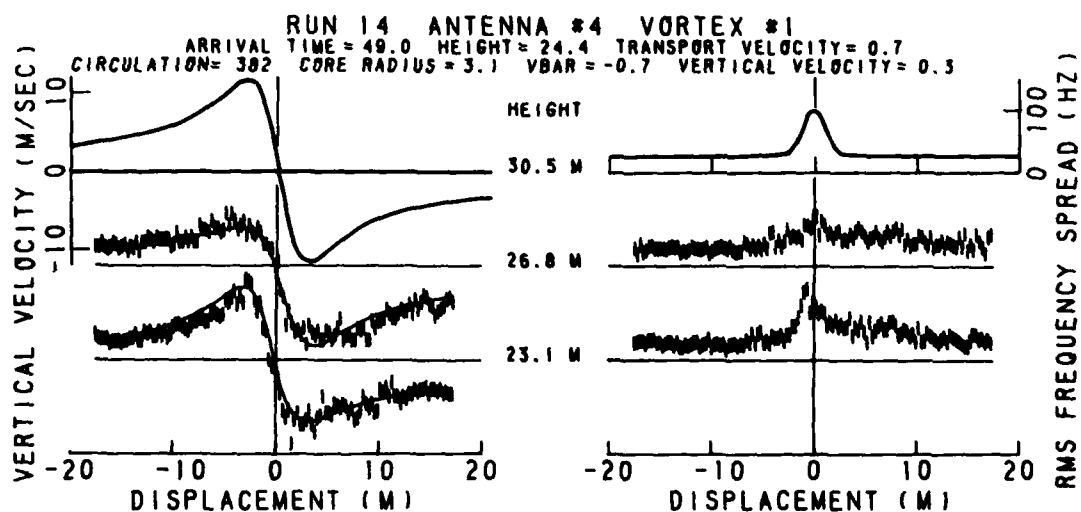
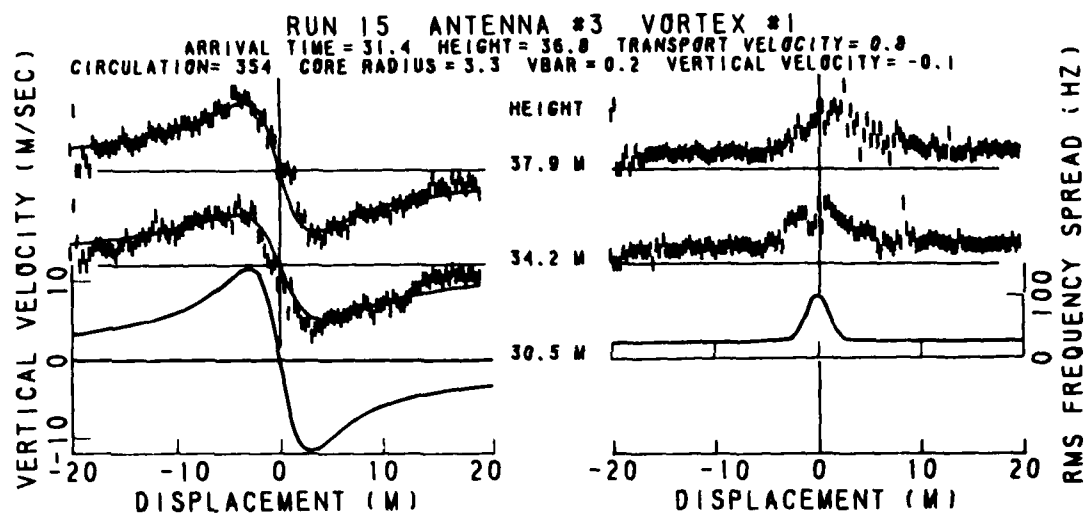


FIGURE 52. ROSAMOND LAKE NON-ALLEVIATED MAVSS DATA (Continued)



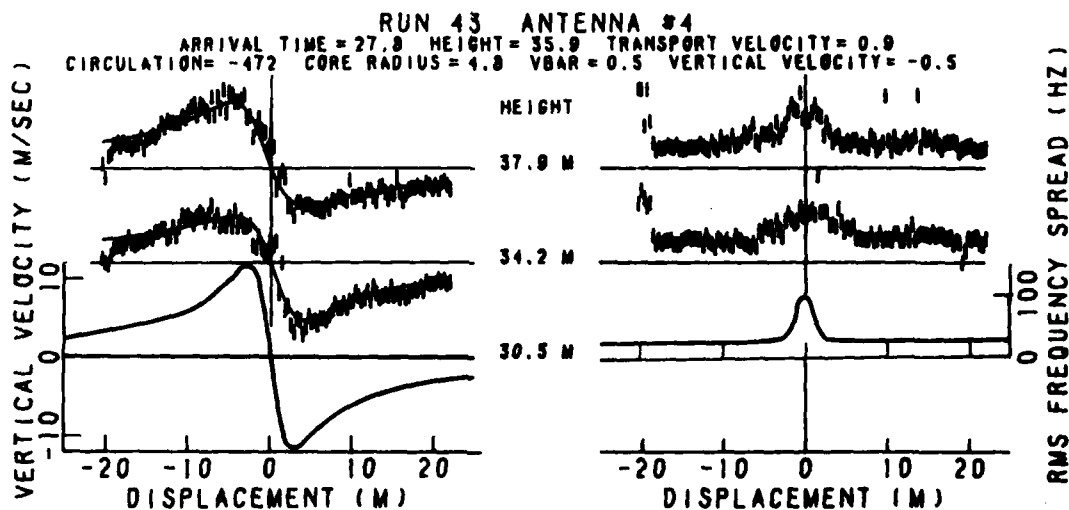
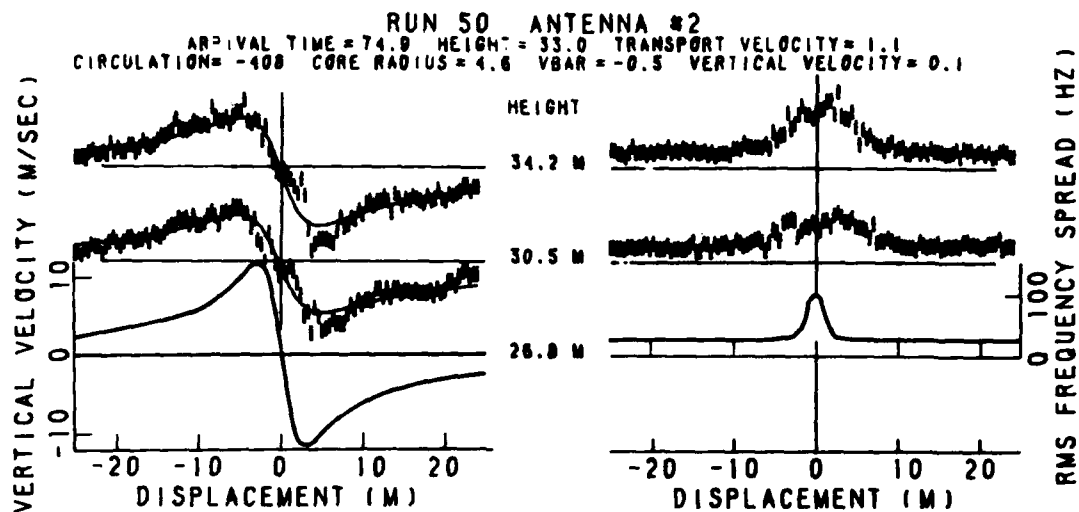


FIGURE 52. ROSAMOND LAKE NON-ALLEVIATED MAVSS DATA (Continued)

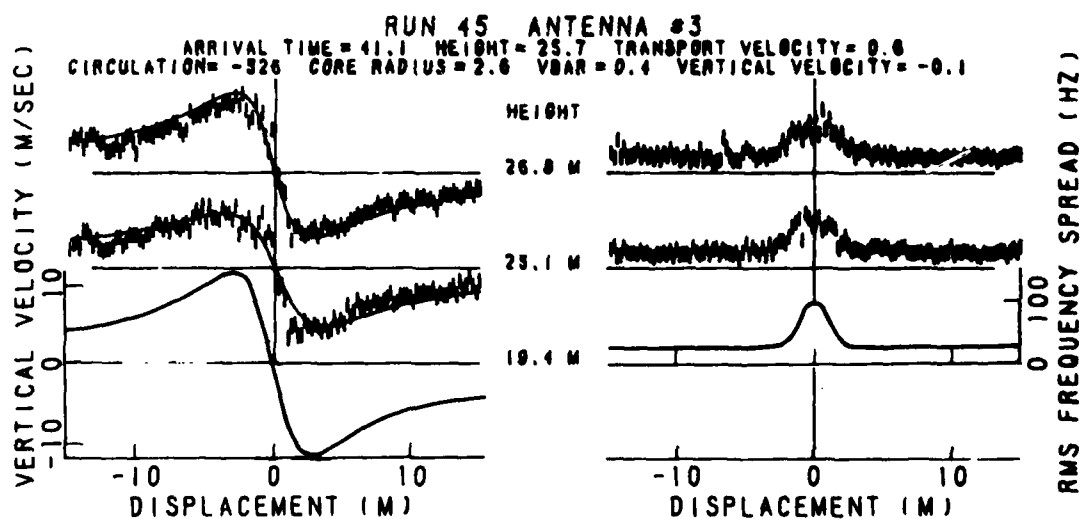
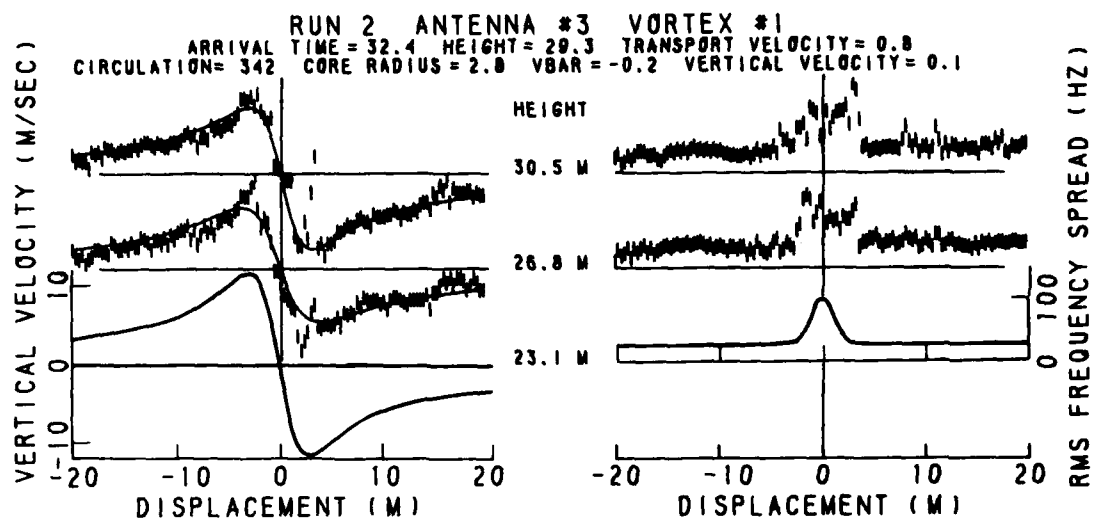


FIGURE 52. ROSAMOND LAKE NON-ALLEVIATED MAVSS DATA (Continued)

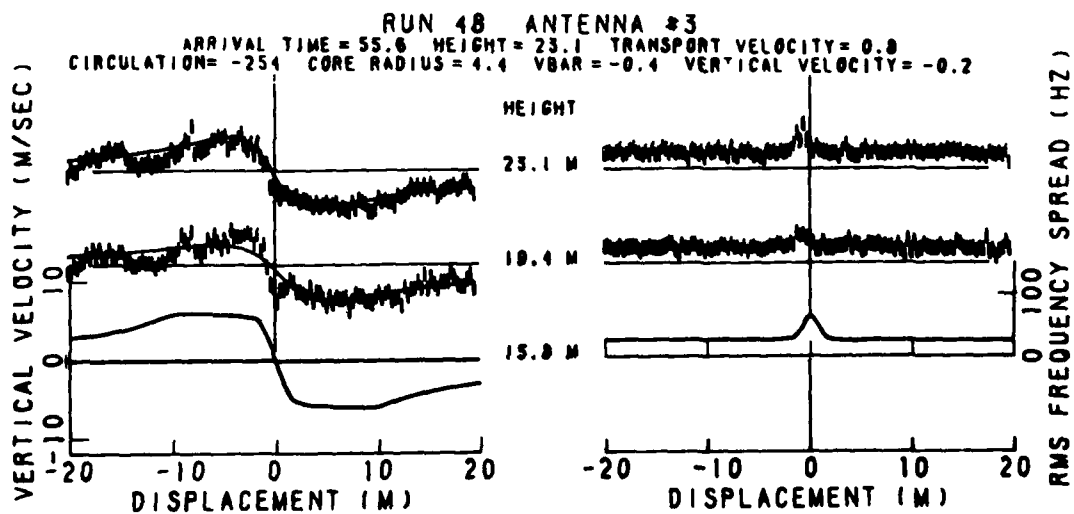
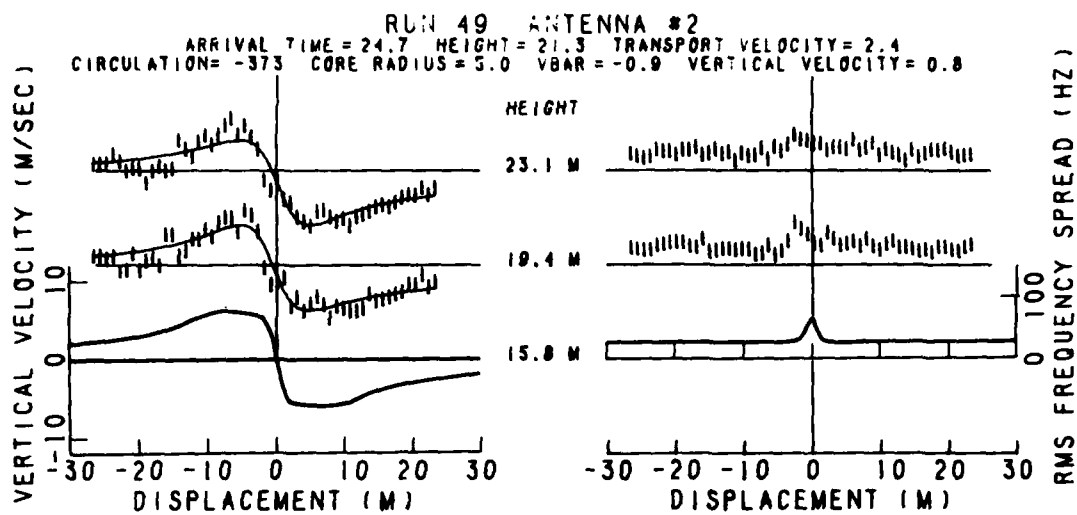


FIGURE 53. ROSAMOND LAKE SPOILER-ALLEVIATED MAVSS DATA

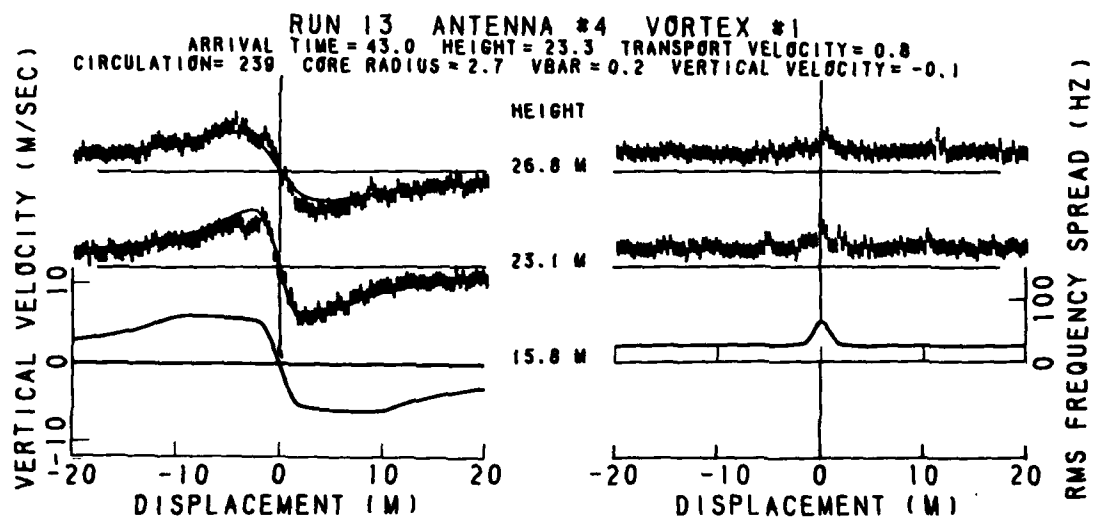


FIGURE 53. ROSAMOND LAKE SPOILER-ALLEVIATED MAVSS DATA (Continued)

## APPENDIX E

### LASER DOPPLER VELOCIMETER (LDV) DATA

This Appendix contains a complete set of the LDV data collected during the flight tests. The plots show some minor differences from those contained in the body of the report because of later developments in the software. One difference appears in the velocity-profile plots. In Figures 14 and 15, the center point is plotted at zero velocity. This procedure tends to give a misleading picture of the data, since  $V_{\max}$  can be quite large at the center point. In this appendix (and also Figure 31), the center point is plotted both positive and negative with a connecting line. Another change is the labeling of the two circulation profiles. In Figures 16 and 17, the profile toward the other vortex is marked with an X, and the profile away from the other vortex is marked with an O. These labels are interchanged for the circulation profiles in this appendix.

The LDV data for February 10, 1979, are organized somewhat differently than for the other days because of the successful photographic tracking of the vortices. The test conditions on February 10, 1979, gave optimum results because the vortices remained above the LDV until they decayed. Figure 54 shows the vortex trajectories before (left) and after (right) the vortex range fits were assigned. Figures 55-58 show, respectively, the average circulation and induced rolling moment versus age, and the velocity and circulation profiles.

The subsequent Figures 59-66 show the data for the four other test days. The first figure for each day shows the vortex trajectories and the decay of average circulation and induced rolling moment. The second figure shows the velocity and circulation profiles.

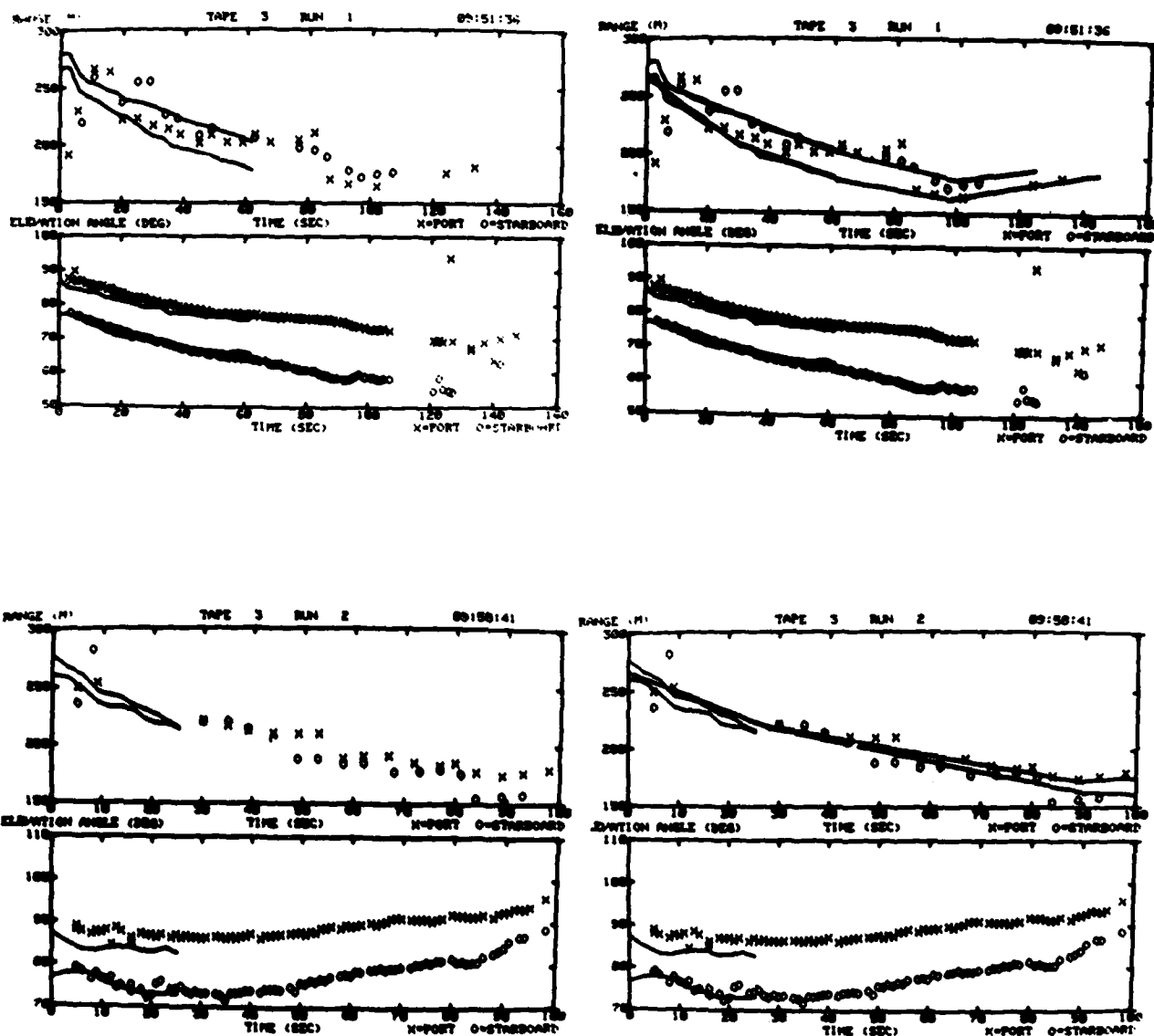


FIGURE 54. VORTEX TRAJECTORIES ON 2/10/79. THE RIGHT PLOTS SHOW THE LINE SEGMENTS FITTED TO THE RANGE.

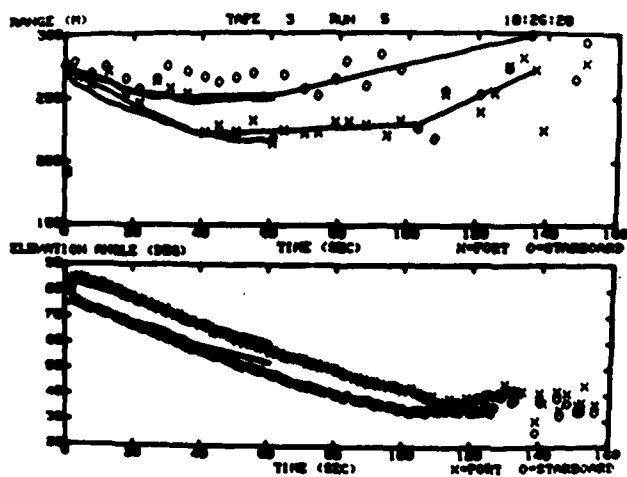
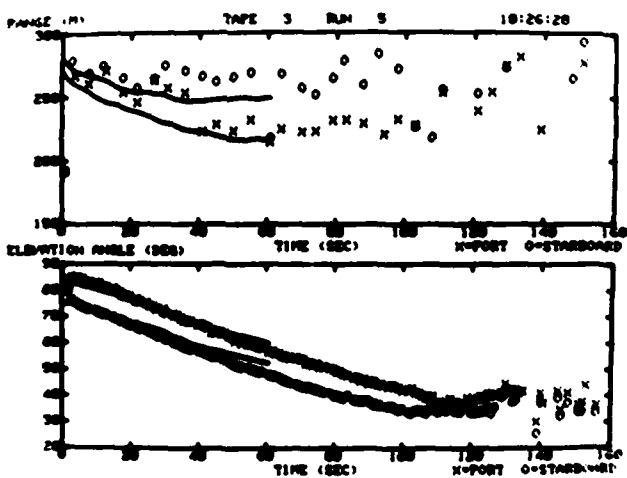
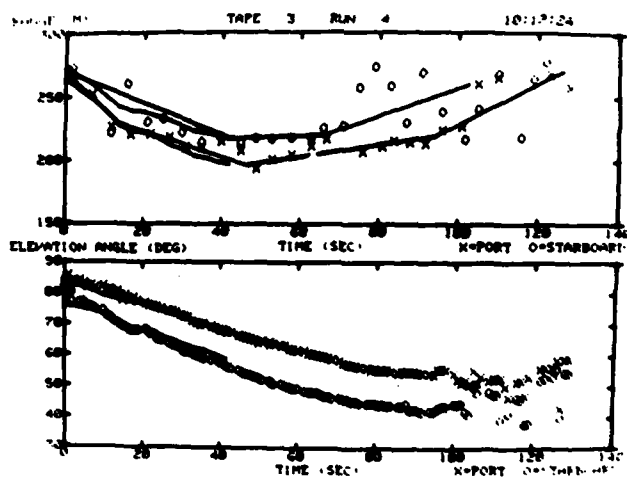
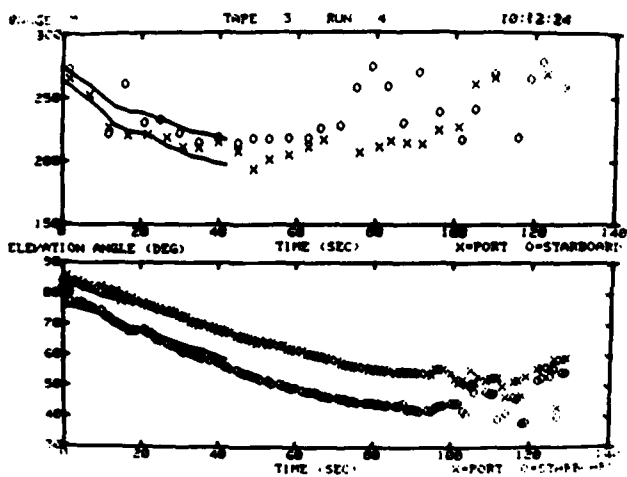
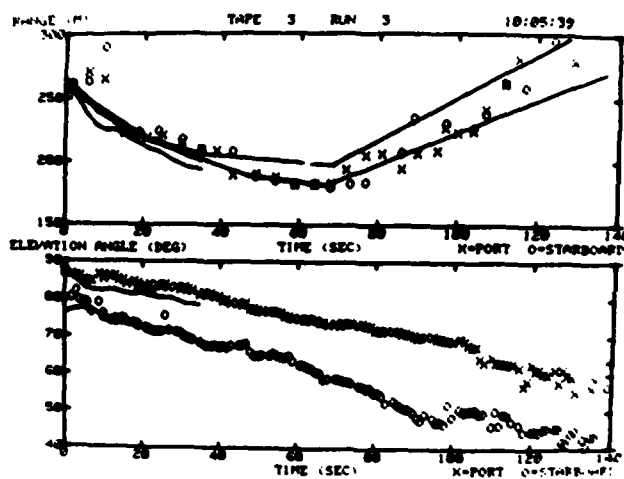
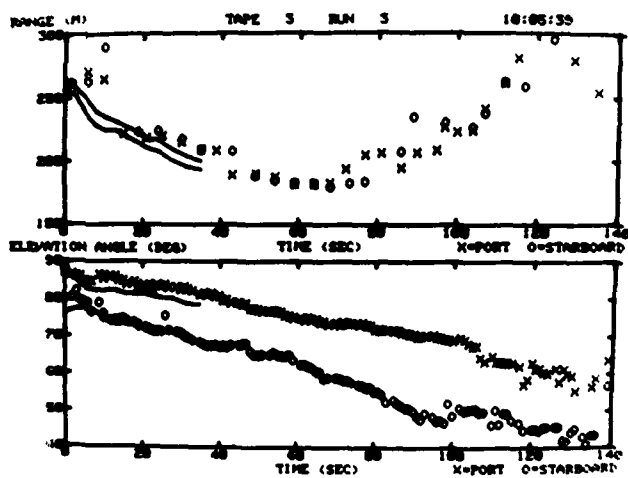


FIGURE 54. VORTEX TRAJECTORIES ON 2/10/79 (Continued)

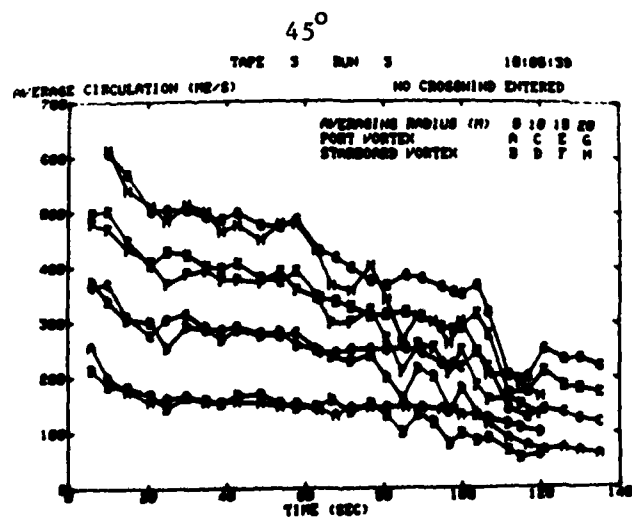
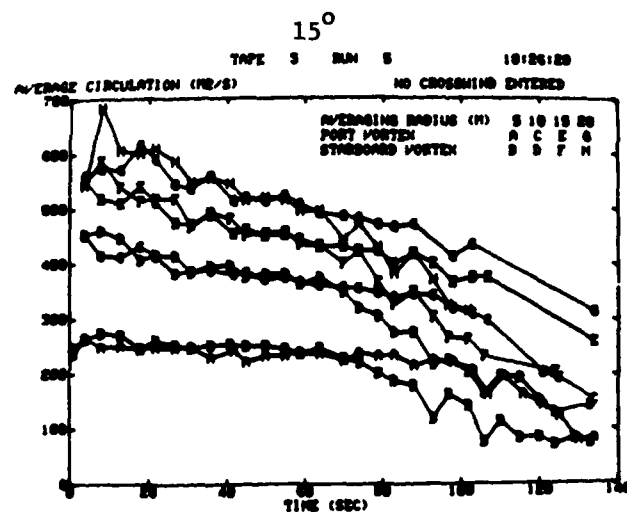
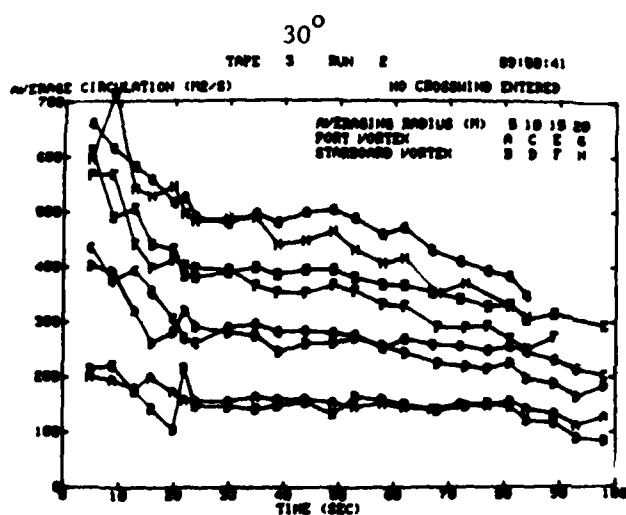
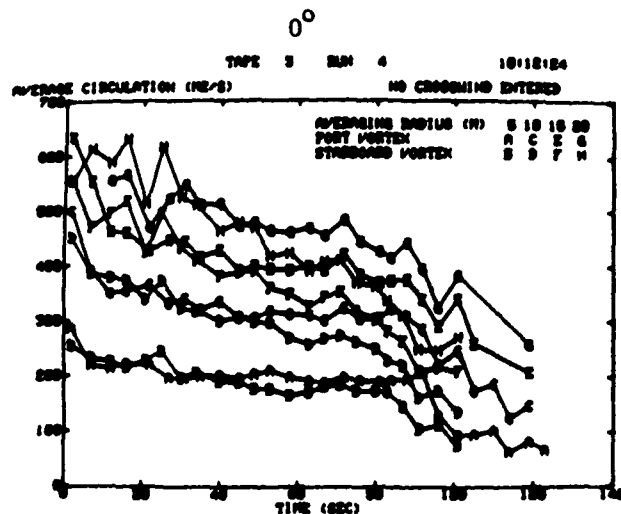
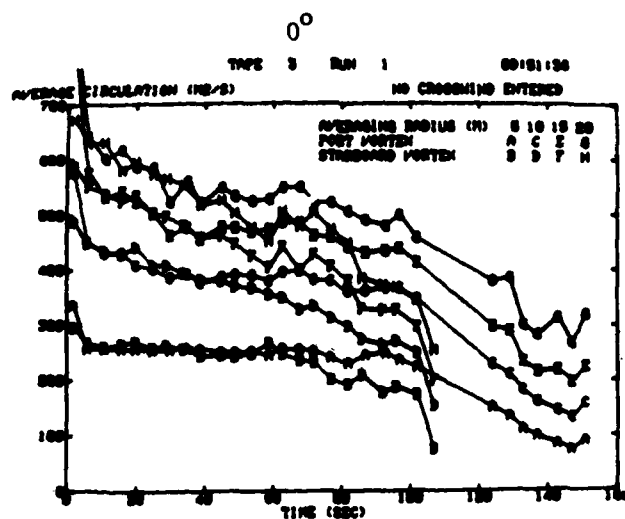


FIGURE 55. AVERAGE CIRCULATION VERSUS AGE FOR RUNS ON 2/10/79  
 (SPOILERS 2,4)



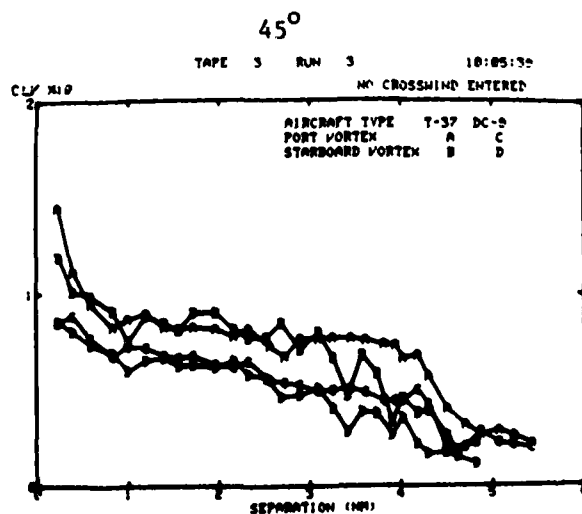
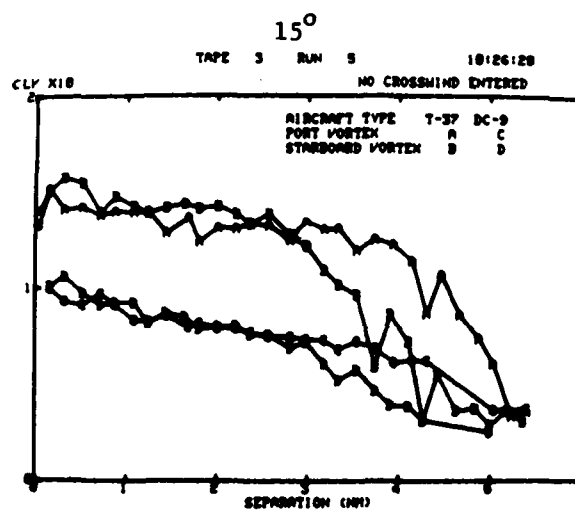
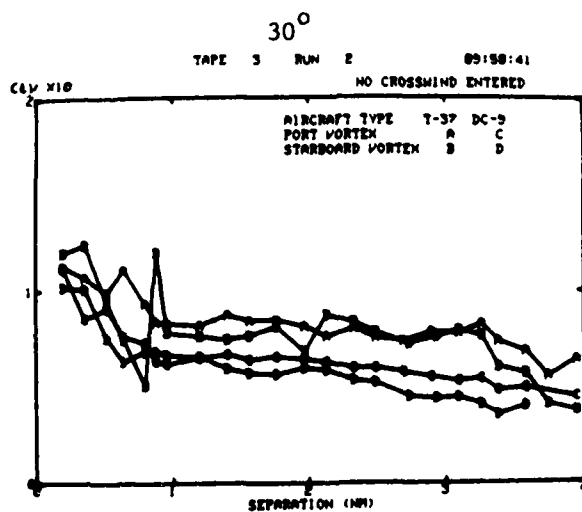
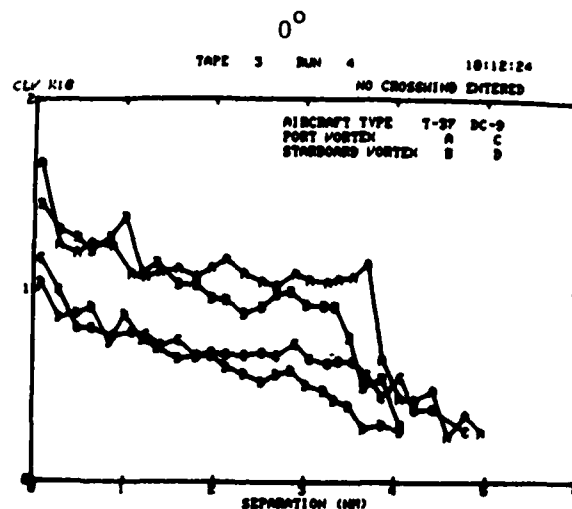
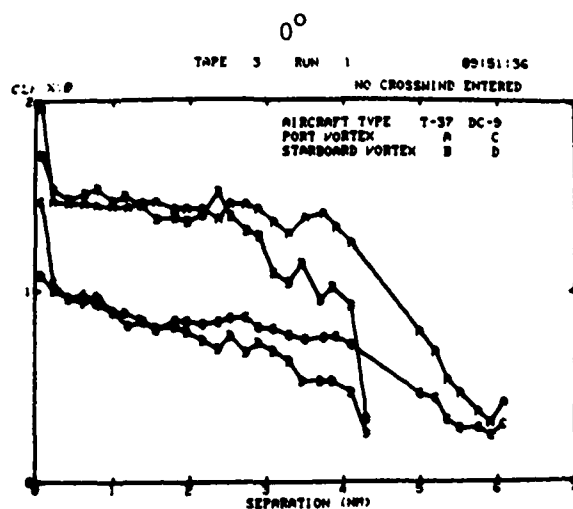


FIGURE 56. VORTEX INDUCED ROLLING MOMENT VERSUS SEPARATION (NAUTICAL MILES) FOR RUNS ON 2/10/79 (SPOILERS 2,4)

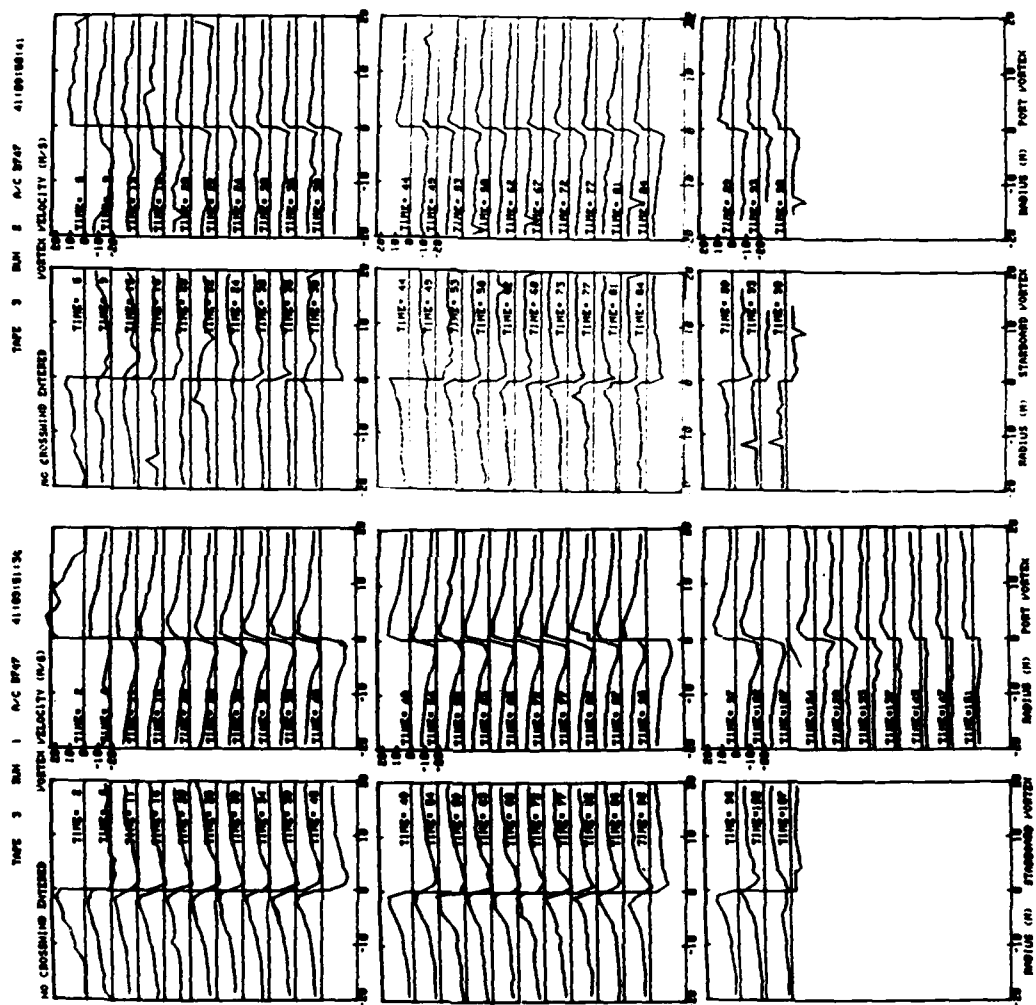


FIGURE 57. VELOCITY PROFILES FOR THE RUNS ON 2/10/79

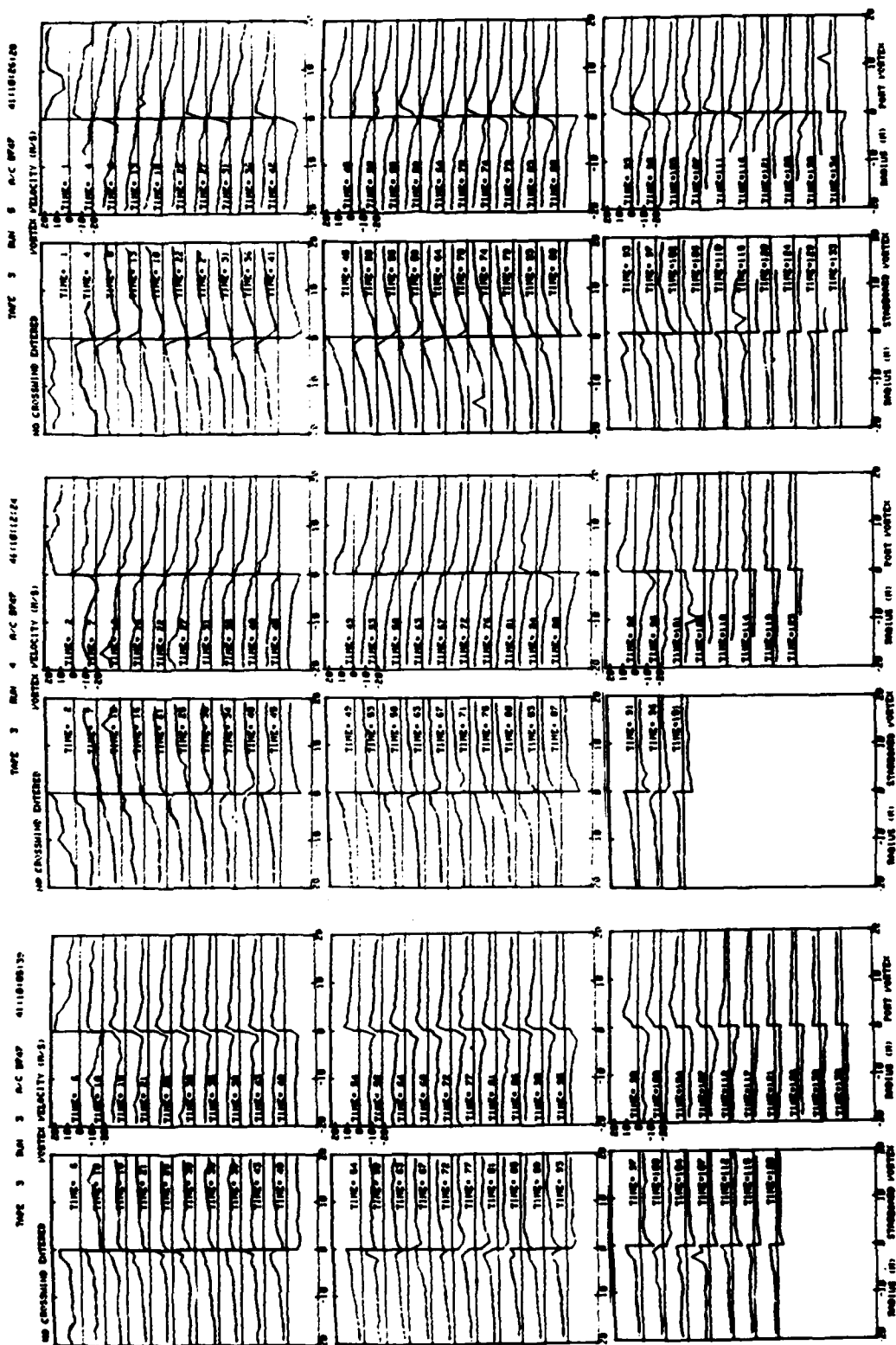


FIGURE 57. VELOCITY PROFILES FOR THE RUNS ON 2/10/79 (Continued)



FIGURE 58. CIRCULATION PROFILES FOR THE RUNS ON 2/10/79



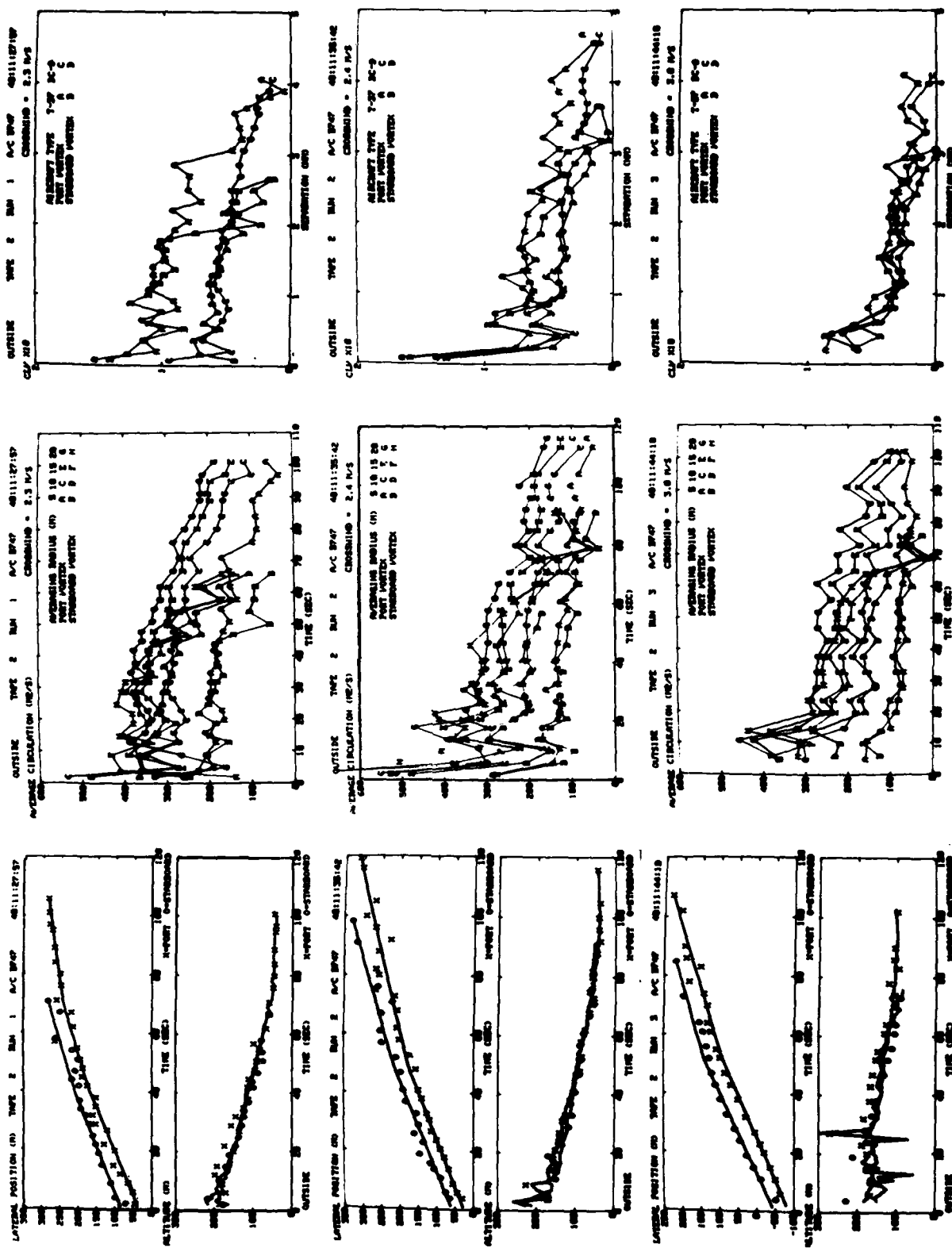


FIGURE 59. VORTEX TRAJECTORIES, AVERAGE CIRCULATION, AND VORTEX-INDUCED ROLLING MOMENT COEFFICIENT FOR THE RUNS ON 2/9/79

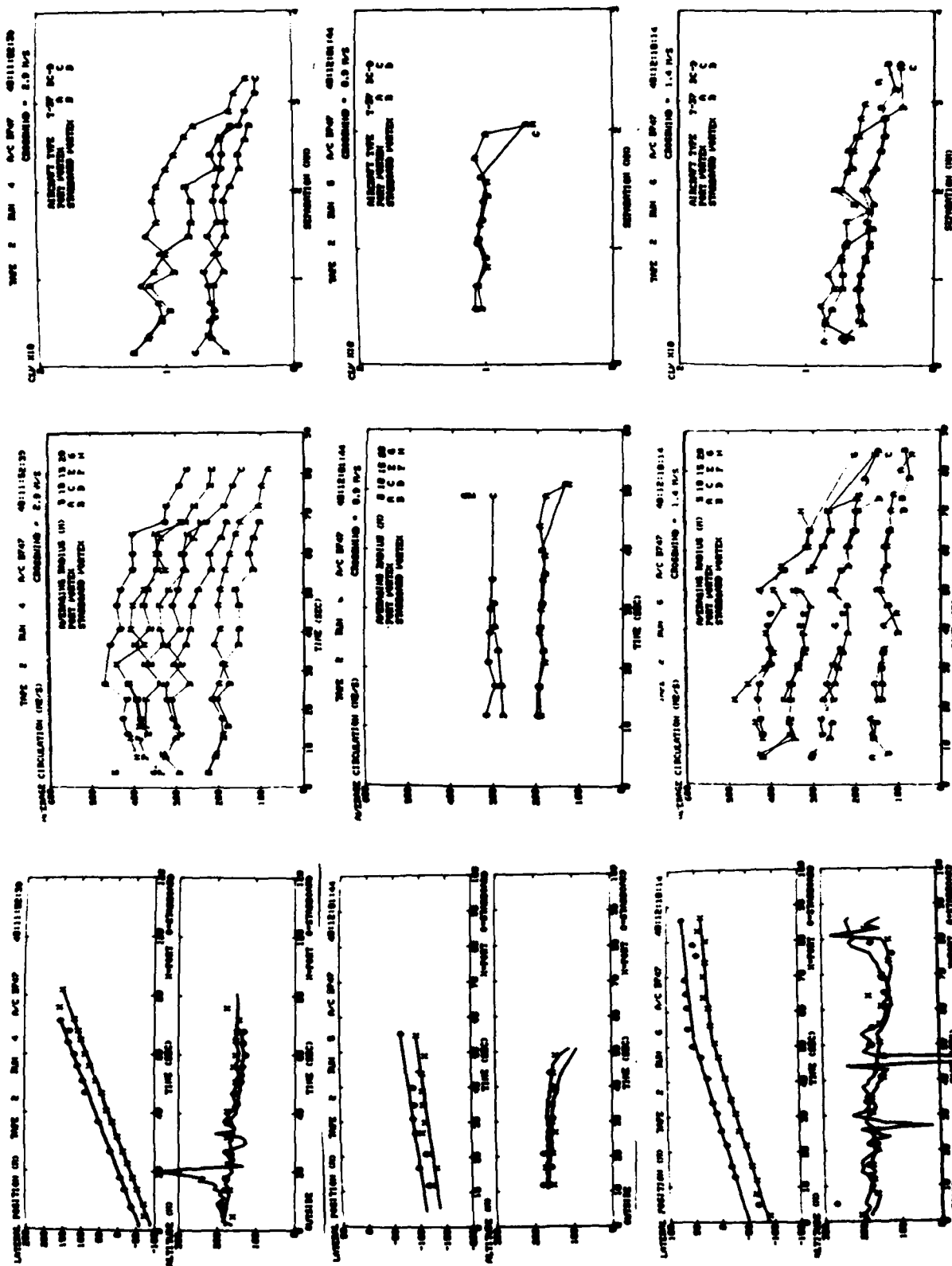


FIGURE 59. VORTEX TRAJECTORIES, AVERAGE CIRCULATION, AND VORTEX-INDUCED ROLLING MOMENT COEFFICIENT FOR THE RUNS ON 2/9/79 (Continued)

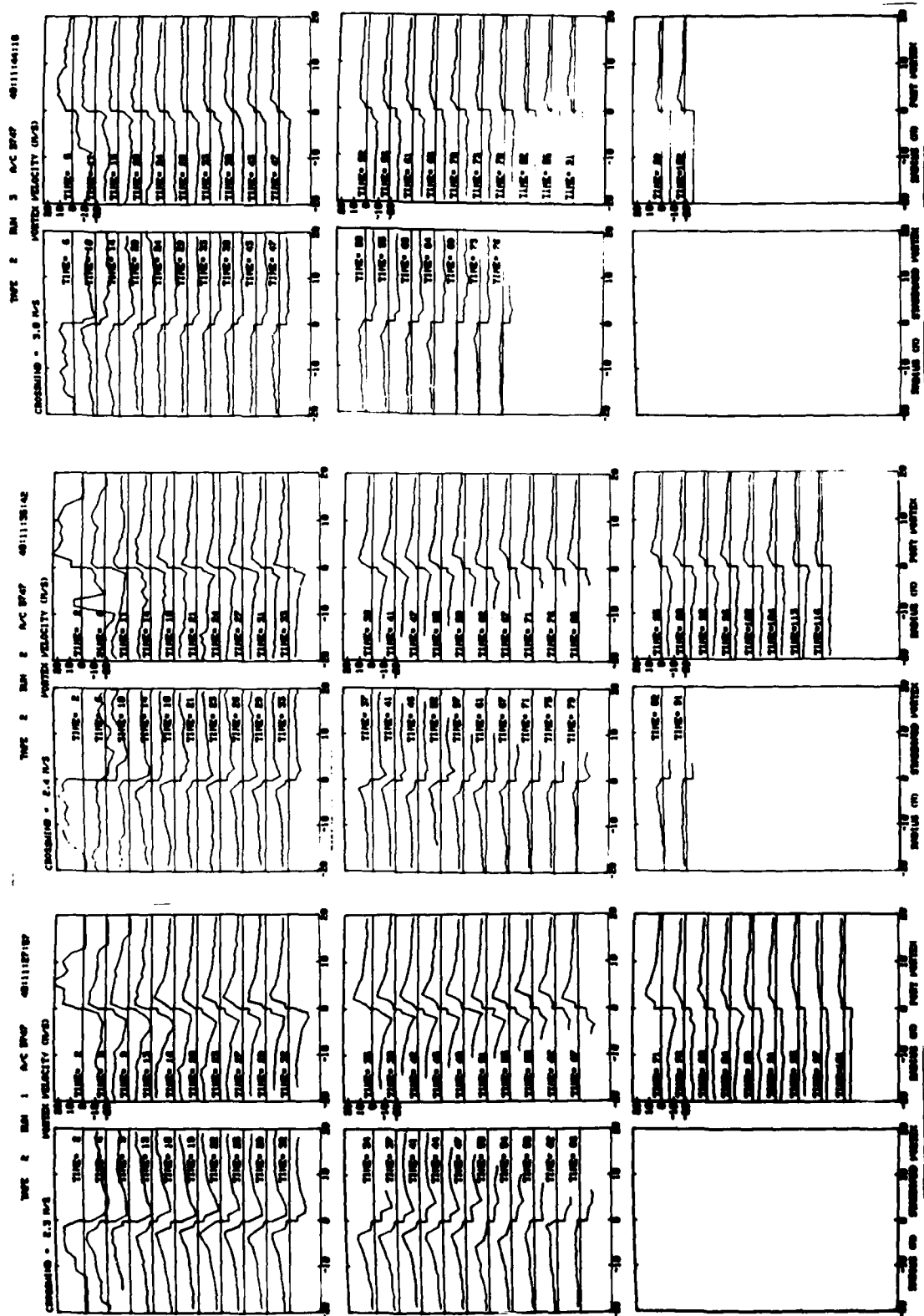


FIGURE 60. VELOCITY AND CIRCULATION PROFILES FOR THE RUNS ON 2/9/79





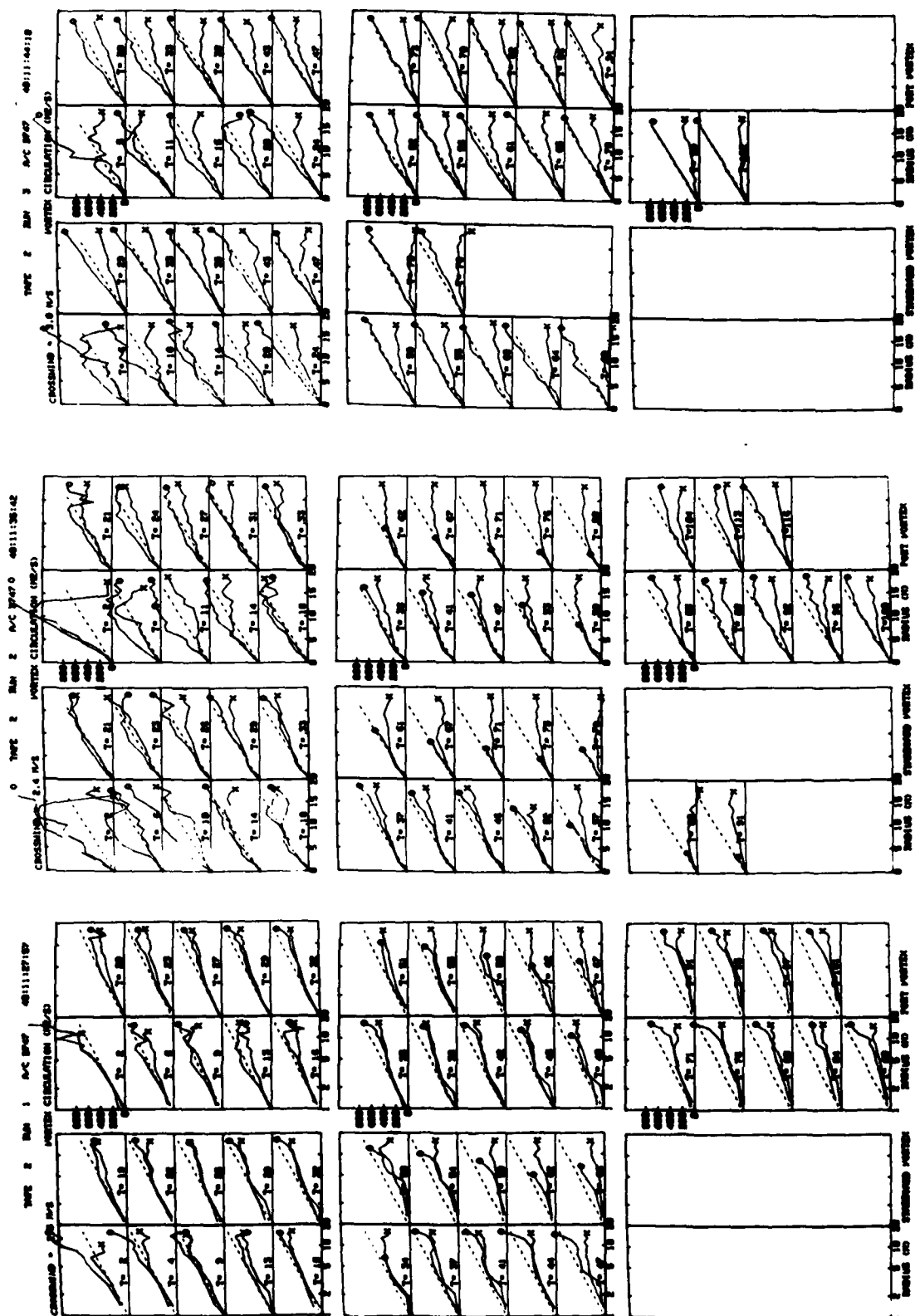


FIGURE 60. VELOCITY AND CIRCULATION PROFILES FOR THE RUNS ON 2/9/79 (Continued)

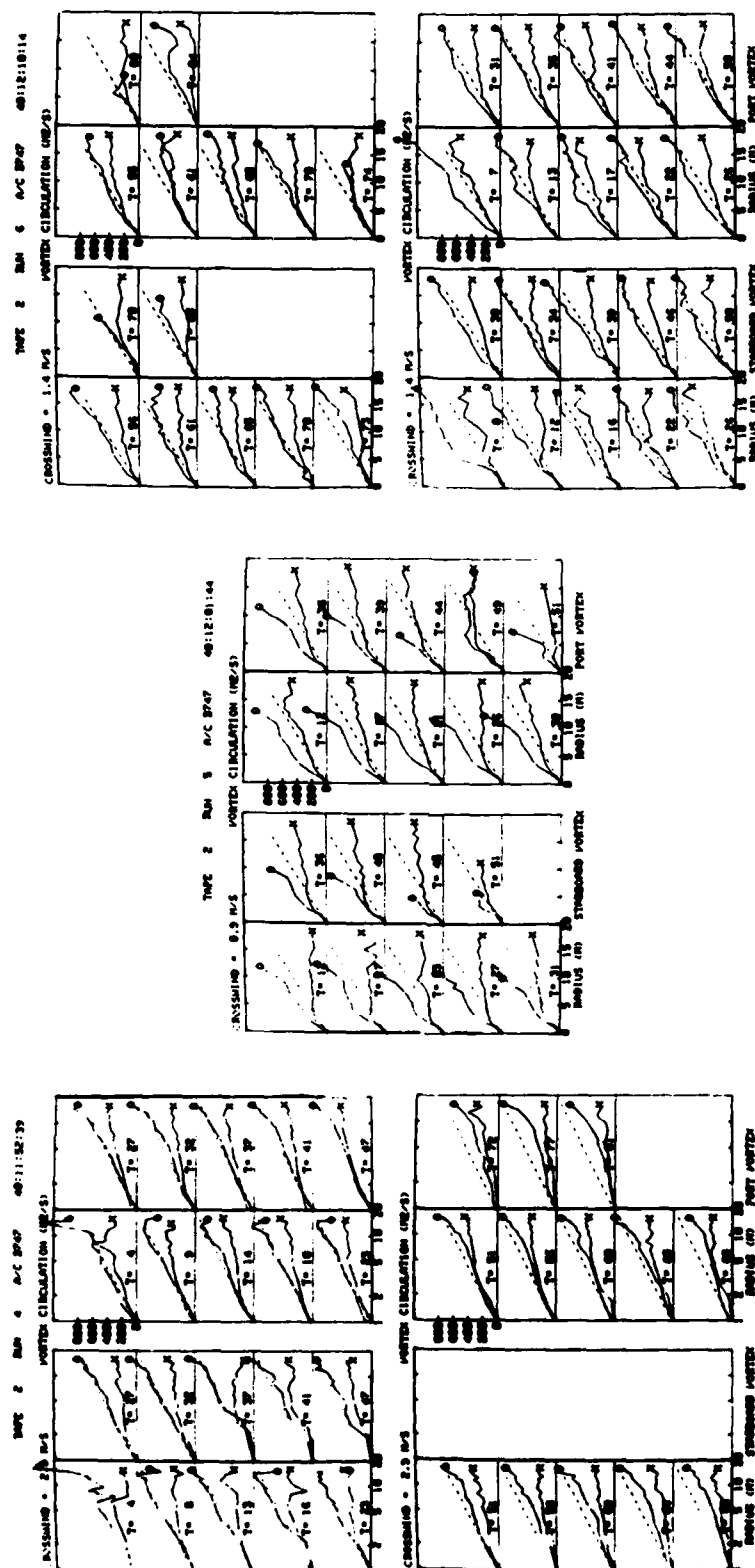


FIGURE 60. VELOCITY AND CIRCULATION PROFILES FOR THE RUNS ON 2/9/79 (Continued)

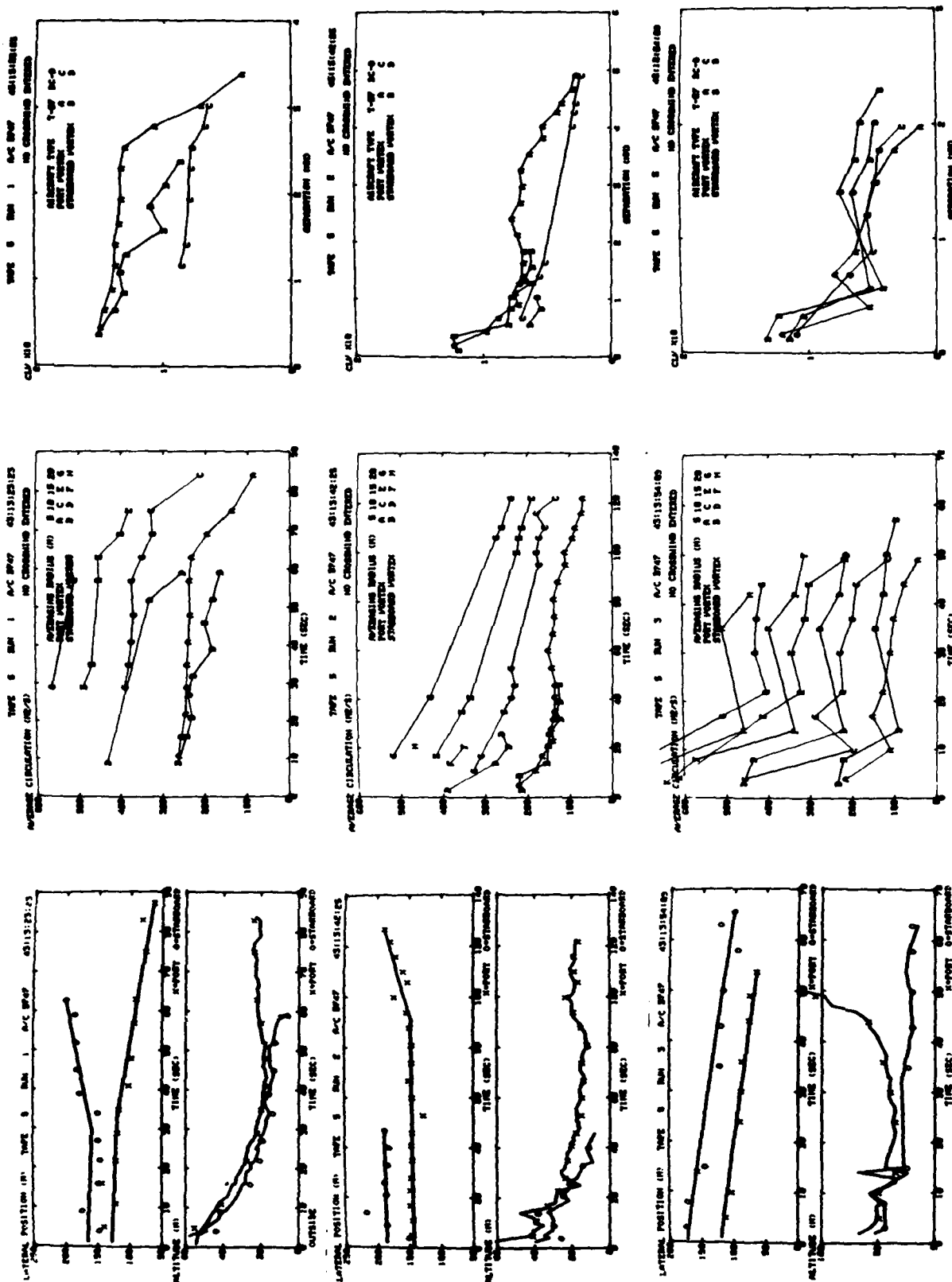


FIGURE 61. VORTEX TRAJECTORIES, AVERAGE CIRCULATION, AND VORTEX-INDUCED ROLLING MOMENT COEFFICIENT FOR THE RUNS ON 2/12/79

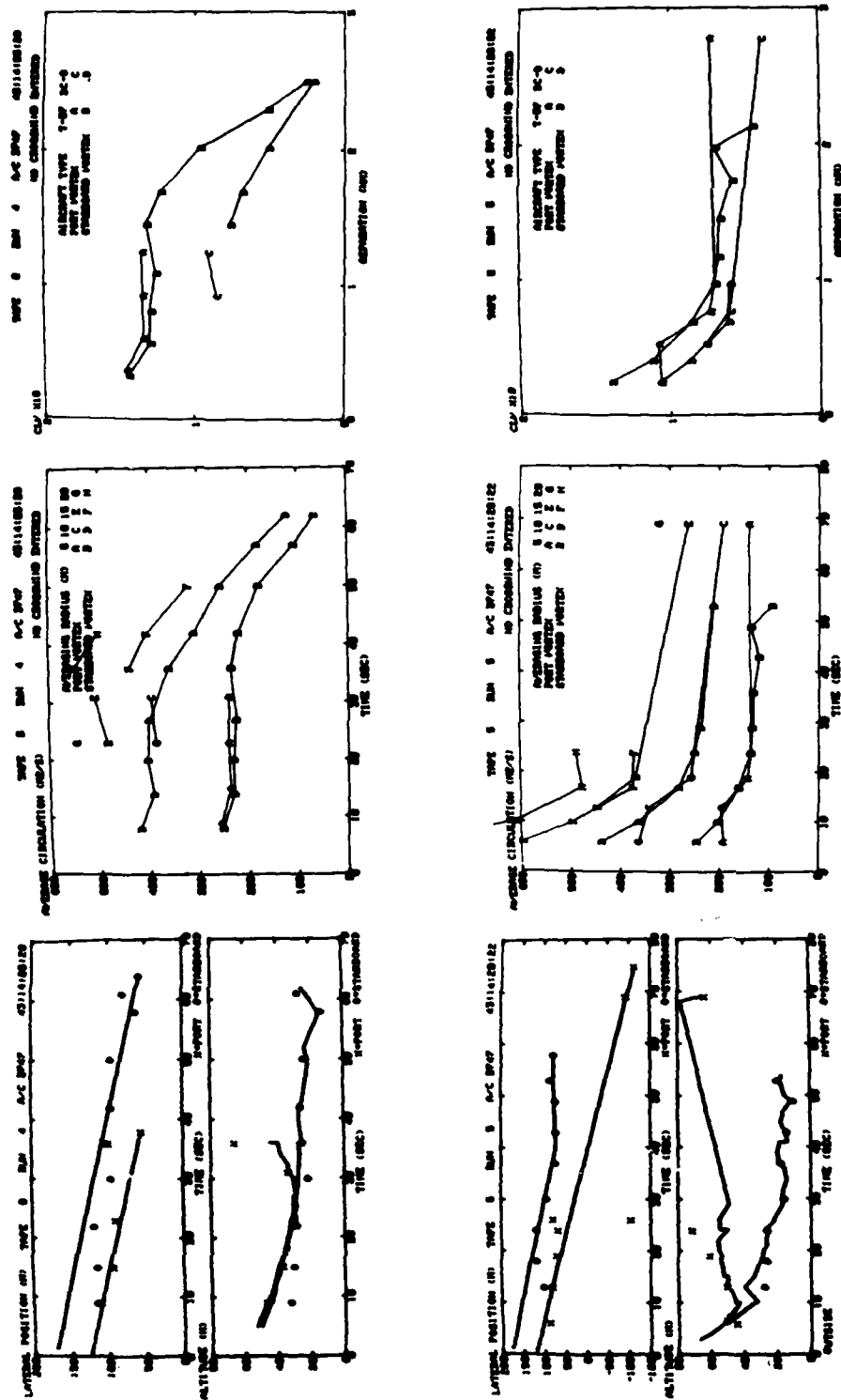


FIGURE 61. VORTEX TRAJECTORIES, AVERAGE CIRCULATION, AND VORTEX-INDUCED ROLLING MOMENT COEFFICIENT FOR THE RUNS ON 2/12/79 (Continued)

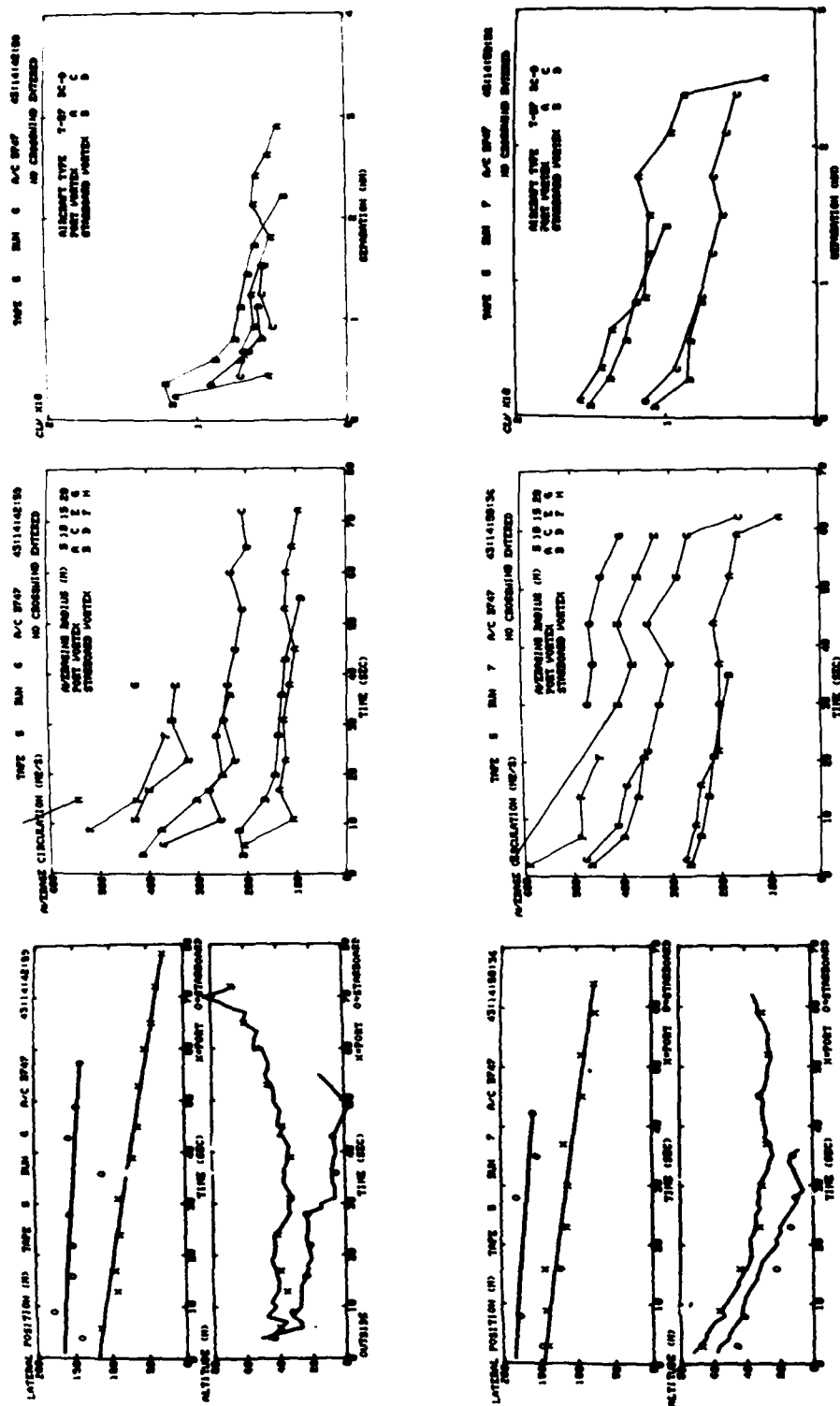


FIGURE 61. VORTEX TRAJECTORIES, AVERAGE CIRCULATION, AND VORTEX-INDUCED ROLLING MOMENT COEFFICIENT FOR THE RUNS ON 2/12/79 (Continued)

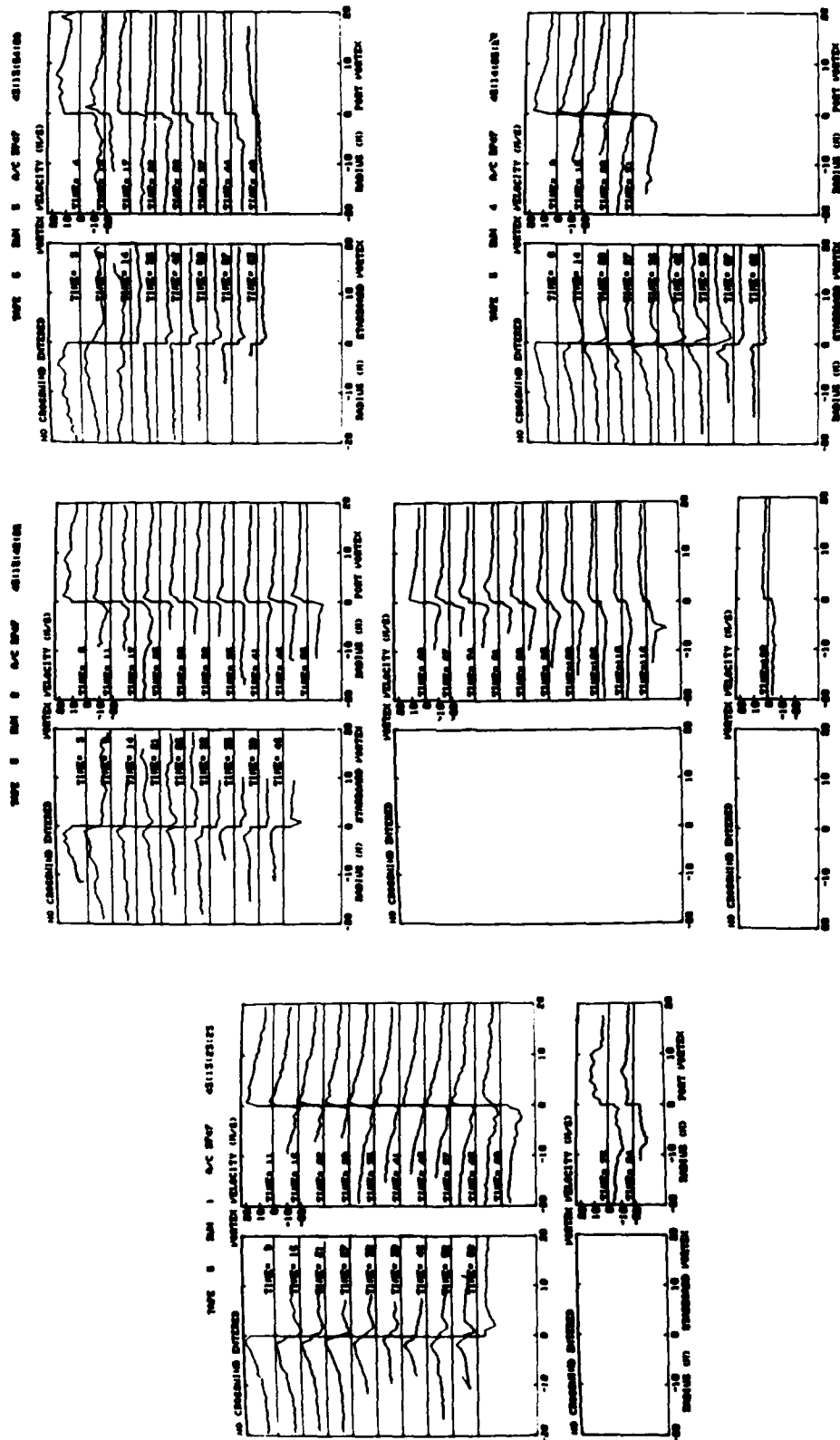


FIGURE 62. VELOCITY AND CIRCULATION PROFILES FOR THE RUNS ON 2/12/79

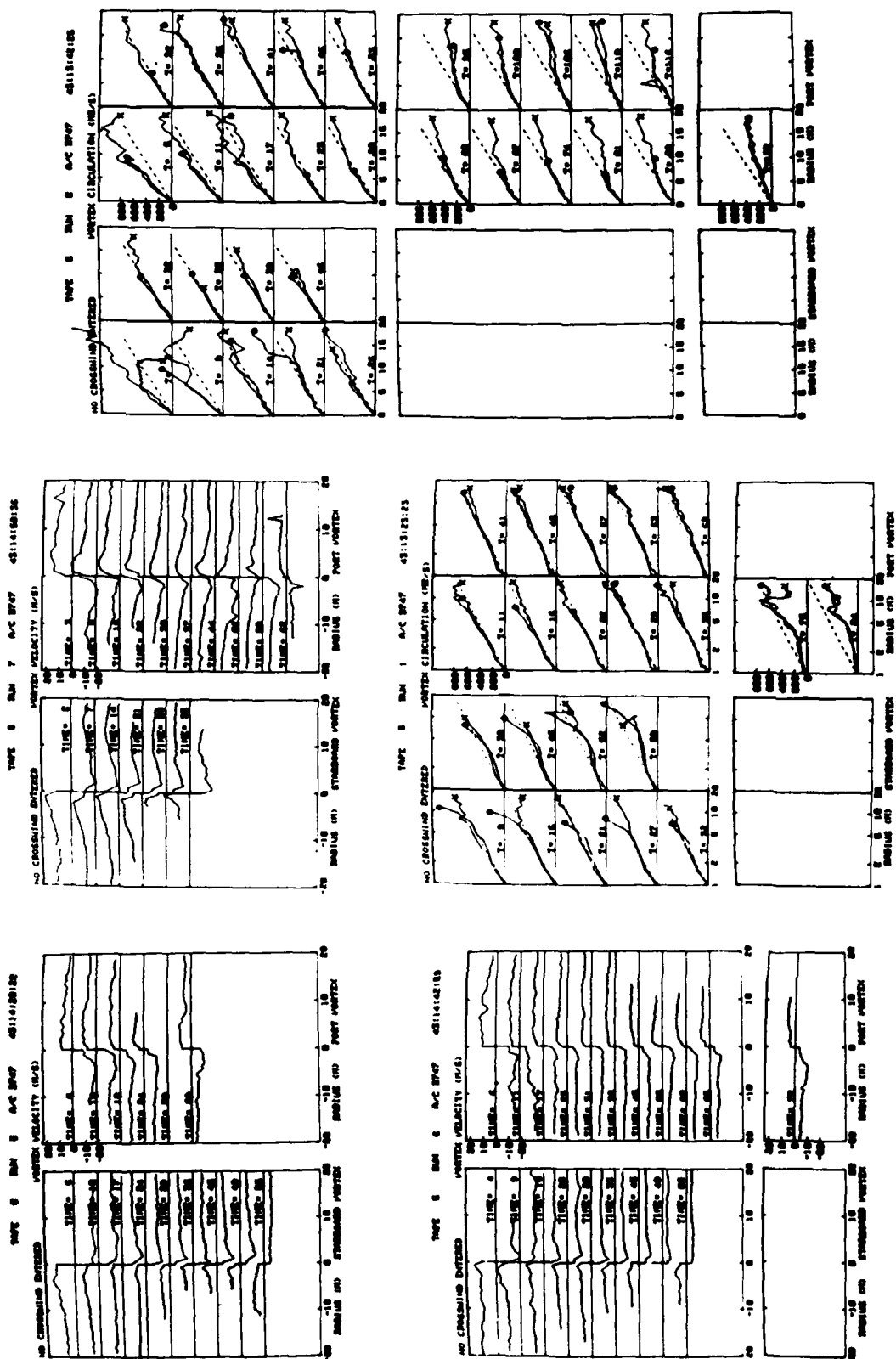


FIGURE 62. VELOCITY AND CIRCULATION PROFILES FOR THE RUNS ON 2/12/79 (Continued)





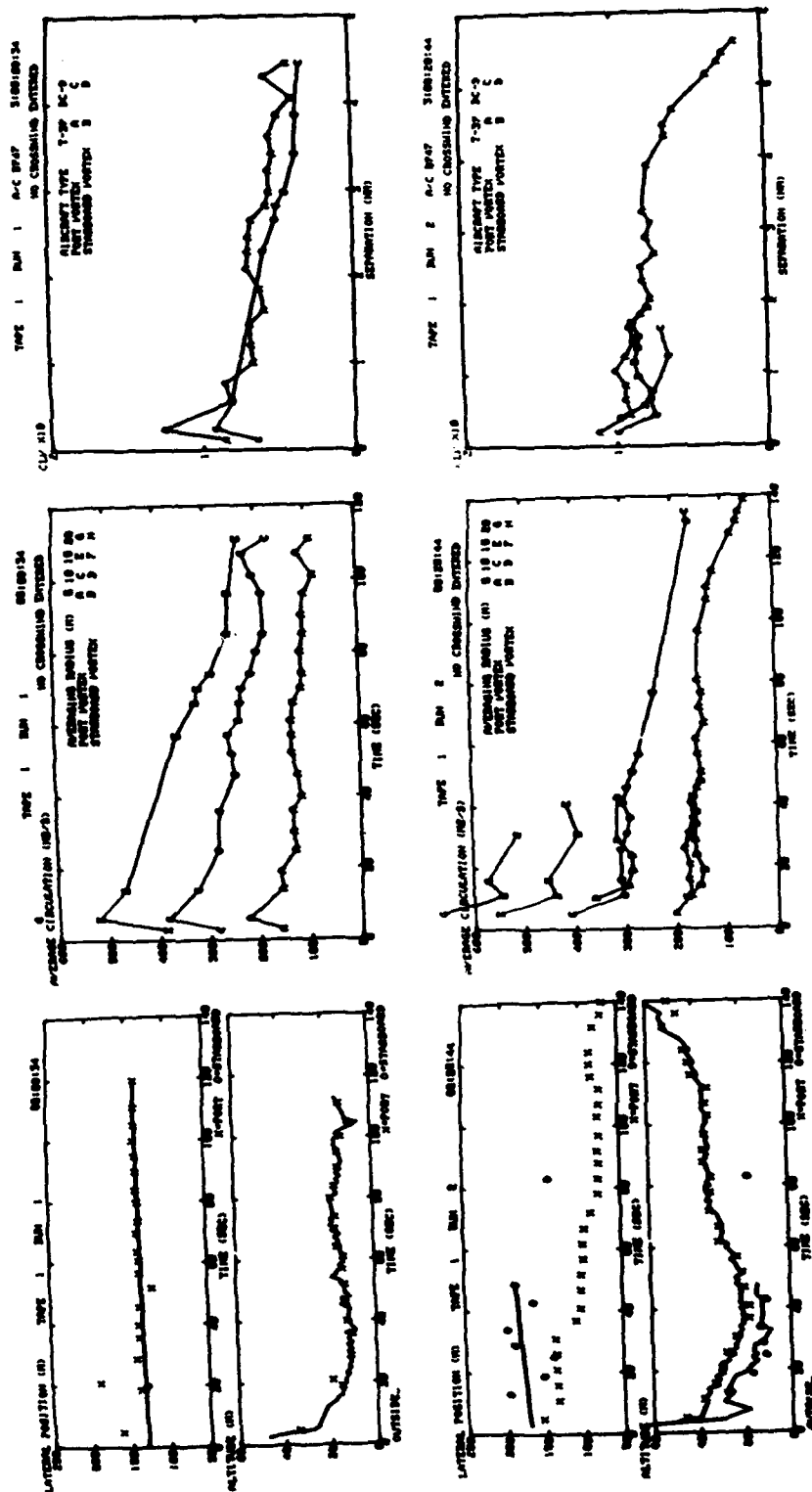


FIGURE 63. VORTEX TRAJECTORIES, AVERAGE CIRCULATION AND VORTEX-INDUCED ROLLING MOMENT COEFFICIENT FOR THE RUNS ON 11/3/79

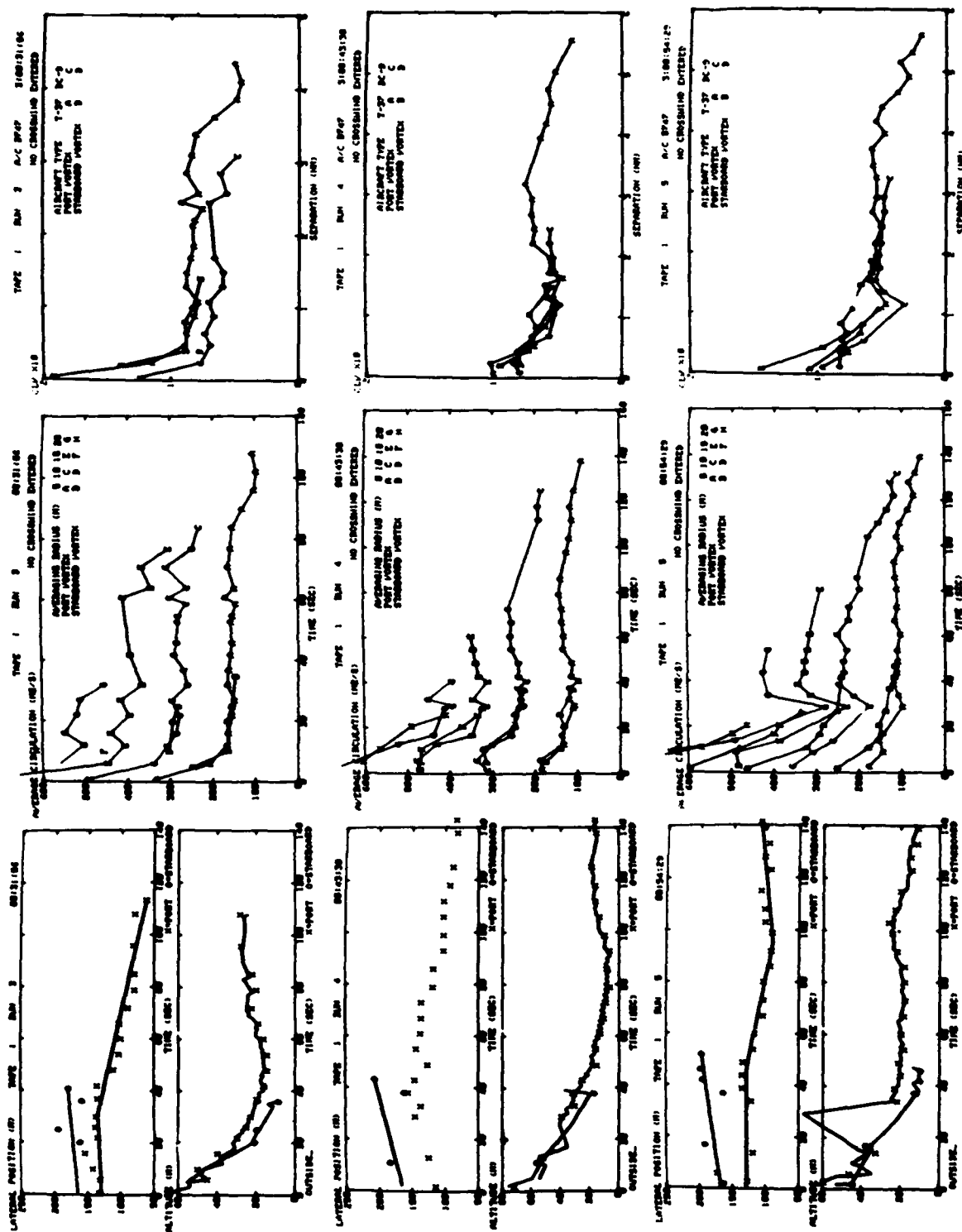


FIGURE 63. VORTEX TRAJECTORIES, AVERAGE CIRCULATION AND VORTEX-INDUCED ROLLING MOMENT COEFFICIENT FOR THE RUNS ON 11/3/79 (Continued)

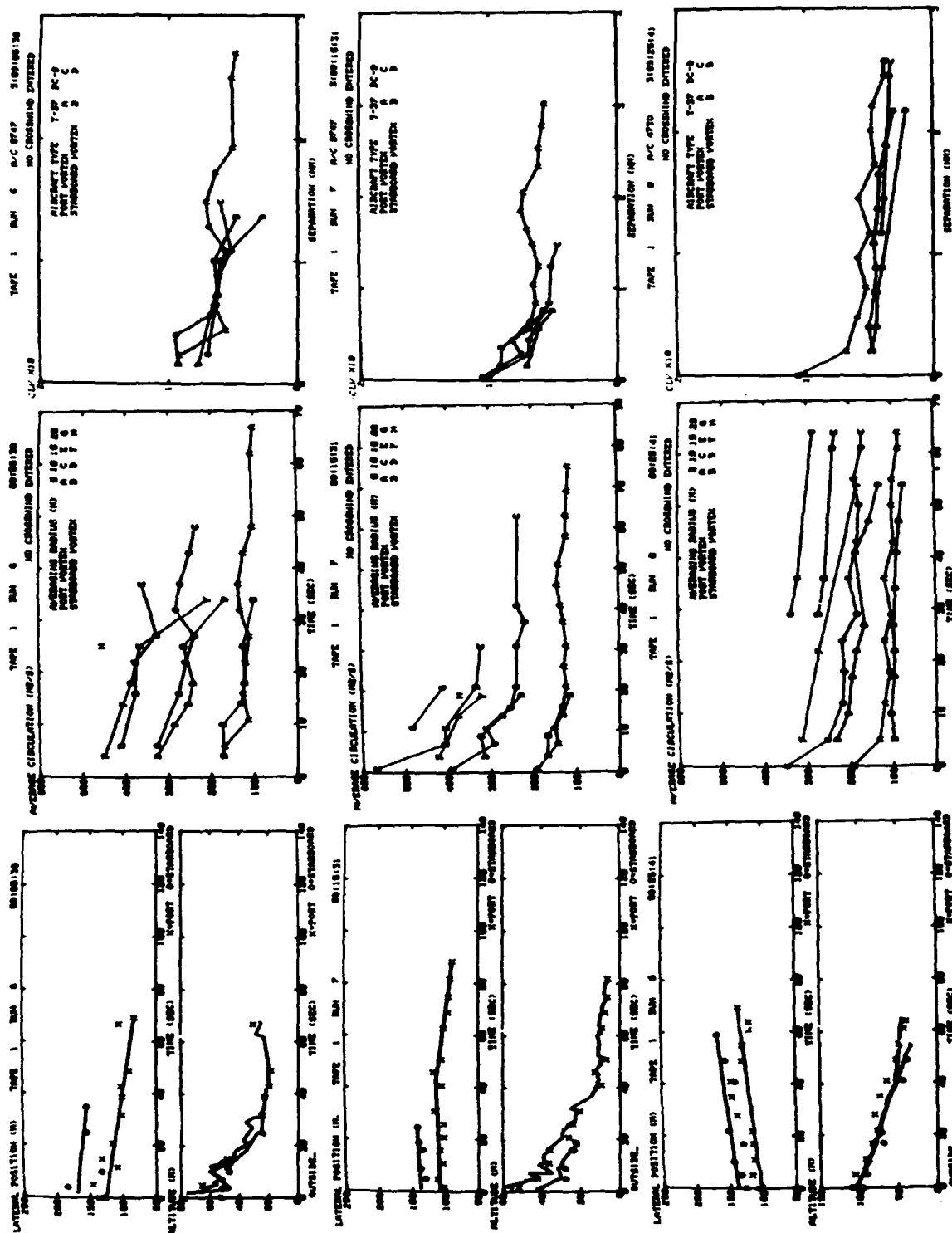


FIGURE 63. VORTEX TRAJECTORIES, AVERAGE CIRCULATION AND VORTEX-INDUCED ROLLING MOMENT COEFFICIENT FOR THE RUNS ON 11/3/79 (Continued)

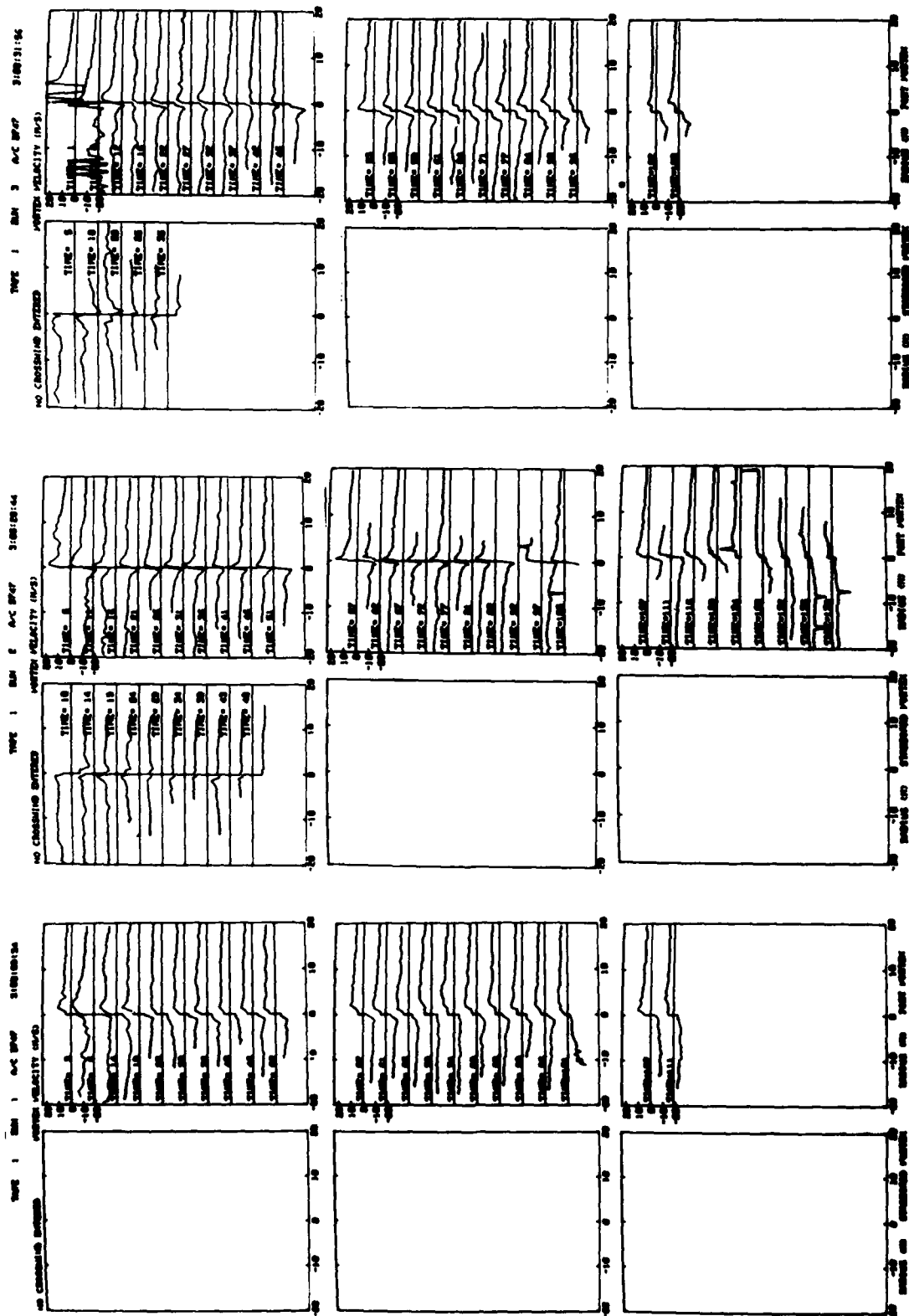


FIGURE 64. VELOCITY AND CIRCULATION PROFILES FOR THE RUNS ON 11/3/79

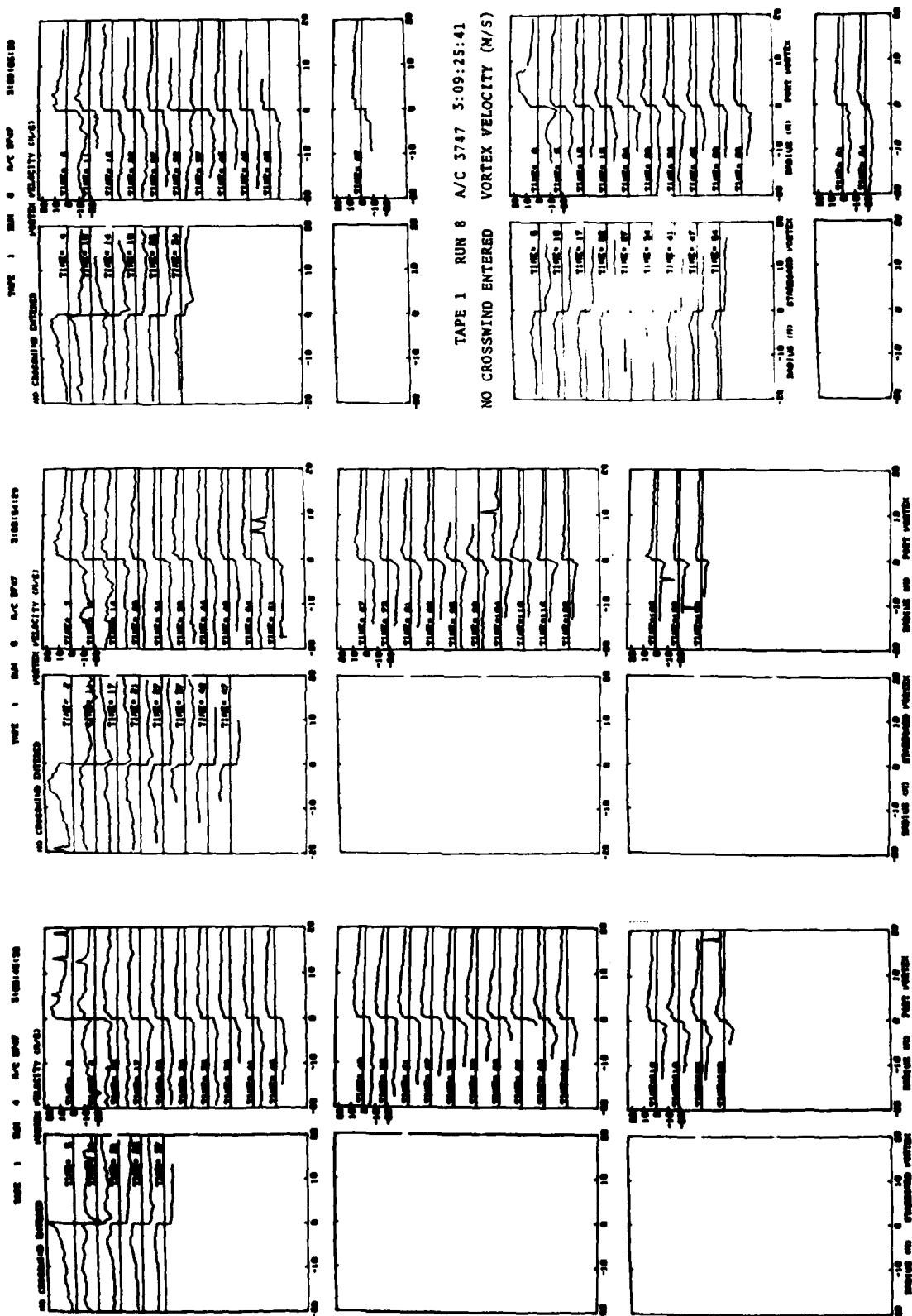


FIGURE 64. VELOCITY AND CIRCULATION PROFILES FOR THE RUNS ON 11/3/79 (Continued)

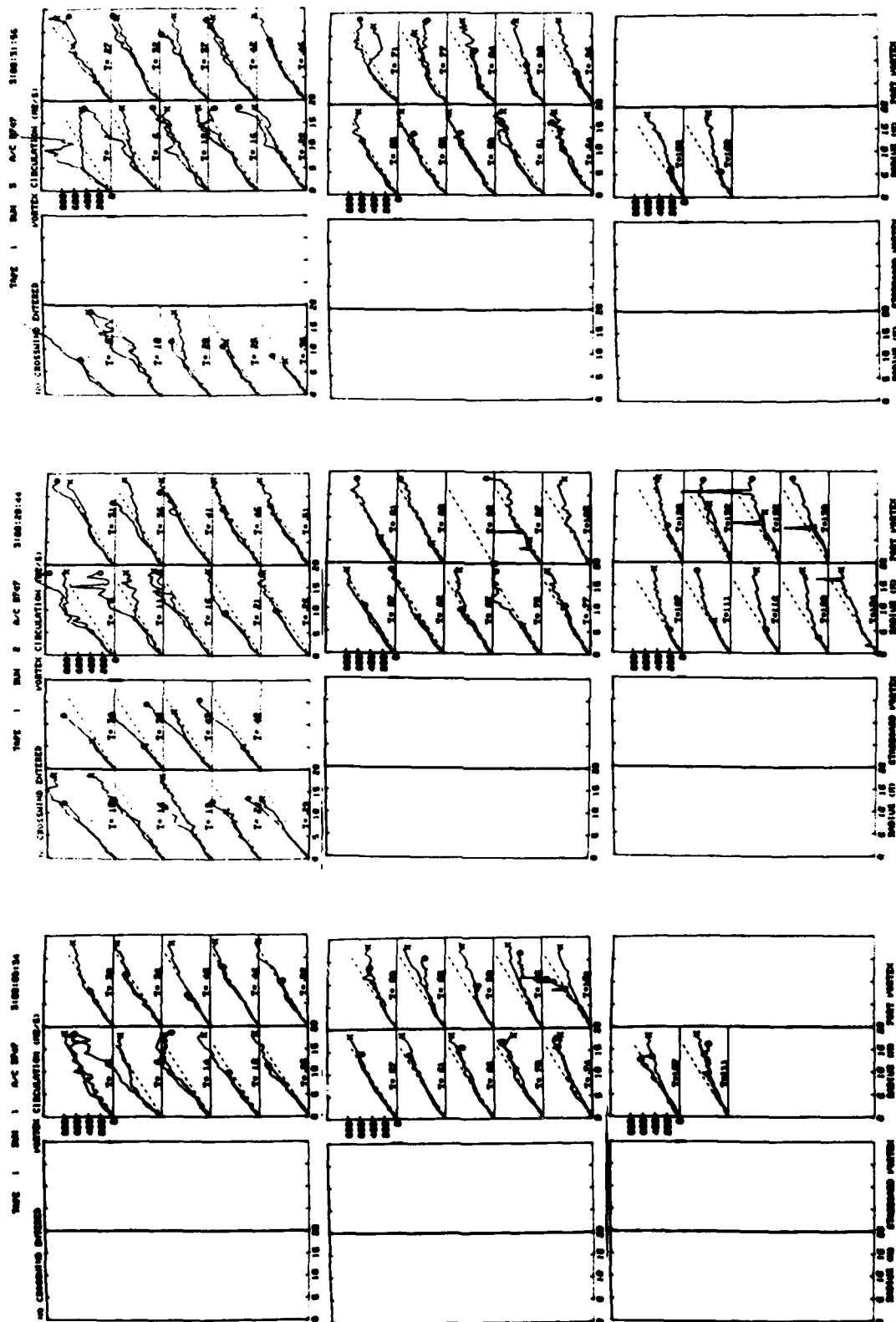


FIGURE 64. VELOCITY AND CIRCULATION PROFILES FOR THE RUNS ON 11/3/79 (Continued)

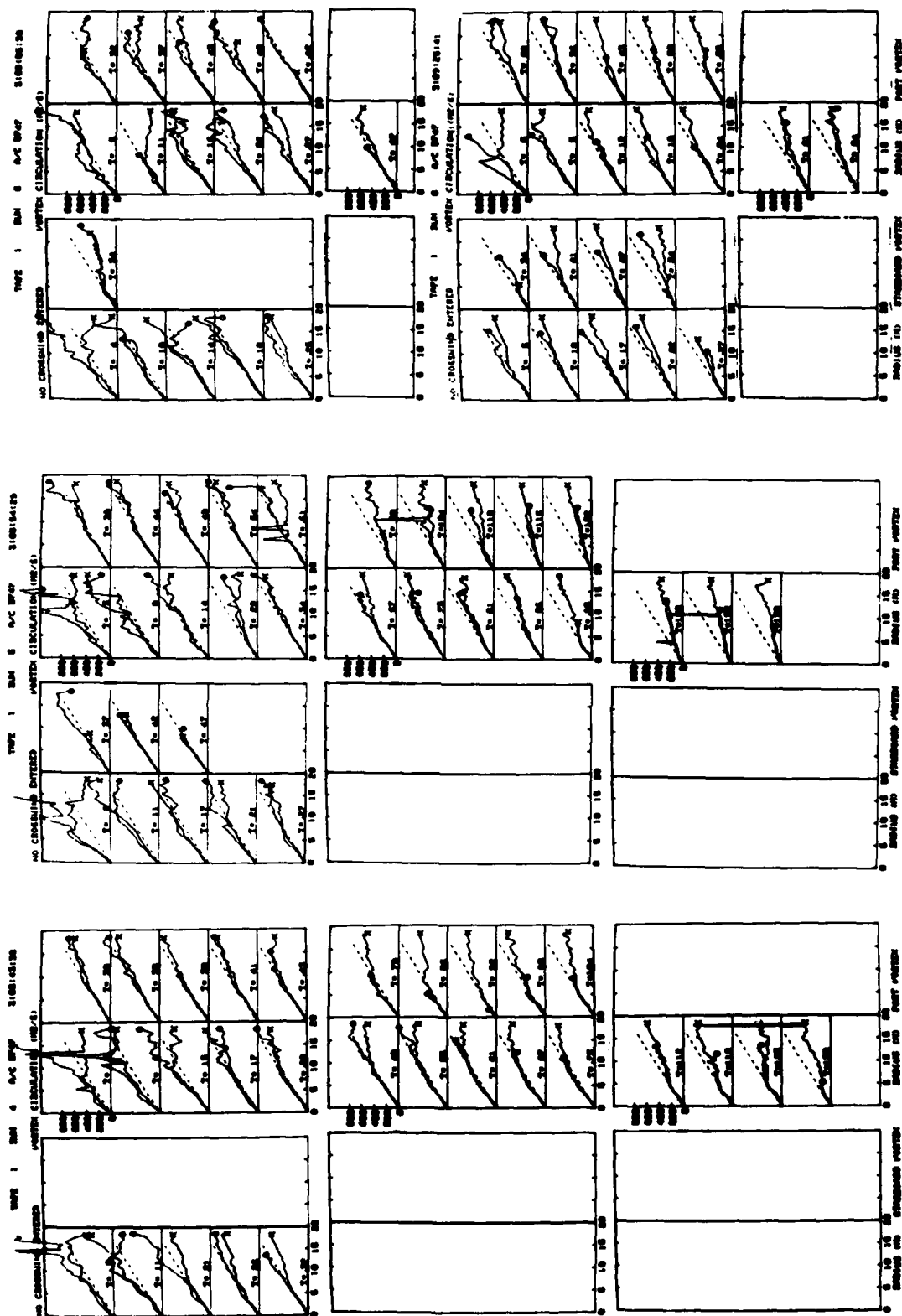


FIGURE 64. VELOCITY AND CIRCULATION PROFILES FOR THE RUNS ON 11/3/79 (Continued)



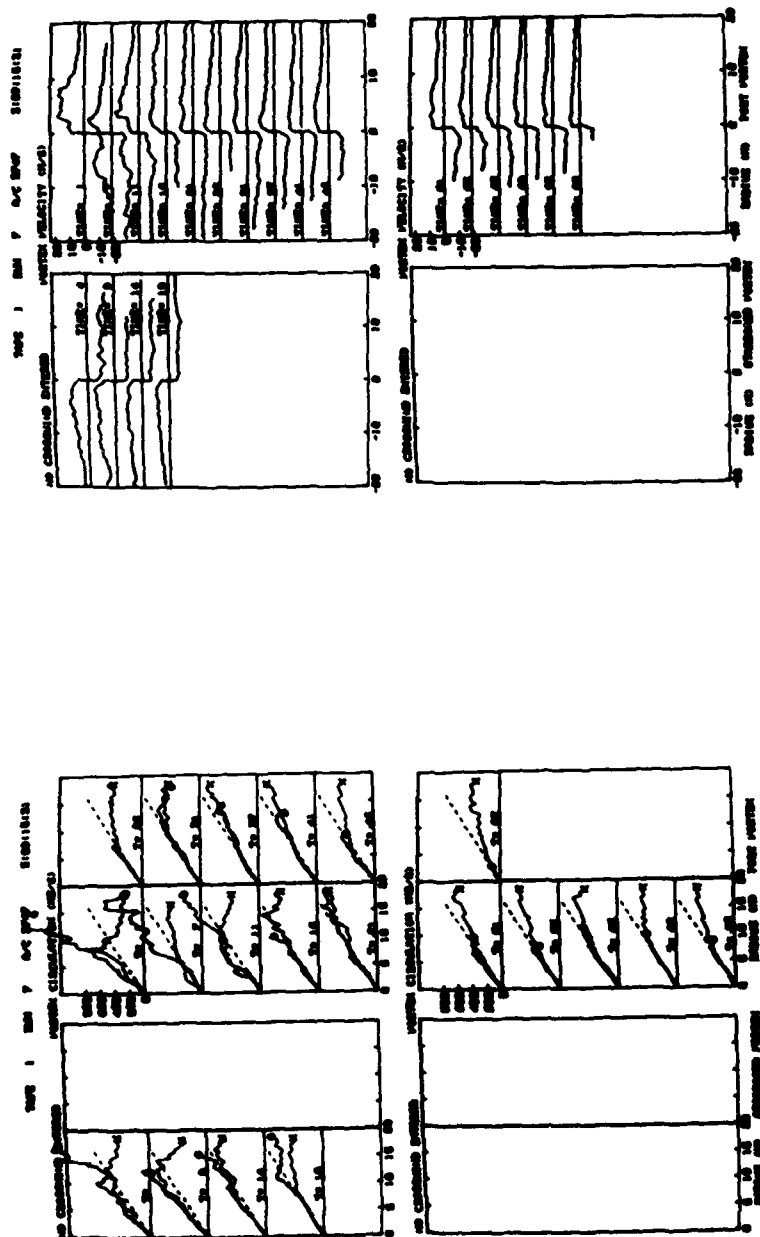


FIGURE 64. VELOCITY AND CIRCULATION PROFILES FOR THE RUNS ON 11/3/79 (Continued)

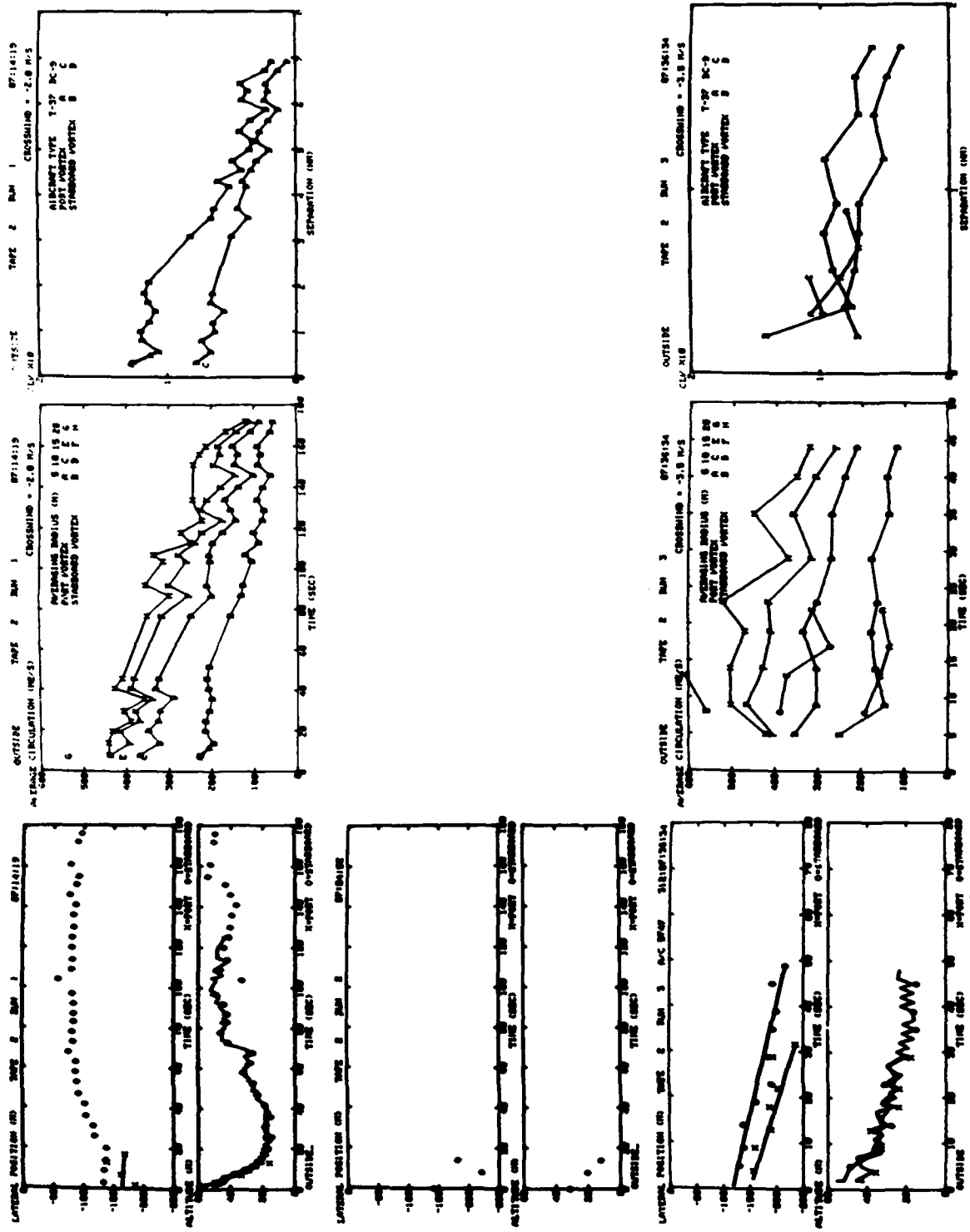


FIGURE 65. VORTEX TRAJECTORIES, AVERAGE CIRCULATION AND VORTEX-INDUCED ROLLING MOMENT COEFFICIENT FOR THE RUNS ON 11/8/79

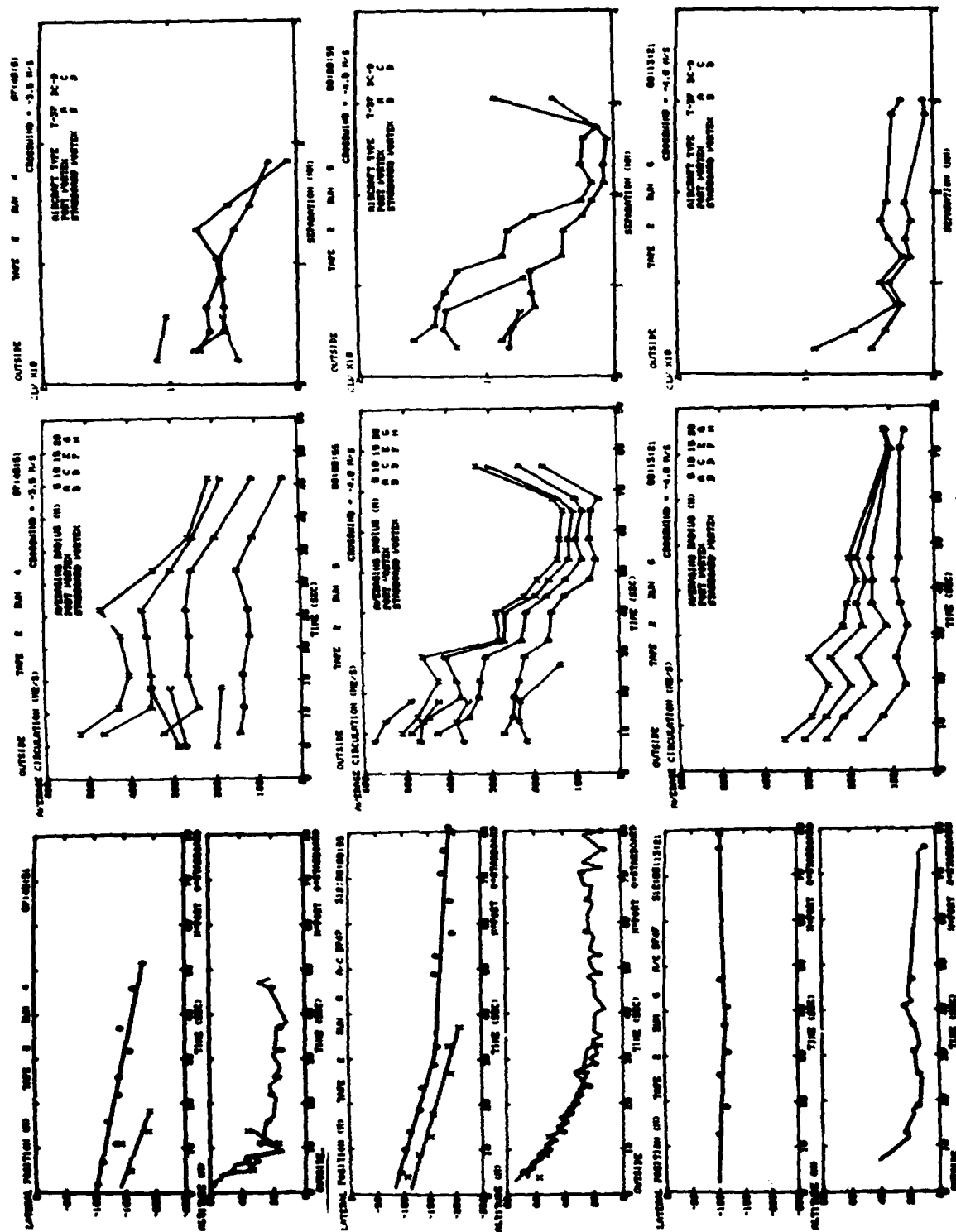


FIGURE 65. VORTEX TRAJECTORIES, AVERAGE CIRCULATION AND VORTEX-INDUCED ROLLING MOMENT COEFFICIENT FOR THE RUNS ON 11/8/79 (Continued)

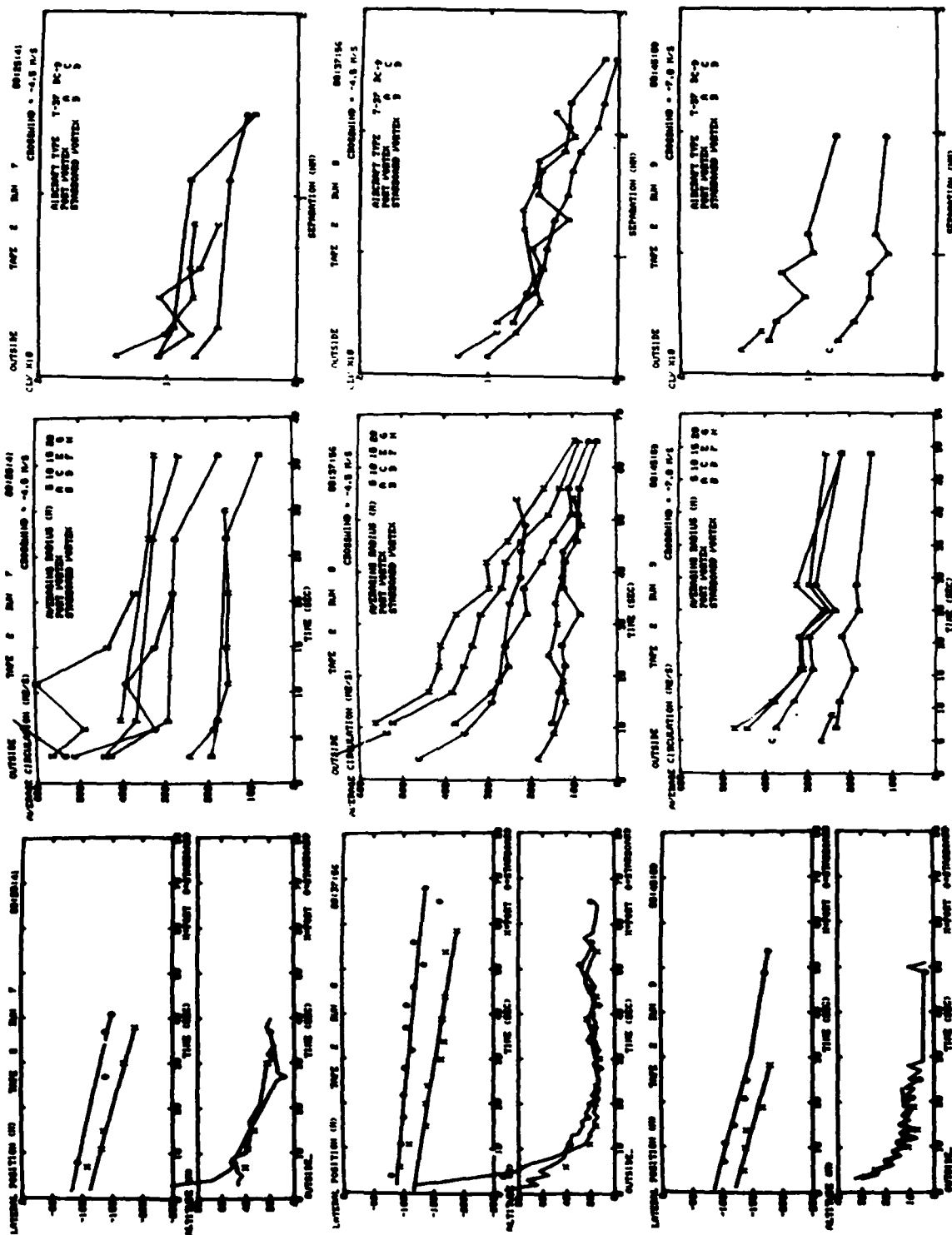


FIGURE 65. VORTEX TRAJECTORIES, AVERAGE CIRCULATION AND VORTEX-INDUCED ROLLING MOMENT COEFFICIENT FOR THE RUNS ON 11/8/79 (Continued)

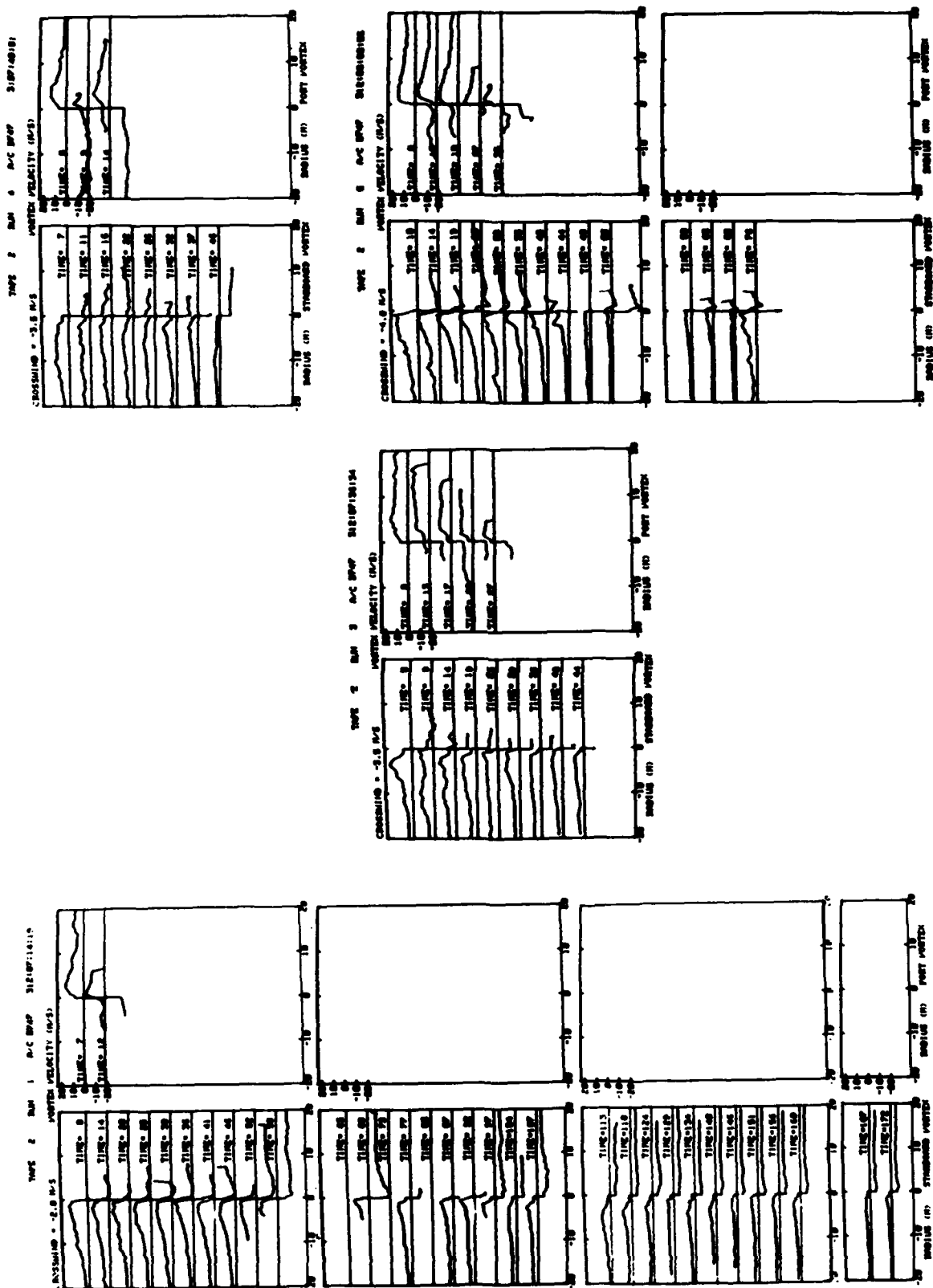


FIGURE 66. VELOCITY AND CIRCULATION PROFILES FOR THE RUNS ON 11/8/79

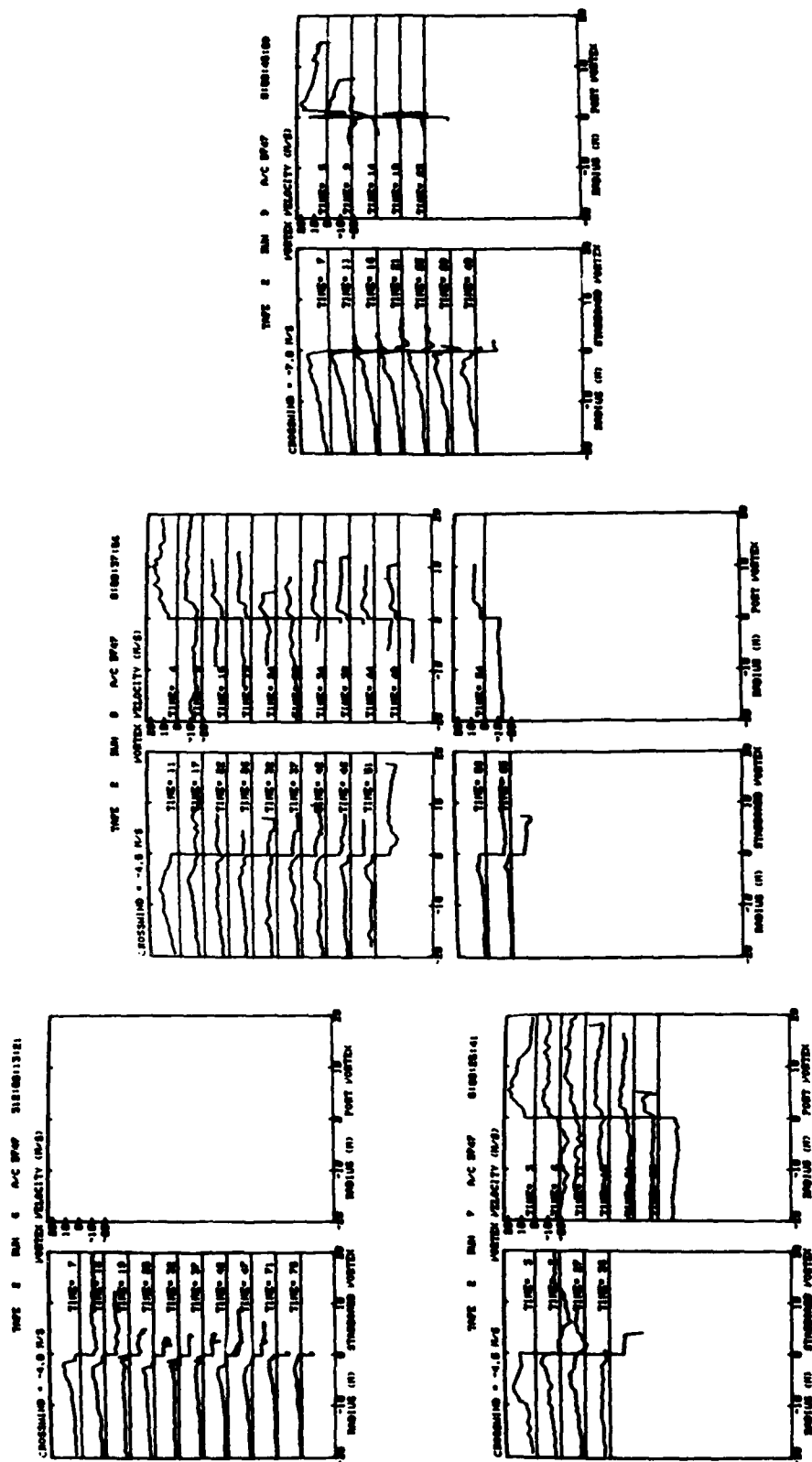


FIGURE 66. VELOCITY AND CIRCULATION PROFILES FOR THE RUNS ON 11/8/79 (Continued)

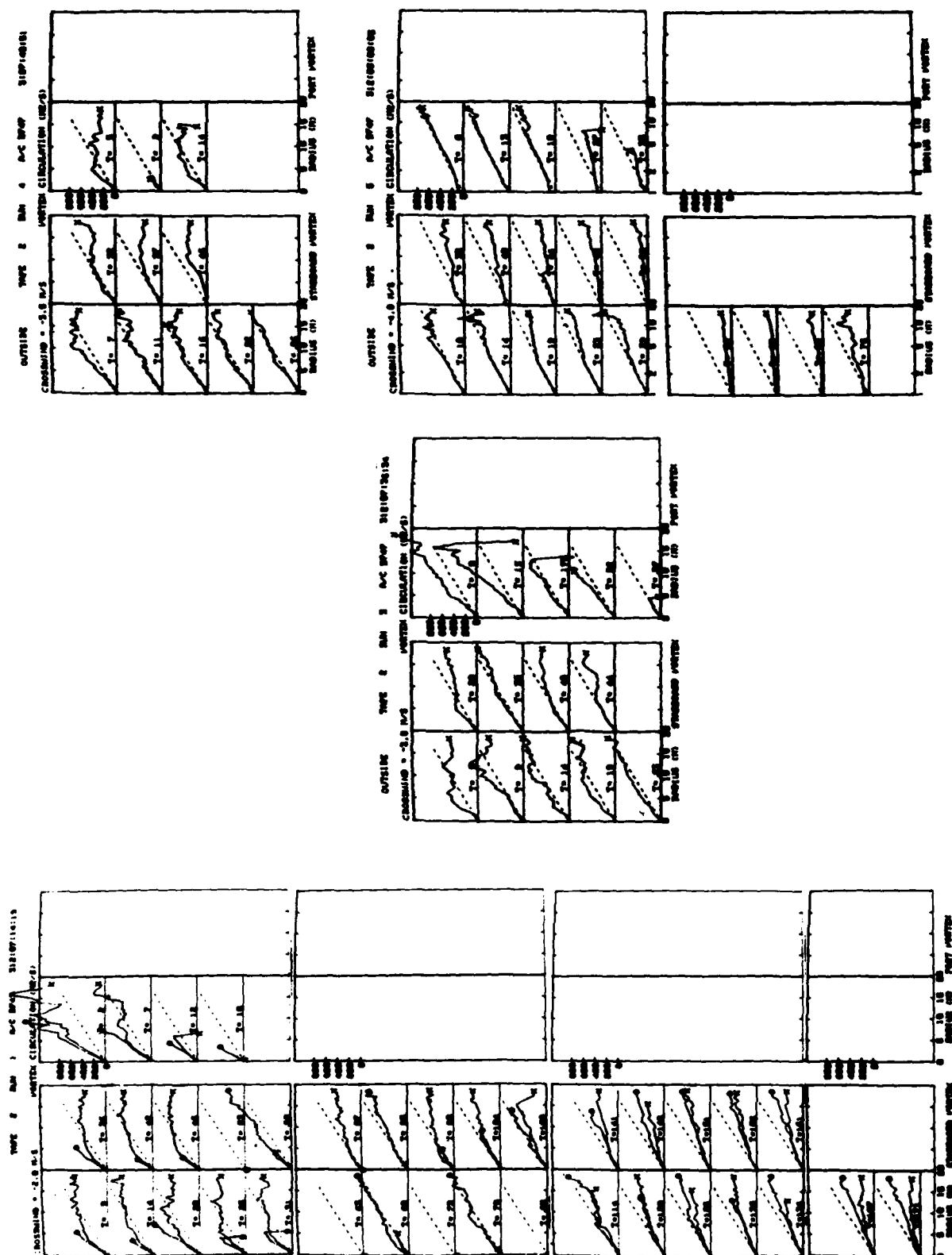


FIGURE 66. VELOCITY AND CIRCULATION PROFILES FOR THE RUNS ON 11/8/79 (Continued)





APPENDIX F  
LATERAL POSITION PLOTS

This appendix contains lateral position plots (like Figure 24 for Run 3, 11/3/79) for the runs in the second test series. Figures 67-72 show Runs 1-2 and 4-7 on 11/3/79. Figures 73-80 show Runs 1 and 3-9 on 11/8/79.

Run 1 11/3/79

VORTEX	GWSS		PHOTO
	B-747	F-86	B-747
PORT	⊙	×	●
STARBOARD	◻	+	◼
AIRCRAFT			↓

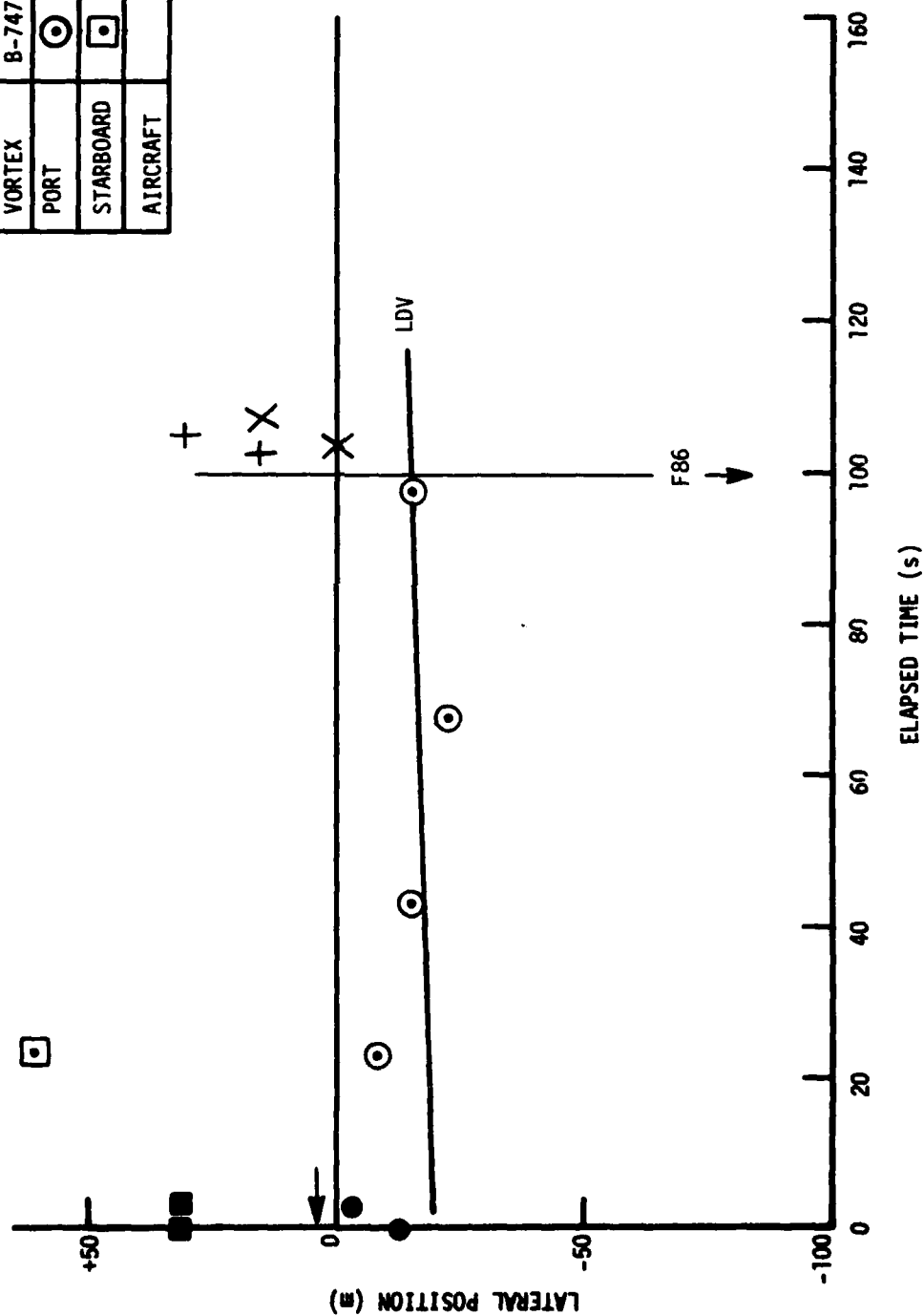


FIGURE 67. VORTEX TRAJECTORIES FOR RUN 1, 11/3/79

Run 2 11/3/79

VORTEX	GWSS		PHOTO
	B-747	F-86	
PORT	⊙	×	●
STARBOARD	◻	+	■
AIRCRAFT			→

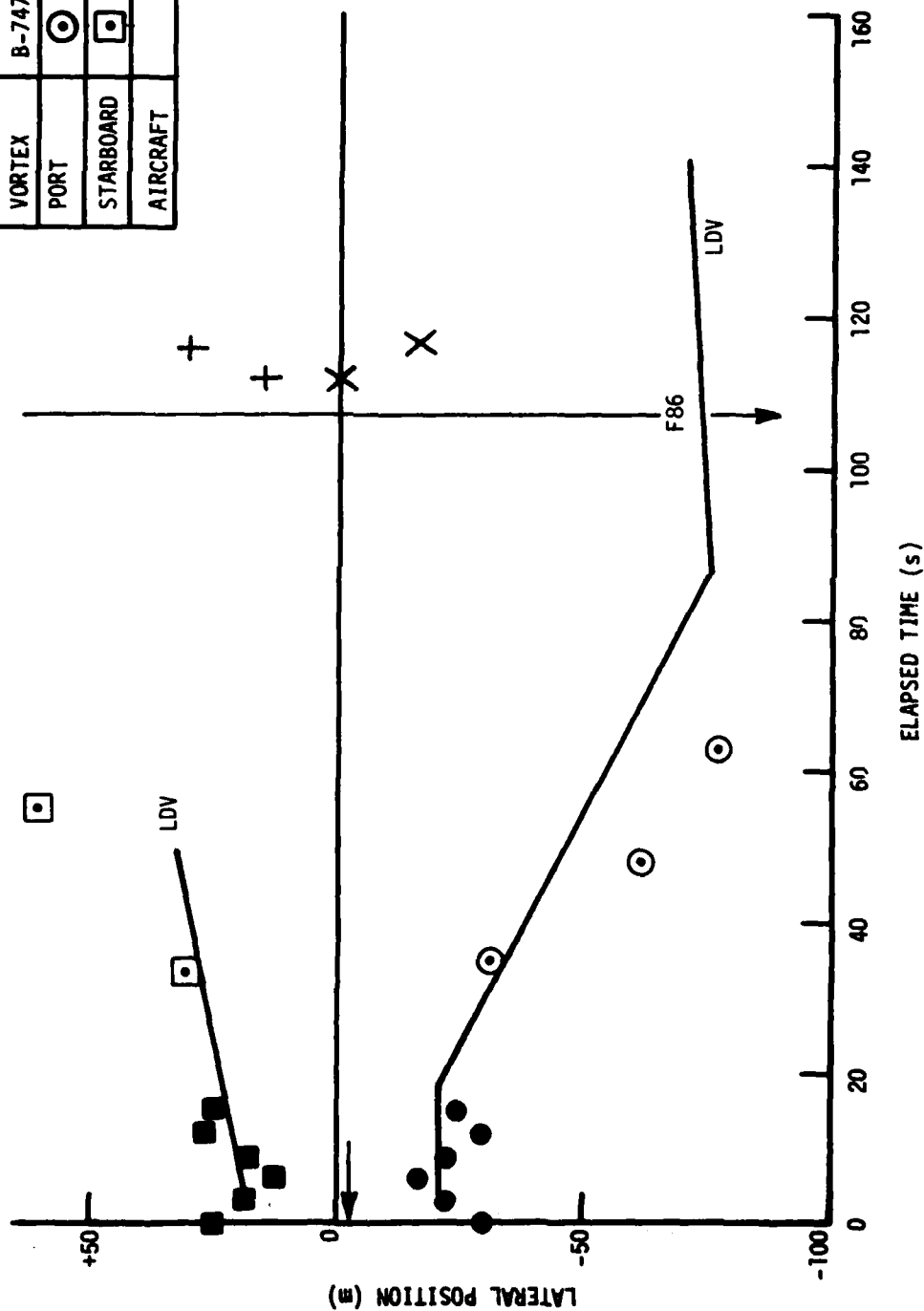


FIGURE 68. VORTEX TRAJECTORIES FOR RUN 2, 11/3/79

GWSS		PHOTO
VORTEX	B-747	F-86
PORT	⊙	×
STARBOARD	⊠	●
AIRCRAFT		→

Run 4 11/3/79

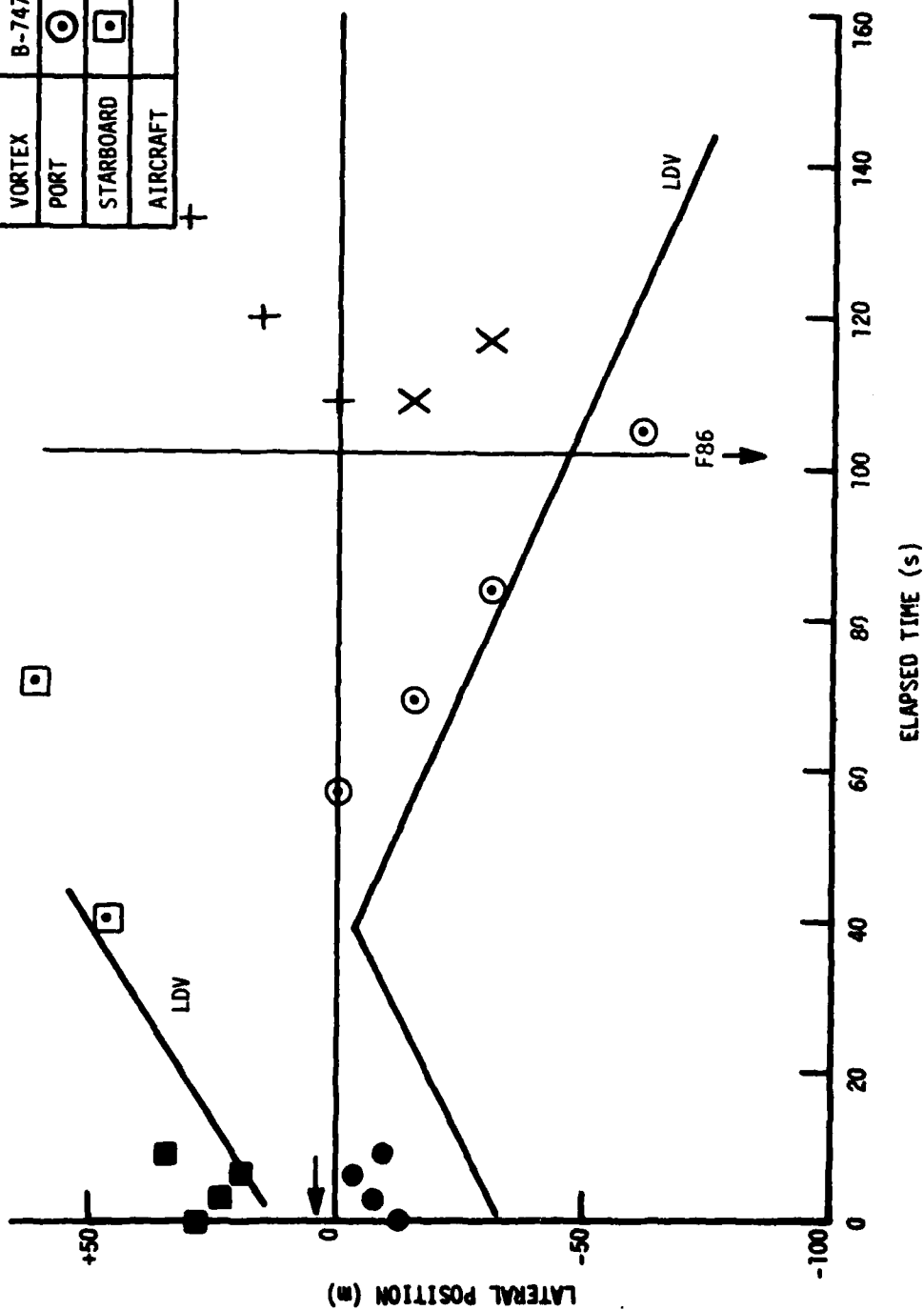


FIGURE 69. VORTEX TRAJECTORIES FOR RUN 4, 11/3/79

GWSS		PHOTO
VORTEX	B-747	B-747
PORT	⊙	●
STARBOARD	⊠	■

Run 5 11/3/79

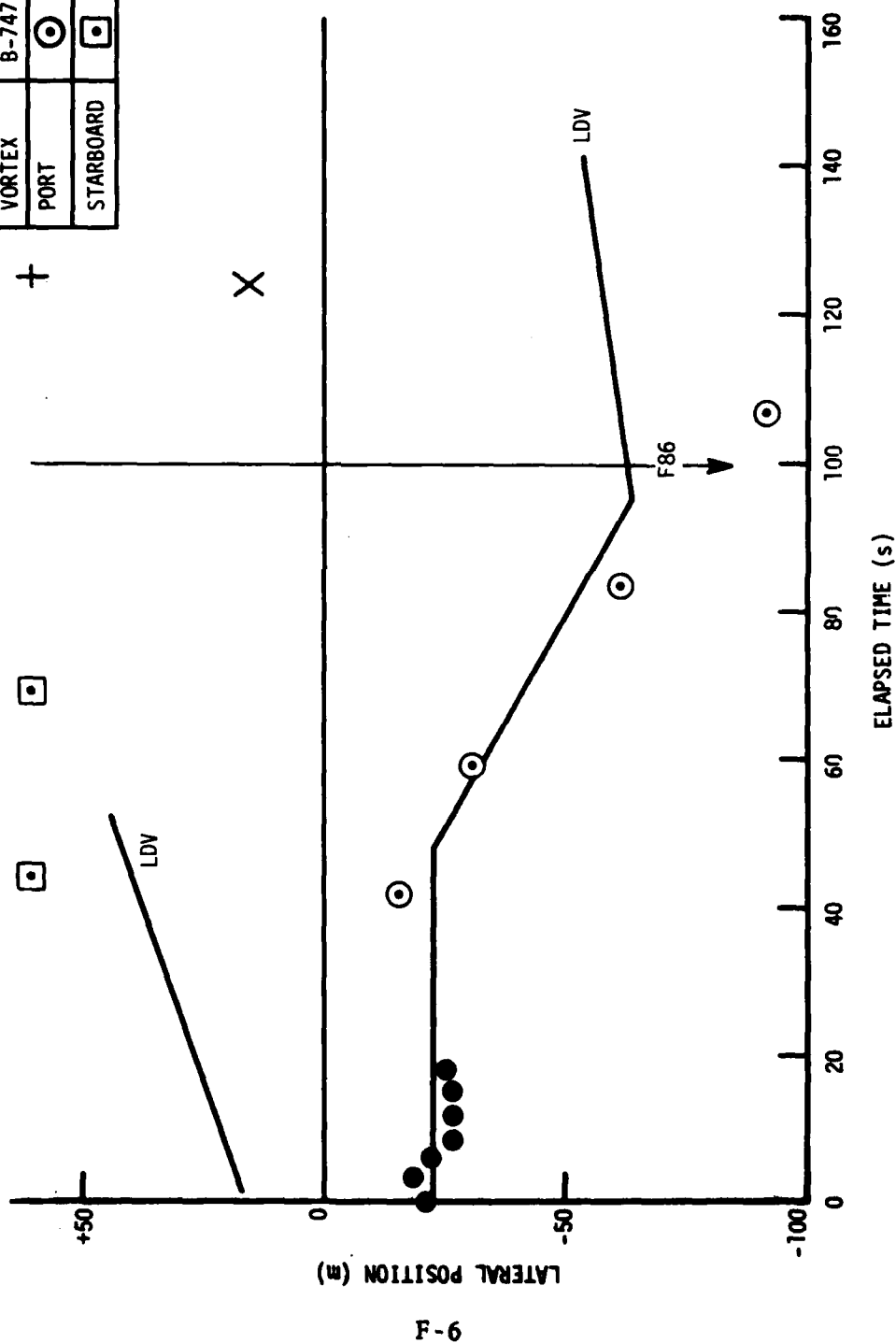


FIGURE 70. VORTEX TRAJECTORIES FOR RUN 5, 11/3/79

Run 6 11/3/79

VORTEX	GWSS		PHOTO
	B-747	F-86	
PORT	⊙	×	●
STARBOARD	◻	+	◼
AIRCRAFT			↓

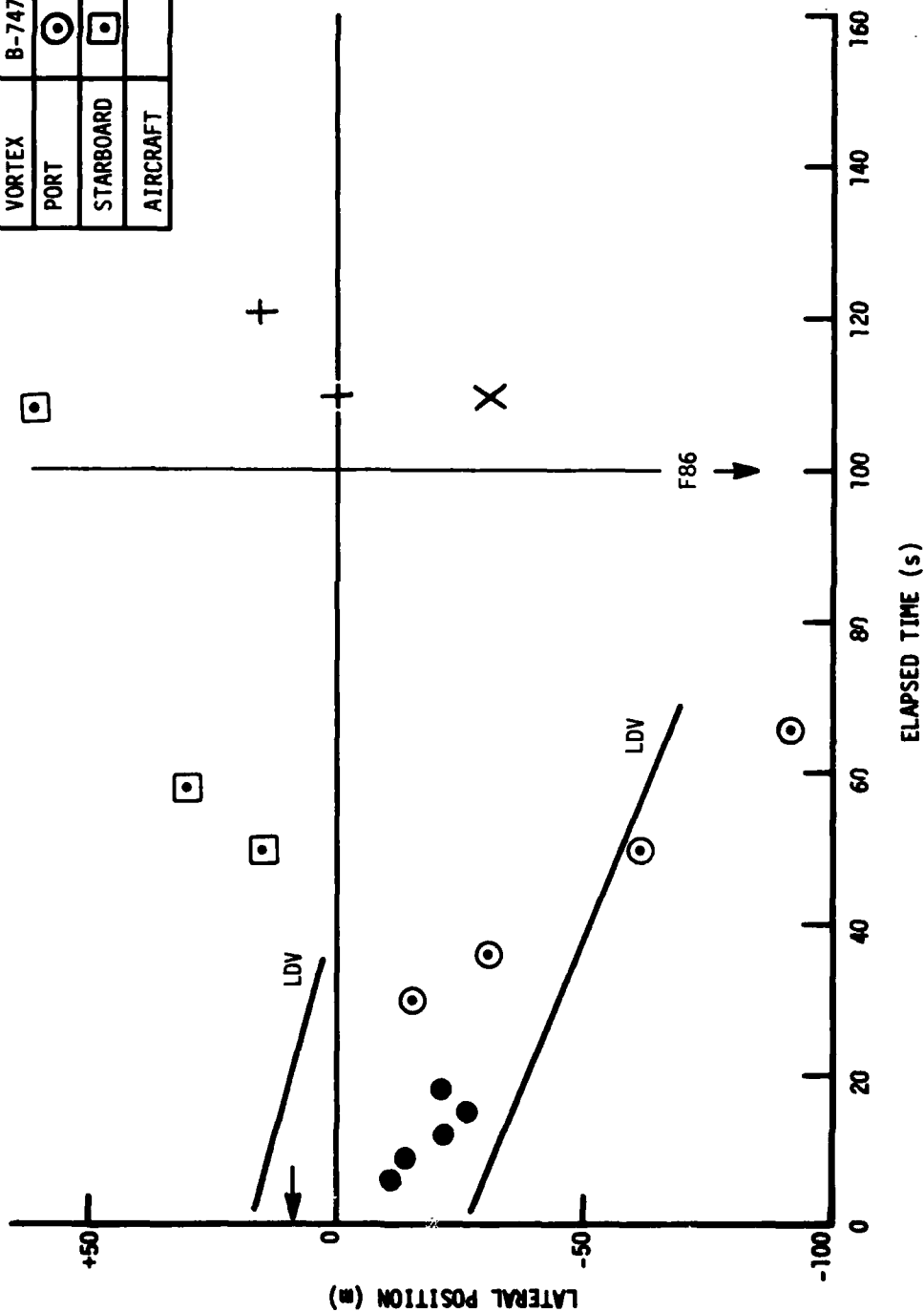
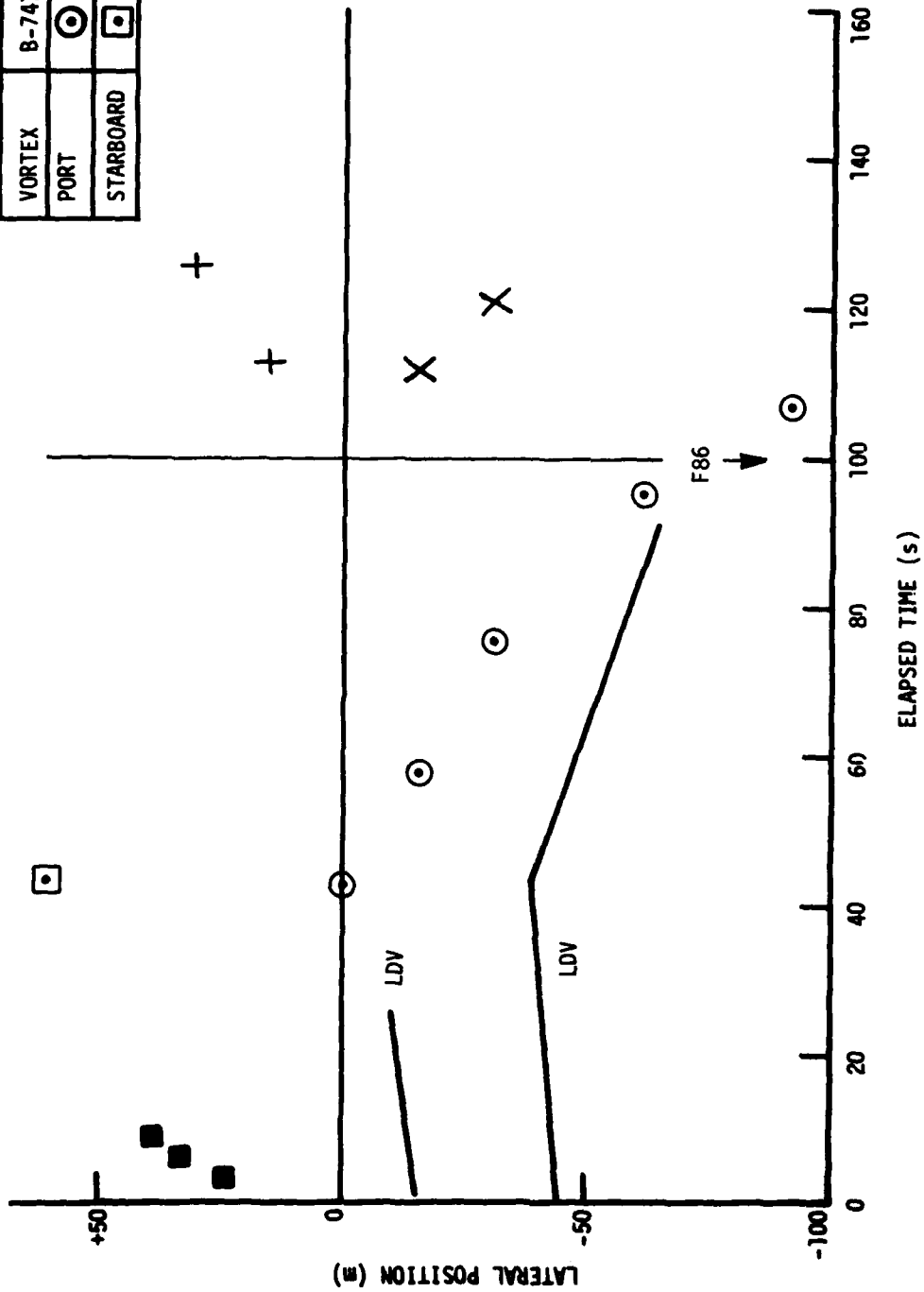


FIGURE 71. VORTEX TRAJECTORIES FOR RUN 6, 11/3/79

Run 7 11/3/79

GWSS		PHOTO
VORTEX	B-747	F-86
PORT	⊙	×
STARBOARD	⊠	+



F-8

FIGURE 72. VORTEX TRAJECTORIES FOR RUN 7, 11/3/79

Run 1 11/8/79

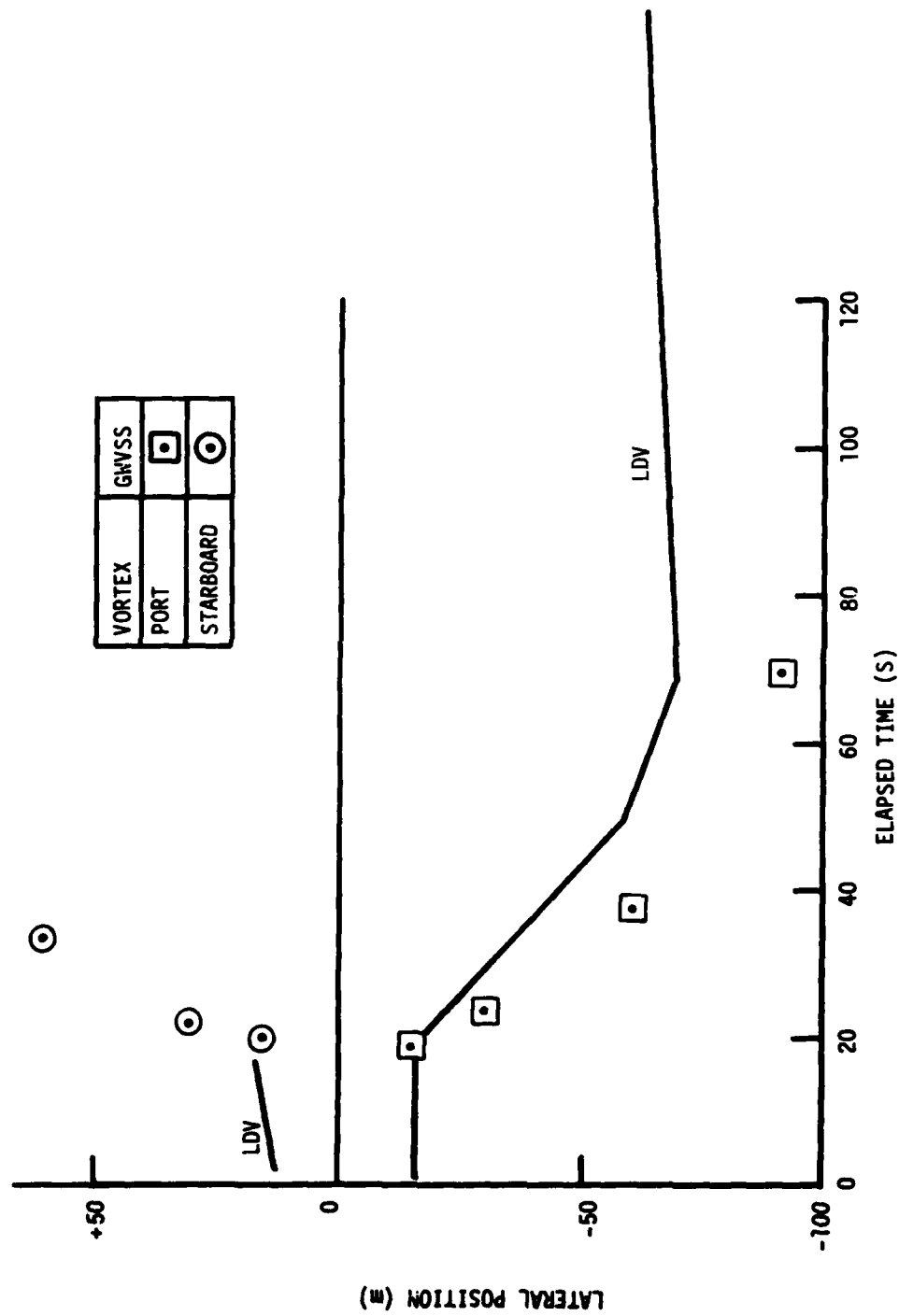


FIGURE 73. VORTEX TRAJECTORIES FOR RUN 1, 11/8/79



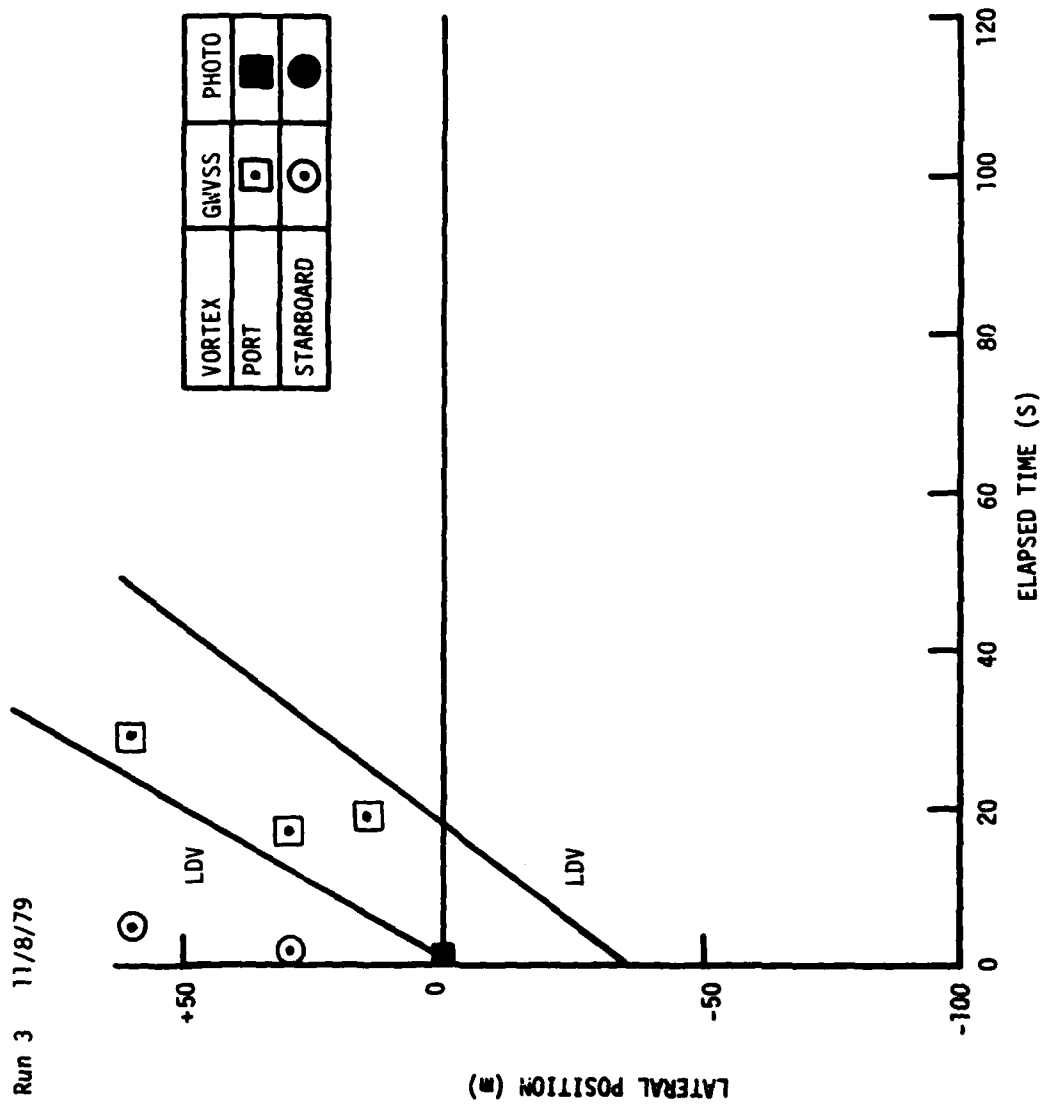


FIGURE 74. VORTEX TRAJECTORIES FOR RUN 3, 11/8/79

Run 4 11/8/79

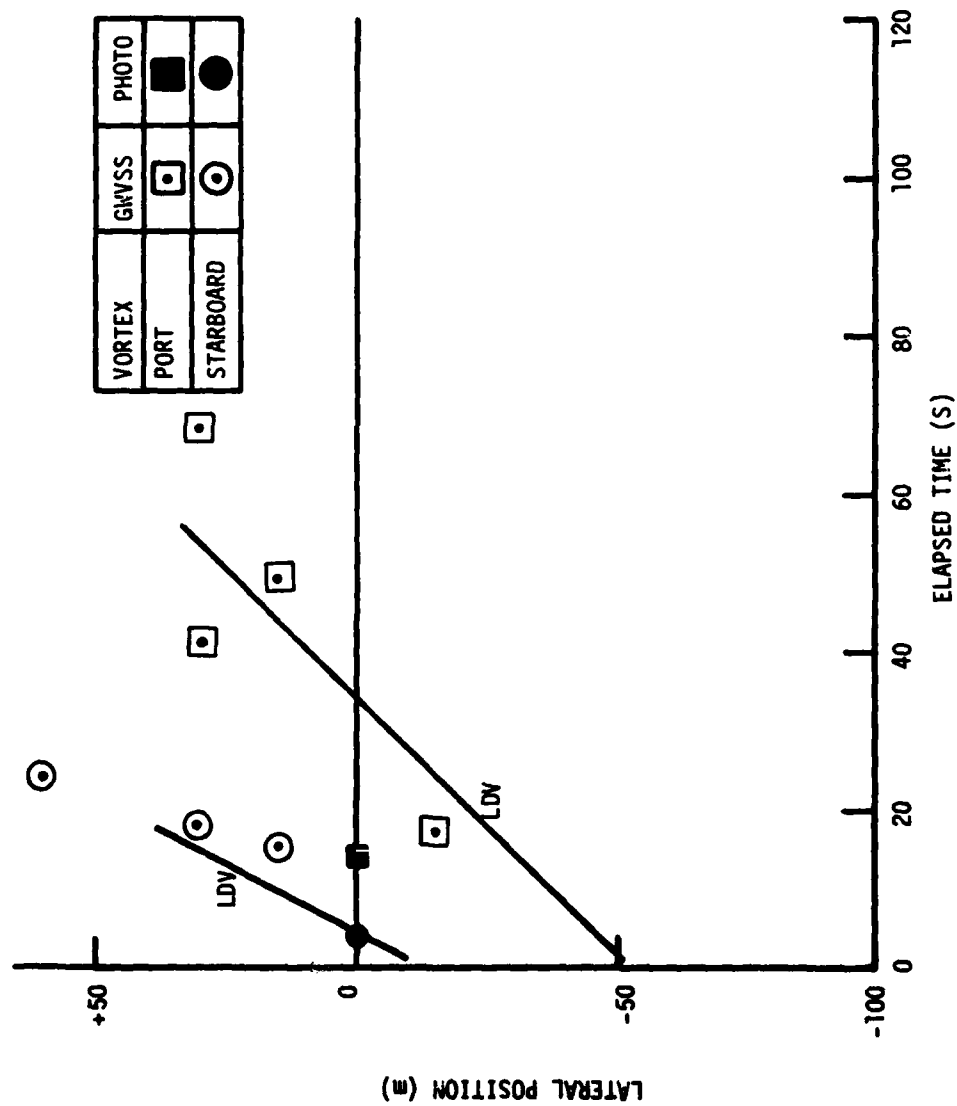


FIGURE 75. VORTEX TRAJECTORIES FOR RUN 4, 11/8/79

Run 5 11/8/79

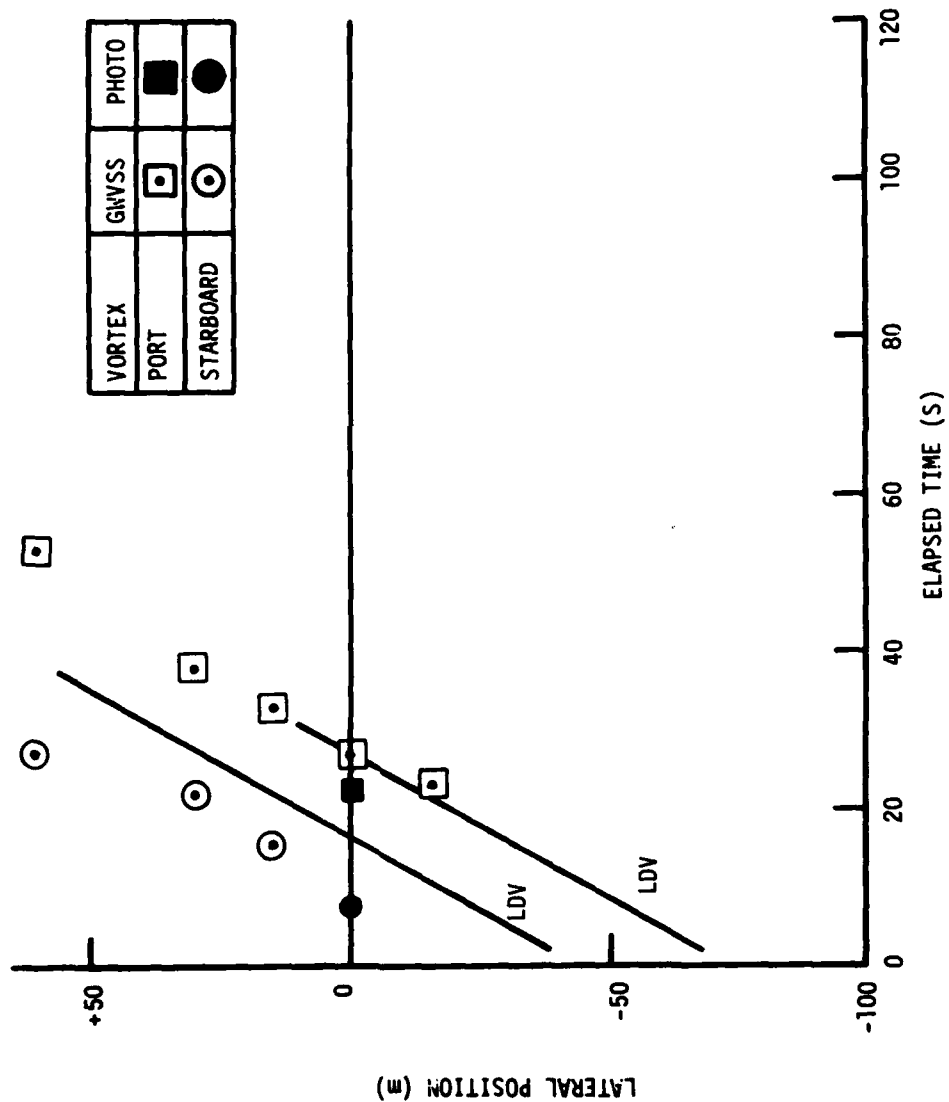


FIGURE 76. VORTEX TRAJECTORIES FOR RUN 5, 11/8/79

Run 6 11/8/79

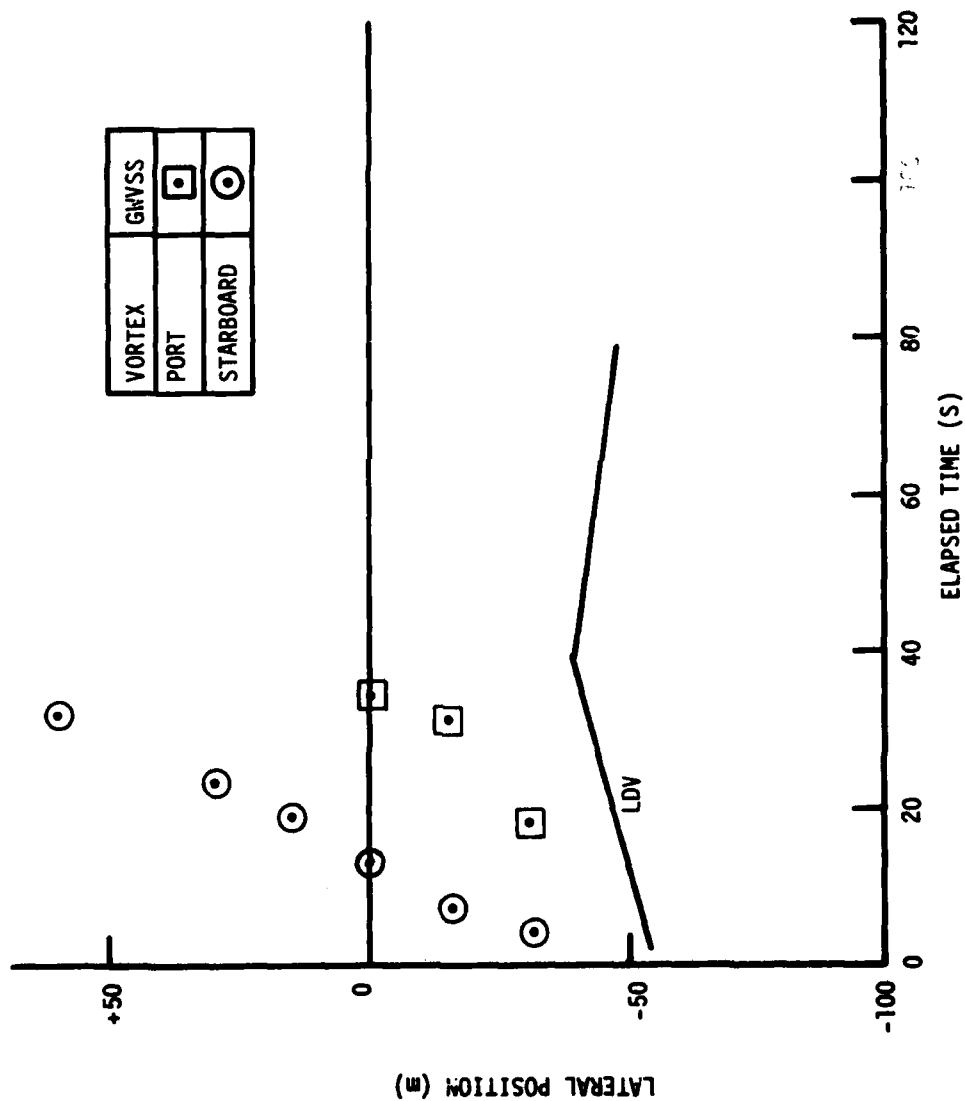


FIGURE 77. VORTEX TRAJECTORIES FOR RUN 6, 11/8/79

Run 7 11/8/79

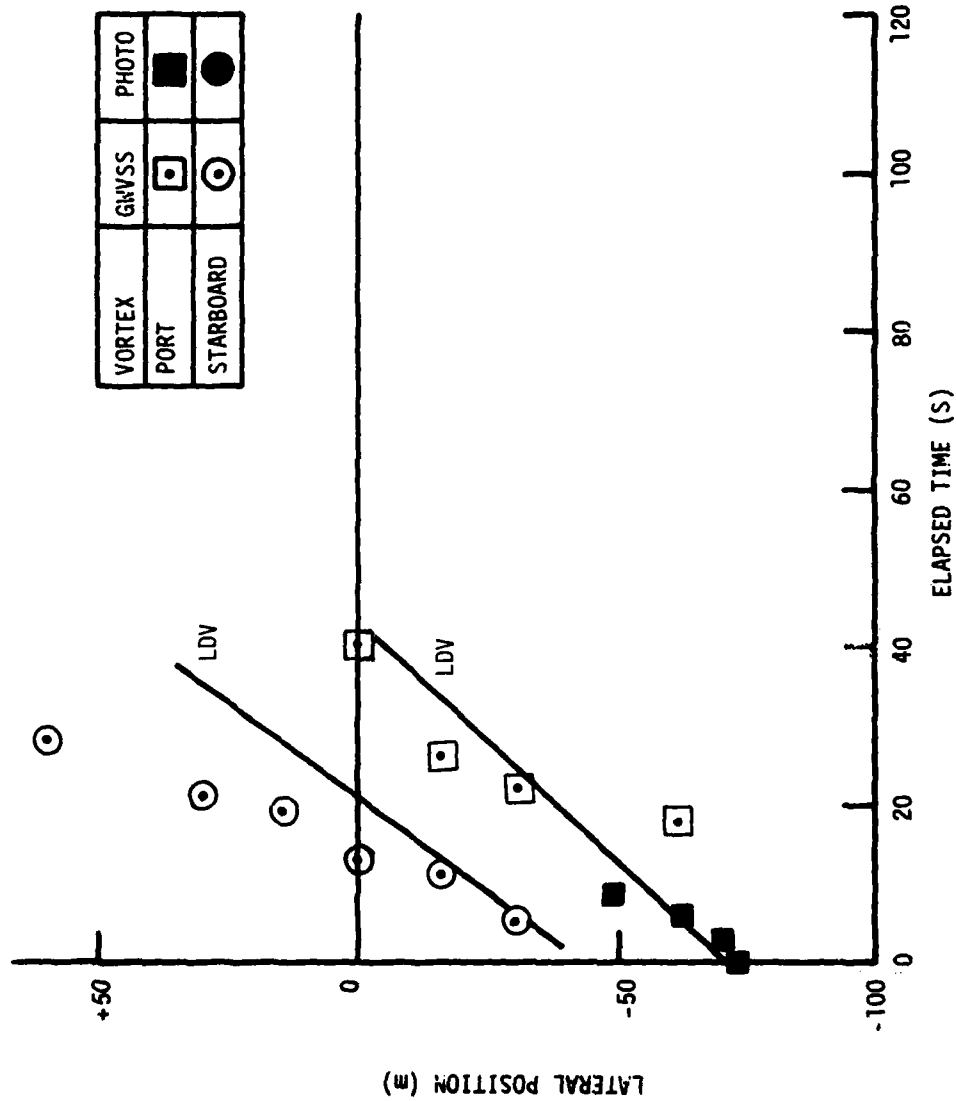


FIGURE 78. VORTEX TRAJECTORIES FOR RUN 7, 11/8/79

Run 8 11/8/79

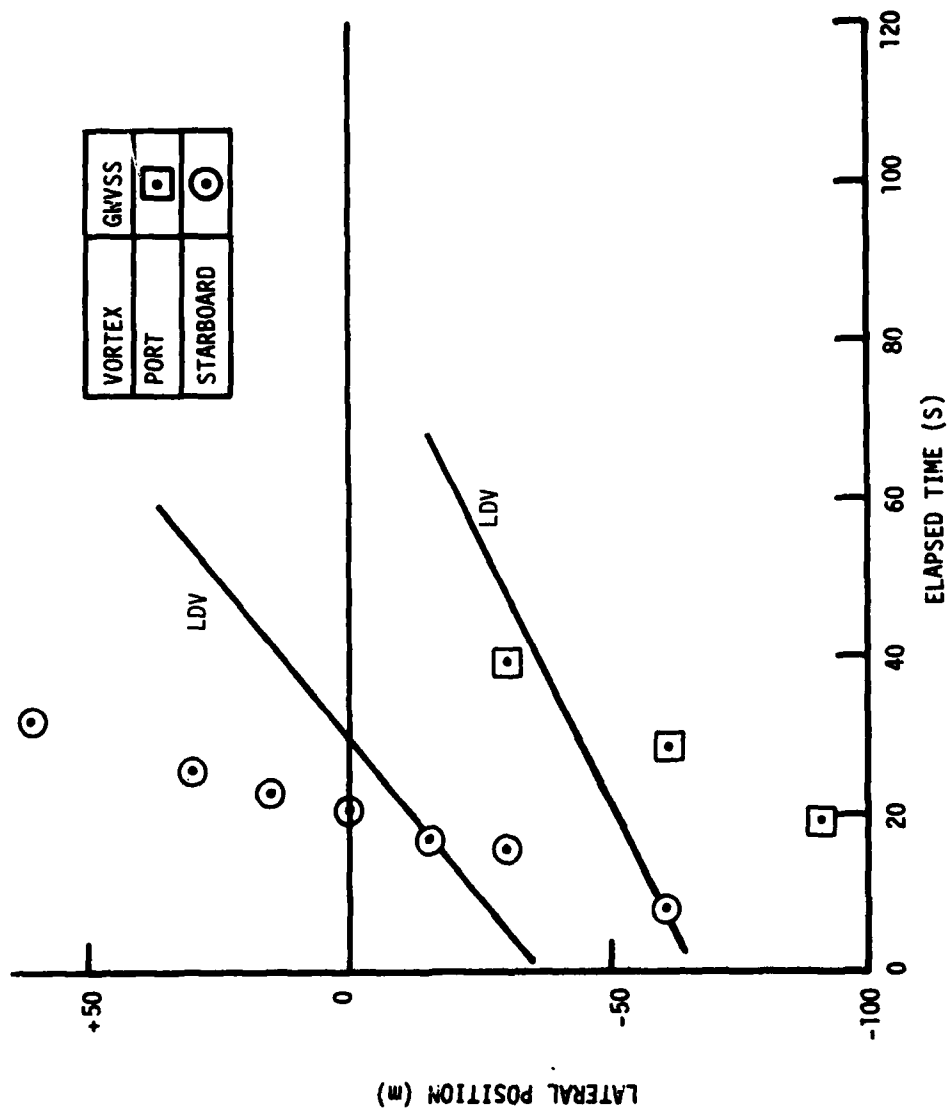


FIGURE 79. VORTEX TRAJECTORIES FOR RUN 8, 11/8/79

Run 9 11/8/79

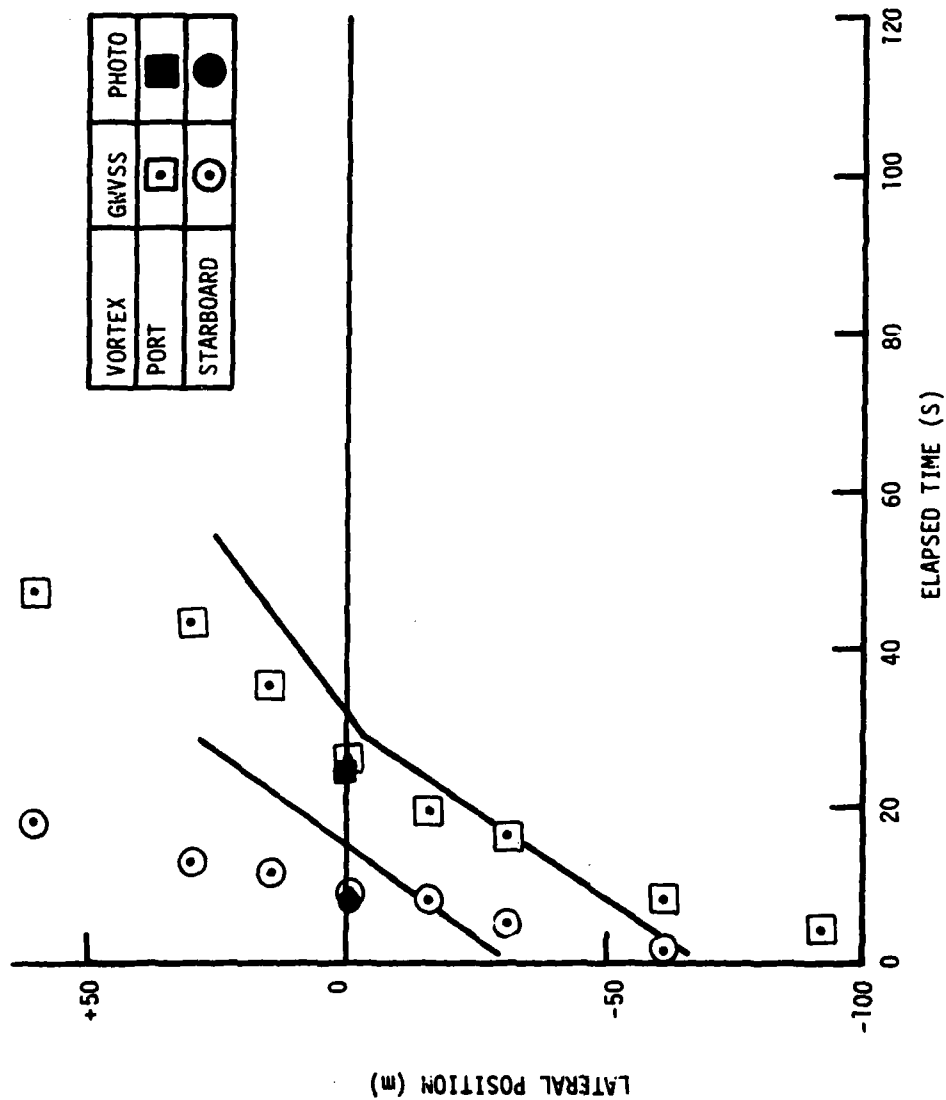


FIGURE 80. VORTEX TRAJECTORIES FOR RUN 9, 11/8/79

## APPENDIX G

### METEOROLOGICAL DATA

Figures 81-83 show the temperature profiles made during the second test series. On 11/2/79, low altitude soundings (Figure 81) were made between each run. The ground-based inversion had dissipated at about the third run (time 851)(between the third and fourth sounding). On 11/3/79, it was planned to take 300 m soundings before and after the test series with lower soundings between runs to monitor the break-up of the ground-based inversion. Because of a communications mixup with the test director, no intermediate soundings were permitted. A comparison of the 11/3/79 data with the 11/2/79 data would lead to an estimate of about 844 (Run 4) or 854 (Run 5) as the time the inversion had dissipated. Figure 83 showing the temperature profiles for 11/8/79 illustrates the planned measurements for 11/3/79. Including a high-altitude profile before and after the flight allows a more reliable interpretation of the low-altitude profiles. Over the measurement time there was no change in the temperature profile above 300 m. The temperature inversion below that level was wiped out by the surface heating.

The winds near the ground are shown in Table 8 for the runs on 11/8/79. Three sources of data are shown: Laser Doppler Velocimeter (LDV) crosswind, B-747 inertial navigation system, and meteorological profiles.



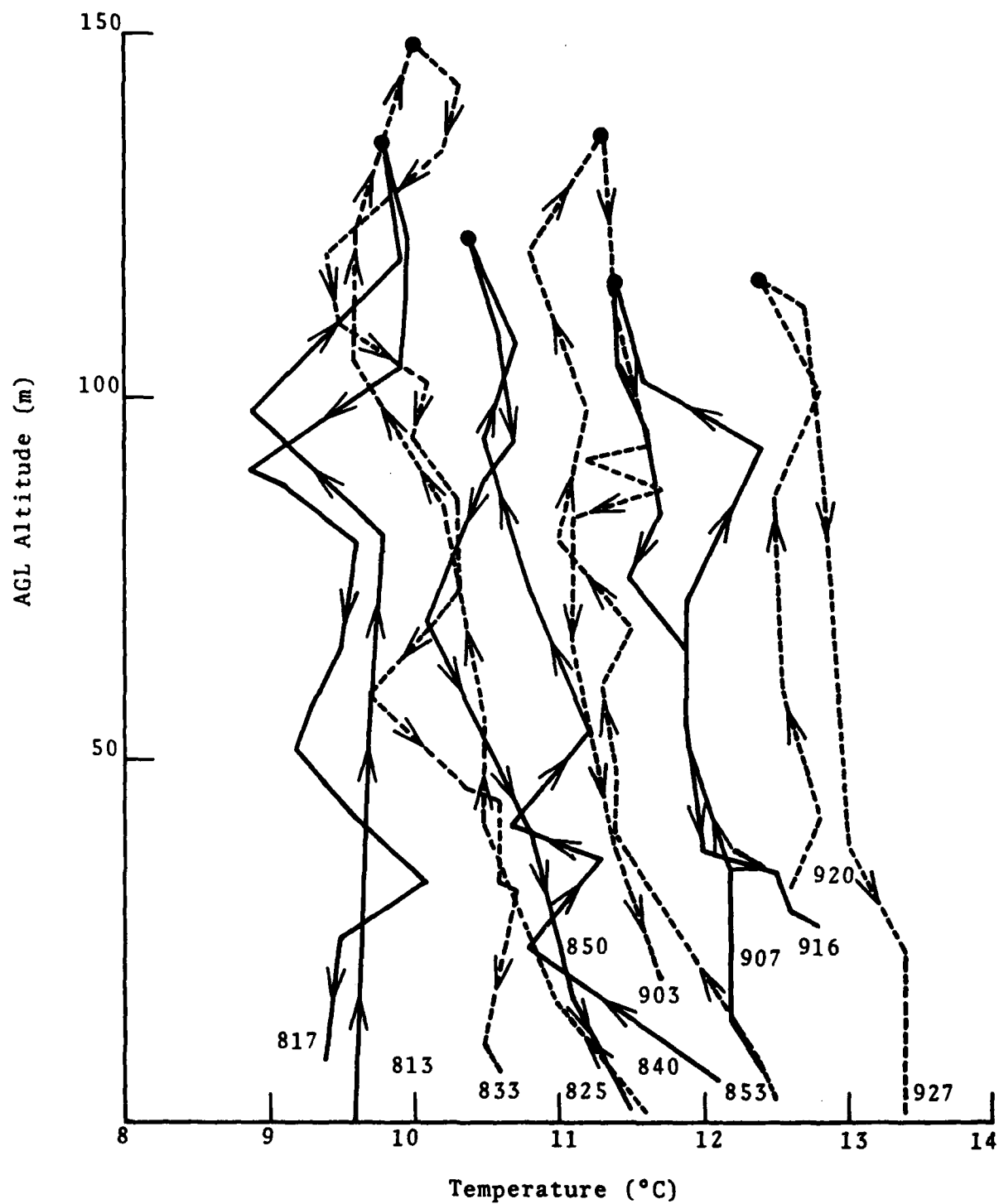


FIGURE 81. TEMPERATURE PROFILES ON 11/2/79

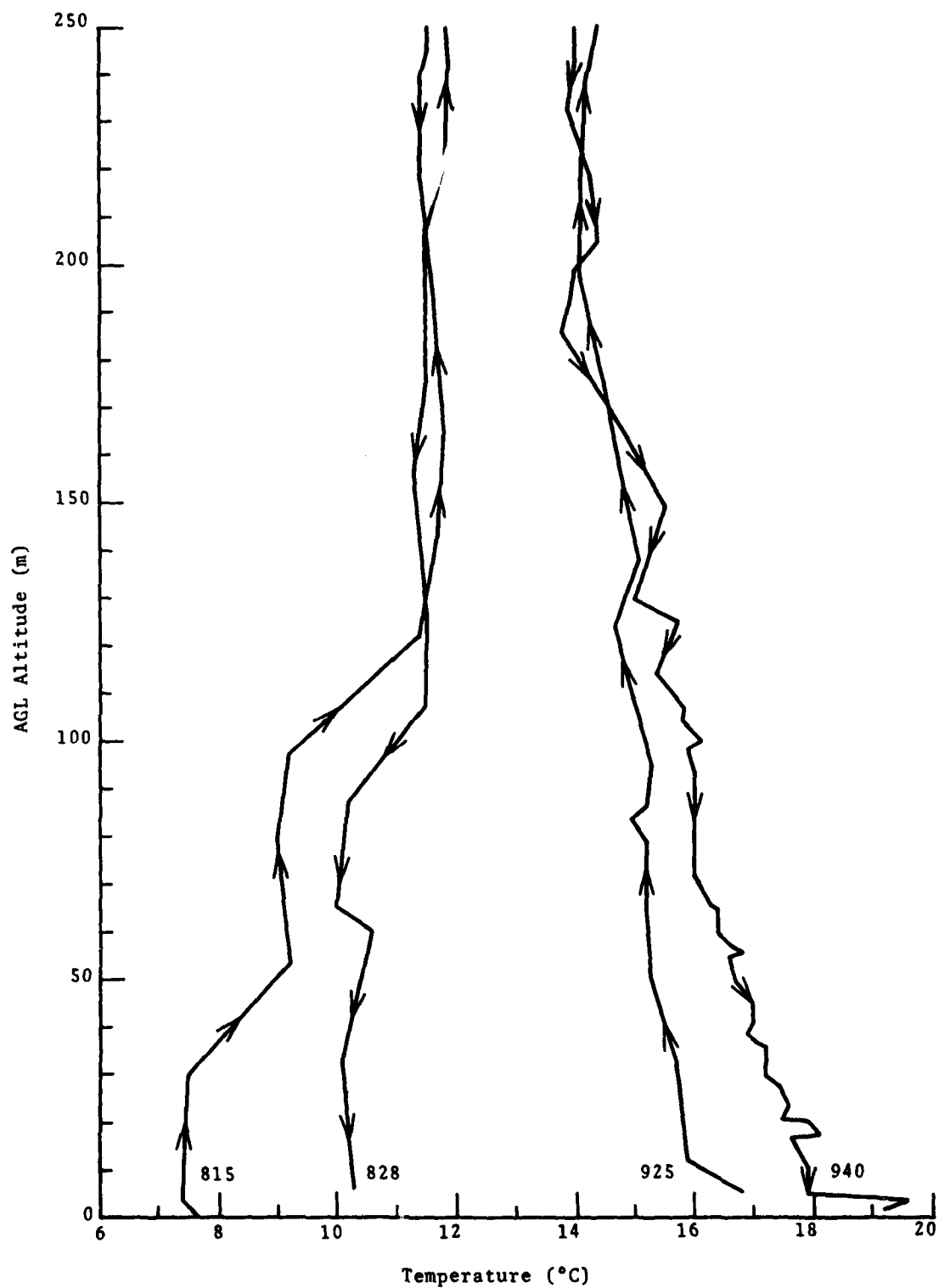


FIGURE 82. TEMPERATURE PROFILES ON 11/3/79

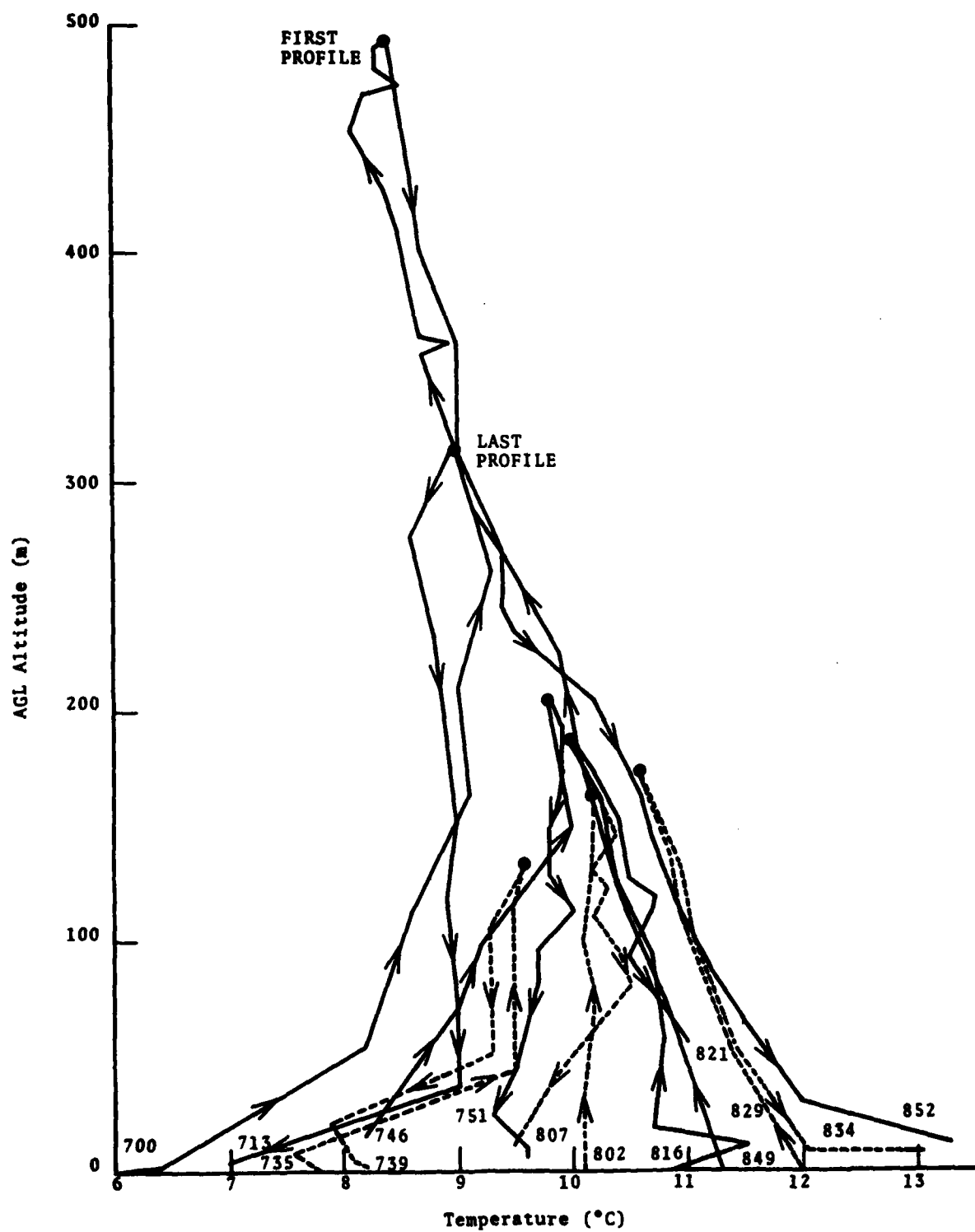


FIGURE 83. TEMPERATURE PROFILES ON 11/8/79

TABLE 8. WIND DATA FOR 11/8/80

RUN	LDV CROSSWIND	KITOON			B-747 INS		
		<u>SPEED</u>	<u>DIRECTION</u>	<u>CROSS</u>	<u>SPEED</u>	<u>DIRECTION</u>	<u>CROSS</u>
1	2. m/s	3.5 m/s	195°	1 m/s	3 m/s	185°	0.5 m/s
2					4.5	193°	1
3	(3.5)*	5	225	3.5	5.5	200°	2
4	3.5	4.5	330	4	6	233°	5
5	(4)*	4	250	4	4.5	239°	4
6	(4)*	6	250	5.5	4	235°	3.5
7	4.5	5.5	255	5.5	5	245°	4.5
8	4.5	7	225	5	6	244°	5.5
9	7	7	260	7	9.5	266°	9.5

\* Used for data processing but not measured

220 copies